EXPERIMENTAL STUDY OF SPRAY-FORMATION PROCESSES IN TWIN-FLUID JET-IN-CROSSFLOW AT JET-ENGINE OPERATING CONDITIONS

A Dissertation
Presented to
The Academic Faculty

by

Tan, Zu Puayen

In Partial Fulfillment
of the Requirements for the Degree
Doctor of Philosophy in the
School of Aerospace Engineering

Georgia Institute of Technology
MAY 2017

EXPERIMENTAL STUDY OF SPRAY-FORMATION PROCESSES IN TWIN-FLUID JET-IN-CROSSFLOW AT JET-ENGINE OPERATING CONDITIONS

Approved by:

Dr. Ben T. Zinn, Advisor
School of Aerospace Engineering
Georgia Institute of Technology

Dr. Eugene Lubarsky
School of Aerospace Engineering
Georgia Institute of Technology

Dr. Jechiel Jagoda
School of Aerospace Engineering
Georgia Institute of Technology

Dr. Caroline Genzale
School of Mechanical Engineering
Georgia Institute of Technology

Dr. Jerry M. Seitzman
School of Aerospace Engineering
Georgia Institute of Technology

Date Approved: Nov 9, 2016

This dissertation is dedicated to the spirit of endless adventures and explorations in aerospace engineering and the sciences.

ACKNOWLEDGEMENTS

The creation of this dissertation has been a turbulent journey with intermittent moments of incredible (and often serendipitous) joy when nature reveals her elegant secrets, and moments of hardship when the cutting-edge pushes back against all efforts to move forward. Reaching the destination of this journey would not have been possible without the support of many people and communities.

First, I want to thank my parents, my siblings and my relatives, whose spiritual and financial support allowed me to complete the Ph.D. program. Their support also gave me the chance to explore the risky frontiers of research, with the comfort of knowing the doors of home will always be kept open. 非常感谢你们!

Secondly, I want to thank my advisors and research mentors: Dr. Ben T. Zinn, Dr. Eugene Lubarsky, Dr. Oleksandr Bibik and Dmitriy Shcherbik, who are all wonderful individuals and top-rate researchers in their own rights. From them I received important lessons and experience on refining my vision and passion into a sharp research direction, on developing and managing large complex aerothermal research facilities, on crafting precision optical diagnostic tools, and on designing instrumentation and sensor suites. I also want to thank my mentors for supporting my often "wild-horse" ventures into new research directions, one of which developed into this dissertation. תודה רבה לך and Спасибо!

Thirdly, I want to thank Dr. Jerry Seitzman, Dr. Jechiel Jagoda and Dr. Caroline Genzale for providing guidance and agreeing to help me complete the Ph.D. defense. Thank you *very* much for your time and energy!

Next, I greatly appreciate Dr. Nayan Patel, Dr. Michael Benjamin and GE-Aviation for supporting the jet-in-crossflow research at Georgia Tech over many years, as well as for having patience and faith when things hit bumpy road.

Of course, I definitely want to thank the support of my combustion lab colleagues, whom I have developed a good camaraderie with over the years. I miss the “ZSTORM” meetings. I will miss the lunchtime intellectual discussions about science, philosophy and math (an area which I dearly want to explore more into). And unfortunately, I have discovered rather too late the entrepreneurial enthusiasms that you all harbour- many missed opportunities to collaborate on something fun there.

Last but not least, I also want to thank the <<Alive>> family on Zalera for keeping me company and allowing me to stay upbeat during the creation of this dissertation. Nothing soothes the mind better than hanging out around Gridania.

TABLE OF CONTENTS

LIST OF TABLES

LIST OF FIGURES

LIST OF SYMBOLS AND ABBREVIATIONS

A	Area or Atwood number ($A \equiv \frac{\rho_H - \rho_L}{\rho_H + \rho_L}$), H and L denotes high/low densities.
AA-JICF	Air-Assist Jet-in-Crossflow
AB-JICF	Airblast Jet-in-Crossflow
AB-SICF	Airblast Spray-in-Crossflow
ALR	Air-to-liquid (fuel) mass-flow ratio, sometimes denoted by researchers as "*GLR*"
B	Empirical constant related to surface tension
B_Y	Transfer coefficient
C_D	Drag coefficient
$C_{D,air}$	Air-nozzles discharge coefficient
$C_{D,f}$	Fuel orifice discharge coefficient
C_i	Empirical/proportionality constant pertaining to subscript *i*
CVP	Counter-Rotating Vortex Pair
d	Hard sphere molecular diameter
d_f	Fuel orifice diameter
dP	Air-nozzle pressure-drop
D_0	Initial droplet diameter.
f_ω	Frequency of vortical structures
g	Gravitational acceleration
h	Disturbance amplitude
I_{shadow}	Shadowgraph image pixel-intensity value
J	Fuel-to-crossflow momentum-flux ratio: $\frac{\rho_f U_f^2}{\rho_{cf} U_{cf}^2}$; sometimes denoted by researchers as "q"

J_{eff}	Twin-fluid-to-crossflow effective momentum-flux ratio: $\frac{A_f\rho_f U_f^2+A_{air}\rho_{air}U_{air}^2}{(A_f+A_{air})\rho_{cf}U_{cf}^2}$
JICF	Jet-in-Crossflow
k	Wavenumber: $2\pi/\lambda$
k_B	Boltzmann constant
K	Evaporation constant
KH	Kelvin-Helmholtz
L	Liquid core length (in TF-jet)
l/d	Injection bore length-to-diameter ratio
LBI	Lean Burn Injector
M	Gas-to-liquid momentum-flu ratio: $\rho_g U_g^2/\rho_f U_f^2$
m	Molecular mass
$\dot{m}$	Mass flow-rate
MW	Molecular weight
N	Degree of light-attenuation: $\left[1-\frac{I_{shadow}(z,x)}{I_{shadow}(Background)}\right]\times 100\%$
P	Pressure
P_1	Parameter describing penetration magnitude
Re_d	Fuel/liquid Reynolds number: $\rho_f U_f d_f/\mu_f$
RT	Rayleigh-Taylor
R_u	Universal gas constant
SG	Specific gravity
SMD	Sauter Mean Diameter
t	Time
t_d	Droplet lifetime
t_ω	Jet profile thickness
T	Temperature

TAPS	Twin Annular Premixing Swirler (fuel-air mixer design)
TF-jet	Twin-fluid jet in quiescent medium
TF-JICF	Twin-Fluid Jet-in-Crossflow
U	Velocity
VR	Air-to-fuel velocity ratio: $U_{air}/\ U_f$
We_{aero}	Aerodynamic Weber number: $\rho_{gas}U_{relative}^2 d_f/\sigma_f$
We_{cf}	Crossflow Weber number: $\frac{\rho_{cf}U_{cf}^2 d_f}{\sigma_f}$
We_{crit}	Droplet critical Weber number: $\frac{\rho_{cf}U_{rel}^2 d_{drop}}{\sigma_f}$
We_{gas}	Gas Weber number: $\rho_{gas}U_{gas}^2 d_f/\sigma_f$
WFF	White Flat-Field image
x	Distance in the penetration/injection direction
X_f	Fuel mole fraction
Y_f	Fuel mass fraction
z	Distance in the crossflow direction
γ	Specific heats ratio
δ	Characteristic length-scale
$\mathcal{D}_{AB}$	Binary diffusion coefficient
η	Rayleigh-Taylor wave temporal growth-rate
λ	Wavelength
μ	Dynamic viscosity
ν	Kinematic viscosity
ρ	Density
σ_f	Fuel surface tension
$\theta_{droplets}$	Droplets ejection angle from jet surface
θ_f	Half vertex-angle of liquid jet

θ_{spray}	Total TF-jet spray angle: $\theta_{droplets} - \theta_f$

Subscripts and Superscripts

‘	Fluctuation/turbulent property
air	Co-injected air or nitrogen, also more generally referred to as “*gas*” when other types of fluid are used
c	Convection (velocity)
cf	Crossflow
drop	Droplet
e	Entrainment (relating to entrainment-velocity)
f	fuel
impinge	Impingement component of velocity
jet	Relating to average jet properties
max	Maximum
p	Solid particles
prompt	Prompt atomization
rel	Relative (e.g., velocity)
s	Droplet surface property
RT,x	Relating to convection velocity of RT-waves in the *x* direction
ω	Relating to vortical structures
∞	Freestream

SUMMARY

The jet-in-crossflow (JICF) fuel-injection technique is widely applied in modern jet-engine fuel-air mixers to provide rapid fuel atomization and mixing. However, the "Classical" JICF places large amounts of fuel into the initial jet/spray's recirculation zone and the wall boundary-layer, both of which can risk flashback and fuel-coking on the wall, particularly for next-generation jet-engines that will operate at increasingly higher pressures and temperatures. Twin-Fluid (TF) JICF, where streams of air are co-injected with the fuel jet into the crossflow, is being considered as a way to mitigate the Classical-JICF's shortcomings. However, the TF-JICF is a nascent fuel-injection technique that is not well understood, especially at the high operating pressures of jet-engines. This dissertation reports an experimental investigation of TF-JICF where liquid Jet-A fuel was co-injected with pressurized nitrogen into a crossflow of air. The developed fuel sprays were characterized using shadowgraphy. The fuel-to-crossflow momentum-flux ratios were varied from J=5-40, the air-nozzles pressure-drops were varied from dP=0-150% of crossflow pressure, and the crossflow Weber numbers were varied from We_{cf}=175-1050. These operating conditions allowed us to obtain a dataset that is both comparable with near-atmospheric studies of TF-JICF in the literature and applicable to jet-engines. The results show that TF-JICF can be classified into four spray-formation regimes (i.e., Classical-JICF, Air-Assist JICF, Airblast JICF and Airblast Spray-in-Crossflow), each containing a unique set of spray characteristics and mechanisms. In the Air-Assist regime that spans dP≈3-13%, the injected air formed a protective air-sheath around the initial fuel jet, which inhibited the development of Rayleigh-Taylor waves and surface-shearing (i.e., disturbances created by the crossflow), thus reducing the near-wall fuel concentrations. Applying higher levels of dP transitioned the spray into the Airblast JICF regime, where the intensified fuel-air impingement and shearing generated new disturbances on the jet. These

generally caused the near-wall regions to become repopulated with fuel droplets (i.e., counter-productive towards mitigating flashback and wall-coking). When *dP* was higher than 100%, the jet became completely atomized by air prior to encountering the crossflow, producing an "Airblast Spray-in-Crossflow". The resulting spray-plume's penetration became related to the combination of the fuel and air's momentum-fluxes, where increasing *dP* caused increasing separation between the spray-plume and test-channel wall. This reduces the near-wall fuel concentrations and is beneficial towards fuel-air mixer design, although the required levels of *dP* for this regime is likely too high for practical jet-engine operation.

CHAPTER 1. INTRODUCTION

This dissertation describes an investigation of a new class of jet-engine fuel-injection technique called the "twin-fluid jet-in-crossflow" (TF-JICF). As Figure 1.1 shows, modern jet-engines have annular combustors that must support stable, efficient and clean combustion of fuel in the smallest volume possible. The combustor volume is continuously supplied with fresh combustible mixtures by a multitude of "fuel-air mixers" that are evenly spaced around the combustor's inlet. While the detailed designs of fuel-air mixers vary between manufacturers, most of them incorporate a centrally located pressure-swirl atomizer surrounded by swirling airflows into which the pilot-fuel is injected for low-power engine operation. Most of them also feature a separate outermost annulus that contains a swirling airflow, which can be introduced into the annulus axially, radially or both, as shown in the case of Figure 1.1 based on General-Electric's design by Hsieh et al. (2008). For high-power engine operation, the main-fuel is radially injected via multiple orifices into this outer annulus, where they form multiple jets in the crossflow (CF) of swirling air whose temperatures and pressures may reach $650^{o}C$ and $50atm$, respectively (Dodds 2005, Tambe et al. 2005, Foust et al. 2012, Myers et al. 2013, General Electric 2015). Subsequently, the momentum of the crossflow redirects the fuel into the flow direction and atomizes the fuel into fine droplets that rapidly evaporate and mix with the air. The rates of atomization, vaporization and mixing determine the minimum length of the fuel-air mixer. On the other hand, the spatial distribution of fuel within the final combustible mixture influences engine emissions, combustion stability and the exhaust temperature patternation. In essence, combustion performance and engine durability is strongly tied to the fuel-air mixer's performance. The main-fuel injection technique described in Figure 1.1 is called a jet-in-crossflow (JICF). This technique is commonly chosen over other methods of liquid fuel atomization because it can provide fuel flow-independent atomization quality and

rapid fuel-air mixing, while requiring low fuel-nozzle pressure-drops (i.e., low pumping requirement).

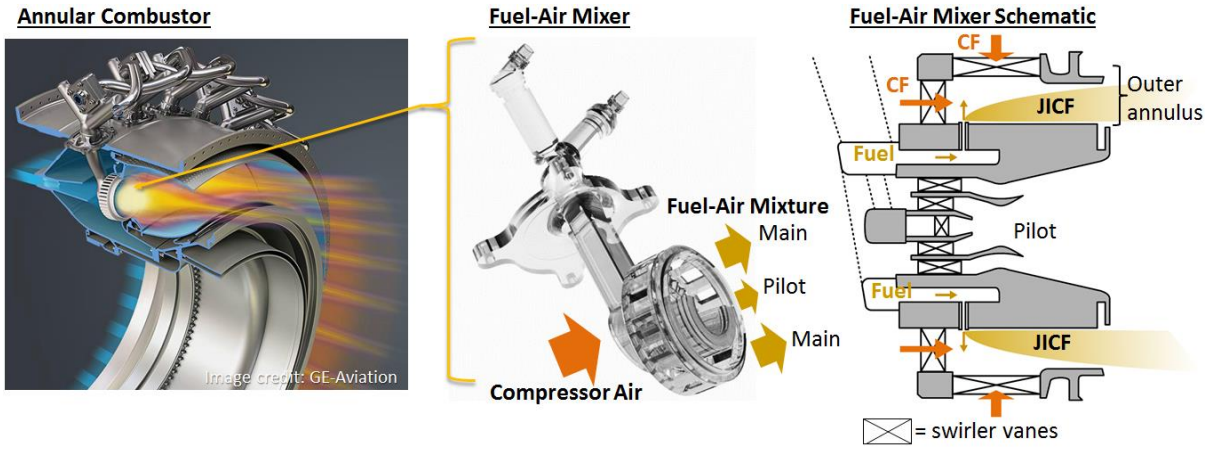

Figure 1.1 – ***Left*****: A cut-away of an annular combustor (GE Aviation 2014).** ***Center and right*****: its fuel-air mixer, illustrated based on Hsieh et al. (2008), Dodds (2005), Foust et al. (2012) and Myers et al. (2013).**

Despite its effectiveness, JICF fuel-injection also raises several design concerns. For example, the penetration of the JICF fuel spray varies strongly with fuel flow-rate, resulting in flow-rate-dependent fuel distribution and flame patternation. At the same time, as shown in Figure 1.2, there is also concern for the potential impingement of fuel droplets onto the near/far-wall of the mixer device's annulus at low/high fuel flow-rates, respectively (Tambe et al. 2005), which can lead to wall-coking that degrades the device's durability. In addition, as shown in Figure 1.2, regions of low-velocity such as the boundary-layer and the JICF spray's wake where hot fuel-air mixtures may reside could lead to flashback that damages the device (Fu et al. 2014)- a problem that is becoming increasingly pertinent as engine operating pressures and temperatures continue to increase.

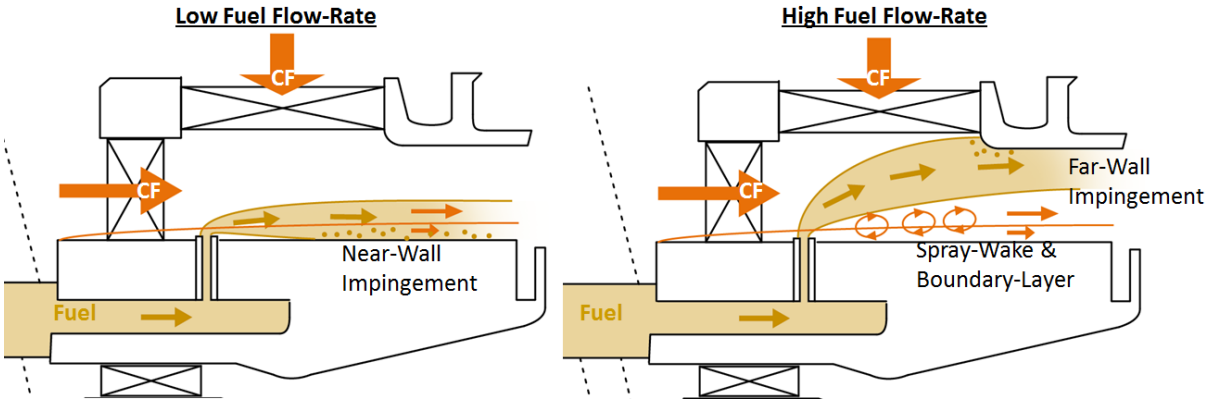

Figure 1.2 – Illustrations of fuel-wall impingement and long residence-time regions in the fuel-air mixer at low (*left*) and high (*right*) fuel flow-rates.

The design concerns associated with JICF injection spurred the recent development of a new class of fuel-injection technique called the Twin-Fluid (TF) JICF, where the liquid fuel is co-injected with airstreams that surround it concentrically, in order to modify the evolution of the spray pattern. The limited number of TF-JICF designs and studies include the works of Samuelsen (1995), Leong et al. (2000, 2001), Li et al. (2006, 2009, 2010 *Part 1*, 2010 *Part 2*), Fu et al. (2014), Sinha and Ravikrishna (2013), and Sinha et al. (2015). A detailed review of these works will be presented in Section 2.2. However, before proceeding further, it is worth discussing a particular new TF-JICF fuel-injector design that is being applied to next-generation jet-engines, and which motivates this investigation. This design is the latest generation of Twin Annular Premixing Swirler (TAPS) fuel-air mixer by GE-Aviation (Hsieh et al. 2008). As shown in Figure 1.3, it contains a central pressure-swirl atomizer for pilot-fuel injection and an outer annulus for main-fuel injection, much like the design shown in Figure 1.1. However, unlike Figure 1.1, the TAPS employing TF-JICF features an additional sleeve-plenum below the main-fuel annulus, into which a portion of the combustor inlet air ("assist-air" in Figure 1.3) is diverted. This air is injected into the crossflow through large radial air-nozzles. At the center of each nozzle orifice is a stem containing the smaller main-fuel orifice. Variations of the air-nozzles exist, where the air can be injected parallel to the fuel, impinging on the fuel or even swirling. As claimed in the patent by Hsieh et al. (2008), the air was intended

to sheath the fuel jet from the crossflow in order to assist its penetration into the center of the annulus away from the walls. Hence, this design was called the "air-assist" (AA) JICF. Notably, because the assisting air in this design is directly extracted from the forward-face of the fuel-air mixer (instead of being pumped from a separate air compressor), the pressure-drop (*dP*) across the air nozzle is driven by the combustor inlet air's dynamic pressure, which is typically on the order of <10% of crossflow static pressure. Thus, based on the latest TAPS design, it is crucial to develop an understanding of TF-JICF characteristics and spray-formation processes, especially for operations with air-nozzle *dP* on the order of 10% of crossflow pressure.

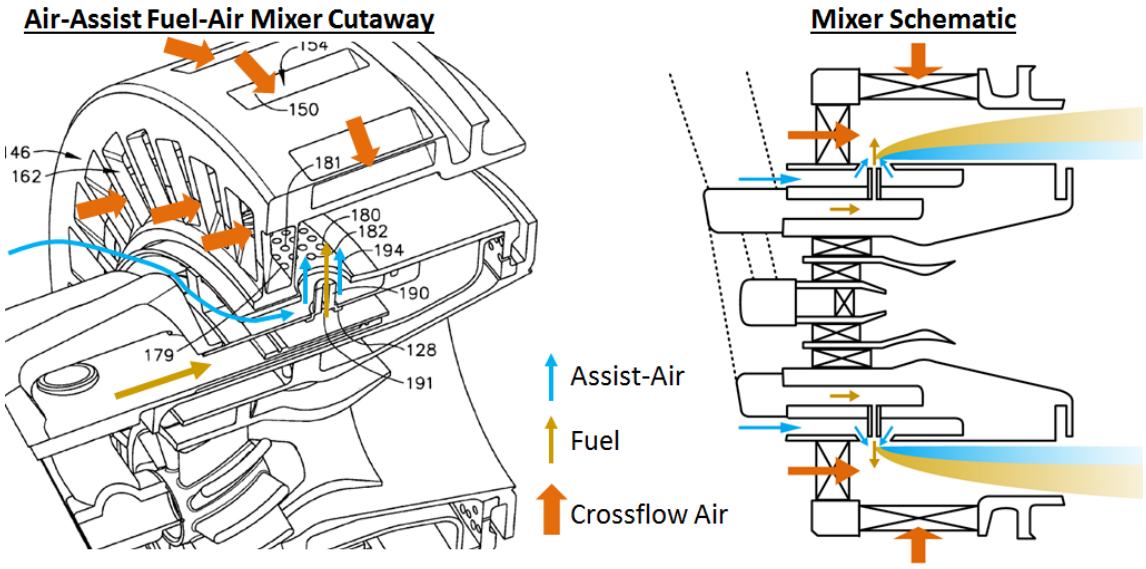

Figure 1.3 – *Left:* A variation of the TAPS fuel-air mixer that employs TF-JICF (Hsieh et al. 2008). *Right:* A simplified schematic of TF-JICF TAPS (compared to "Classical-JICF" TAPS in Figure 1.1).

As shown in the operating parameter space in Figure 1.4, despite the immediate relevance of low *dP* TF-JICF to next-generation jet-engines, most of the existing TF-JICF studies only focused on the domains of high *dP*, where the air's momentum and kinetic energy were very large compared to the fuel's. Although Leong et al. (2000, 2001) investigated TF-JICF with *dP*<10%, their data were obtained at fuel flow-rates and air-to-liquid mass-flow ratios (*ALR*) that were outside of the range anticipated for AA-JICF TAPS operation. As a brief background, in these studies of high *dP* and/or high *ALR* TF-JICF, researchers commonly

observed that the injected liquid jets underwent near-instantaneous atomization and mixing with the co-injected air. Consequently, the generated droplets exchanged their momentum with the high-velocity air rapidly, and the resulting sprays penetrations were found to be scalable by an effective momentum-flux ratio (J_{eff}), defined as follows:

$$J_{eff} = (\textit{air momentum-flux} + \textit{liquid momentum-flux}) / (\textit{crossflow momentum-flux}) \quad (1)$$

The J_{eff} penetration-scaling was first introduced by Leong et al. (2000) and subsequently adopted by the general TF-JICF research community, which applied it to correlate the trajectories of TF-JICF produced by different nozzle designs at different operating conditions. The J_{eff} parameter was considered to be applicable to all TF-JICF until a recent study by Sinha et al. (2015) reported the absence of near-instantaneous jet atomization by air at lower levels of *dP* and, subsequently, deviations from the J_{eff}-scaling. Their results suggested the presence of new TF-JICF regime(s) within the low *dP* and *ALR* domain. These potential new regimes and the spray-formation processes therein were not thoroughly explored by Sinha et al. (2015).

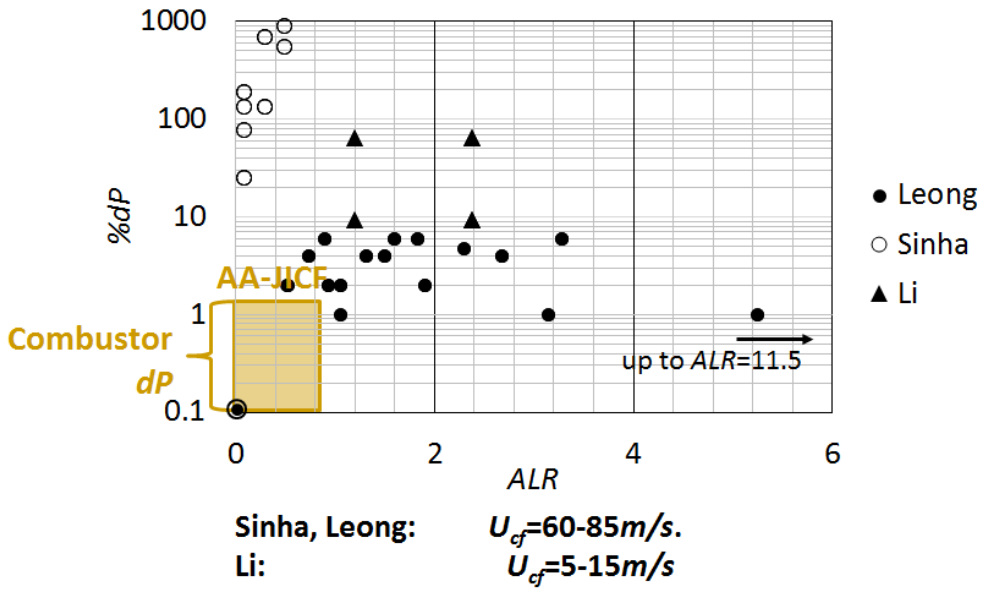

Figure 1.4 – Operating parameter space for TF-JICF. Existing studies were all conducted at 1*atm* where We_{cf} < 200, except Leong et al.'s (2000, 2001)'s tests at 5*atm*. Injector fuel-air relative angles varied from 0-90^o.

Additionally, Figure 1.4 shows that the majority of TF-JICF investigations were carried out at near-atmospheric pressures, where the crossflow's intensities (expressed in terms of the Weber number, $We_{cf} = \rho_f U_{cf} d_f / \sigma_f$) were relatively weak. These conditions are known in the Classical-JICF literature to produce sprays with characteristics that differ significantly from sprays at high, jet-engine operating pressures. Therefore, it is likely that the reported TF-JICF results are not directly applicable to TF-JICF in jet-engine fuel-air mixers.

In essence, an important gap currently exists in the TF-JICF literature. The characteristics of TF-JICF produced by low air-nozzle *dP*, low *ALR* and high crossflow pressure are not well understood, in spite of its immediate relevance to jet-engine applications. To address this gap, this dissertation work was conducted with four objectives:

i. To experimentally characterize the TF-JICF produced by an injector that is representative of the configurations intended for jet-engine application. To characterize the TF-JICF across wide ranges of air-nozzle *dP*, fuel flow-rates and crossflow Weber number, in order to obtain a dataset that is comparable to the existing literature, as well as applicable to fuel-air mixers.

ii. To identify the major characteristics of the TF-JICF, as well as their dependence on *dP*, fuel flow-rate and We_{cf}. To determine whether the characterized TF-JICF exhibit different regimes of behaviour (as suggested by Sinha et al.'s study).

iii. To develop a qualitative understanding of the TF-JICF spray-formation processes that explains the observed characteristics, trends and regimes.

iv. To determine whether the reported findings in TF-JICF literature are applicable to our results; i.e., to assess the generality of the TF-JICF mechanisms proposed in the literature.

The stated objectives were achieved by injecting liquid Jet-A fuel into a specialized high-pressure/temperature JICF test-facility using a custom TF-JICF injector device that is

representative of next-generation jet-engine's fuel-air mixers. Nitrogen gas (approximating air) from high-pressure cylinders were used to drive a large range of *dP* values across the air-nozzles, allowing us to cover a large portion of the parameter space in Figure 1.4. Shadowgraph-imaging was used to characterize the TF-JICF sprays. Characteristics such as the spray's outer-edge and centerline trajectories, spray-density distributions and initial jet disturbance amplitudes were extracted from the shadowgraph images and analyzed to elucidate the TF-JICF's characteristics and mechanisms.

As an overview, Chapter 2 of this dissertation provides the discussion-relevant background knowledge of liquid Classical-JICF, TF-JICF, and TF-jets in quiescent gas. Chapter 3 describes the employed experimental setup, diagnostic tools, data-processing schemes and design of experiment. Chapters 4 to 7 cover the experimental results, where each chapter is dedicated to an identified TF-JICF regime. Finally, Chapter 8 summarizes the developed understandings of TF-JICF and their implications on fuel-air mixer designs for next-generation jet-engines. Future research directions to further the knowledge of TF-JICF are also proposed in Chapter 8.

CHAPTER 2. BACKGROUND

2.1 Classical Jet-in-Crossflow

Figure 2.1 shows four types of liquid atomizers related to this investigation. The simplest case on the left is a plain-jet injected into quiescent gas, where the primary atomization and mixing forces arise from the aerodynamic shearing of the liquid against the quiescent gas. To enhance atomization and mixing, a crossflow or a co-flow of gas can be introduced around the liquid jet to modify its aerodynamic interactions. These more advanced atomizers are called jet-in-crossflow (Classical-JICF) and twin-fluid jets in quiescent gas (TF-jets), respectively. In the most complex case, as shown on the right of Figure 2.1, the crossflow and co-flow are both present. The physics of such a configuration, which is called the Twin-Fluid JICF, is largely unexplored. This chapter provides reviews of research conducted to date on Classical-JICF, TF-JICF and TF-jets in order to set up the necessary background for this dissertation.

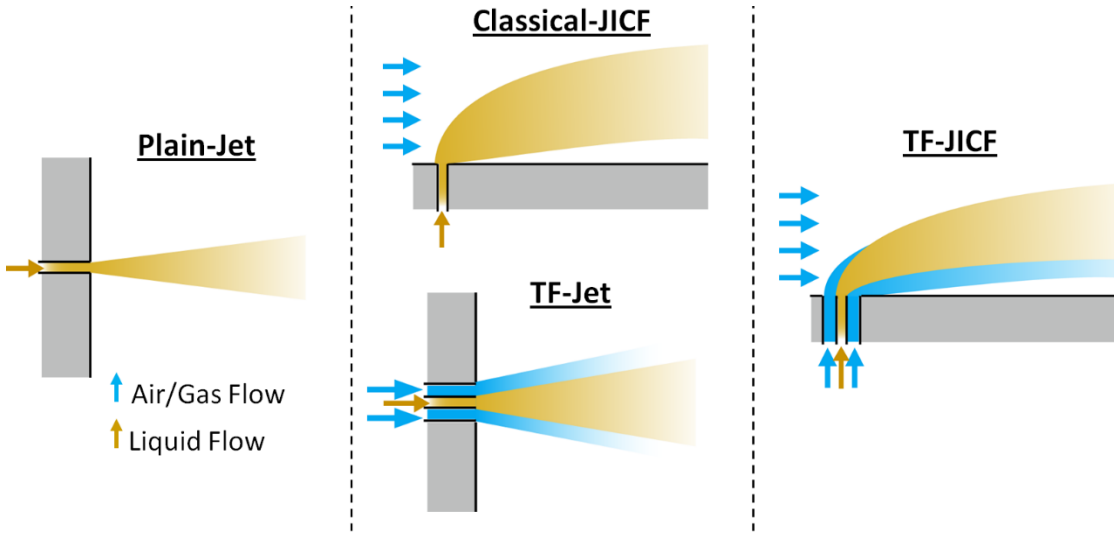

Figure 2.1 – Illustrations of atomizers related to this investigation, from the physically simplest (*left*) to the most complex (*right*) configurations.

The Classical-JICF is a canonical flow configuration that can be found in many industrial applications and has been extensively studied to date. However, despite a Classical-JICF injector's mechanical simplicity and its long history, the characteristics and underlying

fluid processes of a Classical-JICF spray are extremely complex and remain an area of active research. Conceptual models of Classical-JICF can be found in the works of Catton et al. (1968), Schetz et al. (1980), Less and Schetz (1986), Nguyen and Karagozian (1992), Fuller et al. (2000) and Sedarsky et al. (2010) among many others. These models are diverse and generally focus on isolated aspects of the spray. Nonetheless, the diverse Classical-JICF research areas can be chiefly categorized under the studies of i) the initial jet's instability, disintegration and droplets formation, and ii) global spray characteristics such as spray penetration and dispersion. We review both categories below.

2.1.1: Jet Instability, Disintegration and Droplets Formation

The liquids in Classical-JICF are typically injected at low velocities with low nozzle pressure-drops. In the absence of the crossflow, the low-velocity liquid would persist for considerable distance as an intact liquid jet. However, in the presence of crossflow, the impact and acceleration of crossflow gas around the initial jet column (as illustrated in Figure 2.2) form a high-pressure stagnation zone on the jet's windward side and low-pressure zones on the jet's lateral sides. A low pressure zone is also formed on the leeward side where flow separation and recirculation occur. As Mazallon et al. (1999), Thomas and Schetz (1985), Wu et al. (1997) and Sallam et al. (2004) reported, and as Figure 2.2 also shows, the combination of pressure forces flattens the jet's cross-section into an ellipse, which grows progressively wider/flatter with distance from the injection point. At the same time, the shearing forces generated by the acceleration of the gas around the jet's lateral sides causes the jet's cross-section to deform into a kidney-shape. This is accompanied by the formation of a vortex pair within the jet.

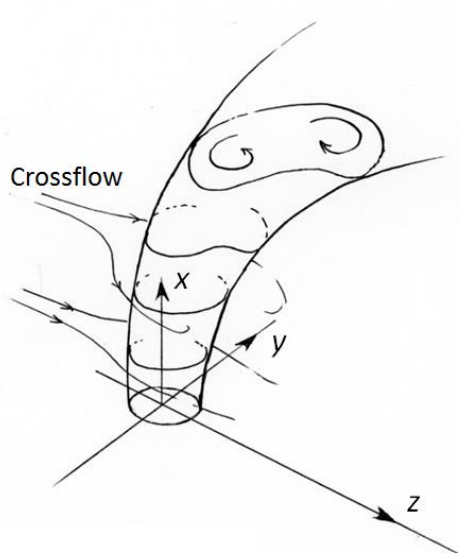

Figure 2.2 – A depiction of a liquid jet deforming under the influence of crossflow.

As shown in Figure 2.2, the combination of pressure forces and viscous shearing on the jet also bends the jet into the crossflow direction. In the process of bending, the jet tends to develop large-scale instabilities. The superposition of these instabilities on the bending jet is illustrated in Figure 2.3. These instabilities are commonly referred to as Rayleigh-Taylor (RT) waves. They form when a light fluid (i.e., the crossflow) is accelerated at a non-zero angle against the interface of a heavier fluid (i.e., the liquid jet) (Schetz et al., 1979 and Sharp, 1984). Images taken by Inamura & Nagai (1993) and Mazallon et al. (1999) show that the structures of the RT-waves strongly depend on the intensity of the crossflow, which is commonly expressed as the crossflow aerodynamic Weber number (We_{cf}), as defined below:

$$We_{cf} = \frac{\rho_{cf} U_{cf}^2 d_f}{\sigma_f} \tag{1}$$

where the subscript cf denotes the crossflow, and f denotes the fuel/liquid. The variables ρ, U and d_f are density, velocity and fuel orifice diameter, respectively. At low We_{cf}, the RT-waves begin development as large sinuous waves. However, with time, the windward-facing wave crests develop into sharp cusps that subsequently thicken into nodes, as illustrated in Figure 2.3. Meanwhile, the leeward-facing troughs are stretched into the crossflow direction and grow thinner until they are eventually pinched off due to capillary forces, thus truncating the jet. At

high We_{cf}, the RT-waves' wavelength becomes smaller, and the growing concentration of fluid in the windward-edge's nodes may give the jet an overall varicose/beaded appearance.

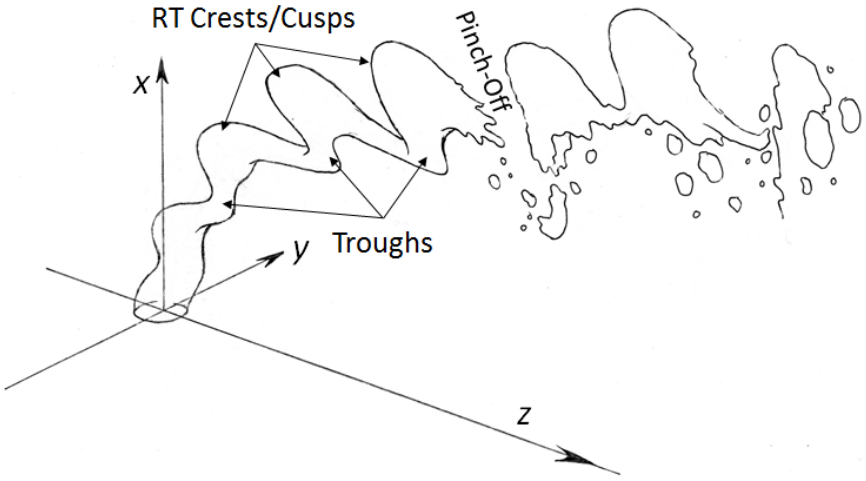

Figure 2.3 – A depicture of Rayleigh-Taylor (RT) waves and jet pinch-off.

As the studies of Sherman and Schetz (1971), Schetz et al., (1979), Thomas and Schetz (1985), Becker and Hassa (2002) and Sallam et al. (2004) found, the truncation of the jet due to pinch-off as described above usually happens only once every few wavelengths when a particularly deep wave trough is encountered. Thus, the pinch-off process usually cause large clusters of liquid, multiple wavelengths long, to be detached from the jet and shed into the crossflow, as illustrated in Figure 2.3. These clusters generated by RT-wave pinch-offs will continue to disintegrate into increasingly smaller clusters and droplets, which generally remain closely located to each other as they are convected along the crossflow. The plume of highly concentrated clusters and droplets originating from RT-wave pinch-offs is referred to as the "spray-core".

Inamura et al. (1993) and Sallam et al. (2004) observed that RT-waves travel along the jet at near the liquid injection velocity when the jet has not been bent by more than 20^o. However, when the jet is bent more than 40^o, the RT-waves travel at close to the crossflow's velocity due to convection by the crossflow. While being convected, the RT-waves continue to grow in amplitudes and wavelengths. The amplitude growth-rate was observed by Inamura and

Nagai (1997) and Wu et al. (1997) to be particularly high when the jet is undergoing its highest rate of bending by the crossflow. On the other hand, the work of Ng et al. (2008) provides an analytical model for the growth of RT-waves. They proposed that the waves' amplitudes (h_{RT}) grow exponentially in time (t) with a temporal growth-rate η; i.e.,

$$h_{RT} = e^{\eta t} \tag{2}$$

In the original study of RT instabilities, where fluid acceleration occurs due to buoyancy forces, the growth-rate was derived as:

$$\eta = \sqrt{gkA} \tag{3}$$

where g is the gravitational acceleration, $k = 2\pi/\lambda$ is the wave number and λ is the wavelength. $A \equiv \frac{\rho_H - \rho_L}{\rho_H + \rho_L}$ is the Atwood number, where subscripts H and L denote the heavier and lighter fluids. Ng et al. (2008) modified η to model JICF's RT-waves by introducing surface tension (which has the effect of setting a preferred wave number for RT growth (Sharp 1984)), replacing g by aerodynamic drag forces and assuming that $\rho_f \gg \rho_{cf}$. The new expression for growth-rate is given as:

$$\eta = \left[k \left(\frac{2C_D \rho_{cf} U_{cf}^2}{\pi \rho_f d_f} \right) - \frac{k^3 \sigma_f}{\rho_f} \right]^{0.5} \tag{4}$$

where C_D is the jet's drag coefficient. As Equation (4) shows, the growth-rate is dependent on wave number k. Next, Ng et al. (2008) proposed that the jet's RT-waves are dominated by the wavelength having the maximum growth-rate. To find this wavelength's wave number (k_{max}), they calculated the k-derivative of η and set it to zero, where:

$$\frac{d\eta}{dk_{max}} = 0 \tag{5}$$

$$\therefore k_{max} = \frac{2C_D}{3\pi} \frac{\rho_{cf} U_{cf}^2}{\sigma_f} \frac{1}{d_f} \tag{6}$$

$$\therefore \frac{\lambda_{RT}}{d_f} = C_\lambda \sqrt{\frac{6\pi}{C_D}} We_{cf}^{-0.5} \tag{7}$$

where λ_{RT} is the primary RT-waves' wavelength, and C_λ is an empirical constant. This derivation agreed reasonably well with Mazallon et al. (1999)'s empirical wavelength correlation:

$$\frac{\lambda_{RT}}{d_f} = 16.3We_{cf}^{-0.79} \tag{8}$$

Equations (4) and (7) show that crossflow velocity and density have dominant roles in RT-wave formation. On the other hand, the liquid velocity does not seem to affect the temporal growth-rate (although, given a constant temporal growth-rate, the spatial growth-rate of RT-waves will be lower when the liquid velocity is higher). Though the expressions above suggest a single preferred wavelength for RT-waves, experimental studies have observed that RT-waves on JICF are, in fact, broadband, consisting of a wide range of wavelengths. Becker and Hassa (2002) proposed that the observed unsteadiness of RT wavelengths may be connected to the unsteadiness in the crossflow, especially in the test-channel's boundary-layer.

In addition to RT-waves, a second type of instability is formed on the jet surface when We_{cf} is high, with wave-fronts that are aligned perpendicular to the crossflow and RT-waves. These instabilities are superimposed upon the RT-waves, as illustrated in Figure 2.4, and are commonly called Kevin-Helmholtz (KH) waves, acceleration wave or shear instabilities by Adelberg (1968), Mashayek et al. (2008), Sedarsky et al. (2010) and Behzad et al. (2015, 2016). The KH-waves are developed through shearing between the crossflow gas and the liquid jet. They have wavelengths that are typically on the order of 10% of the liquid jet diameter, smaller than the RT-waves' wavelengths. As KH-waves travel around the periphery of the jet their amplitudes grow, resulting in the development of liquid sheets that stretch and break into ligaments on the jet's lateral sides, where the local shearing is strongest due to the acceleration of crossflow around the jet. Each ligament then stretches and thins until it is pinched off by capillary forces, forming small droplets that are readily entrained into the crossflow, as shown on the bottom right of Figure 2.4. This mode of disintegration is called "shear-stripping",

"surface-shearing" or "shear-disintegration" by Ingebo (1985), Wu et al. (1997), Mazallon et al. (1999) and Sallam et al. (2004).

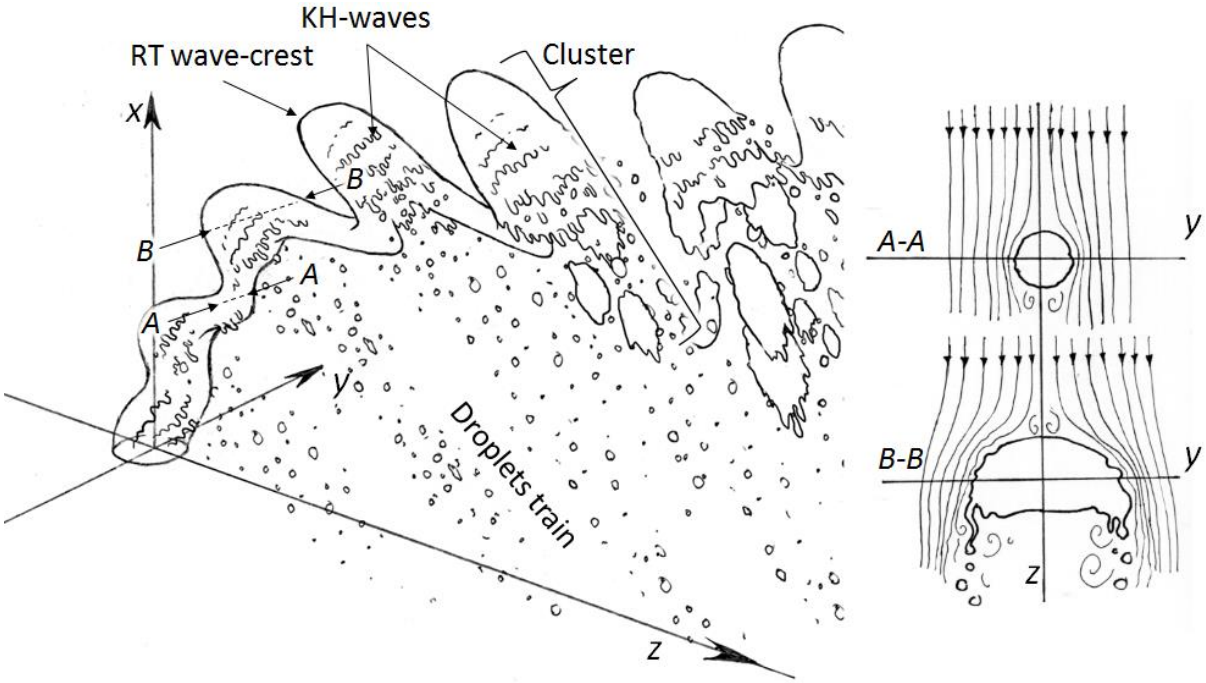

Figure 2.4 – An illustration of Kevin-Helmholtz (KH) waves and surface shear-stripping.

Earlier studies (e.g., Sallam et al., 2004) proposed that shear-stripped droplets originate from the viscous boundary-layer that develop around the jet, causing the droplet sizes to be consequently proportional to the boundary-layer thickness. More recent studies (e.g., Behzad et al., 2016) support an inviscid interpretation, where droplets are generated by the KH-induced surface corrugations that grow and disintegrate as they interact with the crossflow's aerodynamic pressure forces. In either case, the sheared droplets are smaller than both the liquid jet's diameter and the droplets in the developing spray-core. Hence, they have less momentum and are rapidly entrained into the crossflow (Ingebo ,1981, 1985). Consequently, droplets produced by shear-stripping primarily occupy the near-wall wake-region of the JICF spray-plume (in contrast to the spray-core droplet clusters that penetrate far into the crossflow).

Ingebo (1981, 1985) also observed that shear-stripping is generally more intense at the crests of the underlying RT-waves. As shown on the right of Figure 2.4, this is likely because

the wave-crest has a larger diameter than the trough, which causes the crossflow around the crest to locally accelerate to higher velocities than that around the trough, thus resulting in stronger shearing. The non-uniform shear-stripping intensities between the wave crests and troughs produce trains/waves of high droplets number-densities in the jet's wake (e.g., illustrated on the left of Figure 2.4). The droplets trains are particularly evident at higher We_{cf} when shearing is more intense. They can be observed in many experimental images, including those in Wu et al. (1997) and Sallam et al. (2004).

As discussed above, the Classical-JICF's spray-plume consists of two zones (i.e., the spray-core and the wake) having droplets of significantly different sizes, number densities and formation mechanisms. However, as the spray-plume continue to travel downstream, large droplets will undergo "secondary/tertiary breakups" into increasingly smaller droplets until a critical size is reached where the droplets' surface tension balances with (or exceeds) the crossflow's disruptive aerodynamic forces. This critical size is commonly related to the following expression of critical Weber number; e.g., by Hanson et al. (1963), Wu et al. (1994), Madabhushi (2003) and Marmottant and Villermaux (2004):

$$We_{crit} = \frac{\rho_{cf} U_{rel}^2 d_{drop}}{\sigma_f} \approx 10 \tag{9}$$

where U_{rel} is the *time-varying* relative velocity between a droplet and its immediate surrounding gas, and d_{drop} is the droplet diameter. Importantly, the critical droplet size at a downstream location where the droplet has attained the crossflow velocity (i.e., $U_{rel} \approx 0$) will necessarily be larger than the initial jet's critical droplet size when $U_{rel} \approx U_{cf}$. Hence, some large droplets that have yet to be broken up in the initial spray may remain intact indefinitely.

The breakup mechanisms described above are all driven by aerodynamic forces with capillary forces often responsible for the final droplets pinch-off. But in addition to aerodynamic forces, Wu et al. (1997), Ahn et al. (2006) and Reichel et al. (2007) have reported

that inertial forces from liquid turbulence can significantly influence the jet breakup. As illustrated in Figure 2.5, the presence of turbulent eddies diverts liquid momentum away from the injection direction and destabilizes the liquid surface. The diverted momentum contributes to the sum of disruptive forces acting against the surface tension, thus encouraging breakup to occur at lower levels of aerodynamic forces.

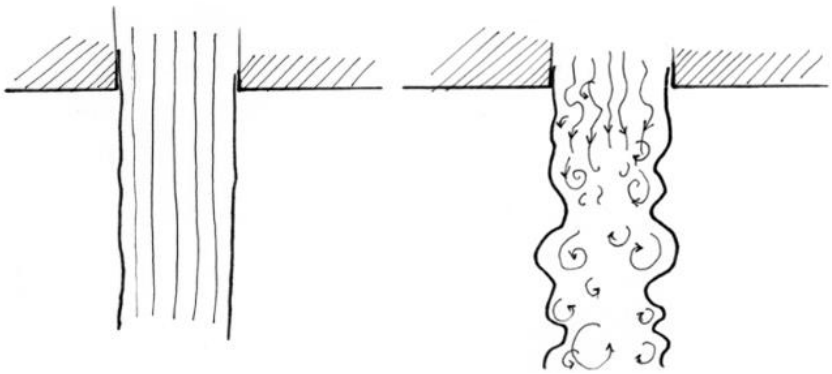

Figure 2.5 – Effect of liquid turbulence on the jet's surface instability.

We have shown that jet breakup is driven primarily by the crossflow's aerodynamic forces (and under certain circumstances by liquid turbulence), which is commonly expressed in terms of the crossflow Weber number. Next, we will expand upon the discussion of We_{cf}'s effects on JICF behavior. We begin by looking at the possible regimes of JICF breakup, which have been extensively researched by Mazallon et al. (1999) and Sallam et al. (2004), among others. The instantaneous images of laminar jets undergoing breakup in crossflows having widely different We_{cf} can be found in Sallam et al. (2004). They showed that the injected liquid jet remained intact and laminar in the photographed domain in the absence of crossflow (i.e., $We_{cf} = 0$). At $We_{cf} = 3$, large RT-waves formed on the jet. Large liquid nodes were formed at the wave-crests, while the wave-troughs were accelerated downstream and stretched out, giving the jet an overall sinusoidal appearance. Capillary forces caused the jet to pinch off at the troughs. This was named the "column breakup" regime. At $We_{cf} = 8$, the wave-troughs were inflated by the crossflow into bags. The inflating bags' membranes were stretched and thinned until they ruptured, releasing small droplets into the crossflow. The thicker rims of the

bags also underwent breakup into larger droplets. This was called the "bag breakup" regime. At $We_{cf} = 30$, aerodynamic shearing was strong enough to form KH-waves, and a combination of bag-breakup and surface-shearing occurred, producing the "multimode breakup" regime. As the We_{cf} continued to increase, the RT-waves' wavelengths continued to decrease, along with a decrease of the bag and ligament dimensions, until $We_{cf} = 220$ when the jet appeared to disintegrate directly into dense tiny droplets. This is commonly referred to as the "shear-breakup" regime, which typically begins at We_{cf}~200 (Lubarsky et al., *Advanced Fluids Dynamics*). The shear-breakup regime is the most regime for jet-engine operating conditions (where We_{cf} ≈1500-3000).

Whether the liquid jet in the shear breakup regime is entirely disintegrated via surface-shearing or a combination of surface-shearing and RT-driven jet pinch-off remains a subject of study. The latter concept is supported by Sherman and Schetz (1971) and Becker and Hassa (2002), and was illustrated in Figure 2.4. It is likely to be the more accurate description of the jet breakup process since it is more consistent with the common observation of intermittent cluster-shedding and droplets-trains at high We_{cf}. Finally, it should also be noted that although spray breakup regimes are usually correlated with We_{cf}, the liquid-to-crossflow momentum-flux ratio ($J = \rho_f U_f^2 / \rho_{cf} U_{cf}^2$) have also been found by numerous researchers to affect the jet breakup (Kush and Schetz 1973, Mazallon et al. 1998, Wu et al. 1998, Rachner et al. 2002 and Gopala et al. 2010). Higher We_{cf} and J both lead to the formation of smaller and more regularly-sized ligaments and droplets.

In general, JICF sprays have poly-dispersed droplet size distributions. In particular, the spray-core and spray-wake's droplet sizes are remarkably different due to their distinct underlying droplet-formation processes. The large variation in JICF's droplet sizes is in fact advantageous to jet-engine fuel-air mixer operation because the larger droplets will penetrate further than the smaller droplets owing to their larger inertia per drag area, and vice-versa.

Consequently, the spray's dispersion is wider and more uniform in the direction of penetration, thus forming a more uniform fuel-air mixture ratio. Because droplets in a JICF are formed through aerodynamic forces, the mean droplet sizes are found to be dependent upon We_{cf}. Specifically, Nejad and Schetz (1971), Nejad and Schetz (1983) and Stenzler (2006) found that lower surface tension, higher crossflow velocity and higher crossflow density (i.e., factors that influence We_{cf}) are all capable of independently causing a decrease in droplets sizes.

It is worth emphasizing that although all Classical-JICF operating at We_{cf}>200 are lumped into the shear-breakup regime, the spray behavior and droplet sizes vary significantly with We_{cf} within this regime. As shown in Figure 2.6 by Lubarsky et al. (2010), droplet sizes in the spray will continue to decrease with increasing We_{cf} beyond We_{cf}=200. However, these effects diminish with increasing We_{cf}. For example, above We_{cf}=800, the droplet sizes are essentially constant. Notably, Figure 2.6 also shows that the spray-wake's mean droplet sizes are always very small and quite insensitive to We_{cf}. On the other hand, the spray-core's mean droplet sizes are much larger, especially at lower We_{cf}.

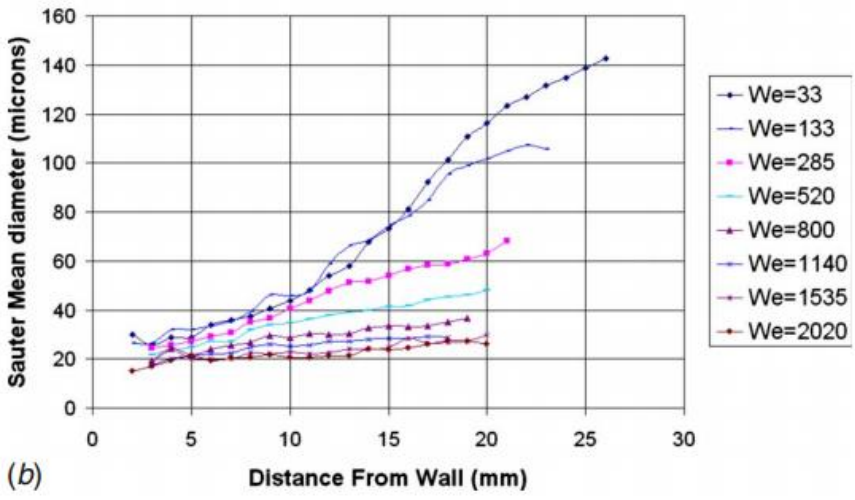

Figure 2.6 – A plot of the effects of We_{cf} on mean droplets sizes and size-distributions. Source: Lubarsky et al. (2010).

The majority of reported JICF studies were conducted at near-atmospheric pressures (<5*atm*) due to the difficulty in developing a high-pressure facility. Hence, the available data

is generally limited to $We_{cf} \leq 250$. In contrast, jet-engine fuel-air mixers typically operate at We_{cf}=1500-3000. As shown in Figure 2.7 (which are instantaneous images of Classical-JICF obtained during this dissertation work), the sprays at We_{cf}=350 and We_{cf}=1050 developed very differently, in spite of the fact that both cases were well in the shear-breakup regime and have the same *J*. The We_{cf}=1050 JICF had significantly finer droplets (as inferred from its "nebulous/foggy" appearance) and a denser wake, suggesting more intense surface shearing. These differences will have large performance implications on fuel-air mixer operation. Thus, care should be exercised in applying observations or conclusions of low-pressure experiments to jet-engine fuel-injector designs.

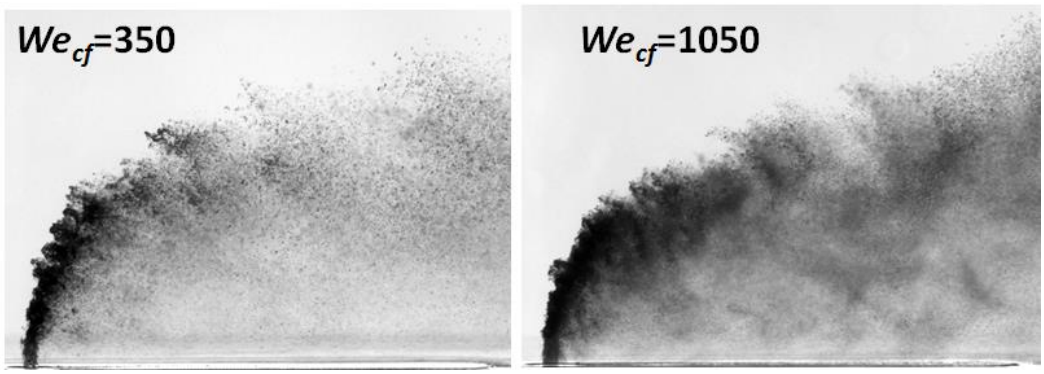

Figure 2.7 – Photos showing the effects of We_{cf} on spray structures in the shear-breakup regime, with identical fuel-to-crossflow momentum-flux ratio *J*.

2.1.2 Spray Penetration and Dispersion

The penetration and dispersion of the jet and spray-plume into the crossflow is another very important aspect of JICF. It is, in fact, arguably the most reported characteristic of JICF as it pertains to the control of fuel placement within the mixer and combustor. It is important to understand that the evolution of droplets trajectories throughout the JICF spray-plume is fairly complex, and a JICF spray is *not* simply a conical jet/spray that is bent into the crossflow direction. A detailed discussion of spray structures and velocity-fields for liquid-JICF can be found in Thomas and Schetz (1985), while those for *gaseous*-JICF can be found in Fric and

Roshko (1994), Smith and Mungal (1998) and Wilde (2014). Figure 2.8 shows a qualitative understanding of droplets trajectories in liquid-JICF. The illustration shows that, as previously discussed, the spray plume can be separated into the densely populated spray-core and sparsely-populated wake region. Droplets in these regions have different origins and, thus, different sizes and trajectories. The smaller wake droplets are continuously produced from the jet/spray's lateral surfaces and are rapidly entrained into the crossflow. Thus, they have nearly horizontal trajectories that originate from the entire span of the initial jet/spray. On the other hand, the spray-core's large droplets have much higher penetration inertia per drag area. Hence, the spray-core droplets penetrate very far, and their trajectories are always found on the windward side of the spray. Notably, the penetration of these droplets are further aided by the spray-core's high droplets density, where the droplets along the core's periphery shield the inner droplets from crossflow entrainment.

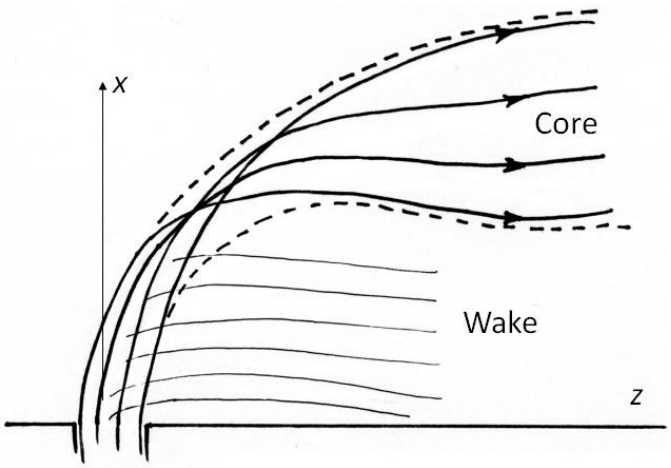

Figure 2.8 – A conceptual illustration of droplets trajectories in a Classical-JICF.

To simplify their analyses, researchers typically study JICF trajectories by use of statistically *averaged* trajectories. Wu et al. (1997) performed an analysis based on momentum conservation to predict the average trajectory of a jet in crossflow. The analysis was performed for a segment of a liquid jet instead of droplets or clusters of droplets. Buoyancy forces were neglected. The jet segment's penetration velocity (U_f) and drag coefficient (C_D) were assumed

to be constant throughout the analysis. Using these assumptions, they derived the following expression for the jet segment's trajectory in units of injection orifice diameter (d_f):

$$\frac{x}{d_f} = \sqrt{\frac{z}{d_f}\left(\frac{\pi}{C_D}\right)\left(\frac{\rho_f U_f^2}{\rho_{cf} U_{cf}^2}\right)} \equiv C_0 \times J^{0.5} \times \left(\frac{z}{d_f}\right)^{0.5} \tag{10}$$

Equation (10) by Wu et al. (1997) related the penetration of the jet to the momentum-flux ratio (*J*). In many following works, the expression was generalized to describe the trajectory of the entire spray plume. To improve the fitting of experimental data to the expression, the constants and powers in the expression were often relaxed to allow for deviations from the original analysis' assumptions. The generalized expression for spray trajectory is as follows:

$$\frac{x}{d_f} = C_0 \times J^{C_1} \times f\left(\frac{z}{d_f}\right) \tag{11}$$

where the spray penetrations at all $\frac{z}{d_f}$ locations are proportional to some power of *J* that is typically close to C_1 =0.5 (Chen et al. 1993, Hojnacki 1972, Yates 1972, Geery and Margetts 1969 and Wotel 1991). $f\left(\frac{z}{d_f}\right)$ is a shape-function that describes the trajectory's profile. It can take on the form of a power law function (Hojnacki 1972), a logarithmic function (Yates 1972) or a function with three exponentials that accounts for the liquid column, ligaments and droplets regions of the spray (Chen 1993).

Notably, Equation (11) can only be used to correlate the trajectories of sprays at a constant crossflow operating conditions. It is generally observed (Leong et al. 2001, Eslamian et al. 2014 and the sources cited therein) that the spray's penetration also has an inverse relationship with We_{cf}. This can be attributed to higher We_{cf}'s effects in decreasing droplets sizes, which reduces the droplets' penetration inertia per drag area. In addition, Becker and Hassa (2002) also found that Equation (11) tends to over-predict spray penetrations at high

We_{cf}, because the intact jet which Equation (11) models only persists for a very short time at high We_{cf}. The high We_{cf} JICF is also very well-atomized into fine droplets, which lose their penetration velocity very rapidly, in violation of Equation (11)'s assumption that jet penetration velocity is time-invariant. The report by Becker and Hassa (2002) delved deeper into the development of an alternative analysis where the droplets' deceleration times are accounted for in penetration prediction.

Finally, it is necessary to remark that Wu et al. (1997)'s analysis was based on an idealized scenario where the liquid segment only interacted aerodynamically with a uniform crossflow. In the research of JICF for wall-film cooling applications (Thompson et al. 2015 and Liang and Kang 2012), JICF of very low *J* are known to develop spray-cores that are attached to the lower-wall due to spray-wall interactions. The wall-attachment fundamentally changes the flow-field and dispersion pattern of the spray-plume. Hence, the wall-attached JICF is not self-similar with wall-detached JICF, and a purely *J*-based penetration scaling cannot strictly be applied simultaneously to both classes of JICF. At typical jet-engine operating conditions and *J*, the spray plumes can be located very close to the lower-wall and potentially become attached. Thus, we need to exercise care in identifying and analyzing wall-attached/detached sprays.

2.2 Twin-Fluid Jet-in-Crossflow

As discussed in Chapter 1, Twin-Fluid Jet-in-Crossflow (TF-JICF) injectors have recently gained the attention of designers and researchers for their potential application in jet-engine combustors (Samuelsen 1995, Leong et al. 2000, 2001 *JPP*, 2001 *JEGTP*, Hsieh et al. 2008, Fu et al. 2014, Sinha and Ravikrishna 2013 and Sinha et al. 2015). TF-JICF has also been considered for non-engine usages like railway friction-surfactant spray-coating (Li et al. 2006, 2010 *Part 1*, 2010 *Part 2*). This section reviews the TF-JICF injector designs and operating

conditions that have been investigated thus far, and the understandings of TF-JICF spray-formation processes that have been developed. It will provide the background for the discussion of our investigation, which spans the *dP* and *ALR* domains reported in the literature and beyond. For the brevity of discussion, we will henceforth refer to the twin-fluid's co-injected air simply as "air", while the crossflow air will only be referred to as "crossflow".

2.2.1 Summary of TF-JICF Injector Designs and Operating Conditions

The earliest design of a jet-engine combustor incorporating TF-JICF, which was called the Lean Burn Injector (LBI) (see Figure 2.9), was patented by Samuelsen (1995). Subsequently, the first study of this injector was published by Leong et al. (2000, 2001 *JPP*, 2001 *JEGTP*). Notable designs and studies that have since followed include the Internally-Staged Combustor by Fu et al. (2014) (see Figure 2.10), the TF-JICF for Trapped Vortex Combustors by Sinha et al. (2013, 2015) (see Figure 2.11), and the TAPS fuel-air mixer by Hsieh et al. (2008) (see Figure 1.3). As shown in Figure 2.9, Samuelsen (1995)'s LBI design had a centrally-supported shaft with concentric sleeves that delivered fuel and air to the fuel-air mixer device. At the end of the shaft, the fuel sleeve had equally-spaced orifices that injected fuel jets radially into the air sleeve, where they were impinged upon by a "ring" of air at a 90^o angle. The air "pre-atomized" the fuel and the resulting fuel-rich mixture exited via multiple large orifices on the air sleeve into the main annulus. There, a swirling crossflow continued to mix the fuel down to the desired equivalence ratio. The final mixture burned in a region anchored by the swirling flow's vortex breakdown bubble. A contraction in the annulus called a "quarl" accelerated the flow locally to prevent flashback. In this design, the pressure-drops (*dP*) of the air nozzles were below 10% of the crossflow static pressure. This *dP* value matched the typical levels of pressure-drop across combustor domes/entrances, such that the injected air can be driven by said pressure-drop without any additional compressor device. However, despite having low *dP* and, consequently, low air velocities, the fuel orifice diameter in the

LBI was reported to be 0.34*mm* while the fuel-air orifice diameter was 2.26*mm* (Leong et al. 2001), which resulted in the air-nozzle having a projected area 43 times larger than the fuel orifice area. Consequently, the LBI operated with very high air-to-fuel mass-flow ratios (*ALR*) of up to 9.4. In their report, Leong et al. (2001 *JEGTP*) claimed that the air was intended to promote both liquid fuel atomization and penetration, especially at low flow-rate conditions. The resulting finer atomization enhances fuel-vaporization, allowing more rapid mixing and leaner combustion with lower NOx production. They referred to their flow configuration as "Airblast (AB)-JICF".

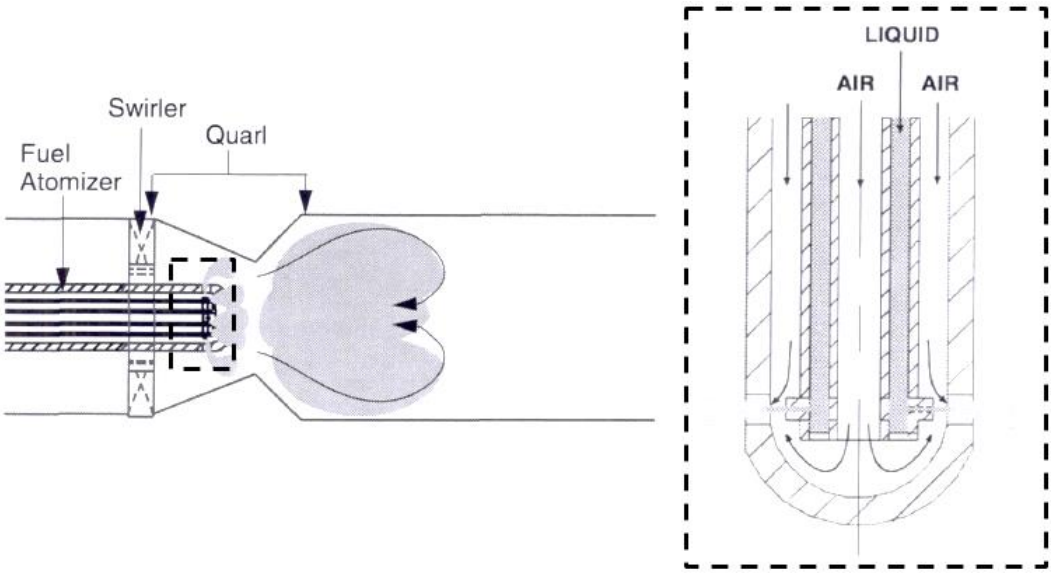

Figure 2.9 – A schematic of the Lean Burn Injector (*left*) and a zoomed-in view of the injector (*right*). Source: Samuelsen (1995), Leong et al. (2000) and Leong et al. (2001).

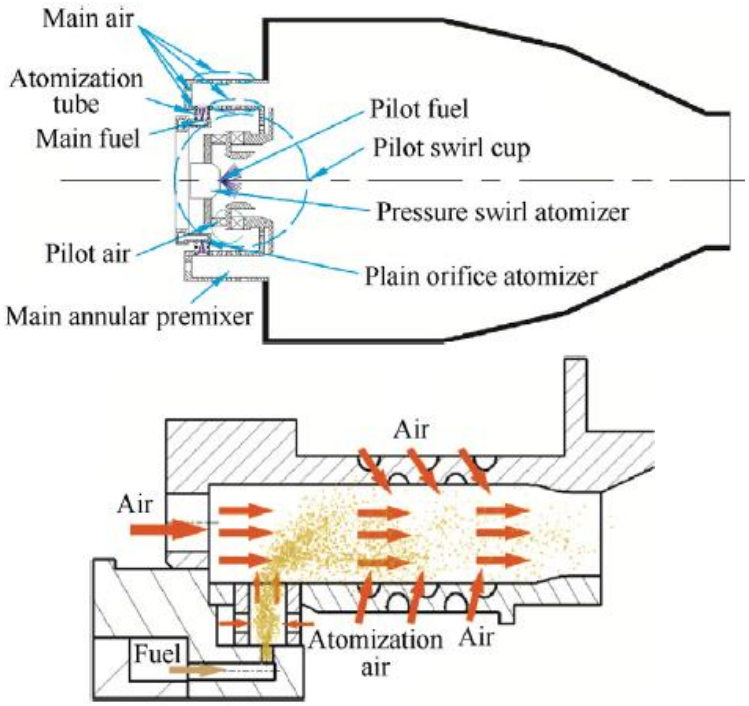

Figure 2.10 – *Top:* A schematic of the Internally-Staged Combustor. *Bottom:* A zoomed-in view of a single TF-JICF injector unit. Source: Fu et al. (2014).

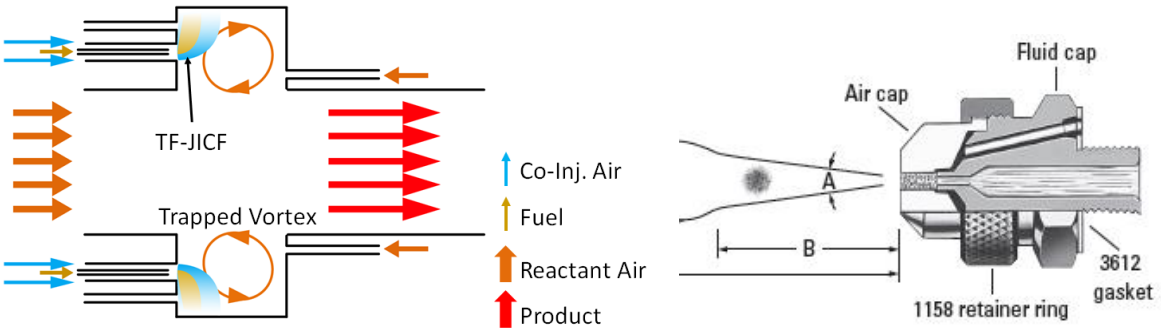

Figure 2.11 – *Left*: A schematic of a typical Trapped Vortex Combustor with TF-JICF injector. *Right*: A depiction of the airblast atomizer used by Sinha et al. (2013, 2015). Source: Spraying Systems Co.

Fu et al. (2014)'s Internally-Staged Combustor, see Figure 2.10, consisted of a central pilot-fuel injector surrounded by a "main annular premixer" containing the JICF injection orifices. The main-fuel was injected through recessed cavities ("atomization tube") near the front of the annulus. The walls of the cavities contained orifices for injecting "atomization air" that pre-atomized the fuel jets before they entered the annulus. Additional air was introduced along the walls of the annulus to sheath the wall from impingement by fuel. Figure 2.10 indicates that the atomization air in this design was also driven by the pressure-drop across the

combustor liner. Their air-nozzles' *dP* was reported to be ~3.16% of the crossflow pressure. The air injected into the atomization tube and along the wall accounted for 12.4% of the total combustor air flow. The employed *ALR* at the point of injection and the effects of air on spray-formation were not reported.

The Trapped Vortex Combustor (see Figure 2.11) is a novel combustor design where a vortex ring of recirculating flow trapped within a toroidal cavity was used to stabilize the flame. This combustor is typically compact and, consequently, has short flow residence times. Thus, a method of very rapid fuel-atomization and mixing is required. The recent studies by Sinha and Ravikrishna (2013) and Sinha et al. (2015) investigated TF-JICF as a candidate fuel-injection technique for Trapped Vortex Combustors. Their effort was in an early phase, where the TF-JICF was studied using a commercially available Spraying Systems Co. SU11 airblast nozzle (see Figure 2.11) mounted onto an atmospheric crossflow test-channel (i.e., *non*-combustor operating conditions). This nozzle allowed the fuel and air to impinge and mix internally in a cavity before being released into the crossflow as a *spray*, thus allowing more rapid mixing than Classical-JICF. The air-nozzle area of the SU11 atomizer was on the order of the fuel orifice area and, thus, *ALR* was typically less than 0.3. However, large air-nozzle *dP* on the order of 250% of crossflow pressure was supplied to creat up to sonic relative velocities between the fuel and air, thus producing intense shearing and interactions.

Finally, a notable non-propulsion-related investigation of TF-JICF was conducted by Li et al. (2006, 2010 *Part 1*, 2010 *Part 2*). They investigated to use of a modified commercial airblast atomizer for spraying water and viscoelastic liquids from a moving train onto railway tracks to modify the train's track-grip. In this case, the crossflow arose from the train's motion (5-15*m/s*) and was much slower than typical fuel-air mixer's crossflows (60-85*m/s*). Their atomizer nozzle had a central liquid orifice with an area of 1.47mm^2 and an axial airblast ring-orifice with an area of 4.55mm^2. The nozzle was operated with *dP* levels of up to 60% crossflow

pressure and *ALR* in the range of 1-2.5, which resulted in rapid liquid atomization and large spray penetrations. Their nozzle was distinct from those employed by Leong et al., Sinha et al. (2013, 2015) and Fu et al. (2014) in that the liquid and air were injected parallel instead of impinging, and fuel-air interactions occurred outside of the nozzle.

The TF-JICF operating parameters (*dP* and *ALR*) employed in the investigations of Leong et al., Li et al. and Sinha et al. have been summarized in Figure 1.4. In addition, a more detailed summary of their test conditions will be presented in Section 3.5, where they are compared against our design of our experiment and choice of test conditions.

2.2.2 The Effects of High-dP and High-ALR Air-Injection on the JICF Sprays

Figure 2.12 shows the time-averaged images taken by Leong et al. (2000, 2001 *JPP*) of spray-formation in the Classical-JICF operating mode with constant fuel flow-rate and different crossflow pressures. These images show that in the absence of airblast, the injected liquid fuel formed an intact liquid jet at 1*atm*, which then persisted for multiple jet diameters before being disintegrated and deflected into the crossflow. The jet breakup length was considerably shorter and the deflection more severe when pressure was raised to 3*atm* (i.e., higher We_{cf}) while the fuel flow-rate was kept constant (i.e., lower *J*), thus placing the spray plume very close to the test-channel wall. At 5*atm*, the liquid jet was almost instantaneously atomized and the generated spray-core attached to the wall. Because the fuel flow-rate (instead of momentum-flux ratio, *J*) was fixed between the three Classical-JICF, it is difficult to determine whether the decreased penetration was due to lower *J* and/or higher We_{cf}.

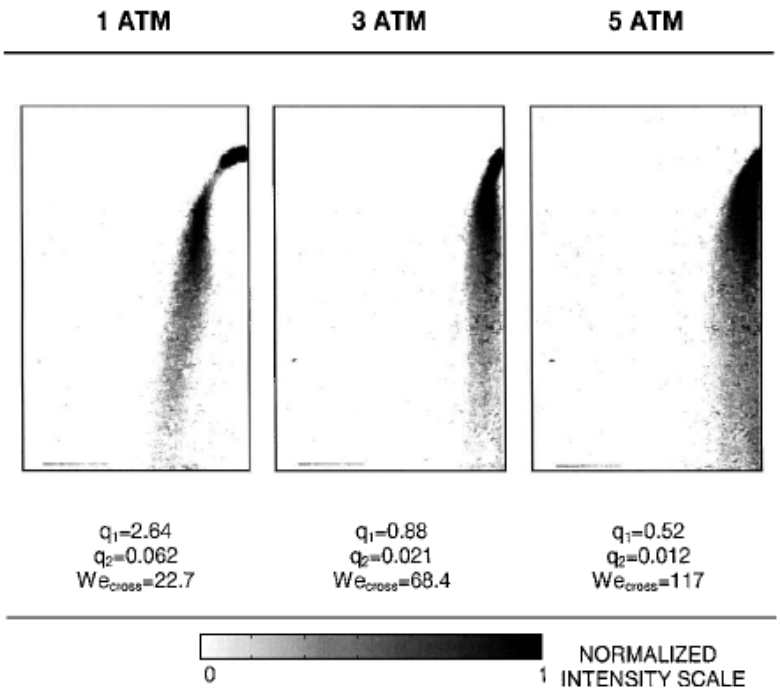

Figure 2.12 – The effect of crossflow pressure on a Classical-JICF spray. Source: Leong et al. (2001, *JPP*).

Figure 2.13 from Leong et al. (2001, *JPP*) describes the effect of airblast upon the sprays shown in Figure 2.12 When a *dP* of 1% was applied to the JICF, the penetrations of the sprays at the same fuel flow-rate as in Figure 2.12 were all enhanced, and the 3-5*atm* sprays separated from the test-channel wall. However, intact initial liquid jets were observed in spite of the presence of atomizing airblast. When a *dP* of 2% was applied to the air-nozzle at 1-3*atm* test pressures, the injected fuel "expanded" across the entire width of the spray nozzle, leading Leong et al. (2000, 2001 *JPP*) to conclude that the fuel had become fully atomized and dispersed within the interior of the nozzle cavity. They referred to this phenomenon of quasi-instantaneous atomization as "prompt-atomization", which was distinct from the KH-waves shear-atomization that requires a longer time-scale for wave-development. Notably, the resulting spray plumes at *dP*=2% also had significantly higher penetrations compared to those at *dP*=1%. On the other hand, the jet appeared to remain intact at 5*atm* and *dP*=2%, while experiencing little penetration enhancement by the air. The absence of prompt-atomization at 5*atm* was not explained. Finally, at *dP* of 3%, all the jets were "fully prompt-atomized" and a

"nodule" of liquid formed on the downstream side of the nozzle, which was attributed to the splashing of prompt-atomized fuel onto the nozzle wall.

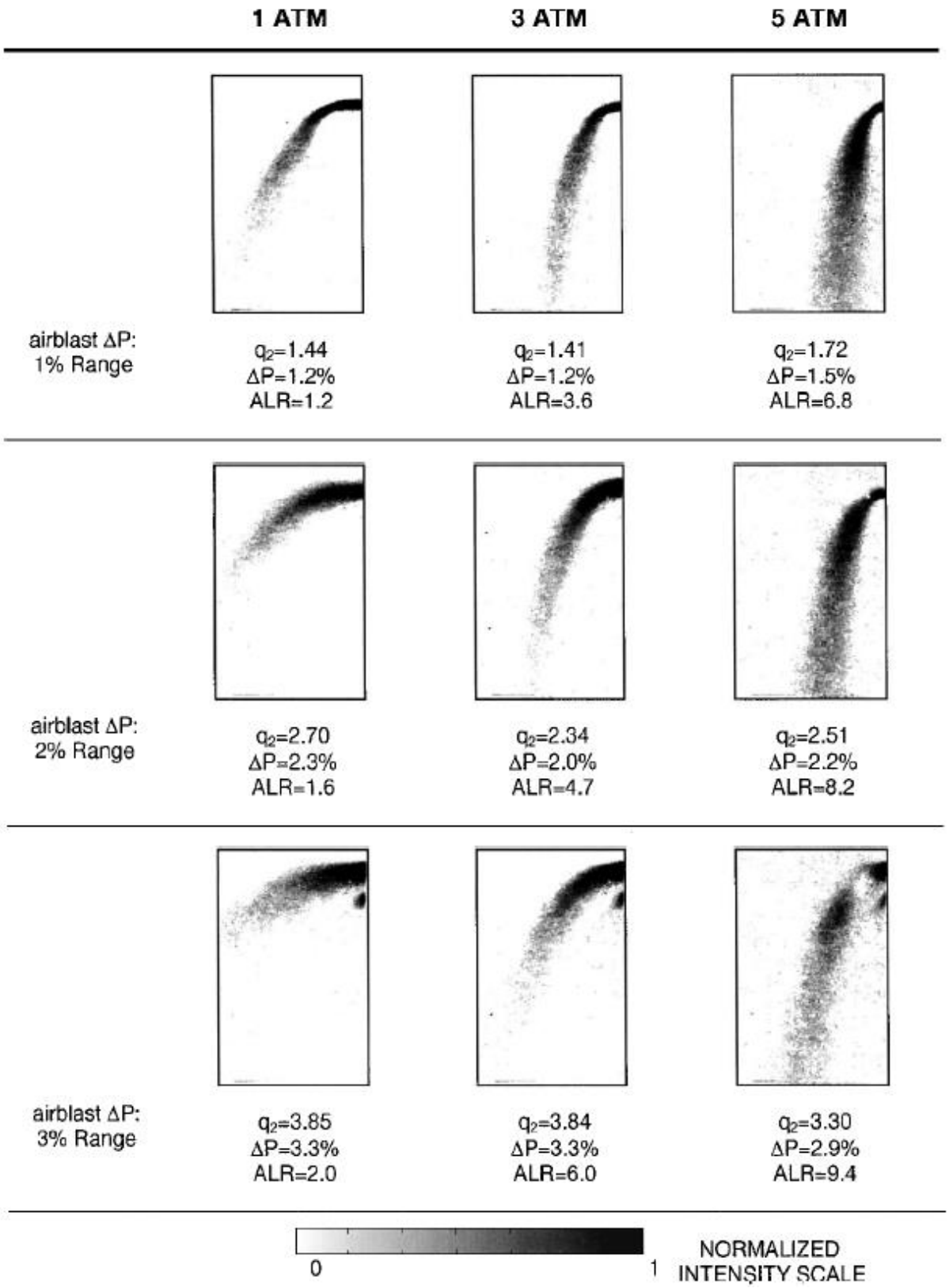

Figure 2.13 – The effects of crossflow pressure and airblast *dP* on the JICF sprays. Source: Leong et al. (2001, *JPP*).

In addition to imaging-based studies, Leong et al. (2000) also employed Phase Doppler Interferometry to characterize the AB-JICF's droplet size distributions. They observed that at low or zero *dP* the droplets' Sauter Mean Diameter (SMD) decreased with distance downstream of the nozzle, indicating continuous droplet break-ups by secondary atomization due to the crossflow's aerodynamic forces. On the other hand, at higher *dP* the SMD remained spatially constant, indicating that the airblast had atomized the fuel into droplets with sizes smaller than or equal to the critical diameters.

Subsequently, Leong et al. (2000, 2001 *JPP*) identified the following three sub-regimes within "AB-JICF": i) the low-*dP* sub-regime where the jet remains intact but experiences penetration enhancement by air, ii) the mid-*dP* sub-regime where the jet is prompt-atomized, and iii) the high-*dP* sub-regime where a liquid nodule forms on the leeward edge of the nozzle. As the AB-JICF transitioned from a low-*dP* to a high-*dP* sub-regime, the spray's cross-sectional liquid distributions transitioned from circular to elliptical to, in certain cases, kidney-shape. They attributed the formation of the kidney-shaped cross-section to the entrainment of small well-atomized droplets into the counter-rotating vortex pair (CVP) flow structure formed by the interaction of the airblast air with crossflow (e.g., see the discussion on CVP by Smith & Mungal 1998). The kidney-shaped spray cross-section is usually not present in a liquid Classical-JICF (e.g., see Wu et al. 1998) and is a unique feature of high *dP* TF-JICF.

Figure 2.14 shows instantaneous inverted-intensity shadowgraph images of TF-JICF sprays formed by the injection of water at varying flow-rates, air-nozzle *dP* and crossflow velocities, provided by Sinha et al. (2015)'s report. The images were all captured at atmospheric pressure and temperature, and We_{cf}~200 (i.e., on the lower borderline of the shear-breakup regime). The first row of images shows the dependence of spray penetrations on crossflow velocity at fixed liquid and air flow-rates. As expected, higher crossflow velocities reduced the momentum-flux ratios (here denoted as "q_2") and decreased the spray penetrations.

Notably, the first row of images was also captured at *ALR*=0.1 (here denoted as gas-to-liquid flow-rate ratio "*GLR*"), which was on the lower end of Sinha et al. (2015)'s TF-JICF operating conditions (i.e., close to Classical-JICF). At this operating condition, large discrete droplets can be observed throughout the entire spray as a result of the low We_{cf}.

The second row in Figure 2.14 shows the dependence of spray characteristics on *ALR*, where We_{cf} and liquid flow-rate were fixed. At the lowest *ALR*, the spray-plume was observed to bifurcate into two branches. The upper branch consisted of large droplets with approximately the same sizes as in the first row of images. The lower branch consisted of much smaller droplets that had a nebulous/foggy appearance, which was previously seen only in Classical-JICF operating at very high We_{cf} (e.g., see Figure 2.6). The bifurcation of the spray-plume was attributed to the presence of bimodal droplet size distribution, where smaller droplets have significantly less penetration inertia per drag area. Sinha et al. (2015) further proposed that the bifurcation and bimodal droplet-sizes indicated the presence of two distinct atomization processes that only occur when the *ALR* is *in*sufficiently high; i.e., (i) partial prompt-atomization of the jet's outer periphery by airblast producing small droplets and (ii) atomization of the remaining jet by crossflow producing large droplets. This form of TF-JICF breakup process is perhaps similar to Leong et al. (2000)'s low *dP* operation where the initial liquid jet remained intact for multiple jet diameters, even though Leong et al. (2000) did not observe bifurcation (e.g., see Figure 2.13).

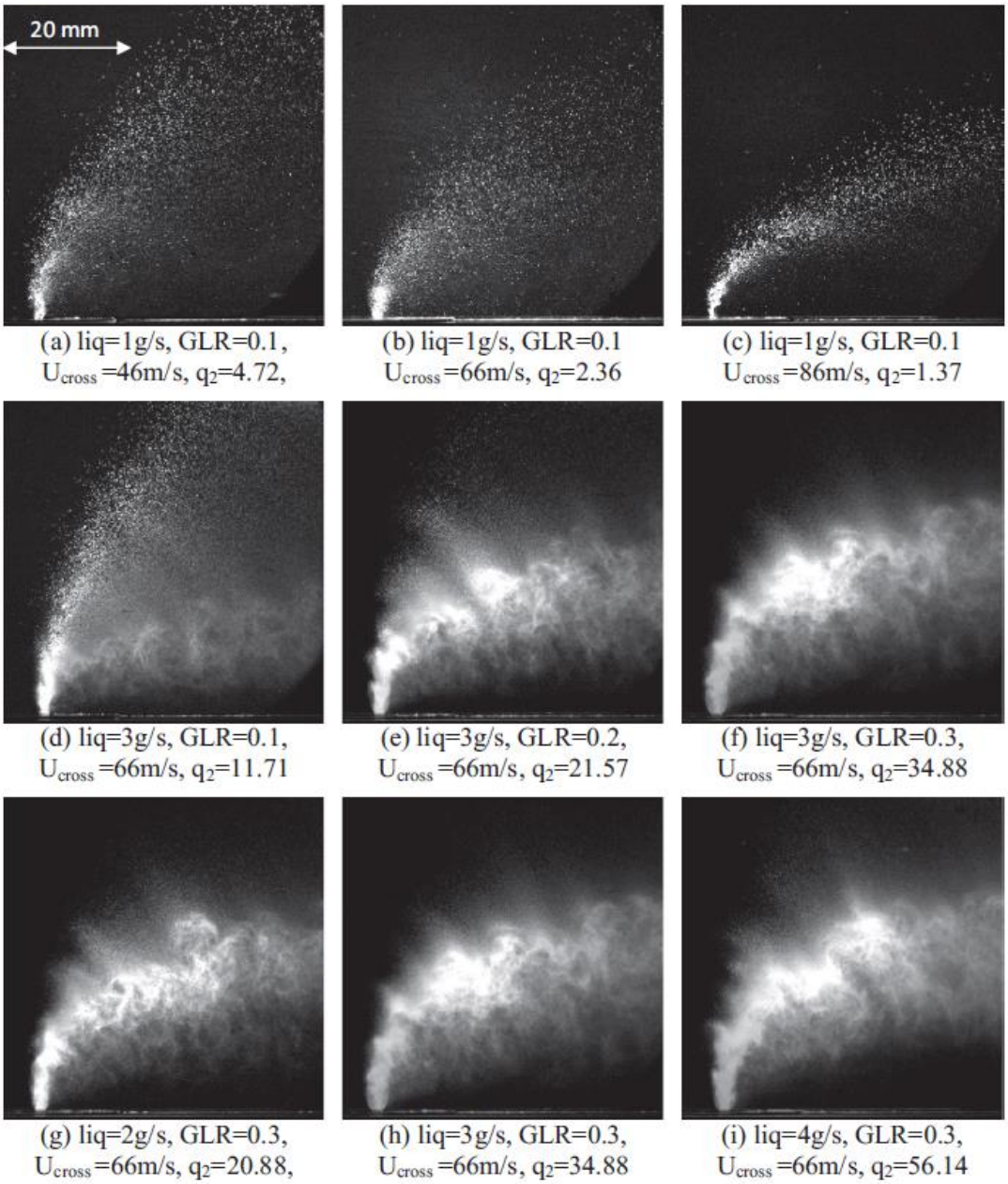

Figure 2.14 – Instantaneous images of water-injection at different liquid flow-rates, *ALR* and U_{cf}. Source: Sinha et al. (2015).

As the *ALR* increased, the penetration of the upper branch in Figure 2.14 appeared relatively unaffected, whereas the lower branch's penetration increased until eventually it merged with the upper branch. At the same time, increasing *ALR* also depopulated the upper branch, redistributing the liquid towards the lower branch; i.e., increasingly large portion of the jet became airblast-atomized. When the upper branch disappeared entirely, the liquid was considered to be fully prompt-atomized by air. Sinha et al. (2015) referred to the bifurcation phase as airblast jet-in-crossflow (AB-JICF), suggesting the presence of an intact jet that

produced the upper branch. Whereas, the fully prompt-atomized phase was referred to as airblast *spray*-in-crossflow (AB-SICF). Notably, Figure 2.14 also shows that the onset of bifurcation and the transition from AB-JICF to AB-SICF are not perfectly described by the non-dimensional parameter *ALR*. E.g., images (b) and (d) have the same *ALR*, but obviously belong to different regimes. Instead, the spray in image (d) was atomized more intensely due to the presence of higher *absolute* air flow-rate.

In addition, through the application of Particle Tracking Velocimetry to their spray images, Sinha et al. (2015) found that at low *ALR*, the accelerations of droplets into the crossflow direction were inversely proportional to their sizes. Hence, larger droplets penetrate farther. However, at high *ALR*, no definite relationships between droplets size, velocity and acceleration can be identified. They proposed that the lack of relationship at high *ALR* was due to the formation of a counter-rotating vortex pair in the injected air, which can entrain and disrupt small droplets (as first suggested in the earlier study of Leong, 2000).

Lastly, we discuss Li et al.'s (2006, 2010 *Part 1*, 2010 *Part 2*) investigation of TF-JICF for railway applications. They did not investigate the differences in spray behaviors between Classical and TF-JICF. Instead, they only reported results from cases where the airblast was in operation and air velocities were approximately two orders of magnitude higher than liquid injection velocities. As a result of the high air velocities, they observed that air momentum-flux always dominated for spray-formation process: higher air-to-crossflow momentum-flux ratios resulted in higher spray penetrations and lower spray dispersion-to-penetration ratios. Different liquid flow-rates had negligible effects on spray penetration and dispersion. Notably, they also observed that in the near-field where the spray had not been deflected into the crossflow the decay of droplets velocities along the maximum-velocity trajectory (s) scaled with s^{-1}, just like a plain-jet. On the other hand, in the far-field where the spray had been

deflected, the velocities decayed at a rate of $s^{-2/3}$, typical of relative-velocity decay-rates in bluff-body wakes.

2.2.3 Modeling of the Airblast-JICF/SICF Mechanism

As discussed in Section 2.1, the trajectories of a Classical-JICF spray is of primary interest to designers and researchers. Thus, there is interest in understanding and modeling a TF-JICF's trajectories. As discussed above, the penetration of TF-JICF is influenced by the properties of liquid, crossflow *and* air. Thus, the classically-defined liquid-to-crossflow momentum-flux ratio (*J*) is inadequate for correlating TF-JICF penetrations. To address this gap, Leong et al. (2000, 2001 *JPP*, 2001 *JEGTP*) developed the first trajectory correlation model for TF-JICF (or "AB-JICF"), which has by now been adopted by other researchers (e.g., Li et al. and Sinha et al.). The development of this new trajectory correlation model was based on the works of Edelman et al. (1971), Salzman and Schwartz (1978) and Han and Chung (1992) in the field of solid particle-laden gaseous-JICF, which Leong et al. (2000) proposed to be phenomenologically similar to AB-JICF.

Edelman et al. (1971) investigated the penetration and dispersion of gaseous (CO_2, N_2 and air) jets laden with 1 μm boron particles and 1-5 μm graphite particles in vitiated crossflows. The carrier gas jets had particle loading ratios ($\dot{m}_p/\dot{m}_{gas}$) of 0.3-0.7. Film photography was used to visualize the distribution of the particles in the JICF, while a traversing thermocouple was used to acquire stagnation temperature profiles across different planes of the flow. The location of the carrier gas was identified by the location of lower temperatures relative to the vitiated crossflow. They found that the experimentally-measured trajectories of the particles and gas were almost identical (i.e., no particle-gas bifurcation).

Salzman and Schwartz (1978) characterized a dust-laden gaseous-JICF and introduced the use of *total* jet-to-crossflow momentum-flux ratio (J_{jet}) as a parameter for scaling the multiphase-jet's penetrations. In their derivation, Salzman and Schwartz (1978) assumed that

the dust particles were always uniformly distributed in the carrier gas, which was reasonable given Edelman et al. (1971)'s results. Furthermore, they assumed that the jet's velocity-profile was always uniform (i.e., velocities and momenta only varied along the axis of jet propagation). Using these assumptions, the following equation for the particle-laden gas' trajectory was derived:

$$\frac{x}{l_m} = C_0 \left(\frac{z}{l_m}\right)^{C_1} \tag{12}$$

where,

$$l_m \equiv d_f \left(\frac{\rho_{jet}}{\rho_{cf}}\right)^{0.5} \frac{U_{jet}}{U_{cf}} \tag{13}$$

d_f is the injector diameter, l_m is a characteristic length-scale, and the subscript *jet* denotes an average jet property. *x* is the jet penetration direction and *z* is the crossflow direction. This expression can be recast into a more familiar form for JICF by combining the two equations, rearranging and defining a new J_{jet} based on U_{jet}:

$$\frac{x}{d_f}\left[\left(\frac{\rho_{jet}}{\rho_{cf}}\right)^{0.5} \frac{U_{jet}}{U_{cf}}\right]^{-1} = C_0 \left(\frac{z}{d_f}\left[\left(\frac{\rho_{jet}}{\rho_{cf}}\right)^{0.5} \frac{U_{jet}}{U_{cf}}\right]^{-1}\right)^{C_1} \tag{14}$$

$$\frac{x}{d_f} = C_0 \left(\frac{z}{d_f}\right)^{C_1} \left[\left(\frac{\rho_{jet}}{\rho_{cf}}\right)^{0.5} \frac{U_{jet}}{U_{cf}}\right]^{1-C_1} \equiv C_0 \times \left(\frac{z}{d_f}\right)^{C_1} \times \left(J_{jet}^{0.5}\right)^{1-C_1} \tag{15}$$

where, C_1 was reported to be 0.33, resulting in an overall J_{jet} exponent of 0.335 (which is close to the values of exponent in typical Classical-JICF empirical correlations); i.e.,

$$\frac{x}{d_f} = C_0 \times \left(\frac{z}{d_f}\right)^{0.33} \times J_{jet}^{0.335} \tag{16}$$

The primary difference between Equation [16] and the "standard" trajectory expression for Classical-JICF lies in the term J_{jet}, defined based on the average jet velocity (U_{jet}), which still needs to be expressed in terms of the carrier gas and particle flow-rates. Salzman and Schwartz

(1978) provided the following expression for U_{jet} based on the conservation of gas and particle momenta under the assumption of no particle-gas velocity-slip:

$$\rho_{jet}U_{jet}^2 = (1-\epsilon)\rho_{gas}U_{gas}^2 + \epsilon\rho_p U_p^2 \tag{17}$$

where, $\epsilon = \frac{V_p}{V_{jet}}$, the volume-ratio of particle to total jet.

Salzman and Schwartz (1978) found that the above correlation model successfully correlated the trajectories of dust-laden gaseous-JICF. I.e., the two-phase jet can be effectively treated as a single homogeneous fluid with a flow-rate weighted average momentum-flux ratio. However, they did not investigate extreme cases where the homogenous-fluid assumption may break down; e.g., the cases where the particles are very large or present in very high quantities.

Han and Chung (1992) conducted a numerical study of particle-laden gaseous-JICF using high-fidelity momentum-conservation equations where pressure-force, buoyancy force, entrainment of ambient crossflow into the jet plume, shearing between the jet and crossflow, and the interactions between the carrier gas and the particles were all accounted for. They found that at the same injection and crossflow velocities, the trajectories of the particles and carrier gas bifurcated when the particles were large. Additionally, when the particles were large, they penetrated much further into the crossflow than smaller particles at identical test conditions. Furthermore, the penetrations of gas in particle-laden gaseous-JICF far exceeded the penetrations of gas in a gas-only JICF at identical conditions; i.e., while the gas "carried" the particles, the dense particles also had the effect of protecting the gas against stripping by crossflow. Their results perhaps agree with Sinha et al.'s (2015) observations (see Figure 2.14) that large and small droplets/particles will bifurcate in a solid-gas/twin-fluid JICF.

Leong et al. (2001) applied the analysis approach used by Salzman and Schwartz (1978) and assumed that droplets in TF-JICF are uniformly distributed within the injected airblast air with negligible velocity-slip. Then, by applying conservation of droplets and air momenta, they obtained the following expression for the spray mixture's momentum-flux:

$$\rho_{mix} A_{total} U_{mix}^2 = \rho_{air} A_{air} U_{air}^2 + \rho_f A_f U_f^2 \quad (18)$$

where the subscript "*mix*" denotes the mixture average properties, A_{total} is the total area of the nozzle that injects the fuel-air mixture, A_{air} is the air-nozzle area within the injector and A_f is the central fuel-orifice's area. A_{total} was defined as the combined area of A_{air} and A_f. The no-slip assumption requires the liquid jet to be completely prompt-atomized and dispersed within the nozzle cavity in order to be satisfied. Furthermore, the conservation of momenta assumed no dissipation due to turbulent interactions between fuel, air and crossflow, as well as negligible energy contribution to overcoming liquid surface tension during atomization.

An effective momentum-flux ratio was subsequently defined (in the same manner as J_{jet}) based on Equation (18), resulting in the following:

$$J_{eff} = \frac{\rho_{mix} U_{mix}^2}{\rho_{cf} U_{cf}^2} = \frac{A_{air} \rho_{air} U_{air}^2 + A_f \rho_f U_f^2}{A_{total} \rho_{cf} U_{cf}^2} \quad (19)$$

Using the parameter J_{eff}, the following correlation for describing the trajectory of the TF-JICF was derived:

$$\frac{x}{d_f} = c_0 \times J_{eff}^{c_1} \times \left(\frac{z}{d_f}\right)^{c_2} \quad (20)$$

This correlation was further modified by Leong et al. (2001) as follows to account for the effect of elevated pressures:

$$\frac{x}{d_f} = c_0 \times J_{eff}^{c_1} \times \left(\frac{z}{d_f}\right)^{c_2} \times \left(\frac{P}{P_0}\right)^{c_3} \quad (21)$$

where, P_0 is a reference pressure. It should be noted that while the pressure-correction term was convenient for engineering applications, it is not based upon fundamental physical considerations.

Leong et al. (2001) attempted to fit Equation (21) to their AB-JICF's windward- and leeward-edge trajectories. The J_{eff} scaling and pressure-correction term performed reasonably well in correlating their experimental data, except on the spray's leeward-edge where

significant deviations consistently occurred, suggesting that some of the assumptions employed in deriving J_{eff} did not adequately describe the physics of the problem. The limited amount of curve-fitted data reported by Leong et al. (2001) makes it difficult to determine the conditions and causes of deviations from J_{eff}. As a sidenote, Leong et al. (2000) also observed that at a fixed air nozzle *dP*, the airstreams penetrated further into the crossflow in the presence of fuel injection; i.e., the fuel droplets and air mutually enhanced each other's penetrations, in agreement with the results of Han and Chung (1992).

Li et al. (2010 *Part 1*) also reported a good fit of Equation (20) to their experimental data, even though the presentation format in their report made it difficult for readers to judge the goodness of fit or which conditions/spatial regions of the spray were most likely to deviate from the fit. As discussed earlier, Sinha et al. (2015)'s data showed spray-bifurcation at low *dP* and a reduction in spray penetration when the far-penetrating spray-core droplets became redistributed into the lower airblast-droplets branch. However, the processed spray trajectories were reported as being in good fit with the J_{eff} correlation model. We could not explain the discrepancy between their images and fitted trajectories based on reported information.

2.2.4 Summary of the TF-JICF Review

In summary, the state-of-the-art knowledge of TF-JICF is limited to the domains of high *dP* and/or *ALR*. In these domains, the air promotes the atomization and penetration of the liquid jet. The J_{eff} correlation model, adapted from the research of particle-laden gaseous-JICF, is widely adopted by the TF-JICF research community with good success. However, it is evident that under conditions where large droplets are produced or when droplets are densely packed (e.g., in the initial spray or at low *dP* and *ALR* conditions), the J_{eff} model's underlying assumptions may not be applicable, which may have led to some reported deviations between the correlation expression and experimental data. Finally, a recent report by Sinha et al. (2015)

notes the absence of complete prompt-atomization by the air at "medium" levels of *dP* and *ALR*, accompanied by spray bifurcation. This suggests that at the very low *dP* and *ALR* domain (i.e., our domain of interest), the bifurcation may worsen and new regime(s) of TF-JICF with unexplored behaviors may exist.

2.3 Twin-Fluid Jets in Quiescent Gas

As described in the previous section, TF-JICF is a recent area of study with a limited knowledgebase. On the other hand, extensive knowledge exists regarding the atomization of twin-fluid jets (TF-jets) in *quiescent* gas, which can provide useful insights into TF-JICF behaviors. This section reviews the aspects of TF-jets that are relevant to TF-JICF.

2.3.1 Regimes and Spray Structures

Similar to JICF, TF-jets undergo different regimes of breakup depending upon the surrounding high-speed gas' density and gas-liquid relative velocity; i.e., the gas Weber number, defined as:

$$We_{aero} = \rho_{gas} U_{relative}^2 d_f / \sigma_f \tag{22}$$

where, ρ_{gas} is the gas density, $U_{relative} = U_{gas} - U_f$, d_f is the liquid orifice diameter, and σ_f is the liquid surface tension. Figure 2.15 from Leong et al. (2000) (which was expanded upon Farago and Chigier (1992)'s original diagrams) illustrates the morphologies of TF jets breakup under different regimes. At low We_{aero}, the liquid undergoes Rayleigh-type breakup where large droplets with diameters on the order of $2d_f$ are formed through Rayleigh instability/capillary jet-pinching. At higher We_{aero} in the membrane-type regime, the liquid jet experiences sinuous instability (i.e., lateral whipping motions). The resulting laterally-oriented liquid strand is impinged upon by the atomizing gas and inflated into a bag/membrane that subsequently ruptures and releases small droplets. The bag's rim, which is thicker than the

membrane, breaks up via Rayleigh instability into medium-sized droplets. When We_{aero} is further increased into the fiber-type regime, very fine ligaments and droplets are sheared directly from the liquid surface (much like the shear-breakup regime in JICF). The shearing gradually erodes the liquid jet until it is entirely consumed. Breakups in these first three regimes depend upon wave instabilities in the entire liquid jet and/or the jet surface. When the relative velocity and/or impingement angle between gas and liquid is very high, the liquid jet undergoes "prompt-atomization" where it is disintegrated instantaneously without time for wave development. Recall from Section 2.2 that prompt-atomization was proposed to be the dominant mode of atomization in high-*dP* and/or *ALR* TF-JICF, where the resulting rapid atomization and exchange of fuel-air momenta allow the developed J_{eff} trajectory-correlation to be applicable.

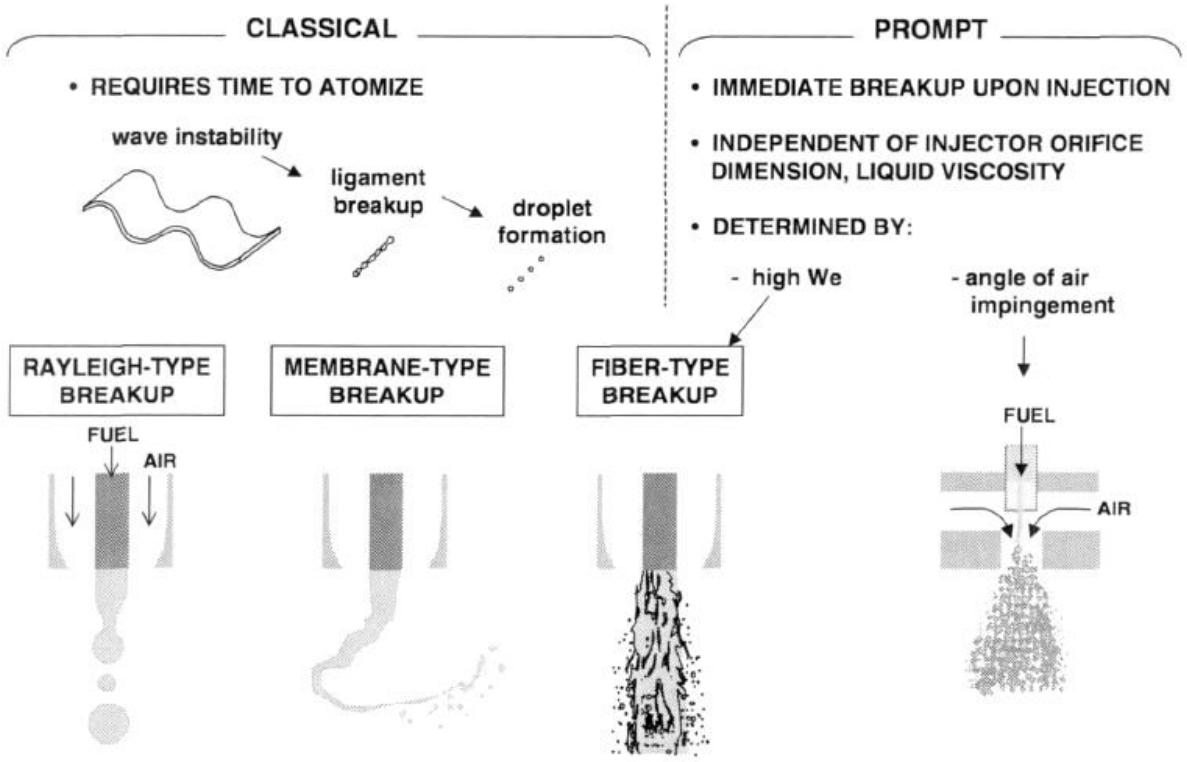

Figure 2.15 – Illustrations of TF-jet atomization in different regimes. (Leong et al. 2000).

Similar to Classical-JICF, liquid turbulence also affects the atomization of TF-jets. Hence, the liquid Reynolds number ($Re_d = \rho_f U_f d_f / \mu_f$) is often employed in the mapping of

TF-jet atomization regimes, in addition to We_{aero}. Table 2.1 summarizes the breakup regimes of TF-jets and their corresponding range of We_{aero} and Re_f. The table shows the further division of each regime into submodes according to Chigier and Reitz (1995)'s report, which also contained representative photographs of spray structures for each of these regimes/submodes. Their photographs showed that in the regular Rayleigh submode at low We_{aero}, periodic jet-pinching caused by varicose instability produced a steady train of large droplets. In the helical Rayleigh submode at higher We_{aero}, the jet developed finer corkscrew-like disturbances. In the subsequent "non-axisymmetric Rayleigh" regime, the entire jet developed large-scale sinuous instabilities. And, when We_{aero} is further increased into the membrane/bag regime, the co-injected gas inflated the sinuous jet into bags that stretched and ruptured, which produced significantly smaller droplets. Finally, at the highest range of We_{aero} was the fiber regime, which was further divided by Chigier and Reitz (1995) into the pulsating and super-pulsating submodes. In the former submode, the jet disintegrated in a steady fashion by surface shear-atomization (i.e., the development and pinch-off of "fibrous" ligaments), while in the latter submode the jet shedded off large clusters of liquid in violent pulses, thus producing a more unsteady and widely-dispersed spray.

Table 2.1 – Classification of twin-fluid jet atomization regimes and submodes, based on Chigier and Reitz (1995).

Regime	**Submode**	**Domain**
Axisymmetric Rayleigh	Regular	We_{aero}=0-10 Re_d=20-20000
	Helical	
Non-Axisymmetric Rayleigh		We_{aero}=10-20 Re_d=60-10000
Membrane/Bag		We_{aero}=20-80 Re_d=1000-20000
Fiber	Pulsating	We_{aero}=80-1000 Re_d=2000-20000
	Super-pulsating	We_{aero}=100-1000 Re_d=100-3000

The classification of TF-jets atomization regimes and their mapping parameters vary slightly between researchers. A very informative regime-map by Lasheras and Hopfinger (2000) employed the mapping parameters of Re_f (which is proportional to fuel velocity) and a Weber number based on the *absolute* gas velocity, defined as follows:

$$We_{gas} = \rho_{gas} U_{gas}^2 d_f / \sigma_f \tag{23}$$

In their map, an increase in Re_d and We_{gas} caused by increasing liquid and gas velocities, respectively, can individually lead to higher regimes of atomization. However, they found that when the absolute liquid and gas velocities match (i.e., minimum relative velocity), the liquid-gas shearing approaches a minimum and the annular gas can serve to sheath the liquid against an otherwise larger shearing with the quiescent ambient gas. This can cause the TF-jet to drop into a less intense regime of atomization. The gas-sheathing effect was also raised in Lefebvre (1992)'s remark that low-velocity annular gas-injection (whether coaxial, impinging or swirling) can be used to reduce relative velocities between the liquid and the surrounding quiescent gas. The effect of air-sheathing is potentially critical to our understanding of TF-JICF, particularly in the low *dP* domain. This is because in the domain of *dP*=0-10% (i.e., typical *dP* available to the fuel-air mixer's air-nozzles), the air's velocity is typically on the order of the liquid jet's velocity, while *also* being *significantly lower* than the crossflow's velocity.

Notably, Table 2.1 and Lasheras and Hopfinger (2000)'s map did not describe the influence of atomizer geometry on atomization regimes. This is chiefly due to the difficulty in fully understanding and reducing the fundamental physics of an infinite variety of TF-jet atomizers down to a single cohesive regime-map.

2.3.2 Atomization Process in the Fiber Regime

In our investigation of TF-JICF at elevated temperatures and pressures, We_{gas} were typically in excess of 100 (except at the lowest *dP*), which would result in shear-atomization

in the fiber regime. To further understand the underlying mechanism of TF-jet shear-atomization, we will discuss Lasheras and Hopfinger (2000)'s study of co-axial liquid-gas TF-jets, where they focused on understanding and modeling the development of vortical shear-layers between the liquid and atomization gas ("inner-layer"), as well as between the atomization gas and quiescent ambient gas ("outer-layer"). Their study was built upon the earlier investigations of Ko and Au (1985), Villermaux (1994) and Rehab et al. (1997) on the growths of shear-layers and the erosions of jet potential-cores in gas-gas and liquid-liquid TF-jets (e.g., as illustrated in Figure 2.16).

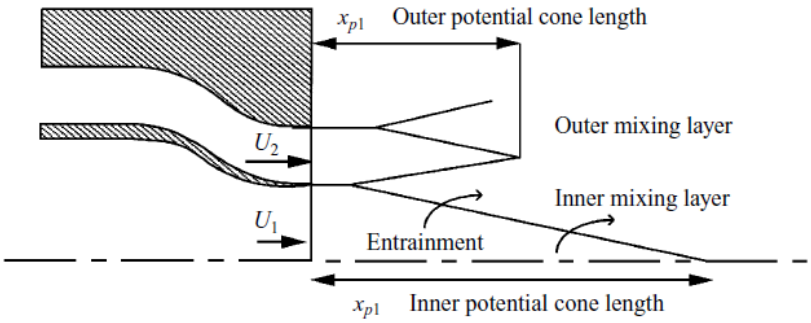

Figure 2.16 – Development of the vortical shear-layers and potential cores in a co-axial TF-jet. Source: Rehab et al. (1997).

Lasheras and Hopfinger (2000) found that the inner-layer's growth-rate was higher at larger gas-to-liquid velocity-ratio (*r*), which consequently causes more rapid erosion of the central liquid jet, causing the jet's potential core length to vary inversely with *r*. On the contrary, the outer-layer's growth was independent of *r*. They also found that fine-scale vortical structures developed along the inner-layer, while the outer-layer developed larger-scale vortical structures. The finer-scale structures were responsible for surface shear-atomization along the liquid jet, while the larger-scale caused gross pinch-off/truncation of the jet. This is perhaps similar to Classical-JICF where large-scale RT-waves cause jet pinch-off, while smaller-scale KH-waves only cause surface shear-atomization. In contrast to Lasheras and Hopfinger (2000)'s model, Rehab et al. (1997)'s model in Figure 2.16 divided the shear-layers development into two phases: (i) an initial phase where growth-rates were governed by slow

molecular diffusion (in the case of single-phase systems) and (ii) a subsequent rapid-growth phase where the growth-rates were governed by vortex mixing processes. The shear-layers' growth-rates are linear in both phases.

In TF-jets research, the evolution of the central jet's potential core is commonly modeled based on the conservation of mass, where the mass flux of injection is balanced by the mass flux of liquid entrainment from the core into the inner shear-layer. Following Lasheras and Hopfinger (2000)'s analysis, assuming a circular liquid orifice, a constant rate of liquid entrainment and, consequently, a conical liquid potential core, the mass conservation can be expressed as:

$$A_f U_f = A_{jet} U_e = \frac{\pi d_f}{2} \sqrt{L^2 + \frac{d_f^2}{4}} U_e \tag{24}$$

where, A_f is the liquid orifice area, d_f is the orifice diameter, U_f is the injection velocity, and A_{jet} is the conical surface area of the jet potential core with core-length L. U_e is the "entrainment velocity" or the average flux of liquid being stripped/entrained into the inner shear-layer. At high We_{aero}, the surface tension force of the liquid was proposed to be negligible and the entrainment velocity was modeled assuming that the stripping process was driven by the dynamic pressure of the gas's turbulent/vortical motions as follows:

$$\rho_f U_e^2 = C_e \rho_g u_g'^2 \tag{25}$$

where, $u_g'$is the turbulent (r.m.s.) velocity of gas in the inner shear-layer. C_e is a constant of proportionality found to be ≈ 0.25. ρ_f and ρ_g are liquid and gas densities, respectively. The turbulent gas velocity u_g' was reported as being correlated to liquid-gas relative velocity:

$$u_g' \approx 0.17\left(U_g - U_f\right) \tag{26}$$

Combining the equations above, the following was obtained:

$$\frac{L}{d_f} \approx \frac{6}{\sqrt{M}} \left(\left| 1 - \frac{U_f}{U_g} \right| \right)^{-1} \tag{27}$$

where, $M \equiv \rho_g U_g^2 / \rho_f U_f^2$ is the gas-to-liquid momentum-flux ratio. Consequently, the liquid core's half vertex-angle (θ_f) can be defined by the liquid orifice diameter and liquid core length:

$$\tan \theta_f = \frac{1}{2} \frac{d_f}{L} \tag{28}$$

The droplets shearing process typically imparts the generated droplets with high kinetic energies, ejecting them radially away from the liquid core. Lasheras and Hopfinger (2000)'s stability analysis predicted a droplets ejection angle ($\theta_{droplets}$) of 45^o on top of the central jet's cone angle θ_f, while Raynal (1997) experimentally measured angles close to 50^o. $\theta_{droplets}$ was generally found to be insensitive to *M*, while θ_f depended directly on *M*, such that total spray angle ($\theta_{spray} = \theta_{droplets} - \theta_f$) decreases as M increases. Villermaux (1998) proposed a simple model for $\theta_{droplets}$, supposing that this angle was formed by the vector addition of the jet surface-normal liquid entrainment velocity (U_e) and the surface-parallel vortex convection velocity (U_c):

$$\tan \theta_{droplets} \approx \frac{U_e}{U_c} \tag{29}$$

For two fluid streams that may have different densities and velocities, Lasheras and Hopfinger (2000), Bernal and Roshko (1986) and Dimotakis (1986) all found the convection velocity to be correlated to:

$$U_c = \frac{\sqrt{\rho_f} U_f + \sqrt{\rho_g} U_g}{\sqrt{\rho_f} + \sqrt{\rho_g}} \tag{30}$$

Equation (29) expresses the spray-angle assuming monosize droplets. However, in many TF-jets the droplet sizes are polydispersed. In such cases, the larger droplets are usually found on the outer edges of the spray, because (i) they can be ejected further out from the atomizing gas layer due to higher inertias, (ii) once out of the atomizing gas, they remain intact indefinitely because the quiescent surrounding gas provides low levels of shearing (Bachalo et al.). In contrast, the smaller droplets generally have narrower dispersion angles.

The average size of droplets generated by a TF-jet is connected to the inner-layer's vortex length-scales, which predominantly depend upon the liquid and gas' relative velocity. A variety of droplets size correlation models have been proposed by researchers of TF jets, which are comprehensively reviewed by Lefebvre (1980). In general, higher liquid-gas relative velocity and higher *ALR* both lead to finer atomization. Larger liquid-air contact/interaction areas (e.g., by pre-filming the liquid into a thin sheet instead of a thick jet) were found to increase the efficiency of energy transfer from the air to the liquid, thus resulting in finer atomization at fixed relative velocity and *ALR*. *ALR* within the range of 1-10 were found to be ideal for TF-jet operations. Outside of this range, the liquid either becomes coarsely atomized due to insufficient air or the excess air becomes wasted as the liquid cannot be more finely atomized. Rizk and Lefebvre (1983) conducted a study of eight different TF atomizers (of the jet and pre-filming types) and found the dependencies described above to be true for all eight atomizers; i.e., these dependencies are likely applicable to most TF-jets.

2.3.3 Onset of the Recirculation-Regime/Prompt-Atomization

As discussed in Section 2.2, existing understandings of TF-JICF were exclusively developed for high-*dP* and/or *ALR* domains, where the jets underwent prompt-atomization and rapid mixing with the blasting air. These understanding may be untrue for the low-*dP* and *ALR* AA-JICF domain where the air is weak compared to the liquid and crossflow. As such, it is worth discussing briefly what governs the onset of prompt-atomization. Leong et al. (2000) and Lefebvre (1992 *Atom. & Sprays*, 1992 *JEGTP*) both proposed that prompt-atomization is likely to occur when a liquid jet is surrounded by an annular gas stream having high velocity and/or impingement angle. Lefebvre further proposed that if a liquid jet is completely prompt-atomized, the resulting mean droplets size can be determined by balancing the available gas kinetic energy against the surface tension energy of the generated droplets. However, to the best of our knowledge, there is currently no widely accepted model that correlates the *onset* of

prompt-atomization to liquid/gas properties, operating conditions and injector geometry. In particular, no model exists to describe the transition between the fiber-regime and the complete prompt-atomization of the jet; i.e., the domain of TF-jet where it is likely that only a portion of the jet is prompt-atomized while the remaining jet breaks up via slower wave-related mechanisms.

The closest analysis we found that potentially describes the onset of prompt-atomization comes from Villermaux et al. (1994), Hopfinger and Lasheras (1996) and Rehab et al. (1997)'s investigations of co-axial TF-jets. In these works, they observed the truncation of the central jet and the development of a recirculation bubble when the annular jet was injected with high velocities and/or swirl numbers, as shown in Figures 2.17 and 2.18. The recirculation bubble dissipated the axial momentum of the central jet and caused rapid mixing between the central jet and its surrounding fluid. Although no direct connection was drawn, this "recirculation-regime" was characteristically similar to the prompt-atomization regime. Thus, we interpret them to be the same phenomenon, and thus the model developed to predict the onset of the recirculation-regime can likely be used to predict prompt-atomization.

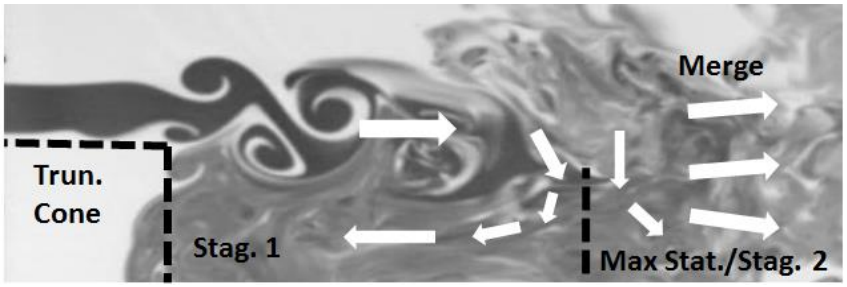

Figure 2.17 – A photo of the truncated central-jet and recirculation bubble that developed at high annular-jet flow-rate. Adapted from: Rehab et al. (1997).

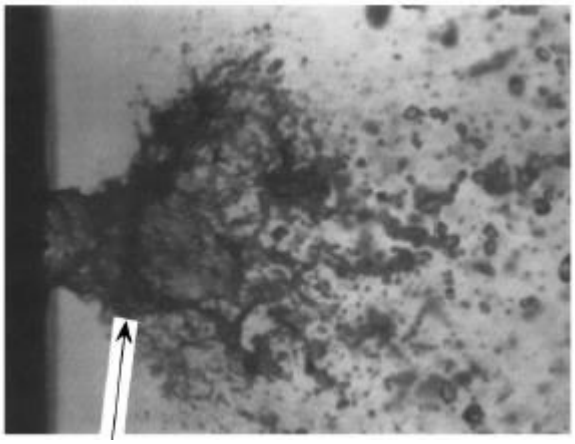

Figure 2.18 – A photo of rapid atomization and the development of a recirculation zone under the influence of high-swirl annular gas. *Arrow*: truncation of the jet. Source: Hopfinger and Lasheras (1996).

To predict the onset of the recirculation-regime, Villermaux (1998) proposed that the recirculation forms when the dynamic pressures of the co-axial annular jet's vortical motions equal or exceed the bulk dynamic pressure of the central jet:

$$\rho_g u_g'^2 \geq \rho_f U_f^2 \tag{31}$$

Using this simple criterion, Villermaux (1998) predicted the onset of the recirculation-regime at $M \approx 35$, while Lasheras and Hopfinger (2000) reported recirculation-regime at $M > 80$.

At the point when the gas' turbulent dynamic pressure just equals the bulk liquid dynamic pressure, the "recirculation bubble" begins its development as a 2D stagnation plane that truncates the jet (i.e., "Stag. 1" in Figure 2.17). As the gas' turbulent dynamic pressure increases further, a second stagnation plane forms downstream (i.e., "Stag. 2" in Figure 2.17). The static pressure at Stag. 2 is equaled to the gas' turbulent dynamic pressure and higher than the bulk liquid dynamic pressure. The consequent pressure-drop from Stag. 2 to Stag. 1 drives the recirculating back-flow, forming the 3D recirculation bubble. Downstream of Stag. 2, the inner and outer shear-layers merge and fluid is ejected axially into the ambient environment.

Critically, in these analyses, the relative size and mass flow-ratio of the two streams were not considered. This is potentially problematic when the annular jet's width is thin with respect to the central jet's diameter, because we can intuitively expect the annular jet's kinetic

energy to be fully dissipated before it can atomize and truncate the central jet, even at $M>>35$. In addition, the analysis above is for co-axial TF-jets only. The effect of the two streams' impingement angle was not considered even though it is practically very important. We can intuitive expect impinging TF-jets to transition into the recirculation/prompt-atomization regime more readily than co-axial TF-jets, because the impinging component of the annular jet's bulk dynamic pressure will directly contribute to the truncation of the central jet; i.e., as modified from Equation (31), prompt-atomization for impinging TF-jets can potentially be described by:

$$\rho_g U_{g,impinge}^2 + \rho_g u_g'^2 \geq \rho_f U_f^2 \tag{32}$$

where $U_{g,impinge}$ is the component of the gas's velocity that is normal to the central jet.

2.3.4 Summary of TF-Jets and Their Similarities to TF-JICF

In this section, we reviewed the essentials of TF-jets in quiescent gas. Like Classical-JICF, TF-jets exhibit different atomization regimes, which are predominantly governed by the annular gas jet's Weber number. The high We_{gas} fiber-type breakup regime where droplets are shear-stripped by gas directly from the liquid jet is of primary interest to us, because our TF-JICF investigation was conducted at high pressure (i.e., high *We*). Thus, an extensive review of liquid-gas shear-layer development and liquid-entrainment processes in the fiber regime was provided. The effective liquid entrainment velocity (U_e), which is related to the turbulent dynamic pressure of the shear-layer's gas, is the dominant parameter that governs the spray-formation process in this regime.

The prompt-atomization regime where the liquid jet is instantaneously disintegrated and mixed with the annular jet's gas is also highly relevant to our TF-JICF study. This is because most of the existing TF-JICF literatures reported prompt-atomization in their tests, whereupon the J_{eff} spray penetration scaling parameter can be applied. We expect prompt-

atomization to be absent in the low *dP* and *ALR* TF-JICF domains. Unfortunately, a model that predicts the onset of the prompt-atomization regime is not available in literature. Nonetheless, concepts and expressions from the phenomenologically similar "recirculation regime" can potentially be applied.

Although many of the TF-jet's physics reviewed above may be applicable to TF-JICF, many areas also exist where they are phenomenologically different. For example, in many of our test points, the air's velocities were higher than the fuel's velocities. In a TF-jet, the faster air would normally have encouraged the atomization of the central liquid jet. However, in a TF-JICF, the air may, in fact, be weaker at atomization compared to the large amounts of crossflow air that impinge perpendicularly on the liquid jet. Hence, the presence of air may deflect the crossflow away from the liquid jet and *discourage* atomization. Thus, we should be careful about drawing parallels between TF-jet and TF-JICF.

CHAPTER 3. EXPERIMENTAL METHODOLOGY

3.1 JICF Test-Facility

Figures 3.1 and 3.2 show the high-pressure and high-temperature test-facility that was developed to perform this thesis' TF-JICF experiments at conditions that simulate jet-engine fuel-air mixer's operating conditions. This test-facility has a double-chamber design, where the hot, pressurized, crossflow air that enters at the top-left and settles within a large air plenum before being accelerated into a small, thin-walled rectangular test-section where the JICF spray is produced. A thick-walled outer chamber supplied with cold pressurized cooling air surrounds the inner test-section. Both the cooling air and fuel-air mixture exits the facility from the bottom where they are combusted in an afterburner before being released into the lab's exhaust-stack. Instrumentations and sensors are installed throughout the facility (see Figure 3.2) to monitor the test conditions in real time.

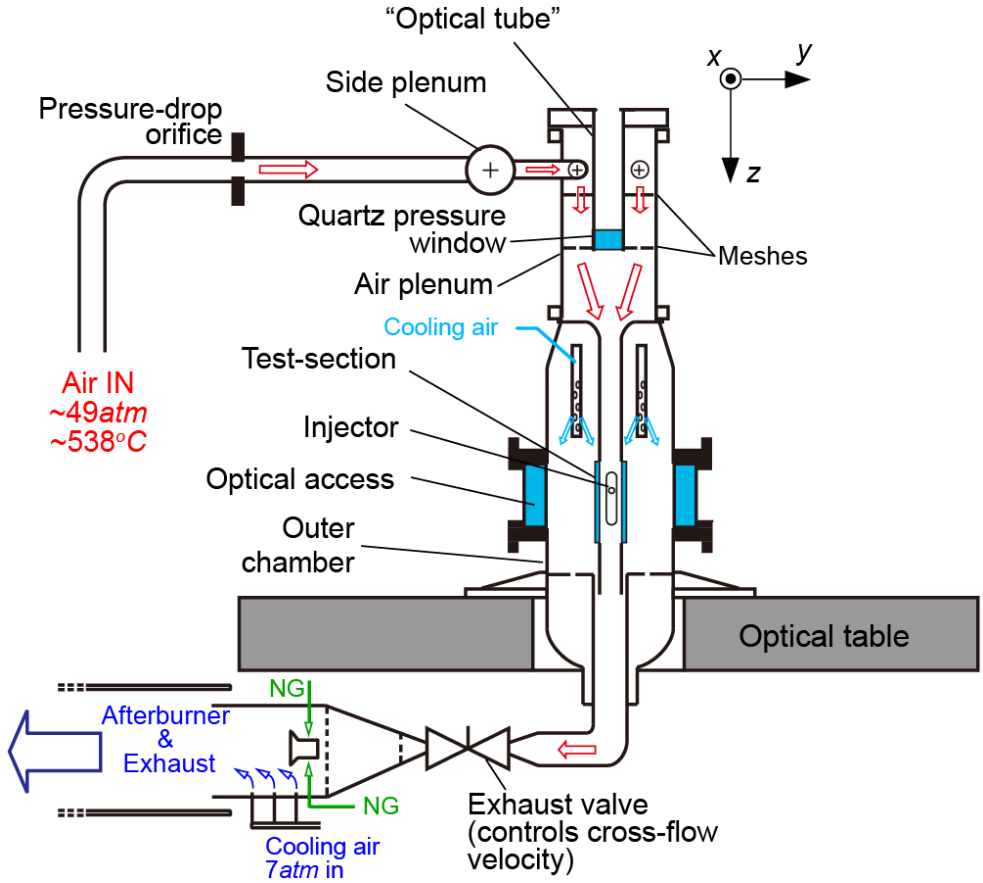

Figure 3.1 – A schematic of the JICF test-facility.

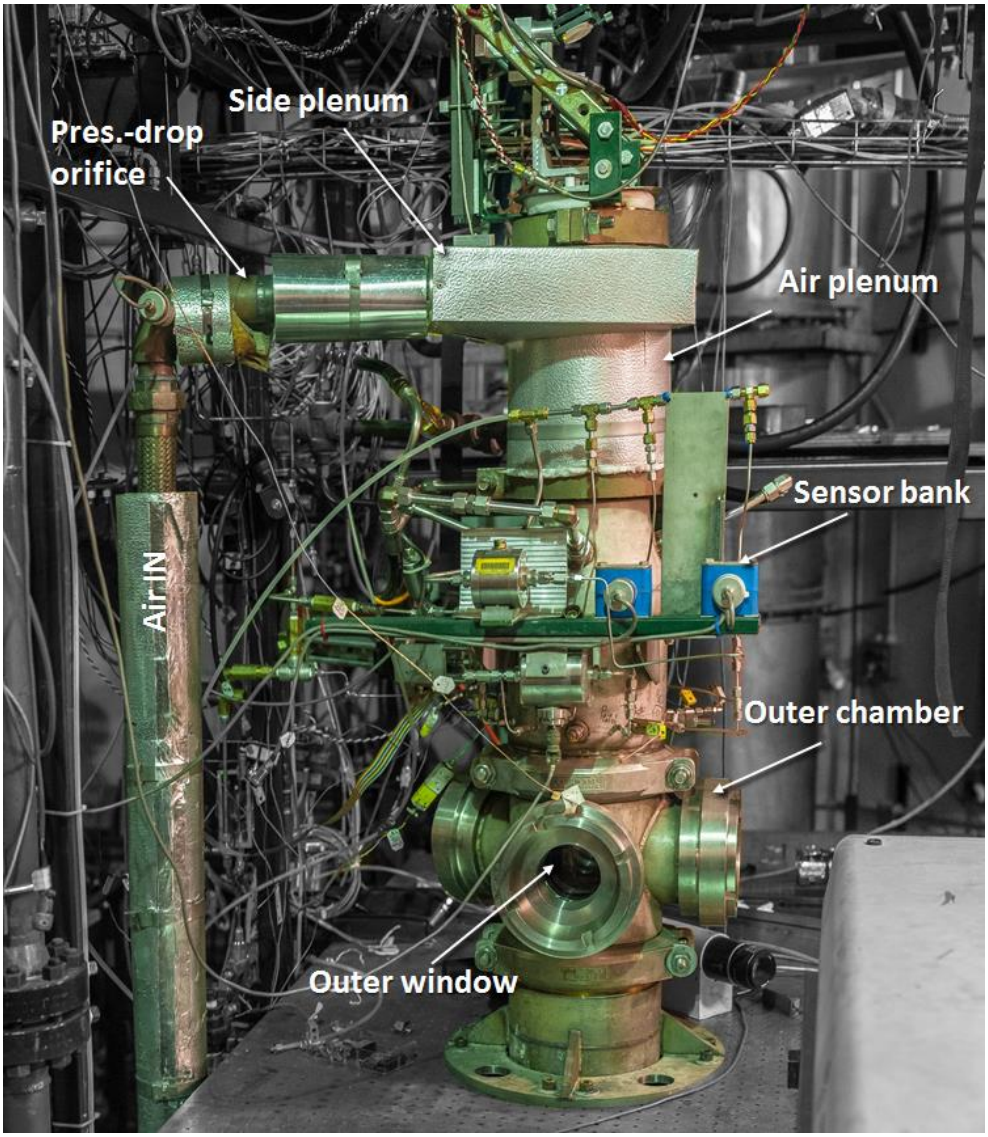

Figure 3.2 – A photo of the JICF test-facility.

During an experiment, the maximum pressure and temperature of the supplied air can reach 720*psia* (49*atm*) and 1000^oF (538^oC), respectively. The air is supplied from the lab's central air-system via a 2.0" (50.8*mm*) diameter stainless-steel pipe shown on the left of Figure 3.1. It then passes through a 1.0" (25.4*mm*) diameter pressure-drop orifice and is distributed by a small horizontal "side-plenum" into four pipes having the diameter of 1.0" (25.4*mm*), which are shown in more details in Figure 3.3. These pipes introduce the hot, high-pressure air into the main test vessel's 6"-diameter (150*mm*) air-plenum via four entry-points that are positioned orthogonally around the air-plenum's circumference. The four entry-points' layout was

designed so that the momenta of the supplied air jets cancel each other in order to maximize the uniformity of the flow downstream.

As shown on the top-right of Figure 3.1 and in more details in Figure 3.4, a 2" (50.8*mm*) diameter "optical tube" with a window mounted on its lower end is located at the center of the air-plenum, thus providing a boroscopic optical access to the facility's interior along the *z*-axis. (This window is used to support other diagnostic systems outside of this dissertation's work). Two layers of flow-straightening meshes are installed in the air plenum to homogenize the airflow. The upper mesh (see Figure 3.4) has 15% average open area and a non-uniform holes distribution, where the holes are spaced more sparsely directly below the air entry-points to block/attenuate any large air jetting velocities. The lower mesh has 30% open area provided by axisymmetrically distributed holes to maximize downstream flow uniformity.

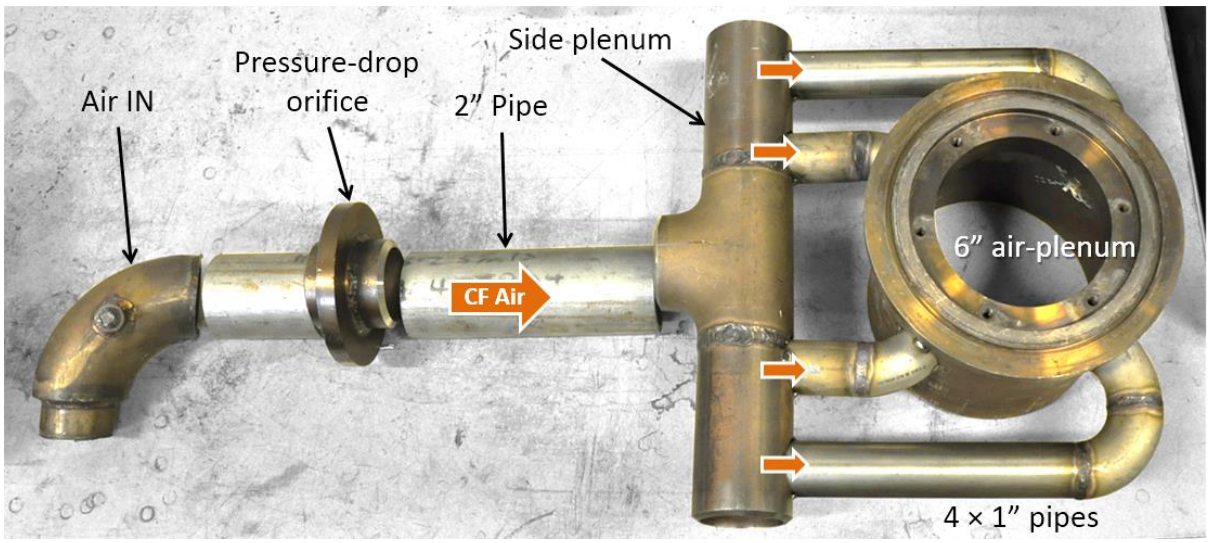

Figure 3.3 – A photo of air-redistribution system in fabrication stage.

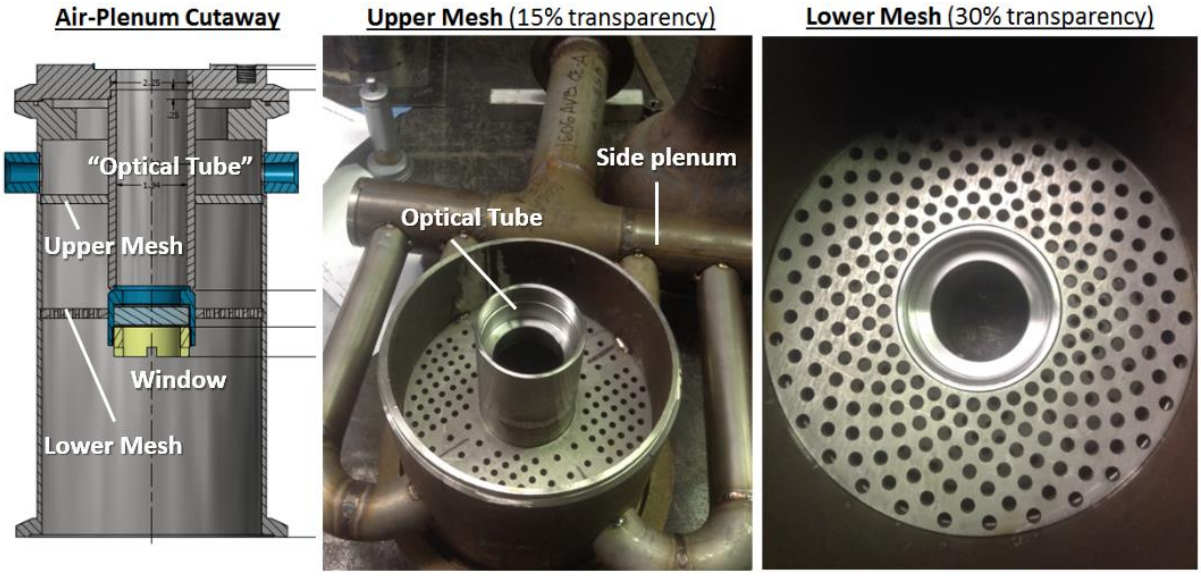

Figure 3.4 – Photos of the air-distribution pipes and flow-straightening meshes.

Figure 3.5 provides an expanded view of Figure 3.1. It describes the inner-channel and test-section downstream of the air plenum. At the downstream end of the cylindrical air-plenum, the hot, high-pressure air enters a rectangular inner-channel via a circular-to-rectangular transition-piece. The initial section of the inner-channel has cross-sectional dimensions of 2.45×1.70" (62.2×43.2*mm*). A pitot-static pressure/temperature probe is installed at the mid-point of this section, where the flow's temperature, stagnation and dynamic pressures are continuously measured during tests. The flow's velocity and density are then determined from these measurements.

At the end of the initial section, the flow is accelerated again across an aerodynamically-shaped contraction into the final 1.25×1.0" (31.8×25.4*mm*) rectangular "test-section" where the JICF spray is investigated. This acceleration decreases the flow's boundary-layer thickness and flow non-uniformity. Crossflow velocity in the test-section is calculated from the known upstream velocity and the contraction ratio by use of a mass conservation equation.

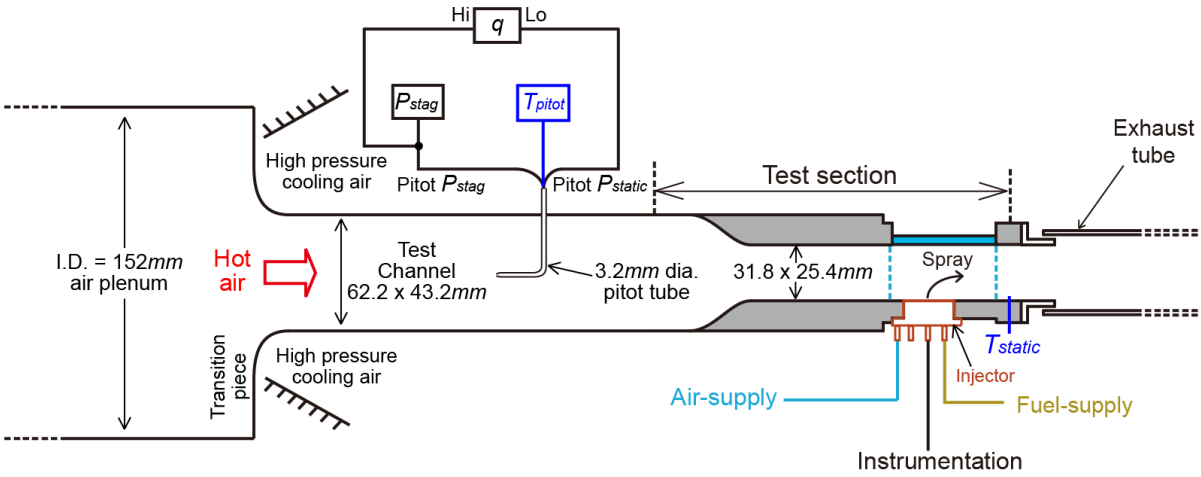

Figure 3.5 – A schematic of the inner-channel and test-section.

Figure 3.6 shows that quartz windows are installed on three of the test-section's sides, while the injector is mounted on the fourth side. The test-section and windows are sized to allow spray-characterization in the spatial domain of z/d_f=0-86 and x/d_f=0-63. Notably, the quartz windows are only 3/16" (4.8*mm*) thick and cannot withstand the full pressure of the crossflow. Instead, the high pressure is supported by the thick-walled outer chamber, which contains relatively quiescent cooling air (~100^oC) at almost the same pressure as the crossflow. The thin test-section walls and windows simply separate the hot crossflow from the cooling air. Optical access through the outer chamber is achieved by four 1.25" (32.0*mm*) thick round quartz windows.

Downstream of the test-section, the cooling air and the crossflow combine into a single flow-path. The cooling air's pressure is maintained at ~2*psig* (~0.14*atm*) above the crossflow's pressure to avoid the ingestion of the fuel-laden crossflow into the outer chamber. Finally, the formed mixture consisting of the "outer" air flow and "inner" fuel-air mixture enters the aft section of the facility (see Figure 3.1) where a remotely-controlled valve modulates the flow's velocity. Due to the valve's low flow capacity, three additional 0.5" (12.7*mm*) valve-bypass pipes are installed to obtain the desired flow-rates. At the final section of the JICF test-facility, the fuel-air mixture is burned in a natural-gas-fired afterburner to prevent the escape of unburned fuel into the lab's exhaust-stack.

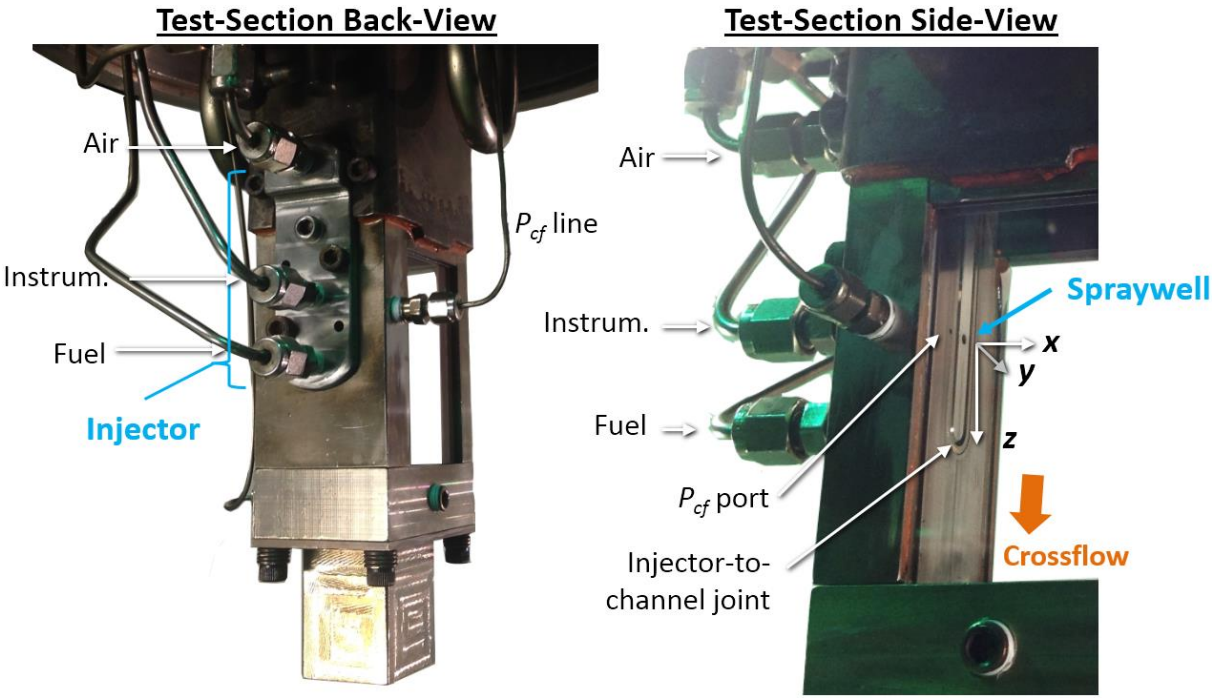

Figure 3.6 – Photos of the test-section with the installed injector.

2D particle image velocimetry was used to characterize the steady state crossflow properties within the test-section in the absence of fuel-injection. Figure 3.7 shows the measurements were conducted over the central (y/d_f=0) *xz*-plane and four lateral planes. Special attention was paid to the velocity profiles at locations where the test-channel wall is uneven; e.g., near the injection orifice and the injector-to-channel joint (see Figure 3.6). The measured average longitudinal velocities ($U_{z,avg}$) are plotted in Figure 3.8 for three measurement locations (as labeled in Figure 3.7). It shows that throughout the test-section volume, the crossflow velocities outside of the boundary-layers were effectively uniform. While the measurements did not resolve the velocity profiles of the boundary-layers, they were sufficient to determine that the boundary-layer thickness was up to 2.5*mm* (or $5d_f$) on the injector-mounting wall. Notably, the velocity profiles were not significantly affected by unevenness on the test-channel wall. Figure 3.9 shows the crossflow turbulence intensities (i.e., root mean square of longitudinal velocity fluctuations) throughout the test-section. Turbulence intensities were

highest in the boundary-layers and were uniform across the freestream region having a magnitude of ~2.5%.

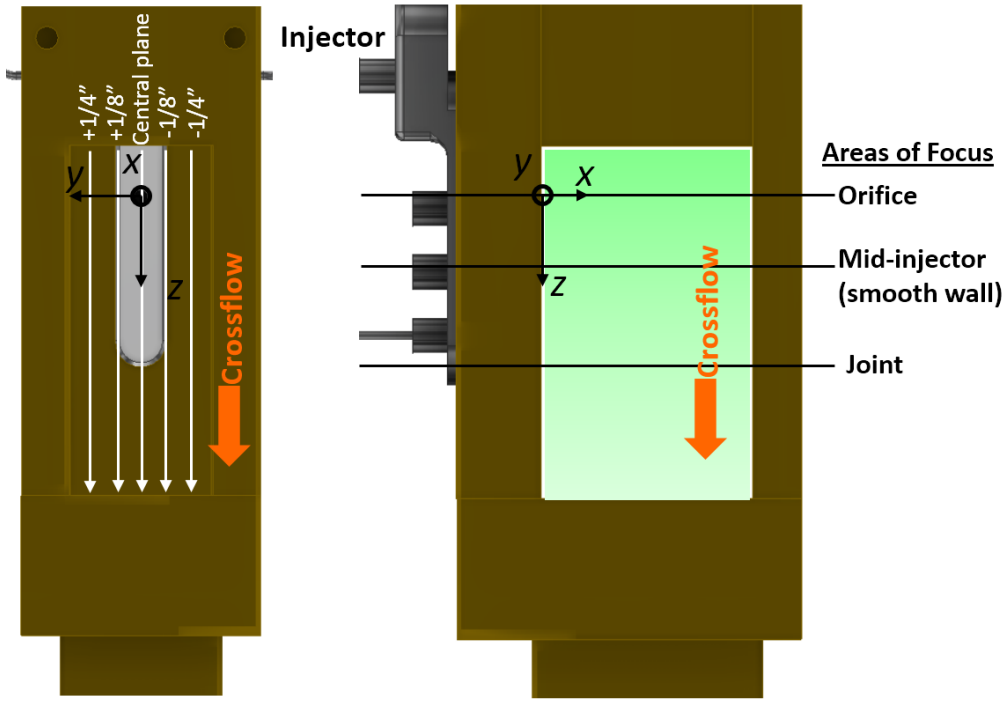

Figure 3.7 – Planes of PIV measurements.

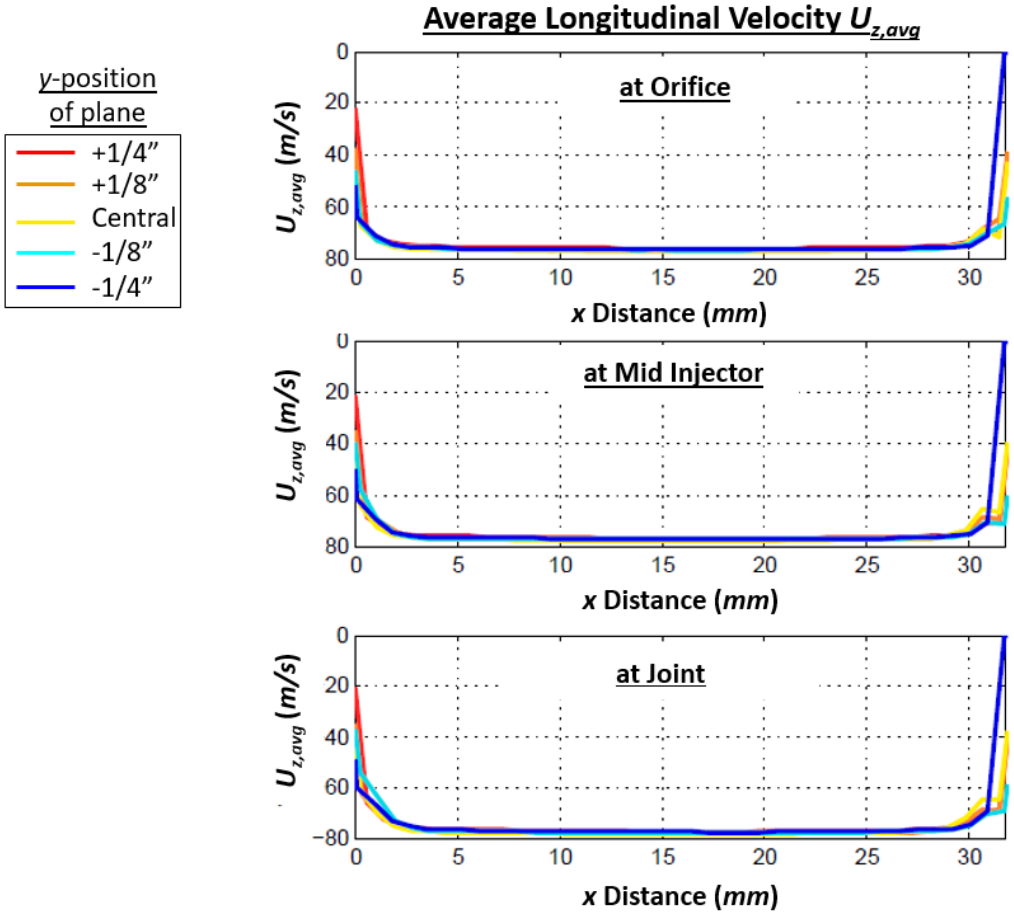

Figure 3.8 – Average longitudinal velocity profiles within the test-section.

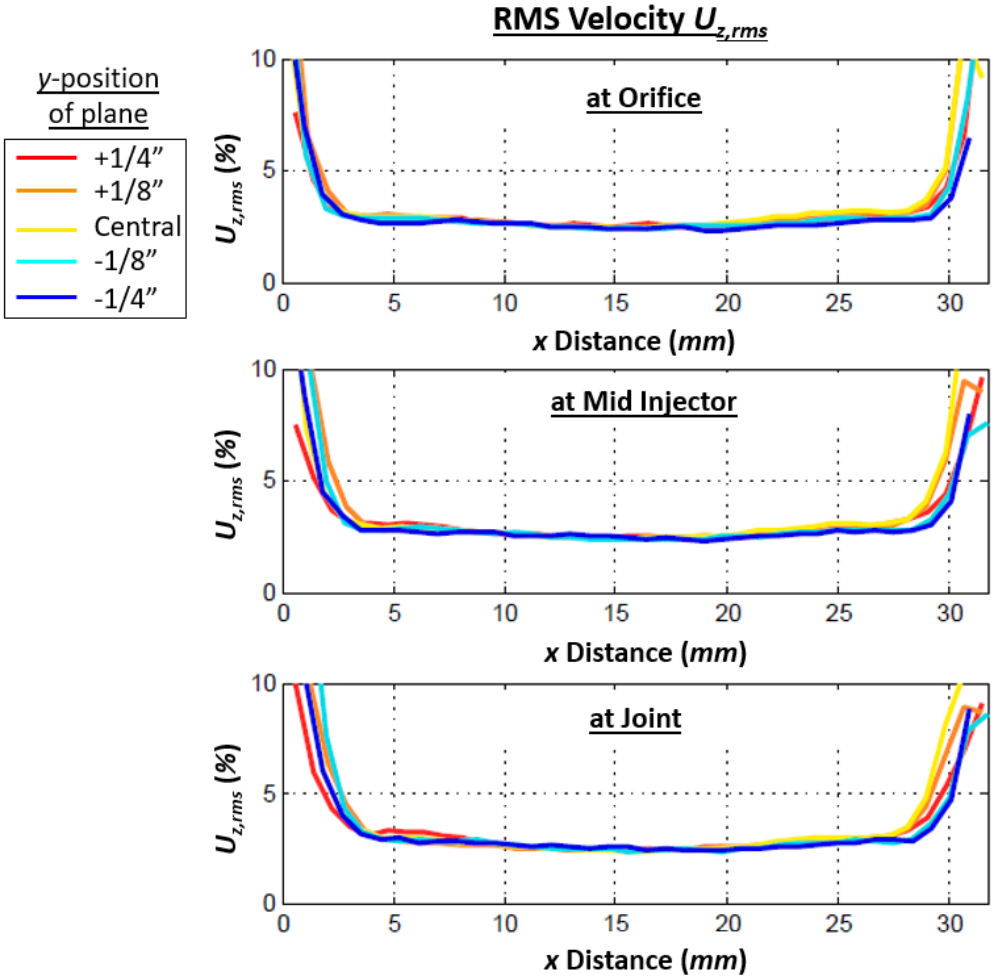

Figure 3.9 – Turbulent-intensity profiles within the test-section.

3.2 The Injector and Fuel-Supply System

This section describes the injector hardware, the fuel-orifice's flow characteristics, and the overall fuel-supply system. Photos of the installed injector are shown in Figure 3.5, while Figure 3.10 shows the injector's flow-paths. The injector's back-side contains four connection ports: the air-supply port, the fuel bypass/out-flow port that was plugged and unused, the fuel-supply port, and the instrumentation port used to measure injector/fuel temperature close to the fuel-orifice. A slender horizontal plenum is located within the top part of the injector, connecting to the fuel bypass and fuel-supply ports at each end. The mid-point of the plenum branches off into a straight injection bore that leads to a circular fuel-orifice having the diameter of 0.506*mm* (e.g., see Figure 3.11). The fuel injection bore's entrance from the horizontal

plenum is rounded, and the bore's length-to-diameter ratio is ~4.4. The fuel-orifice is recessed into a "spraywell" cavity that has a diameter of 1.861*mm* and a depth of 1.27*mm*.

A bench-top test setup was developed and used to determine the hydraulic performance of the custom-made injector's fuel orifice, and to characterize the injected fuel jet's behavior in the absence of crossflow. Figure 3.12 shows the developed bench-top setup. The fuel-supply port of the injector was connected to the lab's central fuel-supply system consisting of a high-pressure pump and an accumulator. A pneumatically-actuated fuel valve with closed-loop control regulated the fuel line's supply pressure, which was measured by a pair of pressure transducers. A turbine flow-meter measured the fuel's volumetric flow-rate that was used to determine the fuel mass flow-rate by assuming that the Jet-A density equaled $\rho_f = 793.3 kg/m^3$. A shadowgraph imaging setup was employed to visualize the characteristics of the resulting fuel jet/spray.

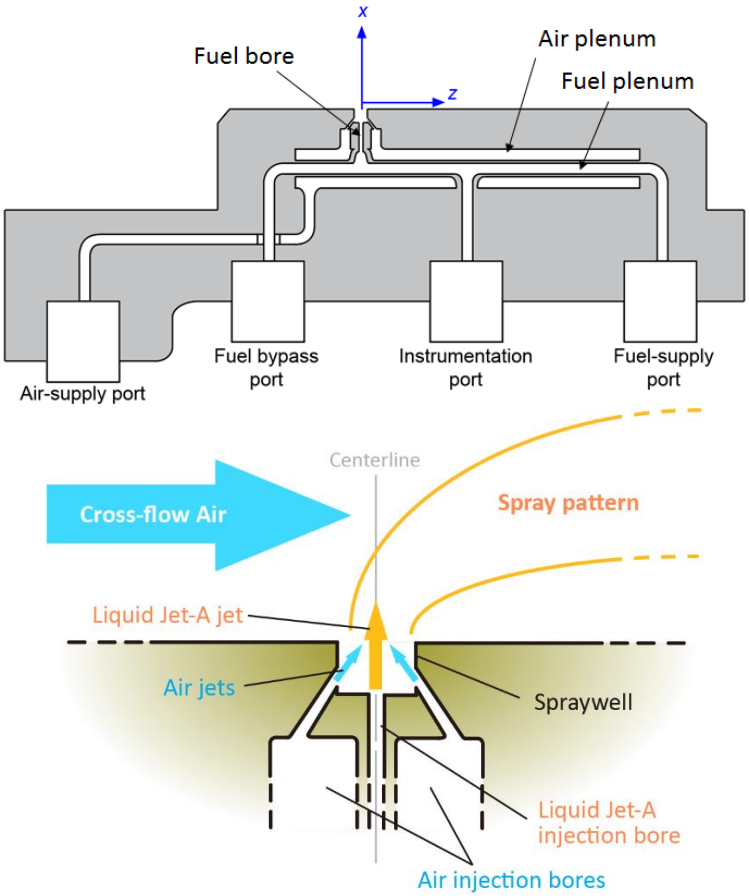

Figure 3.10 – *Top*: A cut-away view of injector. *Bottom*: Zoomed-in view of the spraywell and nozzles.

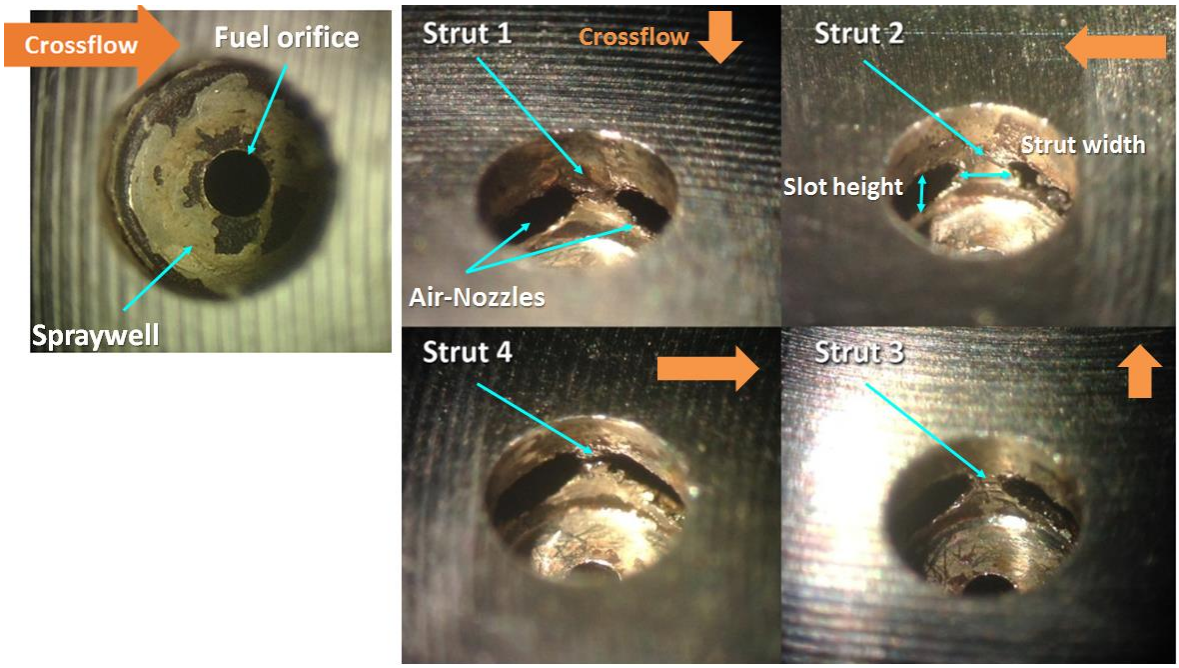

Figure 3.11 – *Left*: A view of the fuel orifice. *Right*: Multiple views of the air-nozzles and supporting struts.

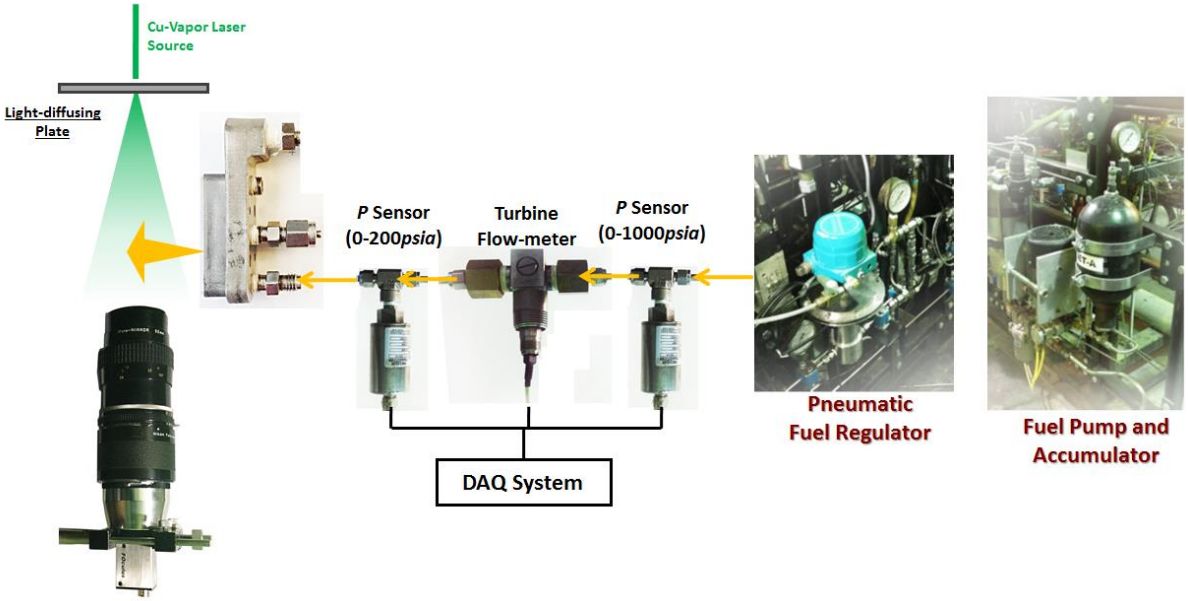

Figure 3.12 – A description of the fuel-orifice flow-characterization setup.

Figures 3.13 and 3.14 show the hydraulic performance of the fuel-orifice, obtained in the bench-top tests. The mass flow-rates of the orifice varied linearly with the square-root of its pressure-drop, in agreement with the standard flow equation derived from Bernoulli's principles:

$$C_{D,f}A_f = \frac{\dot{m}_f}{\sqrt{2\rho_f dP_f}} \quad (1)$$

where $C_{D,f}$ is the fuel-orifice discharge coefficient, A_f is the orifice's area, and $\dot{m}_f$ is the mass flow-rate. The orifice's average discharge coefficient was found to be $C_{D,f} = 0.695$ (shown as a red dashed line in Figure 3.14), while the instantaneous discharge coefficients ranged between 0.65-0.8, with the peak value occurring at Re_d~10,000, where:

$$Re_d = \frac{U_f d_f}{\nu_f} \quad (2)$$

$$U_f = \frac{\dot{m}_f}{\rho_f A_f} \quad (3)$$

and $\nu_f = 1.1 \times 10^{-6} m^2/s$ is the kinematic viscosity of Jet-A. The $C_{D,f}$ peak is customarily attributed to the transition from laminar to turbulent flow. As shown in Figure 3.15, which has been adapted from the work of Lichtarowicz et al. (1965), injection bores with larger length-to-diameter ratios tend to result in transitions at higher Re_d. On the other hand, smooth-edged injection bore entrance will also result in higher transition Re_d. The transition point for sharp-edged bores are typically in the Re_d=5000-10,000 range (Lichtarowicz et al., 1965), while those for smooth-edged bores are typically Re_d=600,000-1,000,000 range (Furuichi et al., 2014). The transition point for our injector (l/d~4.4) is closer to that of a sharp-edged bore. This may be due to the cubic-profile of the injector's bore entrance, which contains a relatively sharp corner.

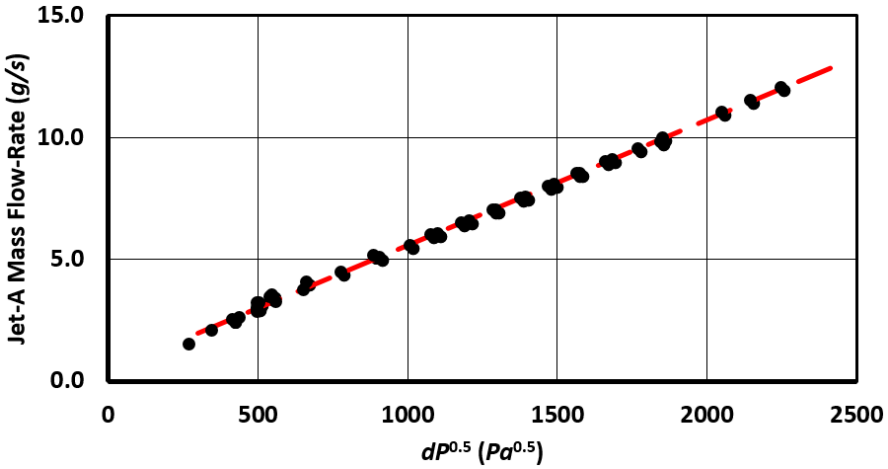

Figure 3.13 – The dependence of fuel mass flow-rate upon the fuel nozzle pressure-drop.

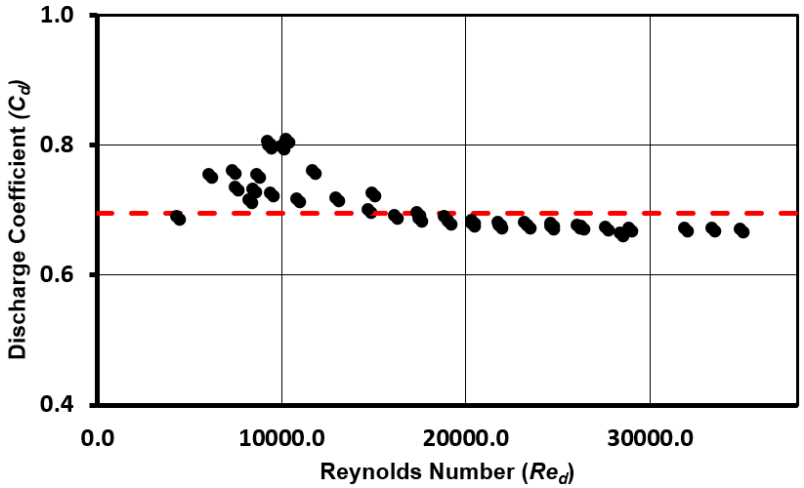

Figure 3.14 – The dependence of fuel-orifice discharge coefficients on Reynolds number.

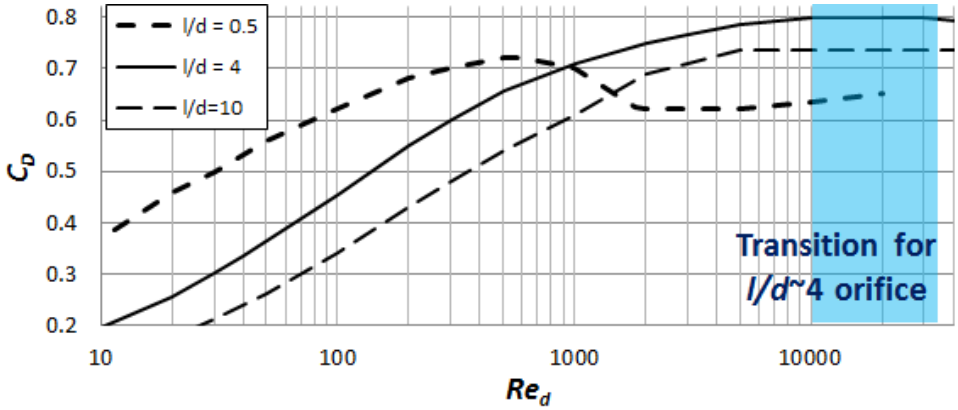

Figure 3.15 – Discharge coefficient for non-cavitating sharp-edge orifice, showing the dependence of typical flow transition points on injector bore *l/d* ratios. Source: Lichtarowicz (1965).

Figure 3.16 shows a series of instantaneous shadowgraph images of the fuel jets generated by this injector at various flow-rates. The mass flow-rates, fuel velocity, Re_d and aerodynamic Weber number ($We_{gas} = \rho_{ambient\ air} U_f^2 d_f / \sigma_f$, where $\sigma_f = 0.0189 N/m$ is Jet-A's surface-tension) are given on top of each image, and the breakup regimes corresponding to each image are listed at the bottom. These regimes are named according to the regime-classification schemes employed by Reitz (1978), Lin and Reitz (1998), Haenlein (1931) and Chigier (1993) for plain-jets in quiescent gas.

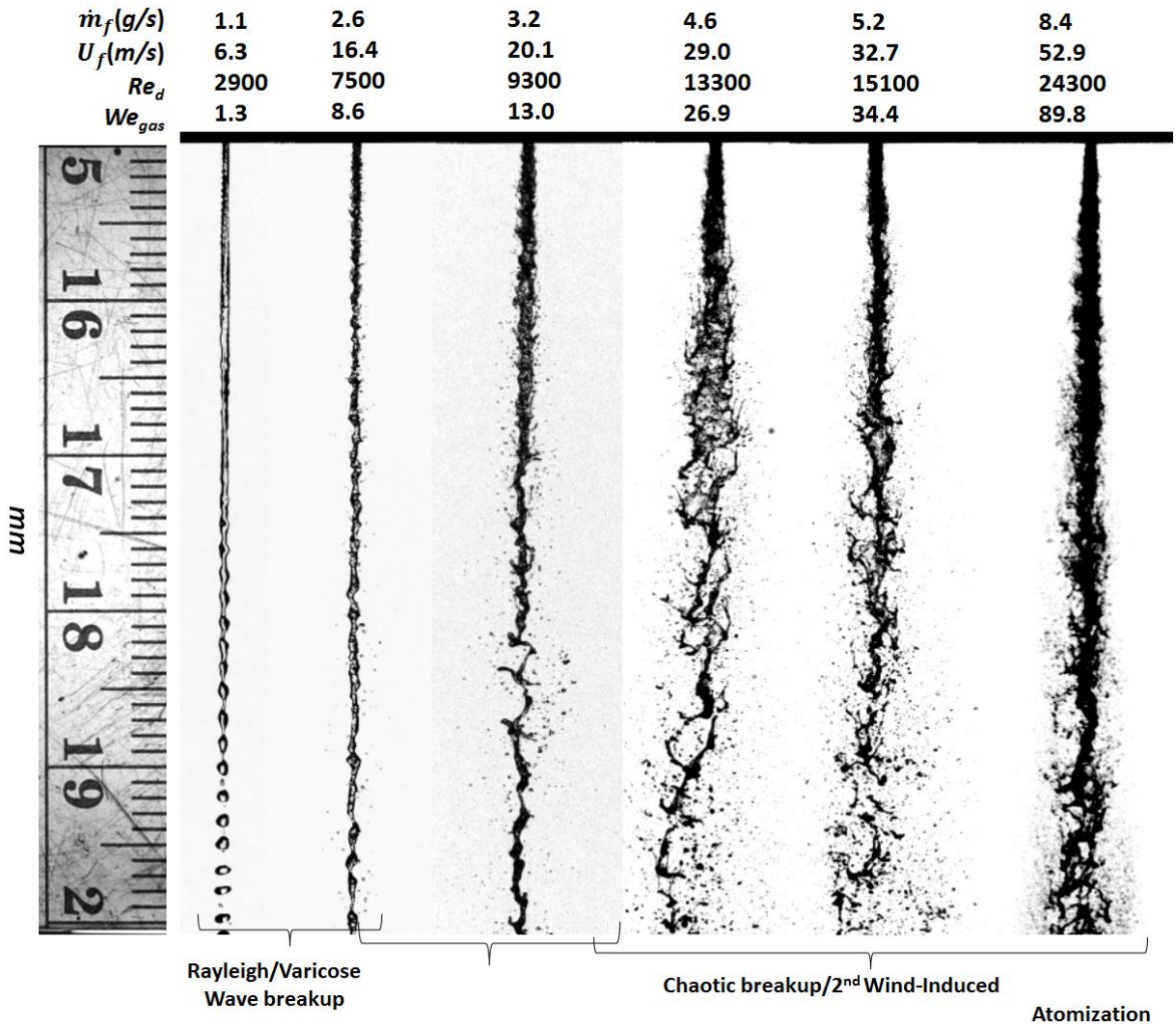

Figure 3.16 – Images of fuel jet structures at different flow-rates.

Figure 3.16 shows that the jets developed disturbances of larger amplitudes (i.e., more intense atomization) at higher injection velocities. The more intense disturbances produced finer droplets and ligaments. At the lowest flow-rate the jet remained intact for approximately 15*mm* (30d_f) before capillary forces caused the jet to develop Rayleigh/varicose-wave instability. The Rayleigh instability eventually resulted in jet pinch-off that produced a uniform train of large discrete droplets with diameters of ~2d_f. As the flow-rate increased to the 2.6-3.2*g/s* range, sinuous wave/1st wind-induced instabilities developed on the jet due to the aerodynamic interaction of fuel with the ambient air. The sinuous wave regime exhibited more vigorous and irregular breakups that generated both large and small droplets. As the flow-rate further increased, the jet transitioned into the chaotic breakup/2nd wind-induced regime, where

strong aerodynamic shearing caused both ligaments/droplets-stripping and gross jet breakups that gave the overall spray a very "chaotic" appearance. At the highest tested flow-rate of 8.4*g/s*, the jet transitioned into the atomization regime, where rapid disintegration was achieved without observable development "wavy"/sinuous motion.

Figure 3.17 shows the observed breakup regimes plotted on the Re_d-vs-We_{gas} regime map cited from Chigier (1993). The sinuous, chaotic and atomization regimes of our data matched Chigier (1993)'s results very well. The Rayleigh/laminar regime extended to slightly higher Re_d than anticipated, but remained in an acceptable range. Based on the observed regimes and discharge coefficients, we have concluded that the current injector's fuel-orifice is representative of a typical plain-orifice with sharp-edged bore.

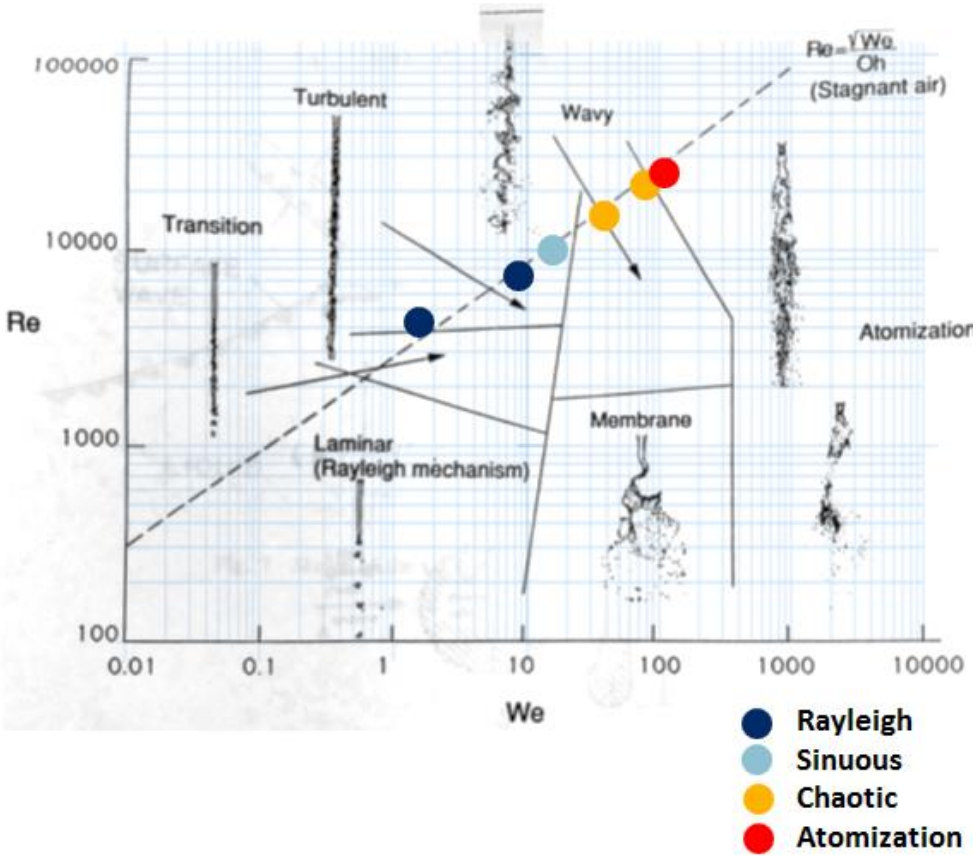

Figure 3.17 – Breakup regimes of jets from the current injector (circles) plotted on the Re_d and *We* regime map adapted from Chigier (1993).

Finally, Figure 3.18 describes the fuel-supply system developed for the TF-JICF experiments. The fuel is first pumped from an external supply into two high-pressure holding tanks. When the tanks are full, the external supply is shut off and the system is pressurized with nitrogen. The pressurized fuel is then delivered to the injector with its flow-rate regulated by a stepper motor-actuated needle valve ("Injection Control Valve" in Figure 3.18). A turbine flow-meter measures the fuel flow-rates, while a pressure transducer and thermocouple connected to the injector's instrumentation port measure the fuel plenum's pressure and temperature, respectively. The measured flow-rate and pressure allow the fuel-orifice's discharge coefficient to be monitored in real time to help identify the occurrence of injector clogging. When fuel is not being injected, nitrogen gas is used to purge the lines and the injector to prevent fuel-coking due to the hot crossflow. Several check-valves are installed along the line to avoid fuel back-flow during test-section pressure transients. Solenoid valves are installed very close to the injector device to allow rapid fuel cut-off when necessary. Notably, this gas-pressurized fuel-supply system has been chosen over a pump-driven system because it is able to supply the injector with a practically steady fuel flow rate.

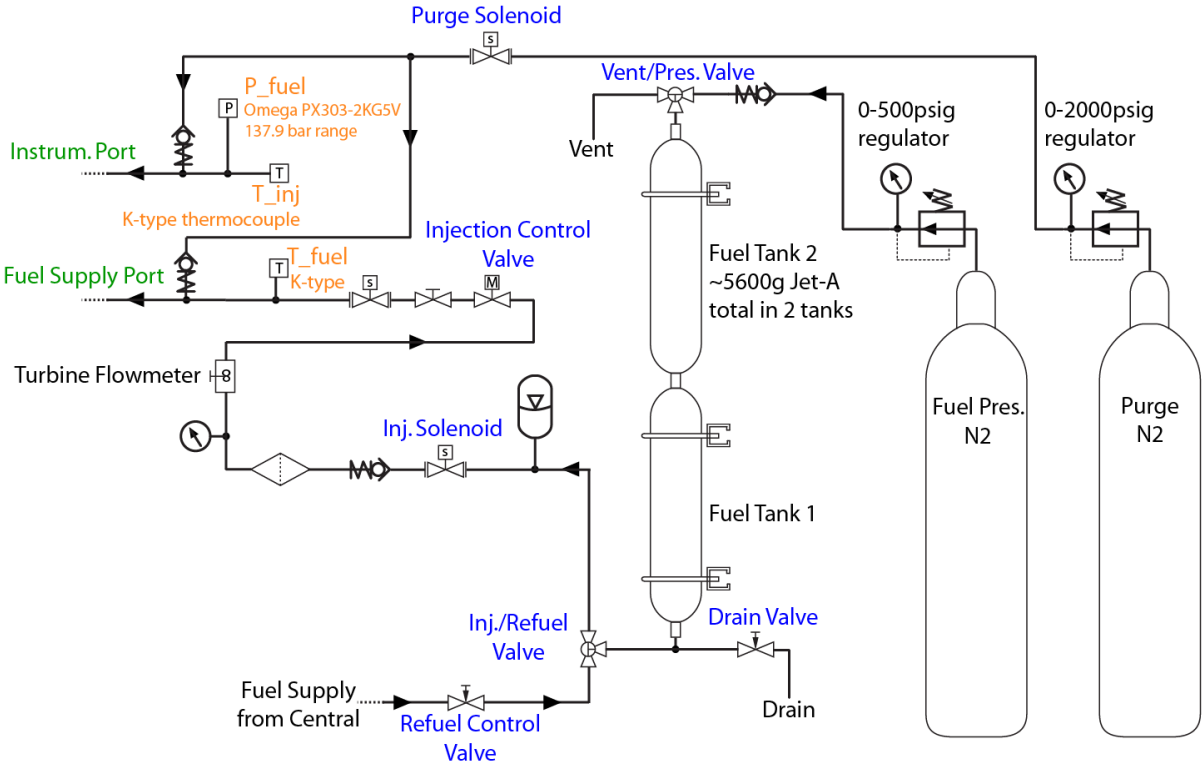

Figure 3.18 – A schematic of the fuel-supply system.

3.3 The Injector's Air-Supply System

This chapter describes the injector's air-nozzles, their flow characteristics, and the TF-JICF experiment's overall air-supply system. As shown in Figure 3.11, the fuel-orifice is surrounded by four slot-type air-nozzles, which span nearly the entire circumference of the spraywell's side wall, separated only by thin support struts. The widths of the struts vary from 0.238 to 0.446*mm*, most likely because of the limited precision of the additive manufacturing technique used to fabricate the injector. The average height of the air-nozzles is 0.394*mm*, resulting in a total air-nozzles area of 1.66mm^2, which equals 8.26 times that of the fuel-orifice area. During operation, pressurized air is supplied to the injector via the air supply port (see Fig. 3.10), which is connected to a horizontal sleeve-plenum that is concentric with the fuel plenum. Four channels branch off from the plenum and lead to the four air-nozzles. These channels are oriented at approximately 45^o with respect to the fuel orifice axis; i.e., the supplied air streams are designed to impinge upon the fuel jet at an angle. Based on the air and fuel

nozzles' relative orientations and positions, the point of impingement is expected to be located at 0.14*mm* below the spraywell's lip (i.e., effectively flushed with the test-channel wall).

As was done with the fuel-orifice, the air-nozzles' flow performance was characterized using the bench-top setup shown in Figure 3.19. The air in this setup was supplied by the lab's 125*psia* (8.5*atm*) central air supply system. A gas pressure-regulator was used to manually control the pressure within the air-supply line. A turbine flow-meter measured the volumetric flow-rate of the air while a pressure-transducer and thermocouple measured air pressure and temperature in the supply line, respectively. The air's density and subsequent mass flow-rate could then be determined using the perfect gas equation. The air-nozzles' pressure drop (*dP*) was defined as the pressure difference between the supply line pressure and the ambient room pressure (1*atm*). During the characterization of the air-nozzles, the fuel-orifice was also supplied with fuel of varying flow-rates to identify any potential coupling between the air and fuel nozzles' performance.

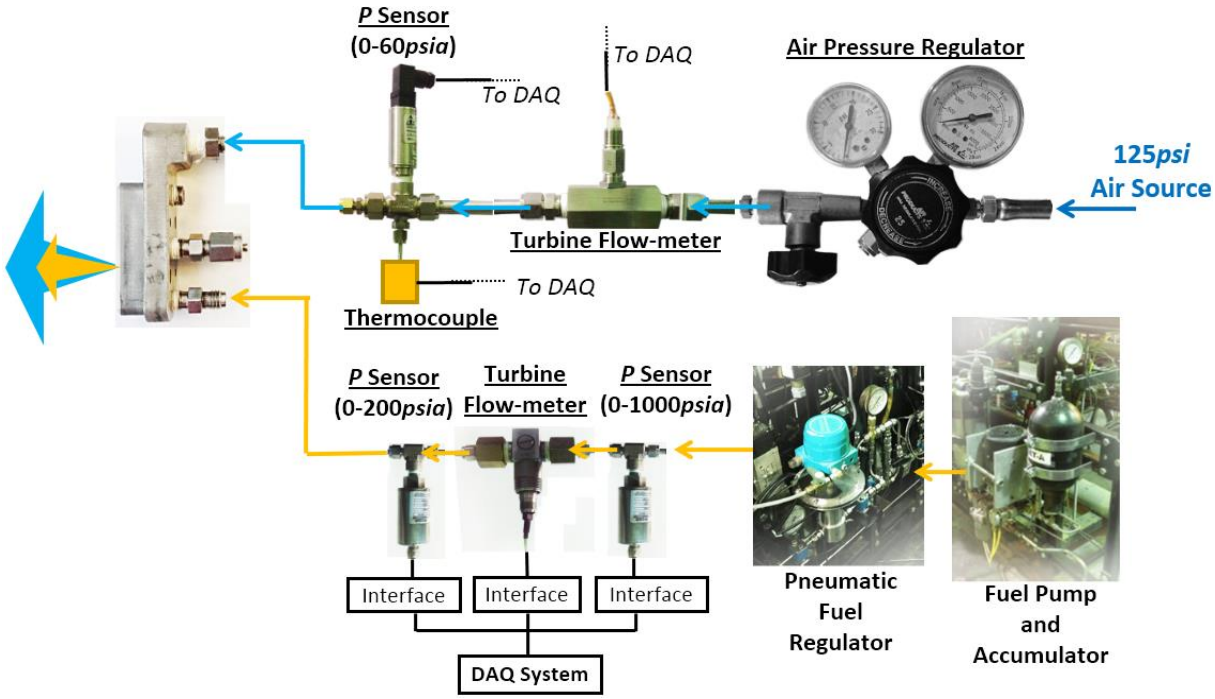

Figure 3.19 – Description of the air-nozzles characterization setup.

Figure 3.20 show the results from the bench-top air-nozzles characterization. The air's mass flow-rates varied as a square-root of the nozzles' pressure-drops and the air's densities. The presence of fuel injection did not significantly affect this flow-rate trend, and the average discharge coefficient of the air-nozzles is $C_{D,air}$ =0.39. Although this value is appreciably lower than those typically exhibited by plain-orifices, it may be reasonable for our thin slot-type nozzles with rough surfaces and complex internal flow-paths (i.e., large viscous losses).

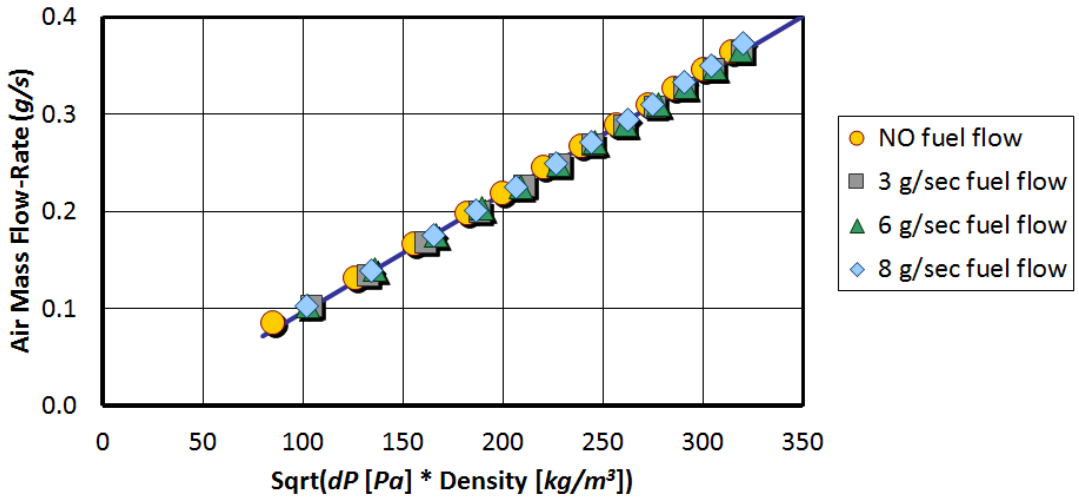

Figure 3.20 – The dependence of mass flow-rate of air upon the nozzles' pressure-drop and air density.

Figure 3.21 shows the setup that is being employed to supply air to the injector during the TF-JICF experiments. This setup has been developed to accommodate a very large range of air-nozzles *dP* ranging from 0% up to (and exceeding) 150% of the crossflow pressure, which spans almost the entirety of the TF-JICF parameter space shown in Figure 1.4. Since a suitable source of high-pressure air is not available, an alternative approach is used where the system is supplied by high-pressure nitrogen gas cylinders. Nitrogen gas is a close approximation of air, having only 3.35% lower density than air at given temperature and pressure. The small density difference is not expected to cause any significant difference to the TF-JICF's behaviors. For the convenience of discussion, we will continue to refer to the co-injected nitrogen gas as "air".

Figure 3.21 shows that the flow-rate of air is controlled by two valves to achieve the desired large air-flow turn-down ratio. A pneumatically-actuated valve with closed-loop control ("Tescom Pressure Regulator") is used to regulate the air flow-rates across the majority of our *dP* range. When this valve reaches its minimum controllable flow-rate at around *dP*=5%, the control of lower air flow rates is achieved by the secondary remotely-controlled needle-valve ("Manual Regulator"). Two sets of pressure transducer and thermocouple are installed in this air-supply system: one to support the determination of air-density/mass flow-rate close to the turbine flow-meter, and another to measure the air-nozzles' *dP* and the air's temperature immediately prior to injection.

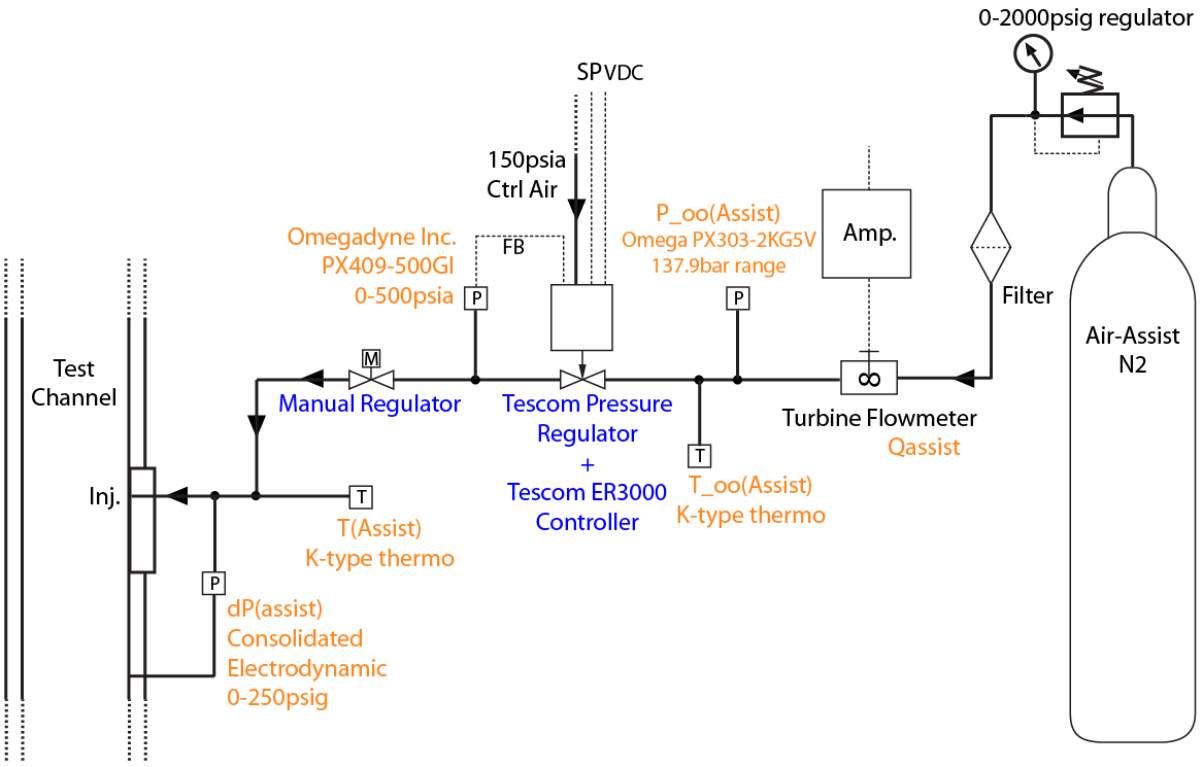

Figure 3.21 – A schematic of the injector's air-supply system.

Finally, the air-nozzles' operation during tests can be categorized into the following three modes: (i) the low-*dP* mode where air flow-rate is below the turbine flow-meter's measurable range, (ii) the subcritical orifice mode where the injected air is ideally expanded to

crossflow pressure (P_{cf}), and (iii) the choked-mode where the flow is sonic at the point of injection. The following operating parameters were used for each of these modes of operation:

Low-*dP* Mode:

The air-flow rate is determined as follows using the measured air-nozzles *dP* and the discharge coefficient found from the bench-top calibration:

$$\dot{m}_{air} = C_{D,air} A_{air} \sqrt{2 \rho_{air} dP} \tag{4}$$

where, the air-density is determined through a perfect-gas equation:

$$\rho_{air} = \frac{P_{air}}{R_{N_2} T_{air}} = \frac{P_{air}}{\left(297 \frac{J}{kg \cdot K}\right) T_{air}} \tag{5}$$

Solving Eqn. [2] assumes (i) $P_{air} = P_{cf}$ due to ideal expansion, and (ii) isentropic pressure-temperature relation:

$$T_{air} = T_{air,0} \left(\frac{P_{cf}}{P_{air,0}}\right)^{\frac{\gamma_{N2}-1}{\gamma_{N2}}} = T_{air,0} \left(\frac{P_{cf}}{P_{cf}+dP}\right)^{\frac{\gamma_{N2}-1}{\gamma_{N2}}} \tag{6}$$

where, $\gamma_{N2} = 1.4$ is nitrogen's specific-heats ratio and $T_{air,0}$ is the air's stagnation temperature as measured inside the injector (see "T(Assist)" in Figure 3.21). Thus, the velocity of the injected air is determined as follows:

$$U_{air} = \frac{\dot{m}_{air}}{\rho_{air} A_{air}} \tag{7}$$

The combination of ρ_{air}, T_{air}, P_{air} and U_{air} completely specify the states of the injected air.

Subcritical Mode:

In the subcritical mode, the air's volumetric flow-rate ($\dot{V}_{air}$) is measured directly by the turbine flow-meter and converted into the mass flow-rate. The conversion uses an air density value ($\rho_{air,line}$) calculated using the perfect gas-equation, based on the pressure

and temperature measured near the turbine flow-meter (e.g., see "P_oo(Assist)" and "T_oo(Assist)" in Figure 3.21, respectively). Due to subsonic velocities, the air is assumed to expand ideally to crossflow pressure. Subsequently, the injected air's temperature, density and velocity are determined in the same manner as for the Low-*dP* Mode by use of Equations (5)-(7).

Choked Mode:

A critical air-nozzles back-pressure (P^*) exists below which the nozzles' flow velocity will become choked. P^* is defined as follows:

$$P^* = P_{air,0}\left(\frac{2}{\gamma_{N2}+1}\right)^{\frac{\gamma_{N2}}{\gamma_{N2}-1}} = \left(P_{cf} + dP\right)\left(\frac{2}{\gamma_{N2}+1}\right)^{\frac{\gamma_{N2}}{\gamma_{N2}-1}} \quad (8)$$

When $P_{cf} \leq P^*$, the air-nozzles operate in the chocked mode. The mass flow-rate of air continues to be determined in the same manner as in the Subcritical Mode. However, the temperature and pressure of the injected air are determined assuming an injection Mach number of 1 (i.e., no supersonic expansion), in which case:

$$T_{air} = T_{air,0}\left(1 + \frac{\gamma_{N2}-1}{2}\right)^{-1} \quad (9)$$

$$P_{air} = P_{air,0}\left(1 + \frac{\gamma_{N2}-1}{2}\right)^{\frac{-\gamma_{N2}}{\gamma_{N2}-1}} \quad (10)$$

From here the injected air's density can be determined from Equation (5) and the *bulk* air velocity from Equation (7). Notably, the bulk air velocity will be lower than sonic speed because the flow in the nozzles' boundary-layer is subsonic. I.e., the difference between the bulk air velocity and the *ideal* sonic velocity is related to the nozzle's discharge coefficient.

3.4 Optical Diagnostics System

Figure 3.22 shows a schematic of the shadowgraph-imaging setup used to characterize the TF-JICF sprays in our experiments. The setup employs a single FOculus FO531SB monochrome, low-speed camera (Aegis Electronic Group, 2016) fitted with a Micro-Nikkor 55*mm* f/2.8 Al-s prime-lens (Rockwell, 2012) to image the spray from the side-view (i.e., imaging the *xz*-plane). This camera's native resolution is 1600×1200*px* and it is installed to capture the spray in the space of $z/d_f \approx$ 0-38, providing a resolution of approximately $13.52\mu m/px \pm 0.87\%$. The captured images are stored in a 12bit lossless raw format to maximize their intensity bit-depth and quality. In some tests, a second FOculus FO531TB camera (Net: New Electronic Technology, 2011) with the same lens is used to simultaneously image the spray from the top-view (i.e., imaging the *yz*-plane).

The laser employed in this setup is a Photonics Industries DS20-355 diode-pumped pulsed Nd:YAG laser (Photonics Industries, 2016) that is operated in its 2nd harmonic to emit 532*nm* light. The laser is triggered to pulse at 30*Hz* using its own internal clock, while its trigger signal is connected to the cameras to synchronize their exposure gating to the laser pulse. Because the cameras' maximum framerate is 15*Hz*, they only capture an image once every other laser pulse. This Nd:YAG laser system has been specified by Photonics Industries to have an average power of 8*W*, a pulse-width of <35*ns* and a pulse diameter of 0.9*mm* when operated in the 3rd harmonic (355*nm*) at 10*kHz*. Laser power when operating at 532*nm* and 30*Hz* was not separately measured as it is not critical to the shadowgraph-imaging technique.

As shown in Figures 3.22-3.23, the emitted laser light is focused by a simple lens onto one end of a fiber-optic cable, which is then threaded through the test-facility's outer pressure vessel wall. The other end of the fiber-optic cable illuminates the laser onto a light-diffusing plate positioned parallel to the inner test-section's window. A filter-cell containing Exciton's pyrromethene 567 fluorophor dye dissolved in high-purity vacuum oil is placed between the

test-section and the diffusing plate. This dye is excited by the 532*nm* laser light and fluoresces in the yellow spectrum (549-592*nm*). The fluorescence forms the back-light for the shadowgraph-imaging. The use of a dye filter-cell for back-lighting (instead of direct laser light) improves the image quality, because the fluorescence is spatially incoherent and does not produce laser light-interference speckling-patterns. A speckle-free image is essential for observing fine spray structures and droplets. Sample images from this setup and the data-reduction schemes are discussed at length in Section 3.6.

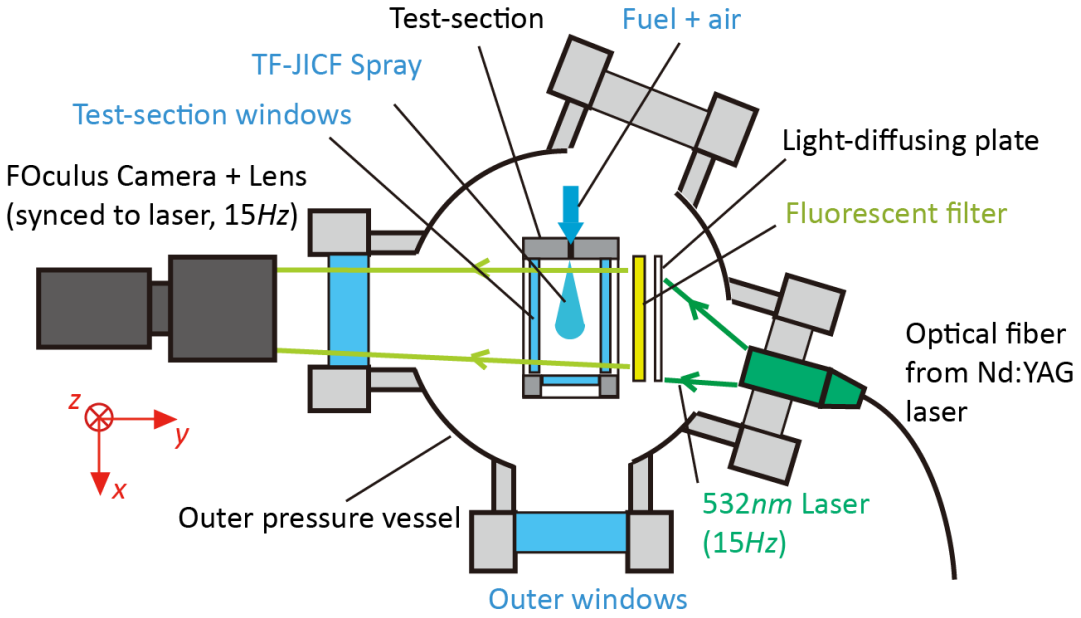

Figure 3.22 – A cross-sectional cutaway of the test-facility, shown along the shadowgraph-imaging setup.

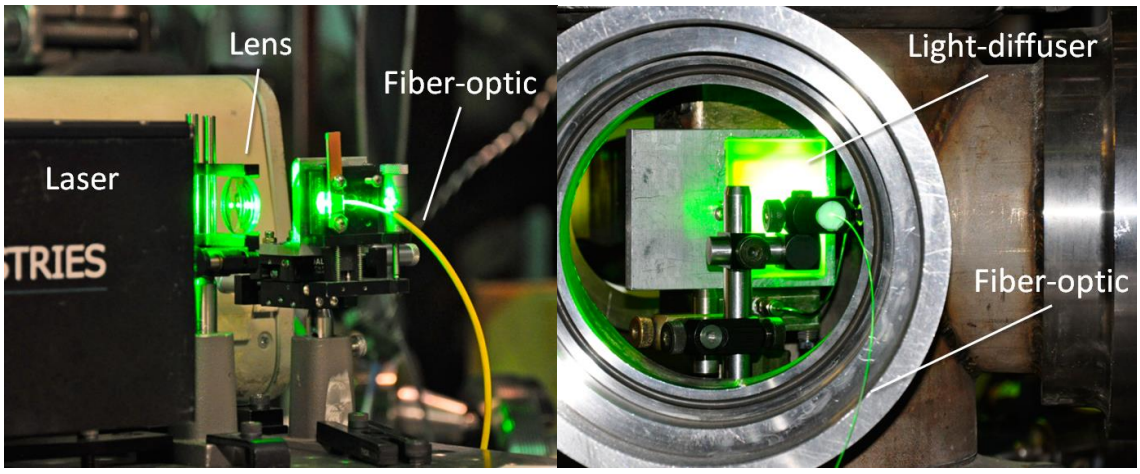

Figure 3.23 – Photos of the laser focused on the fiber-optic (*left*) and the fiber-optic illuminating the light-diffusing plate mounted next to the test-section (*right*).

3.5 Test-Matrix

This section describes the experimental test-matrix that was designed to achieve the investigation's objectives that are discussed in Chapter 1. As presented in Section 3.1, the employed experimental setup is a complex facility with many degrees of freedom. Table. 3.1 provides a list of critical "Test-Control Parameters" that are continuously monitored and controlled during a test to fully specify these degrees of freedom. While some of these parameters (e.g., crossflow pressure and temperature) are directly measured by installed sensors, others (e.g., *J*) are calculated by the data-acquisition system based on multiple sensors' readouts. In addition to the Test-Control Parameters, physical and non-dimensional parameters that are commonly used to describe JICF and TF-jets are also employed in the test-matrix design and to describe the results. These parameters are defined as follows in Table 3.2.

Table 3.3 shows the three dimensional test-matrix developed for this investigation. The parameters of We_{cf}, *J* and *%dP* are varied in this test-matrix in order to study the TF-JICF at different fuel flow-rates, air flow-rates and crossflow conditions. In this matrix, the crossflow velocity (U_{cf}) is fixed at ~70*m/s* to maintain a constant flow residence time within the test-section. This velocity value is typically encountered in jet-engine fuel-air mixer devices. Also, the crossflow temperature is fixed at $T_{cf} \approx 150^{o}C$, which is high enough to prevent water condensation on the test chamber windows, but low enough to limit fuel vaporization to an amount that would not impact the interpretation of the atomization processes (e.g., as shown in the vaporization estimates in Appendix A). Notably, holding T_{cf} constant has the additional benefit of making U_{air} independent of We_{cf} for a given *%dP*, while only ρ_{air} varies.

Table 3.1 – A list of Test-Control Parameters.

Test-Control Parameters		
Crossflow-control	$P_{cf}(atm)$	Crossflow pressure.
	$T_{cf}(^oC)$	Crossflow temperature.
	$U_{cf}(m/s)$	Crossflow velocity.
Fuel-control	$J = \frac{\rho_f U_f^2}{\rho_{cf} U_{cf}^2}$	Fuel-to-crossflow momentum-flux ratio.
Air-control	$\%dP = \frac{dP}{P_{cf}} \times 100\%$	Percentage air-nozzles pressure-drop.

Table 3.2 – A list of Physical Parameters.

Physical Parameters		
Crossflow-related	ρ_{cf} (kg/m^3)	Crossflow density.
	$We_{cf} = \frac{\rho_{cf} U_{cf}^2 d_f}{\sigma_f}$	Crossflow Weber number.
Fuel/air-related	U_f (m/s)	Bulk fuel velocity based on the measured volumetric flow-rate and fuel-orifice area. See Chapter 3.2.
	U_{air} (m/s)	Bulk air injection velocity. See Chapter 3.3 derivations and assumptions.
	ρ_{air} (kg/m^3)	Air density just after injection.
	$ALR = \frac{\dot{m}_{air}}{\dot{m}_{air}}$	Air-to-fuel mass flow-ratio.
	$We_{air} = \frac{\rho_{air} U_{air}^2 d_f}{\sigma_f}$	Air Weber number
	$J_{air} = \frac{\rho_{air} U_{air}^2}{\rho_{cf} U_{cf}^2}$	Air-to-crossflow momentum-flux ratio.
	$J_{eff} = \frac{A_f \rho_f U_f^2 + A_{air} \rho_{air} U_{air}^2}{A_{total} \rho_{cf} U_{cf}^2}$	Effective momentum-flux ratio. Where $A_{total} = A_f + A_{air}$ is the spraywell area.

Table. 3.3 – The developed test-matrix.

Parameter	Values
T_{cf}	$\sim 150^oC$
U_{cf}	$\sim 70 m/s$
We_{cf}	175, 350, 1050
J	10, 20 for $We_{cf} = 175$ 5, 20, 40 for $We_{cf} = 350$ 5, 20, 25 for $We_{cf} = 1050$
$\%dP$	0, 3, 5, 13, 25, 50, 75, 100, 150

As discussed in Chapter 1, the majority of TF-JICF researches to date have been performed at near-atmospheric conditions, which generally resulted in $We_{cf} \leq 200$. In the absence of air-injection, these JICF sprays would lie on the borderline of the shear-atomization

regime, which is not representative of TF-JICF behaviors at engine operating conditions where We_{cf} ≈1000-3000. In order to obtain data under conditions in literature *and* in jet-engines, our test-matrix spans a Weber number range of $We_{cf} = 175$, 350 and 1050. These variations in We_{cf} are achieved by varying P_{cf} and, thus, ρ_{cf}. Selection of the above We_{cf} values is based on Lubarsky et al. (2010)'s findings in Classical-JICF (see Figure 2.6), which shows that a typical spray's droplets Sauter Mean Diameters (SMD) are generally very sensitive to We_{cf} only in the low We_{cf} domain, and that sensitivity diminishes at higher We_{cf}. With these considerations in mind, the lowest We_{cf} in this investigation is chosen to be 175, a value used in reported TF-JICF studies (i.e., at near atmospheric operating conditions). On the other hand, the highest We_{cf} is chosen to be 1050, which is expected to produce SMD's similar to those observed in typical jet-engine with We_{cf} of 1000-3000. The middle point is chosen to be $We_{cf} = 350$, which is comfortably within the shear-atomization regime and anticipated to produce droplets SMD that are approximately halfway between the two extremes. These set-points were expected to allow the determination of We_{cf}'s influence on TF-JICF behaviors.

Table 3.3 shows the ranges of *J* covered in this study generally span *J*=5 to 40. Notably, identical ranges of *J*'s is not achievable at all We_{cf} due to turndown-ratio limitations of the fuel-supply system. Therefore, *J*=20 is used as the common *J* value across all crossflow conditions. This *J* value represents the typical fuel flow-rate encountered near the cruise to full engine power conditions. On the other hand, the lower *J* values in the range of 5-10 are typically encountered at near-idle power setting. *J*'s of 5-10 are phenomenologically interesting based on past operating experience with this injector, because they produce low-penetrating sprays that are attached to the test-channel wall, which (as noted in Chapter 1) can adversely affect engine durability. Consequently, studying TF-JICF in the range of *J*=5-10 allows us to determine whether air-injection can be used to improve adverse fuel distribution patterns. Finally, the *J*=25-40 range represents fuel flow-rates in excess of typical full engine power

setting. The sprays at these *J*'s will have very high penetrations (i.e., minimal spray-wall interactions) and very low crossflow-induced disturbances; i.e., they may respond to air-injection differently than the *J*=5-10 sprays.

Finally, air-nozzles pressure-drop levels of *%dP* = 0, 3, 5, 13, 25, 50, 75, 100 and 150 were studied in this investigation. These values range from the Classical-JICF to the choked-nozzle conditions that can be found in *airblast* atomizers, potentially allowing the full spectrum of TF-JICF regimes/behaviors to be observed. Notably, the *dP* test-points are more closely clustered in the lower *dP* domain, which is the domain of our primary interest. The higher *dP* domain had sparser points, as increasingly high *dP* is expected to have diminishing effects on spray-formation.

Figure 3.24 compares the ranges of *dP* and air-to-fuel mass flow ratio ($ALR \equiv \dot{m}_{air}/\dot{m}_f$) covered in this investigation and in the studies of Leong et al. (2000, 2001 *JPP*, 2001 *JEGTP*), Sinha et al. (2013, 2015) and Li et al. (2006, 2009, 2010 *Part 1*, 2010 *Part 2*)- which represent the bulk of TF-JICF literature. In Figure 3.24 and the plots that follow, not all of the plotted parameters were reported in the literature; best-estimates were made where necessary based on reported information. Furthermore, many of the plotted test-points from Leong et al. (2000, 2001 *JPP*, 2001 *JEGTP*) and Sinha et al. (2013, 2015) were carried out on different injectors and fluids. Thus, their experimental data for a single set of injector and fluid were actually more limited than Figure 3.24 suggests. Evidently, the our test-matrix's *dP* range exceeds the full ranges of Leong et al. (2000, 2001 *JPP*, 2001 *JEGTP*) and Li et al. (2006, 2009, 2010 *Part 1*, 2010 *Part 2*), while missing the topmost *dP* values studied Sinha et al. (2013, 2015). Although our test-matrix exceeds Li et al. (2006, 2009, 2010 *Part 1*, 2010 *Part 2*) and Leong et al. (2000, 2001 *JPP*, 2001 *JEGTP*)'s *dP* ranges, we could not match their *ALR* range, because they employed nozzles with large air-to-fuel area ratio, operated at very low fuel flow-rates. The effects of varying air-to-fuel nozzle area ratio was not explored during this investigation.

Most importantly, Figure 3.24 shows the current test-matrix is developed to cover the lower-left corner of the *dP*-vs-*ALR* parameter space in more details than other researchers.

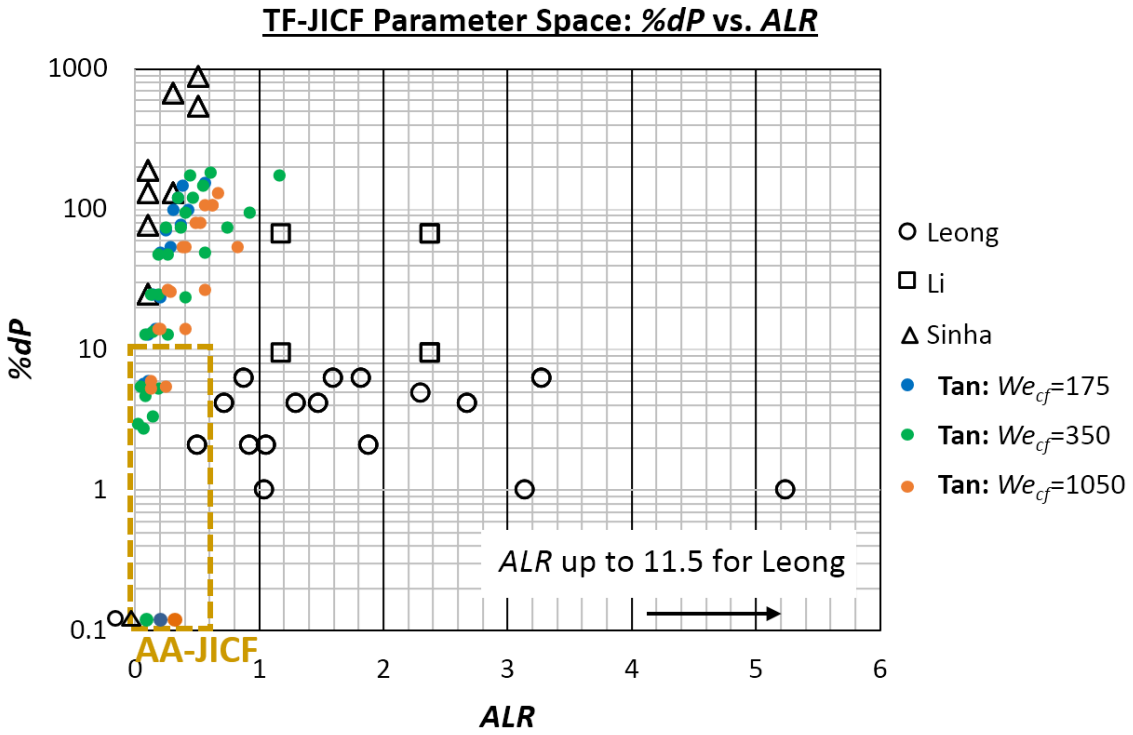

Figure 3.24 – Comparison of *%dP* and air-to-fuel mass flow ratio ($ALR \equiv \dot{m}_{air}/\dot{m}_f$) ranges between the current test-matrix and literature.

Figure 3.25 compares the ranges of air-to-fuel velocity-ratio ($VR \equiv U_{air}/U_f$) and *ALR* covered by the current investigation with those in the literature. *VR* is an important parameter that controls the intensity of shear atomization in twin-fluid jets, as reviewed in Section 2.3. Low air velocities that are close to the fuel velocities (i.e., $VR \approx 1$) can serve to sheath and protect the liquid from shearing against ambient gas/crossflow, while higher air velocities (i.e., $VR >> 1$) enhance shearing. TF-JICF in the existing literature were all studied at $VR >> 1$, where the air was observed to strongly disrupt the liquid jets. In contrast, our test-matrix contains test-points that range from $VR \approx 1$ to $VR >> 1$. This increases the likelihood of observing different types of fuel-air interactions, from fuel jet-protecting to jet-shearing, which may subsequently give rise to different TF-JICF spray-formation behaviors/regimes. It should be noted, however, that the current test-matrix's range of *VR* does not cover the full ranges studied by Leong et al.

(2000, 2001 *JPP*, 2001 *JEGTP*), Li et al. (2006, 2009, 2010 *Part 1*, 2010 *Part 2*) and Sinha et al. (2013, 2015), due to our higher fuel-injection velocities.

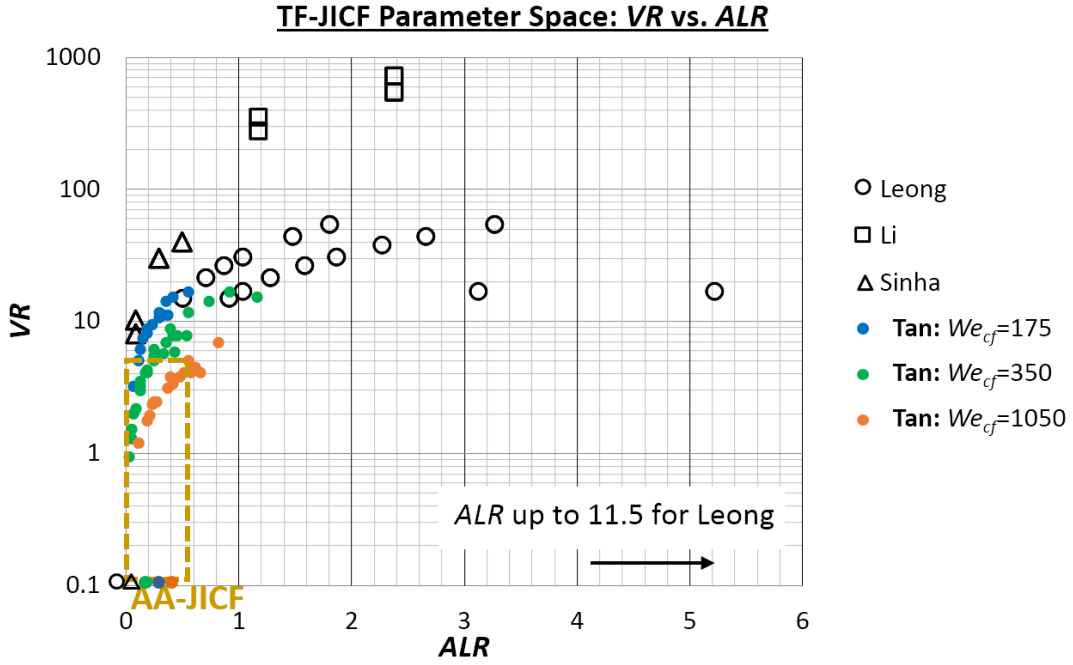

Figure 3.25 – Comparison of air-to-fuel velocity-ratio ($VR \equiv U_{air}/U_f$) and ALR ranges between the current test-matrix and literature.

Figure 3.26 is a plot of the current investigation and the literature's test-points on a We_{air} versus We_{cf} map. The plot serves to compare the atomizing potential of air (We_{air}) versus the atomizing potential of the crossflow (We_{cf}) at each test-point. As described earlier, by design our test-matrix's We_{cf} range far exceeds the literature's We_{cf} ranges in order to simulate jet-engine operating conditions. On the other hand, our We_{air} range covers most of the literature's range, except for the highest We_{air} values by Sinha et al. (2013, 2015), which is due to their air-nozzle's extremely high *dP* and air velocities. In essence, our crossflow has atomizing potentials that are generally far greater than those in literature, while our injected air has up to the same level of atomizing potential as those in literature.

Figure 3.26 also highlights an important distinction between TF-JICF and TF-jets in quiescent gas. Whereas in the latter the surrounding gas has no *active* role in atomizing the liquid, in the former the crossflow is classically the driving force behind atomization. Thus,

whereas the co-injected air can easily enhance atomization in a quiescent environment, it has to compete with the crossflow in TF-JICF. I.e., the air is not expected to enhance atomization if its Weber number is not significant higher than the "omni-present" crossflow's. Based on this principle, a line of $We_{air} = We_{cf}$ has been drawn across Fig. 3.26. Below this line, the atomization process is likely driven by the crossflow, while above this line they are likely driven by the air. The TF-JICF literature's test-points are generally above this line, suggesting that their "airblast's" atomizing power dominated that of their crossflow. In contrast, our test-points straddle this line, which increases the likelihood that we observe a transition in the dominant driver of atomization from the crossflow to the air.

In summary, this investigation's test-matrix has been developed to cover most of the existing literature's domains in order to study whether their conclusions are applicable to our case. At the same time, the test-matrix also extends to the low-*dP* and *ALR* domain, where there is currently a general lack of data and where the next-generation jet-engines' fuel-air mixers will operate. Based on the test-matrix's velocity-ratio and Weber number ranges, we expect to obtain results with remarkably different TF-JICF behaviors than those reported in literatures.

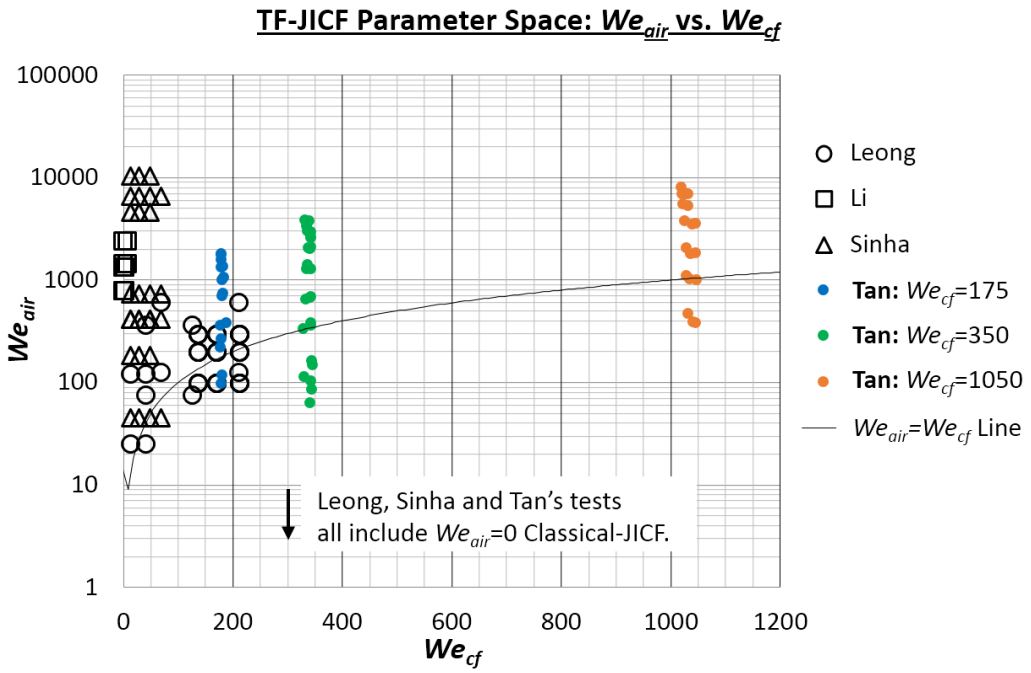

Figure 3.26 – Comparison of We_{air} and We_{cf} ranges between the current test-matrix and literature.

3.6 Image Post-Processing

3.6.1 Raw Images and Image-Correction

This section describes the post-processing and interpretation of the acquired shadowgraph spray images. A set of 100 images was obtained at each test condition to form a statistically representative set. One such image is shown on the left of Figure 3.27. It shows the shadowgraph backlight intensity across this image is non-uniform. To correct for the non-uniformity and the non-zero image black level, each raw image was subtracted by its darkest value (i.e., the black wall at the bottom) and then divided by a white flat-field (WFF) image similar to the one shown in Figure 3.28. The WFF image was acquired without fuel injection and, thus, captures the profile of the background light and lens vignette. Dividing by the WFF yields a "clean" image with uniform background intensity, as shown on the right of Figure 3.27. Notably, the raw images contained a dark strip near the bottom of the test-channel wall. This strip was due to a window stain located on the window's front-edge and blocked/blurred the spray image behind it. The effect cannot be entirely corrected by WFF, evident from the bright strip near the wall on the right image in Figure 3.27. Thus, small droplets/dilute spray behind this strip cannot be clearly identified, while high-contrast features such as the initial jet still can.

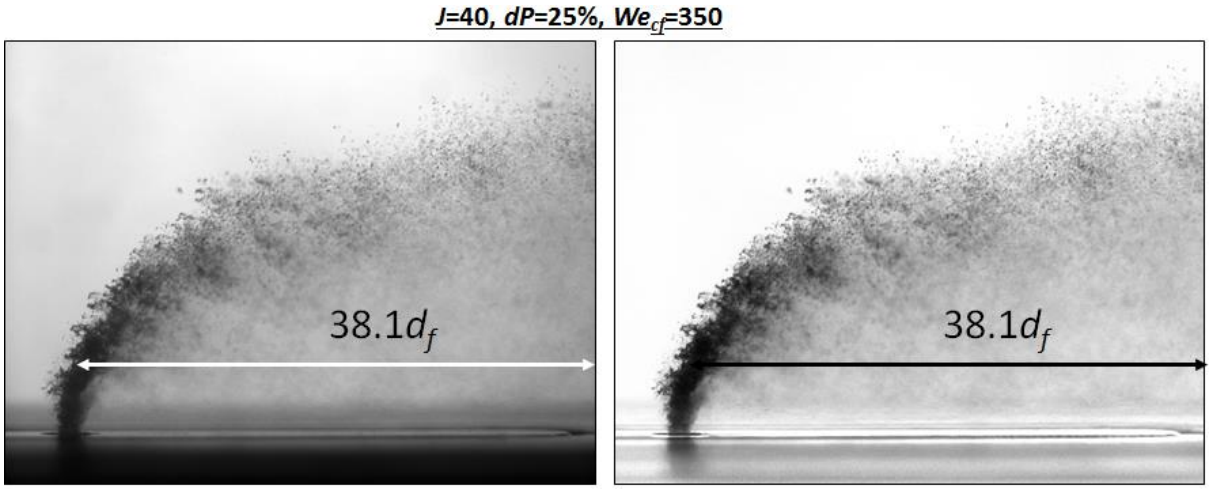

Figure 3.27 – "Raw" (*left*) and "corrected" (*right*) instantaneous image the TF-JICF.

Figure 3.28 – The white-flat-field image used to correct Figure 3.27.

Figure 3.29 shows an image of the gridded target that was used to calibrate the scale and orientation of the spray images. Using this target, the spray images' pixel-resolution was determined to be 73.967px/mm±0.86% (or 13.52$\mu m/px$, sufficient to visualize the majority of the anticipated droplet sizes). On the other hand, camera alignment was made to image the spray over a domain of $z/d_f \approx$ -4.5-38 (exact value varied by test-day), which covers the general domain of interest for jet-engine fuel-air mixers. The imaged scale's printed grid lines were straight to within the coarseness of the printing (i.e., ~3px), suggesting the absence of significant pin-cushion/barrel distortion. Furthermore, the horizontalness of the imaged injector and test-section wall (e.g., bottom of Figure 3.28) was used to ascertain that the camera was rotationally aligned with the test-channel to within 0.18^o. Finally, the determined image size scale was also cross-checked against the diameter of the imaged spraywell (which has known physical dimensions) to confirm the scale's accuracy.

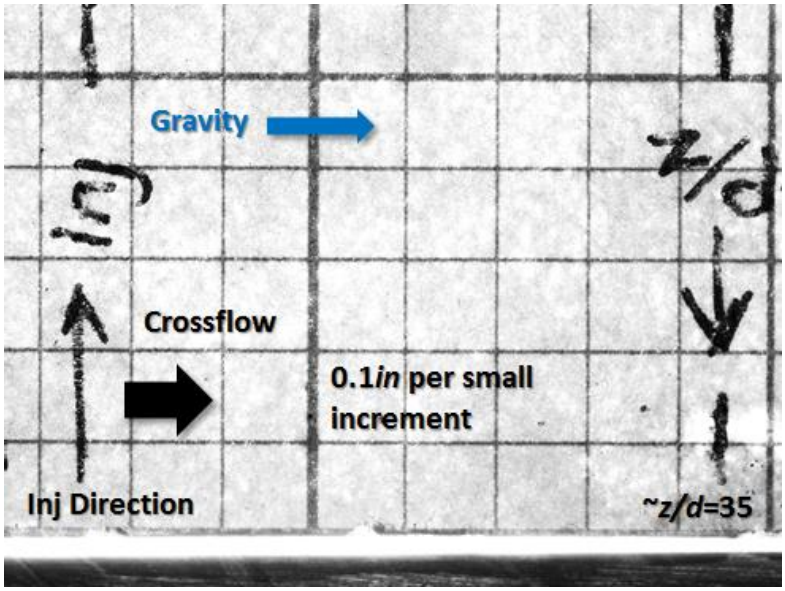

Figure 3.29 – An image of the gridded target used for scale calibration and alignment.

At this point, it is worth discussing the interpretation of pixel intensities in the shadowgraph images. Shadowgraphy is a line-of-sight imaging technique where a pixel is bright when the back-light propagates to the camera sensor unattenuated. If a droplet (having a different index of refraction (n) from its surrounding gas) is located in the light's path, the light is refracted and scattered away from its original propagation direction, and the camera sensor records a lower pixel brightness. As discussed by Goldstein and Kuehn (1996), the amount of light-attenuation in a shadowgraph setup is proportional to the second spatial derivative of n. For a droplet where n is discontinuous across the gas-liquid interface, the process of light-attenuation can be modeled using the theory of Mie-scattering (if the droplet is spherical). Figure 3.30 contains plots of liquid droplets' scattering properties, simulated using the MiePlot software by Laven P. (2016). The top plot shows that the incident light is redirected in all direction during Mie-scattering; however, the peak scattering intensity is directed forward towards the camera. Up to 90% of the incident light can be found scattered within 5^o of its original propagation path. Furthermore, Figure 3.30 shows that when a droplet is large compared to the wavelength of incident light, the scattering efficiency ($Q_{sca} = \sigma_{sca}/\pi r^2$, where σ_{sca} is the scattering cross-section and r is the droplet radius) asymptotes to

a constant value. This means the amount of light attenuated by a single droplet becomes directly related to its projected area. In our experiment, the droplets diameters are expected to range from 10-150 μm (based on Figure 2.6), which are much larger than the incident light's wavelength of 549-592*nm*. Therefore, the degree of light attenuation in our shadowgraph images can be considered to be positively related to the number of attenuating events (i.e., droplets) between the backlight and the camera, as well as each attenuating droplet's projected area. Under such a circumstance, numerous JICF researchers (e.g., Li et al. 2010 and Eslamian et al. 2014) have suggested that the scattering (or attenuation) intensity can be interpreted as a measure of summed droplet projected area in the path of light propagation, which is treated as a qualitative measure of liquid mass concentration. We will employ this interpretation for our shadowgraph data. On the smaller side of the 10-150μm range, Q_{sca} may vary up to 2.2, which could introduce a 10% error into the interpretation of summed projected area based on constant Q_{sca}. However, given the oscillatory values of Q_{sca} versus droplets diameter, and the established understanding that a JICF is polydispersed in droplets sizes, the *time-average* Q_{sca} is likely much closer to 2 even near the 10μm range.

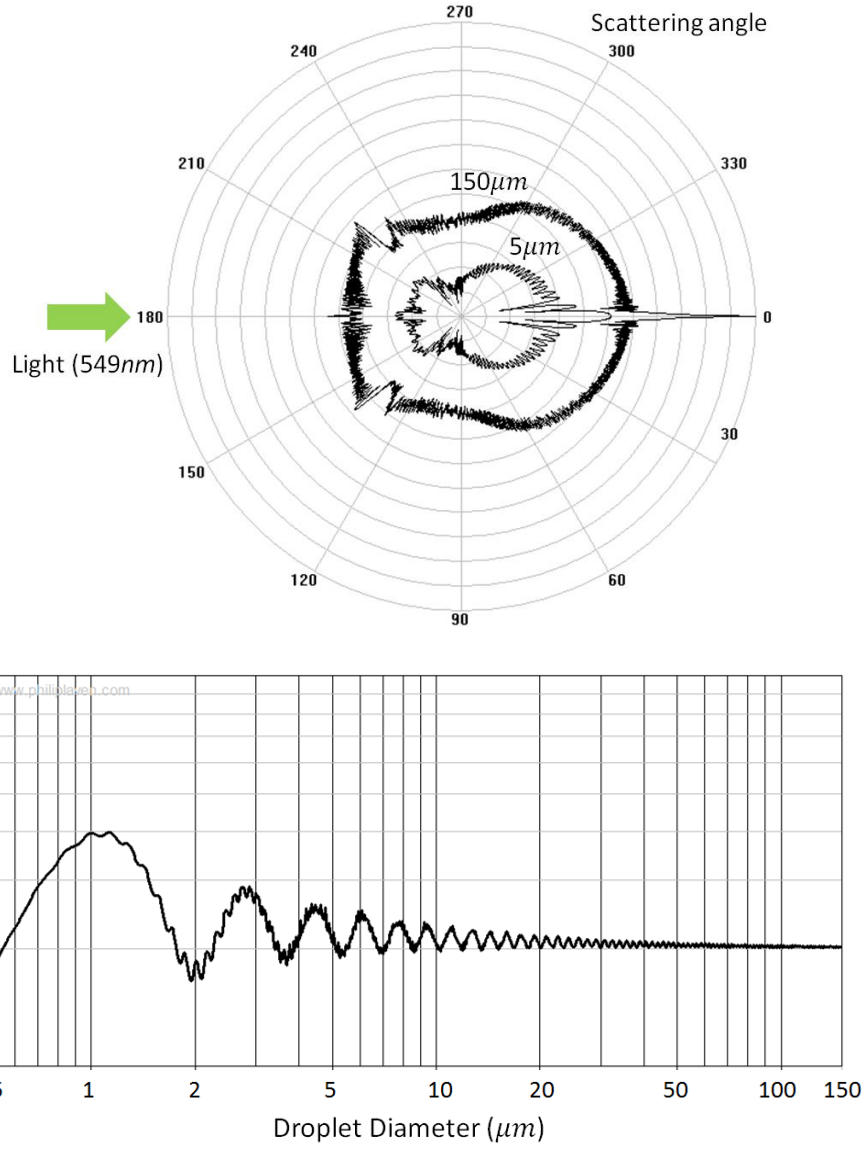

Figure 3.30 – *Top:* Polar plot of 549*nm* light intensity versus scattering angle for 5μm and 150μm droplets of water in air (150^oC, 5*atm*). *Bottom*: Scattering efficiency of 549*nm* light versus the diameter of a water droplet in air. Simulated using MiePlot v4.6 by Laven P. (2016).

Figure 3.31 shows the light-scattering effect of liquid fuel in our JICF images. The right image is cropped from the downstream region where the spray is dilute and composed of mostly near-spherical droplets. The Mie-scattering theory results in Figure 3.30 likely applies well in this region and, thus, the amount of light attenuation represents the droplets projected areas in the light of sight. In contrast, near the initial-jet (see the left of Figure 3.31) where the liquid is highly non-spherical and has very corrugated/complex surfaces, the Mie-scattering

theory does not apply. Instead, we see that the incident light is typically almost completely attenuated whenever a corrugated liquid structure is present in the line-of-sight. As such, images of the initial-jet region capture the intermittency of liquid structure at a given location, instead of the liquid's summed line-of-sight projected area. Although not shown in Figure 3.31, the near-wall wake-region of the spray typically consists of small near-spherical droplets even close to the initial-jet and, thus, more closely resembles the downstream region optically. Given the optical properties of JICF in a shadowgraph setup, the sub-sections below describe how the acquired images are post-processed to extract important spray characteristics.

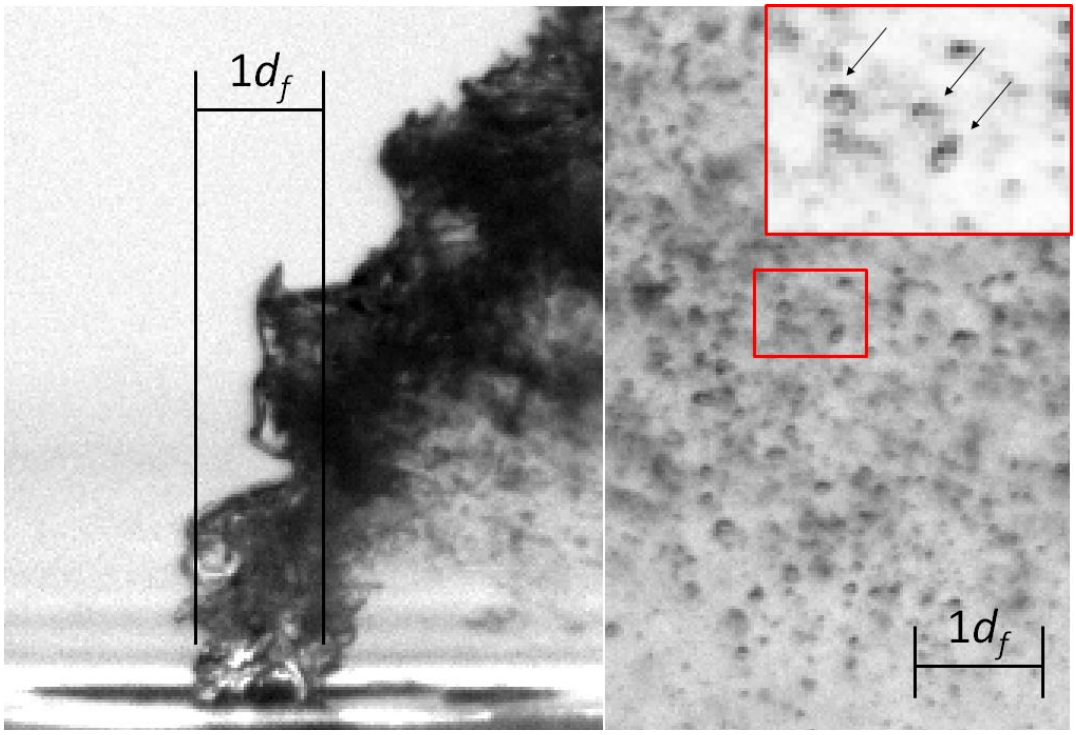

Figure 3.31 – Instantaneous image showing near-complete light-attenuation by the initial jet's corrugated surface (*left*) and partial light transmission by downstream near-spherical droplets (*right*). *Inset*: Zoomed-in, contrast-enhanced image of droplets, showing higher light transmission near the center of the droplets.

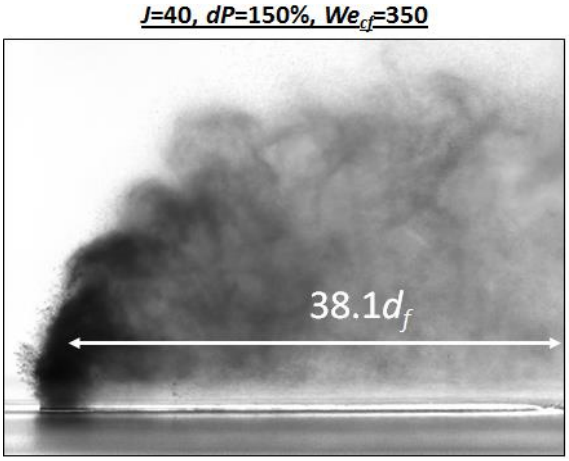

Figure 3.32 – An image of a TF-JICF under high-*dP* airblast. The initial region of the spray has high droplets number-density and appears completely black on the image (i.e., appearing like a solid jet).

3.6.2 Outer-Edge and Centerline Trajectories

As discussed in Section 2.1, an important characteristic of a JICF is its average trajectory in the *xz*-plane. Three types of trajectories are commonly defined by researchers from shadowgraph and Mie-scattering images of JICF: (i) the outer-edge trajectory that captures the average path taken by the largest droplets with the highest penetration inertia, (ii) the inner-edge trajectory that captures the path of the smallest droplets, and (iii) the centerline trajectory, which is often defined as the locus of maximum droplets flux and interpreted as the trajectory of the spray-core. Only the outer-edge and centerline trajectories were determined in this investigation, because the inner-edge is not well-defined at high We_{cf} due to the large population of surface-sheared droplets that occupy the near-wall region.

Tan et al. (2016) summarizes the numerous techniques for extracting spray trajectories from images. The selection of an optimal technique for a given image type/quality significantly influences the accuracy and repeatibility of the results. In this investigation, the instantaneous images were first binarized into spray-containing versus background regions. Subsequently, the outermost spray-containing pixels along the crossflow (*z*) direction were traced to obtain the instantaneous outer-edges, which were then averaged to obtain the average outer-edge trajectory. Binarization is performed using the Otsu method (Greensted, 2015 and Shahangian

et al., 2012), which assumes that the intensity distribution of the image is bimodal (i.e., dark droplets versus bright background) as shown in Figure 3.33. A threshold value for binarization is then automatically determined, generally close to the trough of the bimodal distribution. The Otsu method was used in this study primarily due to its robustness and automation, which help to produce very repeatable results.

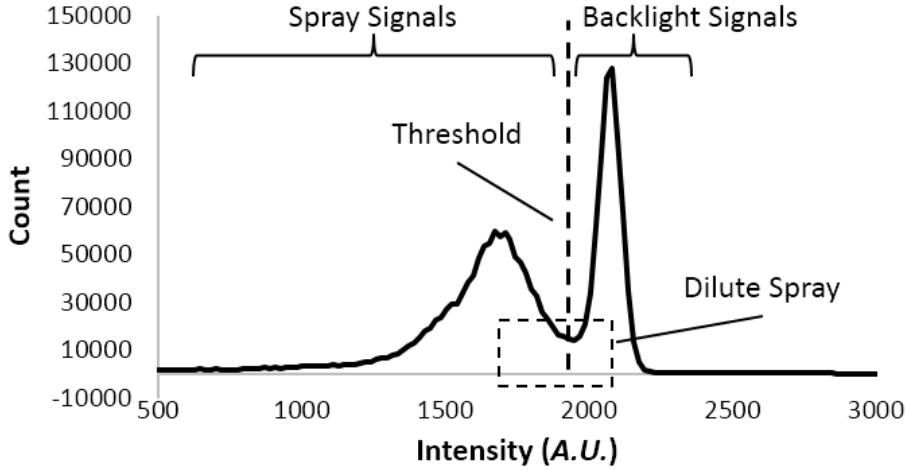

Figure 3.33 – An intensity histogram for the instantaneous image in Figure 3.27.

To determine the centerline trajectory of a TF-JICF, the complete set of images at the given test condition were averaged to produce a single image similar to that shown in Figure 3.34. Similar to Li et al.'s (2010 *Part 1*) and Eslamian et al.'s (2014) analyses, we assume that the shadowgraph/Mie-scattering intensity is proportional to the total projected area of droplets in the line-of-sight since the droplets are larger than the incident wavelength. The summed surface area is subsequently interpreted as a qualitative representation of fuel droplets concentration. Using this assumption, we define the spray centerline as the locus of lowest pixel intensities along the crossflow (z) direction, as shown by the red line in Figure 3.34. Notably, while the centerline may not be well-defined around the point of injection where the initial jet is nearly vertical, it does not otherwise affect the interpretation of global spray behaviors.

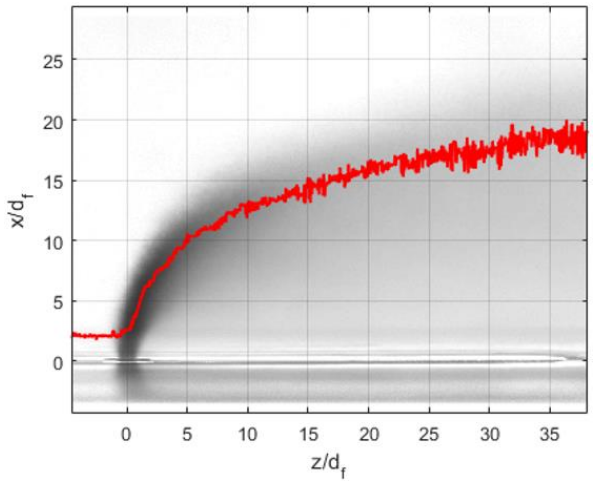

Figure 3.34 – An example of the centerline trajectory determined from an average spray image.

3.6.3 Cross-Sectional Light-Attenuation Profiles

In our investigation, it was often insufficient to analyze the TF-JICF solely based on the outer-edges and centerlines, because the effects of air-injection can constitute subtle modifications to the droplets distributions (especially near the wall), which are not well-described by the outer-edge or centerline trajectories. To describe these effects, we employed a new parameter called the "degree of light-attenuation (N)", defined as the inverse of pixel intensity (I_{shadow}) on the average spray image, as follows:

$$N(z,x) = \left[1 - \frac{I_{shadow}(z,x)}{I_{shadow}(Background)}\right] \times 100\% \qquad (11)$$

As previously discussed, in the downstream region and the wake region where liquid is present in near-spherical droplets that range from 10-150μm in diameter, and where the spray is sufficiently dilute that the back-light is not completely attenuated, a given pixel's N value can be interpreted as a measure of total droplets projected area in the line-of-sight, which is qualitatively representative of droplets concentration.

The variation in N across a vertical (x) cross-sectional slice of the spray can then be plotted for a given z/d_f location; e.g., at z/d_f=15 (see dotted line) as shown in Figure 3.35. Although true droplets concentration cannot be determined from shadowgraph images and N is not a conserved quantity, N profiles such as Figure 3.35 provides a qualitative description of

the droplets distribution that is capable of elucidating important spray-formation physics. For example, the peak in *N* that is the centerline and the gradual reduction in droplets concentrations around the wake region and outer-edge are all captured in this plot. More complex and costly tools for quantifying the droplets distribution (such as Phase Doppler Particle Analyzer, quantitative planar laser-induced fluorescence or phosphor thermometry) can be employed in future works to build on the results of this investigation.

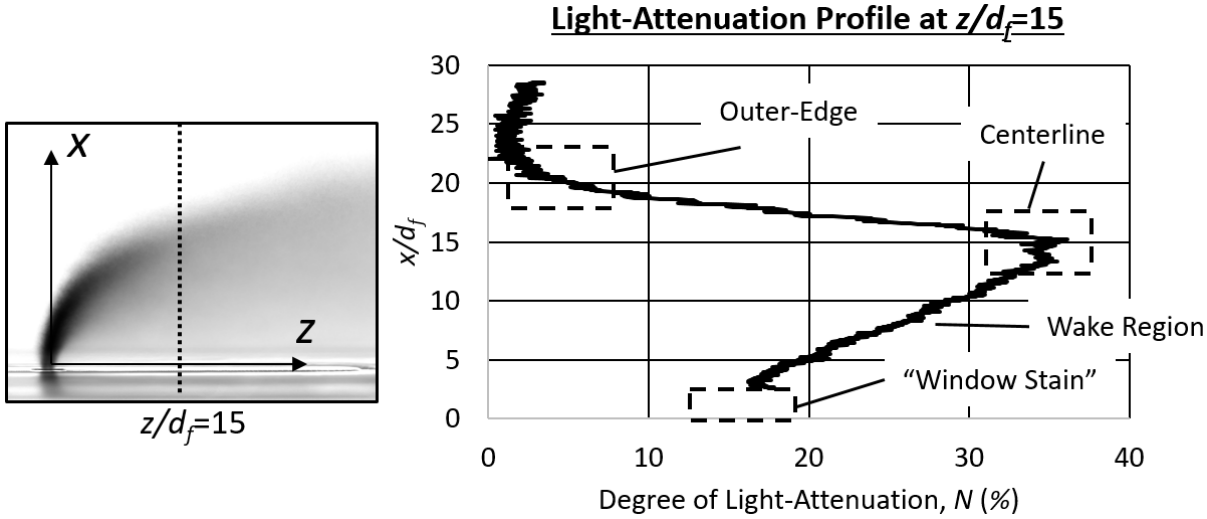

Figure 3.35 – The cross-sectional light-attenuation profile (*right*) based on an average spray image (*left*).

3.6.4 Profile Thickness of the Initial-Jet's Windward-Edge

In a Classical-JICF, the development of the spray's downstream characteristics is significantly tied to the disturbances (e.g., RT- and KH-waves) that develop along the initial jet. Thus, it is important to analyze how the injected air affects these disturbances; e.g., does the air promote or inhibit the existing disturbances, and can the air introduce its own disruptions to the fuel? In most cases, the different types and structures of instabilities on the initial jet are fairly apparent (e.g., see the corrugated fluid structures on the left of Figure 3.36), and useful qualitative conclusions can be drawn from an analysis of a sequence of instantaneous spray images. However, in some cases it is necessary to quantitatively compare the *magnitude* of

disruptions/disturbances at different operating conditions and locations. For this purpose, we define the measure of "windward-edge profile thickness (t_ω)."

As the right of Figure 3.36 and the left of Figure 3.37 show, when the instantaneous spray images are averaged and the degree of light-attenuation (N) across a horizontal slice is plotted, the center of the initial jet appears as a plateau having $N \approx 100\%$, because fuel is almost always present in the intact jet and the backlight is almost completely attenuated all the time. At the windward locations where unsteady waves, corrugated structures or droplets (in the case of very high dP) are found, N drops below 100% because these structures are intermittent. Under certain conditions where the *entire* intact jet "flaps" laterally due to large-scale disturbances such as RT-waves, N of the flapping intact jet will also drop below 100%. Finally, in the background where fuel is never present, $N \approx 0\%$. Therefore, we interpret the amplitude of these disturbances/structures as being approximately equal to the width of space where $10\% \leq N \leq 90\%$ on the windward-edge of the jet, which we called the jet's "profile thickness (t_ω)." The thresholds of 10 and 90% were employed based on the images' noise levels. t_ω was defined based on the windward-edge's features only, because the leeward-edge of the jet is typically shrouded behind dense surface-sheared droplets. The definition of t_ω is ideologically similar to the definitions of wake or boundary-layer thickness, where the contour of 99% of the freestream velocity is commonly used to define the layer's edge. t_ω is also similar to the definition of shear/mixing-layer thickness of twin-fluid jets employed by Villermaux (1998), where the mixing-layer's edge is defined as the location where the initial fluid's average concentration fraction drops below 100%.

Since the disruptions on the jet typically vary with location, t_ω varies as a function of distance (x/d_f) from the test-channel wall. The right of Figure 3.37 shows an example of the t_ω plotted against x/d_f. The resulting curve elucidates the amplitude and spatial growth-rate of the windward-edge disruptions.

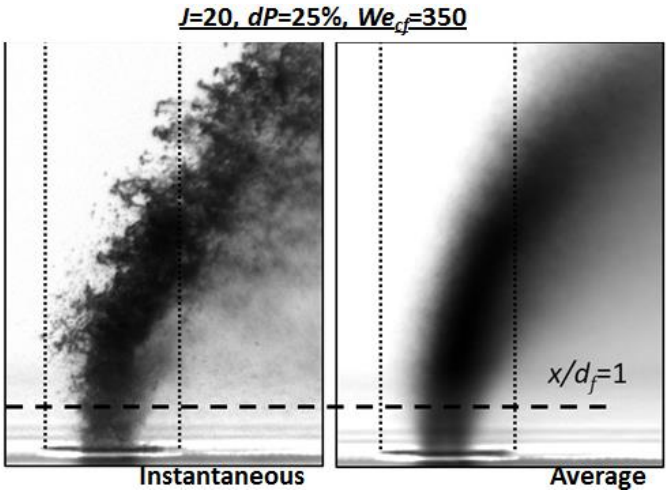

Figure 3.36 – Instantaneous (*left*) and average (*right*) zoomed-in views of Figure 3.27.

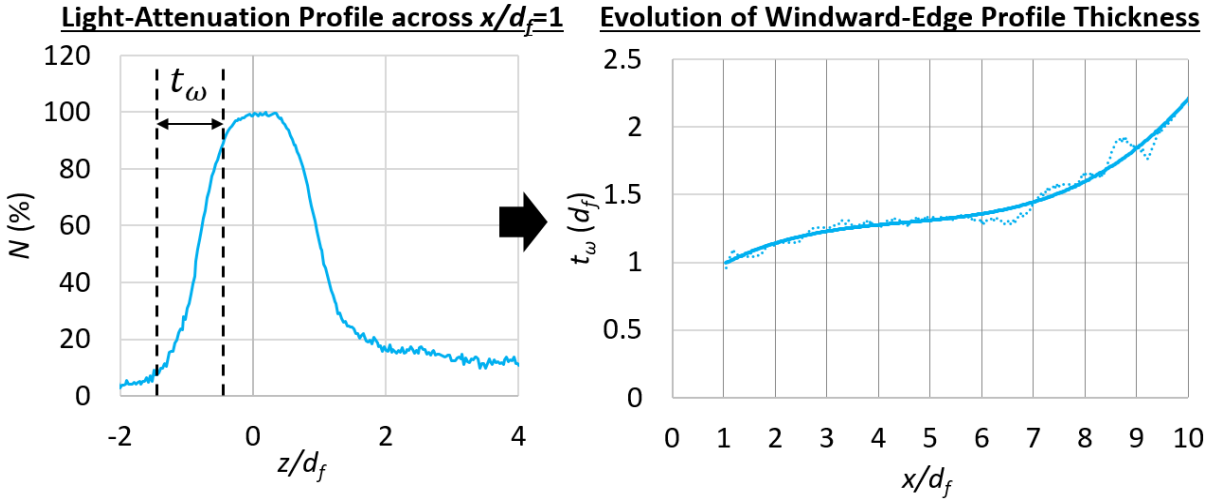

Figure 3.37 – *Left*: The initial-jet's light-attenuation profile across x/d_f=1. *Right*: The windward-edge profile thickness as a function of distance from the wall (x/d_f).

Figure 3.38 demonstrates t_ω's accuracy in measuring the amplitude of windward-edge disruptions. The left column shows instantaneous raw images of the jet/spray superimposed with two curves that bound the average region of space containing the detected windward-edge disruptions (i.e., the width between the red and teal curves is t_ω). The center column shows the detected edges of the instantaneous jet/spray (using Otsu binarization followed by Sobel edge-detection) superimposed with the same curves. Finally, the last column shows the collection of all edges detected from the 100 frames captured at each test point, which represents the full range of motion/unsteadiness that the injected fuel exhibit on the windward side. The top row shows a low-*J* and low-*dP* condition where the disturbances were dominated by large-scale

Rayleigh-Taylor waves, while the center row shows a medium-*J* and medium-*dP* condition where small-scale Kelvin-Helmholtz corrugated-structures can be seen. The last row shows a very high-*dP* condition where the injected fuel is likely already converted into a spray at the point where it left the spraywell.

From Figure 3.38, it is evident that the curves accurately bound the regions of space where almost all of the jet/spray's unsteady edges can be found. Therefore, the measured t_ω can accurately capture the amplitude of large- and small-scale structures. The interpretation of t_ω has to be modified when the air creates a layer of finely-atomized fuel on the windward side at high-*dP*. In this case, t_ω does not measure the jet's surface disturbances, but rather the size of space containing atomizes droplets (i.e., similar to the definition of spray-width or mixing-layer thickness in twin-fluid jets). The interpretation of t_ω is further complicated at very high-*dP* when the injected fuel is atomized into a very dense spray (e.g., the last row in Figure 3.38), where the entire opaque region to the right of the teal curve is interpreted as a solid/undisturbed jet despite actually being a spray. Our discussions of t_ω in the results chapters are provided together with analysis of raw images to ensure the interpretation of t_ω is correct.

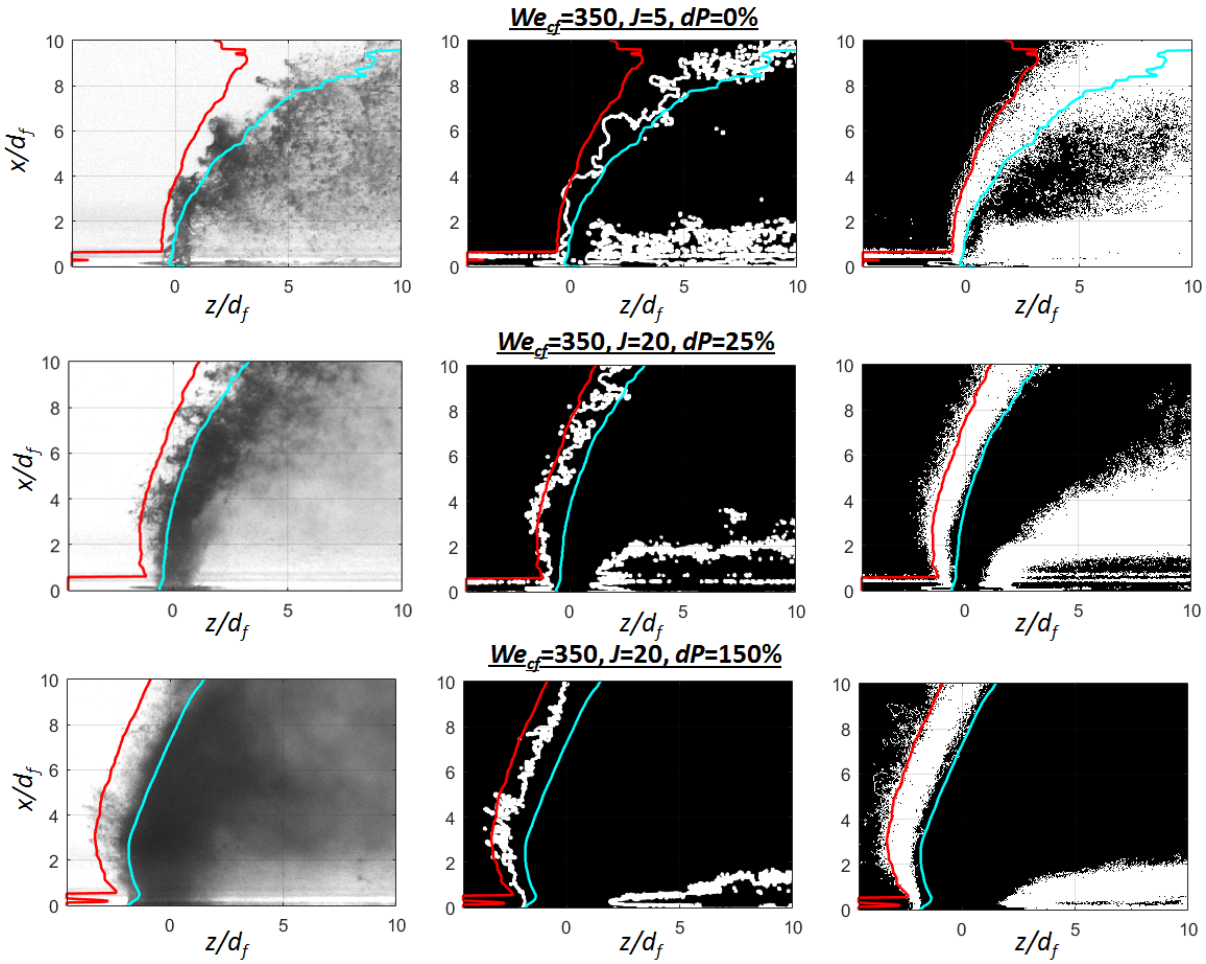

Figure 3.38 – The determined front and rear bounds of space containing the jet/spray's disruptions, superimposed on instantaneous raw images (*left*), instantaneous edges (*center*) and the collection of all detected edges from captured frames (*right*).

CHAPTER 4. OVERVIEW OF THE INVESTIGATION'S RESULTS

This chapter first presents the results from the tests employing *only* fuel injection into the crossflow (i.e., the Classical-JICF) to show that the investigated injector produces JICF sprays whose characteristics agree with results reported in the literature. More crucially, these data provide a set of reference spray behaviors against which the TF-JICF can be compared. Subsequently, this chapter provides a high-level overview of the TF-JICF test results from across the full operating range of dP=0-150%. From these results we will identify a spectrum of new TF-JICF trends and regimes, some of which differ from those reported by Leong et al. (2000, 2001 *JPP*, 2001 *JEGTP*), Li et al. (2006, 2010 *Part 1*, 2010 *Part 2*) and Sinha et al. (2013, 2015).

4.1 Characteristics of Classical-JICF

Figure 4.1 shows instantaneous images of the Classical-JICF obtained for ranges of J and We_{cf} while Figure 4.2 shows their corresponding averaged images. These images have the same grayscale-mapping so their intensities are directly comparable. They show that at J=20 and We_{cf}=350 the spray-plume contained two distinct zones: (i) a densely-populated spray-core containing droplets that may be quite large and (ii) a dilute near-wall wake with mostly small, barely resolvable droplets. These two zones were formed through different atomization mechanisms, as described in Sub-section 2.1.2 and Figure 2.8. The cross-sectional light-attenuation (N) profiles of the Classical-JICF are shown in Figure 4.3. As discussed in Section 3.6, N is an approximate representation of droplets concentration in the line-of-sight, especially at downstream regions (e.g., z/d_f=15 and 25) where the spray is dilute and well-developed. Figure 4.3 shows that the J=20 spray-core had very high N that gradually decreased with the distance z/d_f as the spray-core expanded and mixed with the crossflow. On the upper (windward) side, the N values decreased to $N\approx0$ where the spray's outer-edge can be found. On the lower (wake) side, the N values generally decreased less rapidly with distance and never reached $N\approx0$

even at $x/d_f \approx 0$ (i.e., some wake droplets were always found immediately next to the wall). Notably, Figure 4.3 also shows that the transition in N between the spray-core and wake was gradual and, thus, it is difficult to precisely demarcate the two regions.

Next, the J=20 images in Figures. 4.1 and 4.2 show that increasing We_{cf} increases the wake region's droplets concentration, while also reducing the spray's droplets sizes globally (as evident from the "nebulous/foggy" appearance of the higher We_{cf} sprays). As a result of the smaller droplets, which have lower penetration inertia, the spray's centerline and outer-edge penetrations both decreased with increasing We_{cf} (even while J was fixed), as shown in the trajectory plots of Figure 4.4. These observations are all consistent with the known behavior of Classical-JICF as reviewed in Section 2.1; i.e., higher We_{cf} produces stronger aerodynamic shearing that increases the rate of droplets-shearing from the liquid surface (thus causing a denser wake) and reduces the critical droplet size (causing smaller droplets globally).

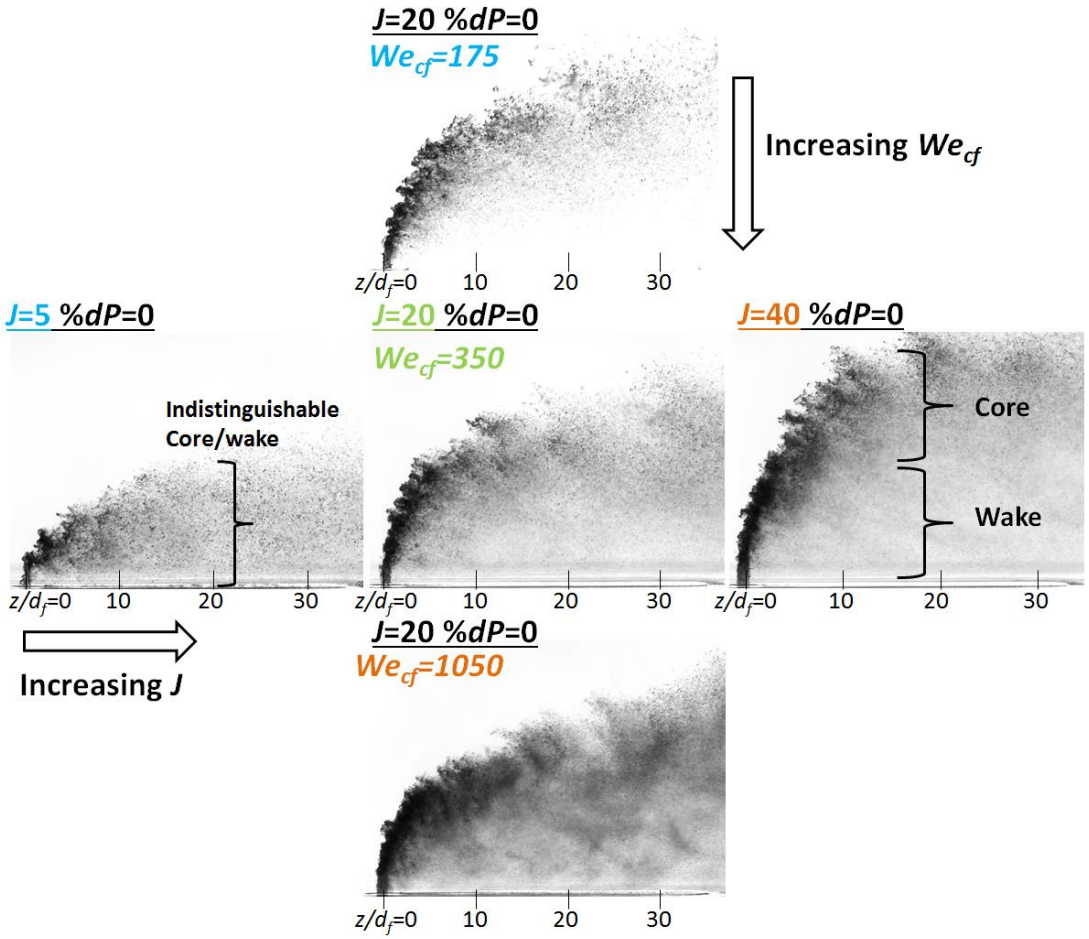

Figure 4.1 – Instantaneous images of Classical-JICF at different J and We_{cf}.

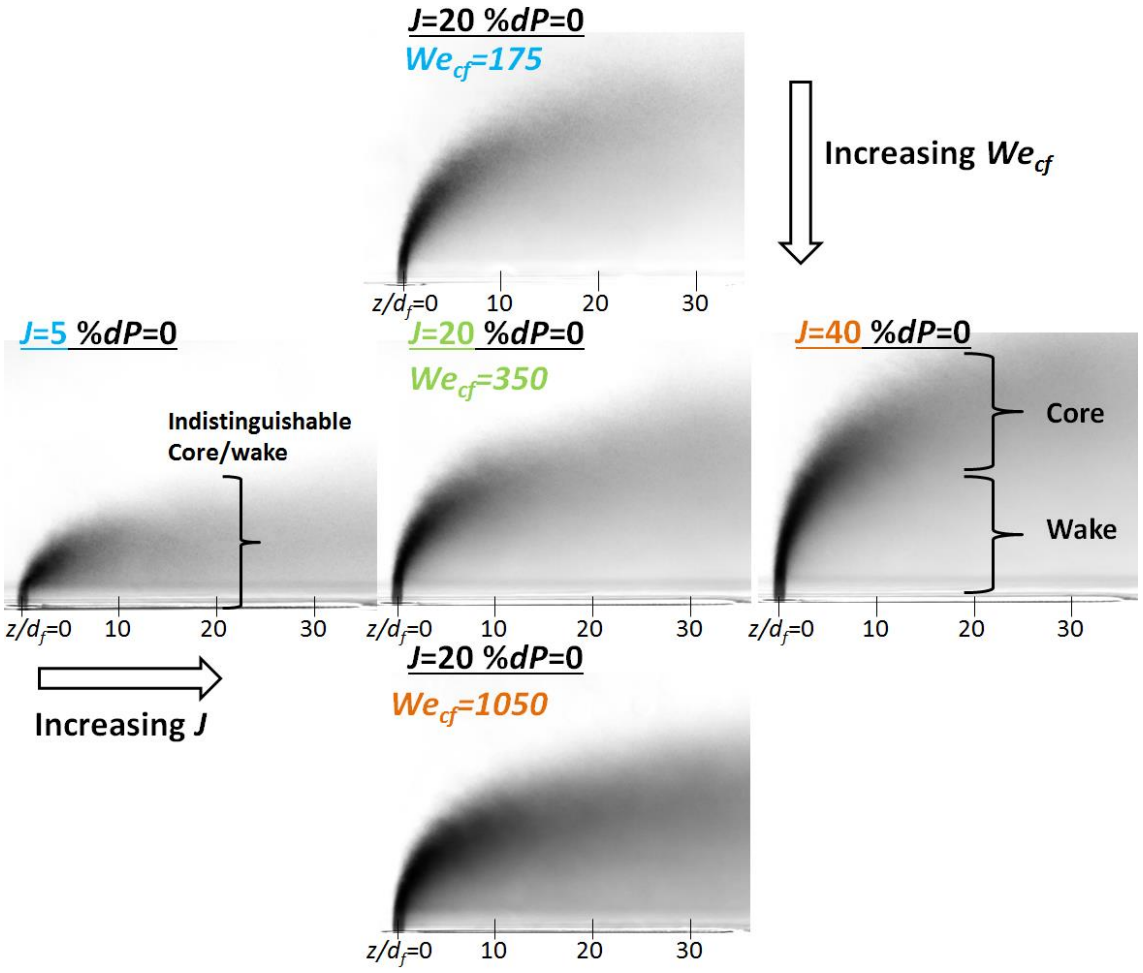

Figure 4.2 – Average images of Classical-JICF at different *J* and We_{cf}.

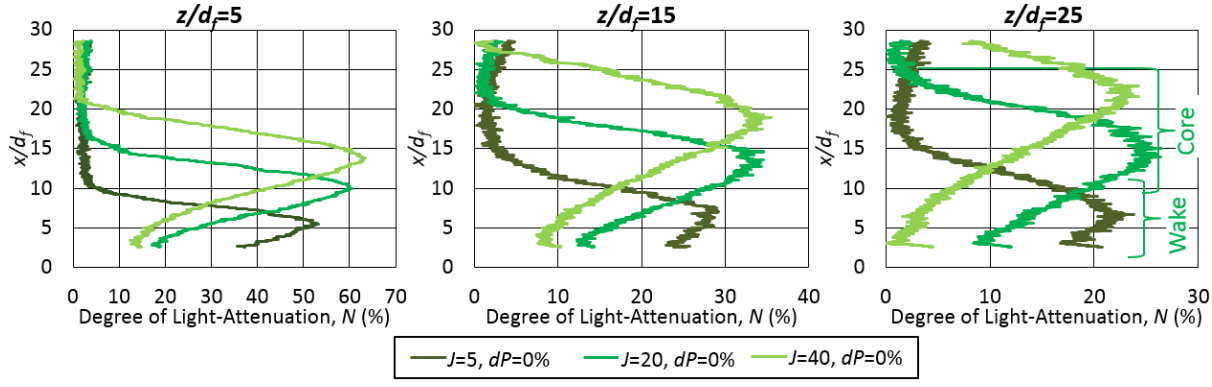

Figure 4.3 – Cross-sectional light-attenuation profiles across z/d_f = 5, 15 and 25 for Classical-JICF at We_{cf}=350.

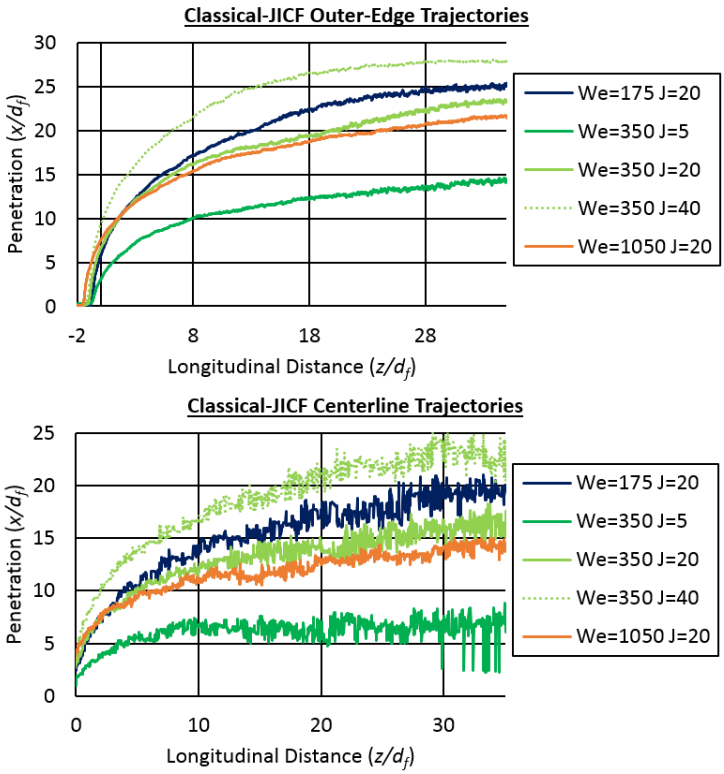

Figure 4.4 – Average outer-edge and centerline trajectories of the Classical-JICF at varying *J* and We_{cf}.

Examining the results for We_{cf}=350 in Figures 4.1 and 4.2, as well as in Figure 4.4, shows that spray penetration increases with *J* at a given We_{cf}. This is a well understood behavior of Classical-JICF, which was elucidated by studies of the *J*-based trajectory correlation function (e.g., see Sub-section 2.1.2). Interestingly, in addition to increasing spray penetration, the increase in *J* from 5 to 20 appears to detach the spray-core from the test-channel wall. Specifically, between *J*=20-40, the sprays have two distinct regions (i.e., core and wake) and appear similar to each other. However, at *J*=5 the liquid jet disintegrated almost directly along the bottom wall, resulting in a spray-core that is attached to the test-channel wall without a clearly distinguishable wake. Figure 4.3 shows that the absence of wake made the *J*=5 spray's near-wall *N* (i.e., approximate droplets concentration) significantly higher than the *J*=20-40 sprays'.

To further examine the effect of "wall-attachment" on the spray-core's penetration, we attempted to scale the *J*=5-40 sprays' trajectories by J^{C1}, knowing that such a scaling is

technically only applicable to sprays with similar flow-fields and dispersion patterns, as discussed at the end of Sub-section 2.1.2. The applicability of the scaling was tested by normalizing the J=5-40 sprays' outer-edge and centerline trajectories by J^{C1}. Figure 4.5 shows that when C_1 was adjusted until the J=20-40 normalized-trajectories became well-collapsed into a single curve, the J=5 normalized-trajectories remained deviated from the others, which suggests it obeys a different scaling law, if one exists. This supports our claim that the J=5 JICF is *dissimilar* to J=20-40 JICF because of its attachment to the test-channel wall.

We emphasized the distinction between wall-attached and wall-detached sprays in this discussion because a primary objective of applying low-*dP* "air-assist" to JICF in applications (e.g., jet-engines) is to reduce the concentration of fuel along the wall in order to minimize flashback and wall-coking risks. Thus, understanding the effects of air-assist on wall-attached sprays where high concentrations of fuel are found along the wall is particularly important.

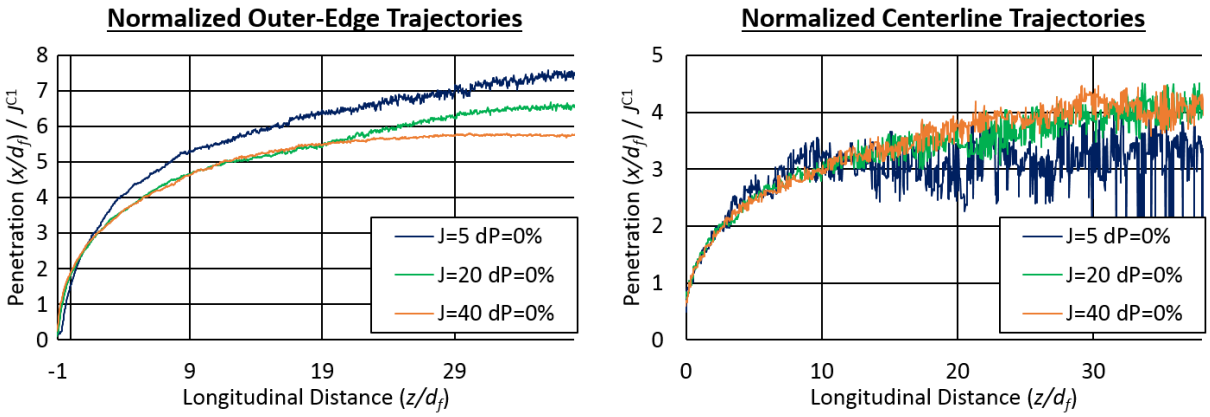

Figure 4.5 – Plots of normalized spray trajectories, showing the deviation of J=5 Classical-JICF from the other cases.

Next, we examine the development of instabilities on the initial sections of Classical-JICF's jets, which will become highly relevant in the discussion of air-injection's effects in the subsequent chapters. The discussion in Section 2.1 has stated that a Classical-JICF exhibits large-scale wave-like Rayleigh-Taylor (RT) instabilities on the initial portion of the jet that are responsible for the gross jet break-up. Superposed on top of these RT-waves are smaller-scale Kelvin-Helmholtz (KH) shear-instabilities that develop on the lateral and leeward sides of the

jet. While the small KH-waves are difficult to observe experimentally, the large-scale RT-waves' average amplitudes can be quantified by measuring the jet's windward-edge profile thickness (t_ω) as introduced in Section 3.6. The left plot in Figure 4.6 describes the dependence of t_ω upon penetration distance for J=5, 20, 40 at We_{cf}=350. All three curves show that t_ω grows exponentially with x/d_f with growth-rates that are inversely proportional to J.

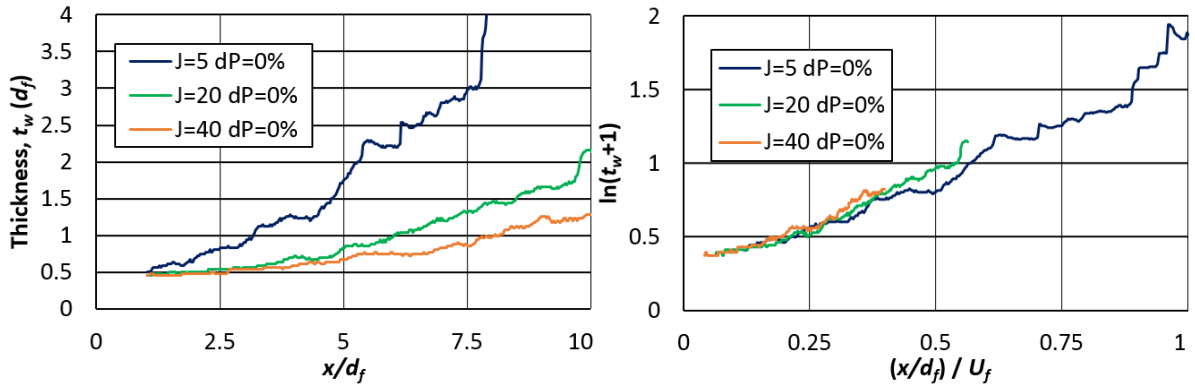

Figure 4.6 – *Left*: Profile thickness (t_ω) of We_{cf}=350 initial-jets as a function distance from injection. *Right*: The t_ω curves scaled according to the RT-waves scaling law.

To further understand the relationship between the t_ω's growth-rate and J, we perform the following scaling analysis, starting with the following equation for the *temporal* growth-rate of RT-waves in Classical-JICF (as introduced in Section 2.1):

$$h_{RT} = \exp(\eta t) - 1 \tag{1}$$

where h_{RT} is the RT-wave's amplitude, η is the growth-rate and t is time. Equation (1) assumes $h_{RT}(t = 0) = 0$. The equation above can be expressed in terms of spatial coordinate by assuming that the RT-waves' convection distance in the x direction occurs at a fixed velocity $U_{RT,x}$ within the domain of interest; i.e.,

$$x_{RT} = U_{RT,x} t \tag{2}$$

Substituting (2) into (1) we obtain:

$$h_{RT} = \exp\left(\eta \frac{x_{RT}}{U_{RT,x}}\right) - 1 \tag{3}$$

which can be rearranged into:

$$\ln(h_{RT} + 1) = \eta\left(\frac{x_{RT}}{U_{RT,x}}\right) \tag{4}$$

Finally, to express Equation (4) in terms of experimentally measured parameters, we assumed that $U_{RT,x} = U_f$ (i.e., the RT-waves are convected at the fuel injection velocity), as proposed by Inamura et al. (1993) and Sallam et al. (2004). Additionally, assuming the RT-wave amplitude equals the profile thickness (i.e., $h_{RT} = t_\omega$), because only RT-waves are present on the windward-edge of the jet where t_ω is measured, yields the following relationship:

$$\ln(t_\omega + 1) = \eta\left(\frac{x_{RT}}{U_f}\right) \tag{5}$$

Since the growth-rate (η) of RT-waves is independent of *J* and only depends on We_{cf} (e.g., see Equation (4) in Section 2.1), then a plot of log of t_ω as a function of "convection time" $\left(x_{RT}/U_f\right)$ should yield straight lines whose slopes equal to η. Also, if the data from cases having the same We_{cf} (and different *J*) are plotted, their slopes should be identical. These are successfully demonstrated by the plot on the right of Figure 4.6. Hence, the evolution of RT-waves measured at different *J*'s and We_{cf}=350 can be scaled by convection time. The scaling above has been found to be applicable at all the tested We_{cf}, but the results will not be shown here for brevity. Notably, the close fit of the measured t_ω to well-known RT-wave scaling laws supports the notion that RT-waves dominate the jet's disturbances in Classical-JICF. Thus, any deviation of the TF-JICF data from this scaling can be used to infer the presence of new TF-related instability mechanisms.

4.2 Identification of the TF-JICF Regimes

In this section, we will briefly overview the TF-JICF experimental results and identify regimes of TF-JICF based on the trends of spray penetration versus *dP*. To begin, Figure 4.7 shows instantaneous and average images of the TF-JICF at *J*=20 and We_{cf}=350, across the full

range of tested *dP* from 0% (Classical) to 150%. It is immediately apparent that the spray structures and dispersions strongly depend on *dP* as the injected fuel appears to be more finely-atomized and widely dispersed at higher *dP*. For example, between *dP*=0 and 50%, the TF-JICF had relatively intact initial jets that developed into narrowly dispersed spray-cores. On the other hand, at *dP*≥100%, the injected fuel appears to be atomized and dispersed across the entire spraywell orifice *prior* to encountering the crossflow, which resulted in wider spray-cores and much more densely-populated wakes. Notably, the *dP*≥100% sprays seem to be structurally more similar to the "Airblast Spray-in-Crossflow (AB-SICF)" that was widely studied and discussed in the TF-JICF literature.

In our experimental data we observed different spray characteristics that dominated at different ranges of *dP*. Consequently, the data can be "grouped" into different TF-JICF regimes, where each "regime" is defined as a range of *dP* where a new set of spray-formation processes dominates. A method for classifying regimes based on spray penetrations was developed, where we assumed the onset of new spray-formation processes will cause changes in the spray's penetration *trends*. Thus, transitions between TF-JICF regimes can be inferred from observing significant shifts in the spray penetration trends as *dP* is incrementally changed.

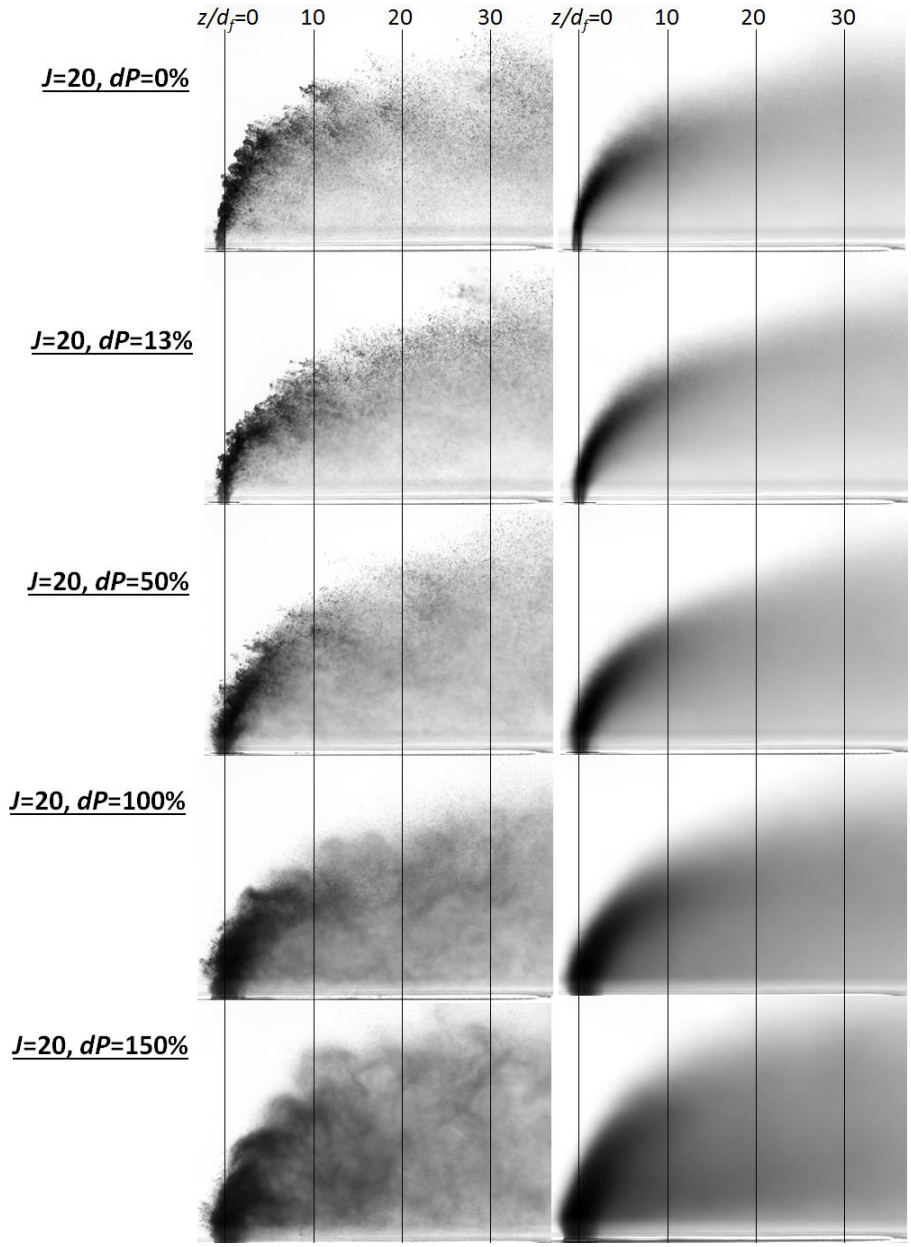

Figure 4.7 – Instantaneous (*left*) and average (*right*) images depicting the effects of *dP* on TF-JICF structures at *J*=20 and We_{cf}=350.

In this analysis, the spray's penetration is expressed in terms of the metric P_1. Based on our previous research work, it was known that the trajectories of Classical-JICF at elevated pressure can be fitted to the following correlation function:

$$\left(\frac{x}{d_f}\right) = P_1 \times f\left(\frac{z}{d_f}\right) = P_1 \times \ln\left[\frac{z}{d_f} - \frac{z}{d_{f,origin}} + 1\right] \quad (6)$$

where $f\left(z/d_f\right)$ is described by a natural logarithmic shape-function and P_1 is a "penetration parameter" that "accounts" for the effects of *J* and other test conditions-dependent variables.

P_1 scales $f(z/d_f)$ to the raw trajectory data (x/d_f). The position of $z/d_f = 0$ is located at the fuel orifice's center and $z/d_{f,origin}$ is a parameter used to adjust for the raw trajectory's virtual origin, which may be significantly offset from $z/d_f = 0$ especially at high *dP* when the spray was widely dispersed by the airblast. Although this correlation was originally developed for Classical-JICF, we found that the log-based shape-function also fits the TF-JICF trajectories very well. For example, Figure 4.8 shows the correlation function fitted to a TF-JICF's raw centerline and outer-edge trajectories. The discrepancies between the correlation curves and raw data are practically negligible in this and other TF-JICF cases. Thus, using Equation (6) to relate the raw TF-JICF trajectory (x/d_f) to the function $f(z/d_f)$, it is possible to obtain the parameter P_1 that is a measure of the spray's magnitude of penetration. In essence, the 2D trajectory curve is reduced down to a convenient number (P_1).

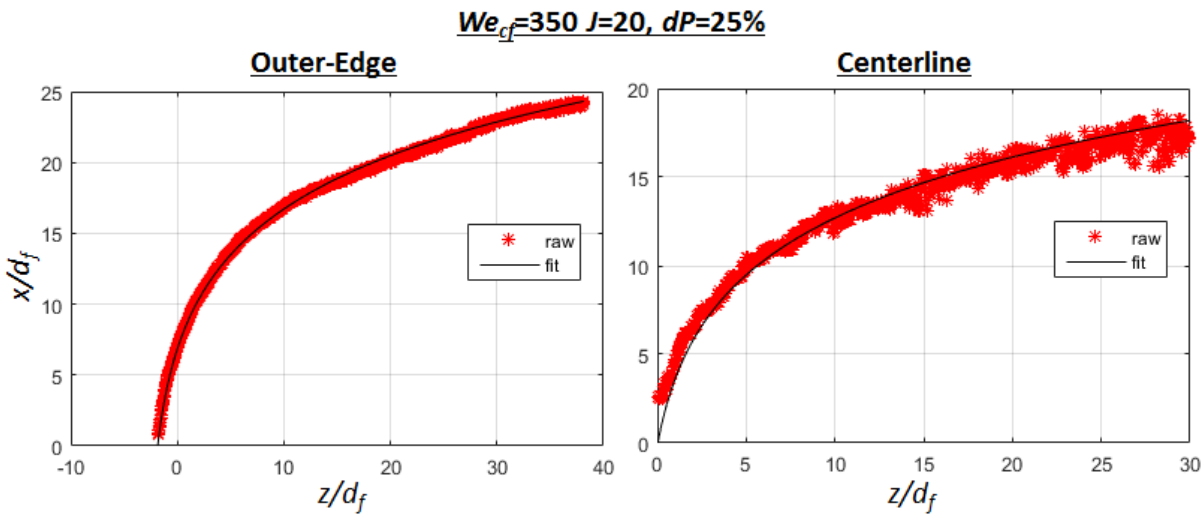

Figure 4.8 – Plots of raw outer-edge and centerline trajectories versus their log-based curve-fit (see Equation (6)).

Using the developed trajectory data-reduction scheme, Figures 4.9 and 4.10 show the *J*=20 TF-JICF's outer-edges and centerlines P_1 values as a function of *dP* and We_{cf}. Notably, in the Classical-JICF test-points where the air-supply valve was completely shut and air flow was zero, the interaction between the crossflow and fuel often create a "suction effect" that resulted in small negative *dP* values. These values are small compared against the entire tested

range of *dP*=0-150%. Contrary to Leong et al. (2000, 2001 *JPP*, 2001 *JEGTP*) and Li et al. (2006, 2010 *Part 1*, 2010 *Part 2*)'s results (and in some agreement with Sinha et al. (2015)'s qualitative results), Figures 4.9 and 4.10 show the spray penetration (P_1) did *not* vary monotonically with *dP*. Instead, the "penetration" P_1 of both the outer-edge and centerline trajectories generally increased in the range of $dP \approx$0-13%. Beyond *dP*=13%, the trends were reversed as the penetration P_1 became inversely proportional to *dP* in the range of $dP \approx$25-100%. Subsequently, at $dP \geq$100%, the trajectories' penetration P_1 increased with *dP* once again. Although the outer-edges and centerlines' penetrations responded to *dP* with different magnitudes, their general trends were in qualitative agreement.

As annotated on Figures 4.9 and 4.10, we will refer to the first range of $dP \approx$0-13% as the "Air-Assist (AA) JICF" regime, where the air seems to "assist" the penetration of the spray. The next regime is named "Airblast (AB) JICF", where the spray penetration decreases with increasing *dP*, likely due to the disruptive effect of the strong "airblast". The last regime is referred to as "Airblast *Spray*-in-Crossflow (AB-SICF)" because its penetration trends and instantaneous spray structures (see Figure 4.7) both appear to be phenomenologically similar to the "AB-SICF regime" described by Leong et al. (2000, 2001 *JPP*, 2001 *JEGTP*), Li et al. (2006, 2010 *Part 1*, 2010 *Part 2*) and Sinha et al. (2015) It is also evident from Figures 4.9 and 4.10 that the transitions between regimes occurred at lower *dP* when We_{cf} is higher, a dependence that will be explored in more details in the subsequent chapters.

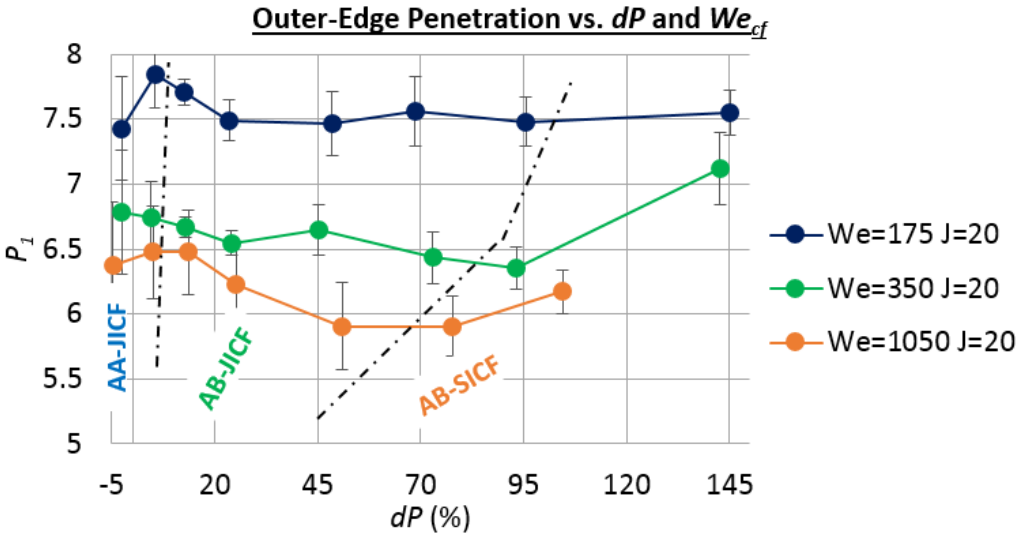

Figure 4.9 – Spray outer-edge penetrations as a function of *dP* and We_{cf} for *J*=20. Dotted line: regime boundaries.

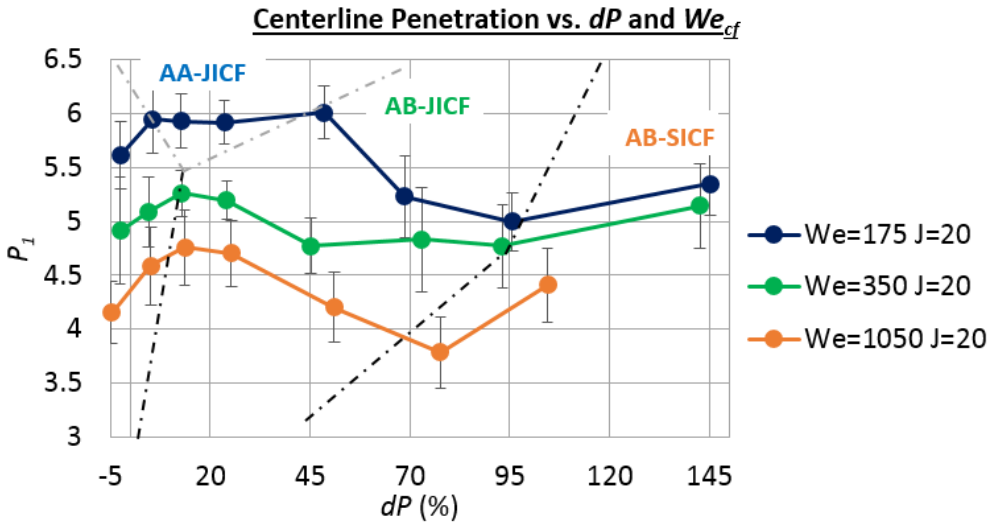

Figure 4.10 – Spray centerline penetrations as a function of *dP* and We_{cf} for *J*=20. Gray-dotted line indicates an ambiguity in the regime boundary.

Figures 4.11 and 4.12 plot the outer-edge and centerline penetration P_1 as a function of *dP* and *J* for a given We_{cf}. The previously observed non-monotonic relationship between P_1 and *dP* can also be observed here. Interestingly, the transition *dP* values between the AA-JICF and AB-JICF regimes was insensitive to *J*, while the transition *dP* values between AB-JICF and AB-SICF were significantly lower at lower *J*. Additionally, the figures show that TF-JICF with initially higher penetrations (i.e., a higher *J*) seem to experience generally declining penetrations as *dP* increased, whereas the lower *J* sprays generally experience increasing

penetrations. This phenomenon could explain why Leong et al. (2000, 2001 *JPP*, 2001 *JEGTP*) and Li et al. (2006, 2010 *Part 1*) only observed increased penetration with increasing *dP*, since their experiment's *J* values were very low compared to ours.

In summary, using the shifts in spray penetration trends as an indicator of changes in the underlying TF-JICF spray-formation processes, we categorized our experimental data into four regimes: Classical-JICF, AA-JICF, AB-JICF and AB-SICF. The boundaries between these regimes are influenced by *J*, *dP* and We_{cf}. Some of these regimes exhibited characteristics that differ from those reported in TF-JICF literature, suggesting the presence of new unexplored spray-formation processes.

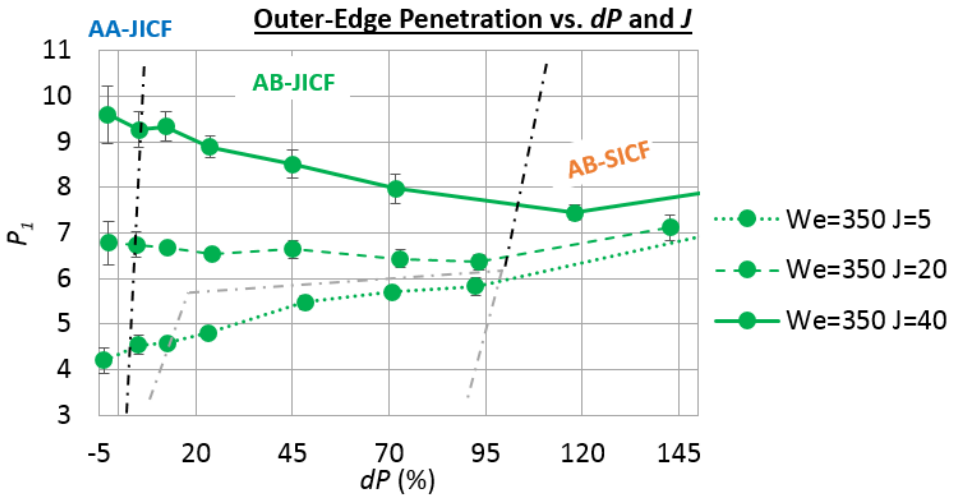

Figure 4.11 – Spray outer-edge penetrations as a function of *dP* and *J* for We_{cf}=350.

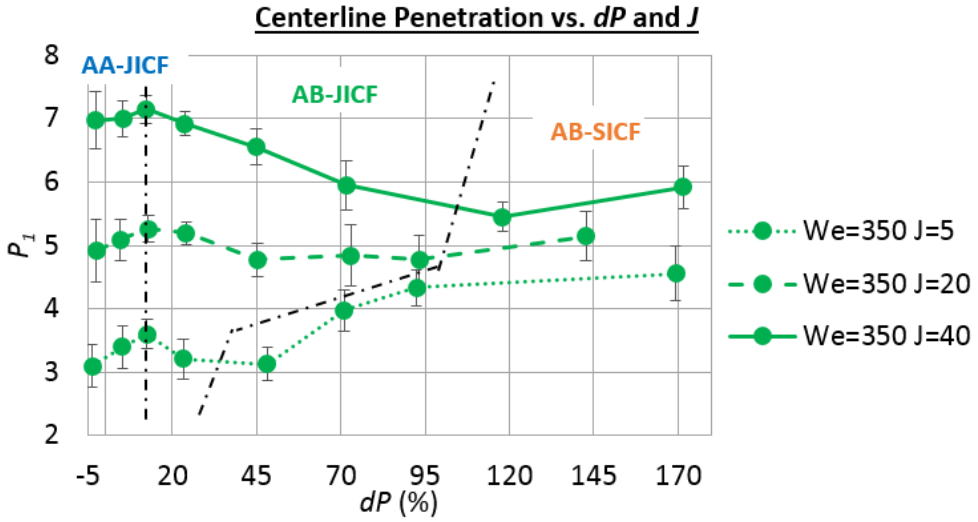

Figure 4.12 – Spray centerline penetrations as a function of *dP* and *J* for We_{cf}=350.

4.3 Application of J_{eff} Correlation to TF-JICF Trajectories

Leong et al. (2000, 2001 *JPP*, 2001 *JEGTP*) first introduced the J_{eff} parameter for correlating the trajectories of TF-JICF. As discussed in Section 2.2, the J_{eff} parameter describes the spray penetration as being governed by the combination of fuel and air momentum-fluxes. It assumes the injected fuel is promptly atomized and the fuel-air momenta are rapidly exchanged, a condition which is typically only encountered in high-*ALR* and high-*dP* TF-JICF. In the subsequent investigations by Li et al. (2006, 2010 *Part 1*) and Sinha et al. (2015), the J_{eff} correlation was applied to the measured TF-JICF trajectories without necessarily justifying the applicability of the underlying physics. Nevertheless, these correlation attempts were mostly successful because the investigations were performed at high *ALR* or *dP* values where the jet atomization by air was very rapid. In this section, we examine whether the J_{eff} parameter can correlate our data, which include operating conditions well beyond those tested before. Notably, if the J_{eff} correlation fits our data well, it would suggest that the high-*ALR* and *dP* mechanism/assumptions may apply equally well to lower *ALR* and *dP*. On the other hand, if the J_{eff} correlation fails, it suggests different mechanisms govern the lower *dP* regimes.

We begin the analysis by considering the data presented in Figure 4.13, which shows the raw outer-edge trajectories of TF-JICF at J=5 and 40, and We_{cf}=350. The plotted trajectories are for a *dP* range of 0% to 150% (i.e., our entire dataset) and have been grouped by colors into their respective regimes, following the classification presented in Figures 4.11 and 4.12. Next, we attempt to fit these trajectories to Leong et al. (2000, 2001 *JPP*, 2001 *JEGTP*)'s J_{eff} correlation function, which is shown in Equation (20) of Section 2.2, and reproduced below:

$$\frac{x}{d_f} = c_0 \times \left(\frac{A_f \rho_f U_f^2 + A_{air} \rho_{air} U_{air}^2}{A_{total} \rho_{cf} U_{cf}^2}\right)^{C_1} \times \left(\frac{z}{d_f}\right)^{c_2} \equiv c_0 \times J_{eff}^{C_1} \times \left(\frac{z}{d_f}\right)^{c_2} \qquad (7)$$

The constant C_1 is usually freely adjusted until a best fit is found. For example, Leong et al. (2001 *JPP*) found C_1 to be 0.375 and 0.570 for the outer- and inner-edge trajectories of TF-

JICF, Li et al. (2010 *Part 1*) found C_1 to be 0.273 for the centerline defined based on maximum Mie intensity, and Sinha et al. (2015) found C_1 to be 0.17 for outer-edge trajectories. But in this case, knowing that Equation (7) will *not* fit all the regimes equally well, and observing that C_1 varies so significantly in TF-JICF literature, we chose to set C_1 to 0.5, which is a typical value for the exponent of J based on Wu et al. (1997)'s original derivation (see Equation (11) in Section 2.1). We tested the applicability of the correlation by normalizing the raw trajectories by $J_{eff}^{0.5}$ and replotting them again in Figure 4.14. If the J_{eff} scaling is applicable, the normalized trajectories should collapse into a single curve. A comparison of Figures 4.13 and 4.14 shows, however, that while the AB-SICF's trajectories are reasonably well-collapsed at both J=5 and 40 using an exponent of C_1=0.5, the AA-JICF and AB-JICF regimes' trajectories are all very poorly correlated. This observation suggests that the AB-SICF regime corresponds phenomenologically to the reported results of Leong et al. (2000, 2001 *JPP*, 2001 *JEGTP*), Li et al. (2006, 2010 *Part 1*, 2010 *Part 2*) and Sinha et al. (2013, 2015). It also suggests that the AA-JICF and AB-JICF regimes' physics are fundamentally different from those in AB-SICF, and that the J_{eff} scaling no longer applies. These conclusions also hold for our We_{cf}=175 and 1050 results, which will not be shown here for brevity.

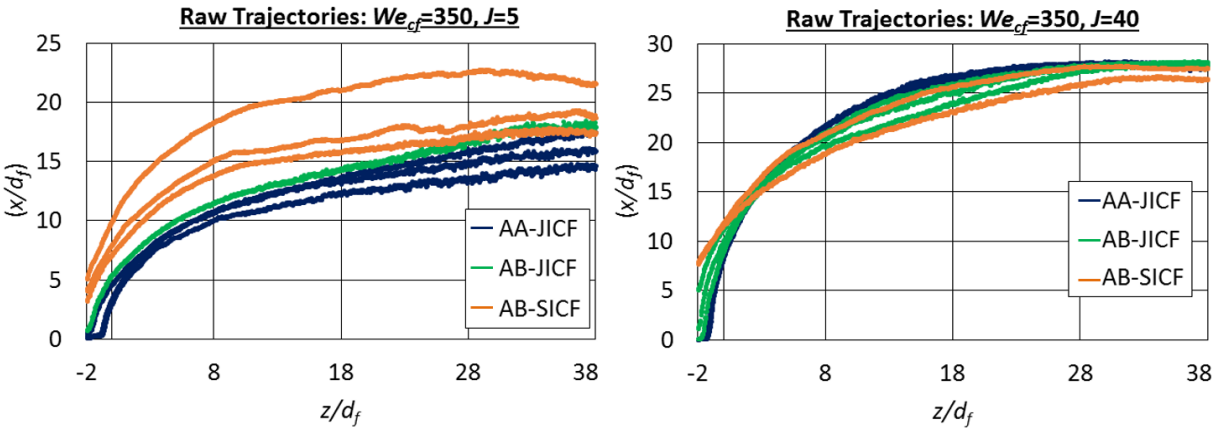

Figure 4.13 – Raw outer-edge trajectories of TF-JICF at J=5, 40 and We_{cf}=350, grouped in colors by their corresponding regimes.

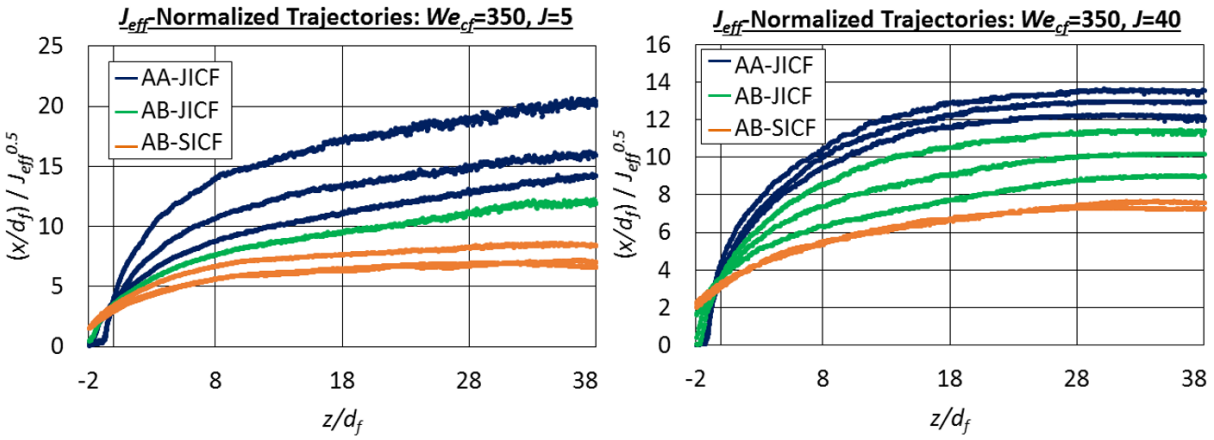

Figure 4.14 – $J_{eff}^{0.5}$-normalized outer-edge trajectories of TF-JICF at J=5, 40 and We_{cf}=350, grouped in colors by their corresponding regimes.

We have now provided an overview of the investigations' results and introduced the regimes of TF-JICF. The subsequent chapters will provide in-depth discussions of results from the individual regime, culminating in a conceptual understanding of TF-JICF spray-formation processes that tie all the observed spray characteristics together.

CHAPTER 5. DISCUSSION:

THE AIR-ASSIST JICF REGIME

This chapter discusses results from the AA-JICF regime, which generally spans the range of $0 < dP \leq 13\%$. We first discuss how the characteristics of the initial fuel jet depended upon *J*, *dP* and We_{cf}, accompanied by descriptions of the mechanisms that most likely caused those dependencies. We then present a similar type of discussion for the global (i.e., z/d_f=0-38) spray characteristics. Finally, this chapter concludes by tying all the observations and proposed mechanisms into a cohesive conceptual understanding of AA-JICF.

5.1 Effects of the Air-Assist on the Initial Jet's Characteristics

Figure 5.1 shows instantaneous images of the initial fuel jets at *J*=5, We_{cf}=350 and *dP*=0-13%, which elucidates the interactions of the fuel, air-assist and crossflow immediately around the injection orifice. Although the presented images were sequentially-captured, they are effectively statistically random and represent the general spray characteristics because of the camera's slow frame-rate. The top row of Figure 5.1 shows that without air-assist the fuel exited the spraywell as an intact liquid jet. On average, the jet traveled ~3d_f before developing large-scale RT-waves (e.g., see black arrows) that "snapped" it into a sinuous motion, as traced by the white dotted-lines. This was followed by a complete pinch-off of the jet at the wave troughs (e.g., see purple lines), which shed large liquid clusters into the crossflow. In agreement with our review in Section 2.1, the RT-waves did not exhibit a clear preferred wavelength, as seen from the non-uniformly spaced black arrows. In addition, throughout the jet disintegration process (even prior to jet pinch-off), droplets were continuously sheared from the jet surface and entrained into the wake region. The sinuous motion of the jet and the surface-shearing produced a widely dispersed spray that placed many droplets very close to the test-channel wall. In addition, fuel was observed to dribble from the back edge of the spraywell (e.g., see red

arrows), producing a small stream of liquid fuel that traveled along the wall. Both of these may produce such detrimental effects as wall-coking and flashback.

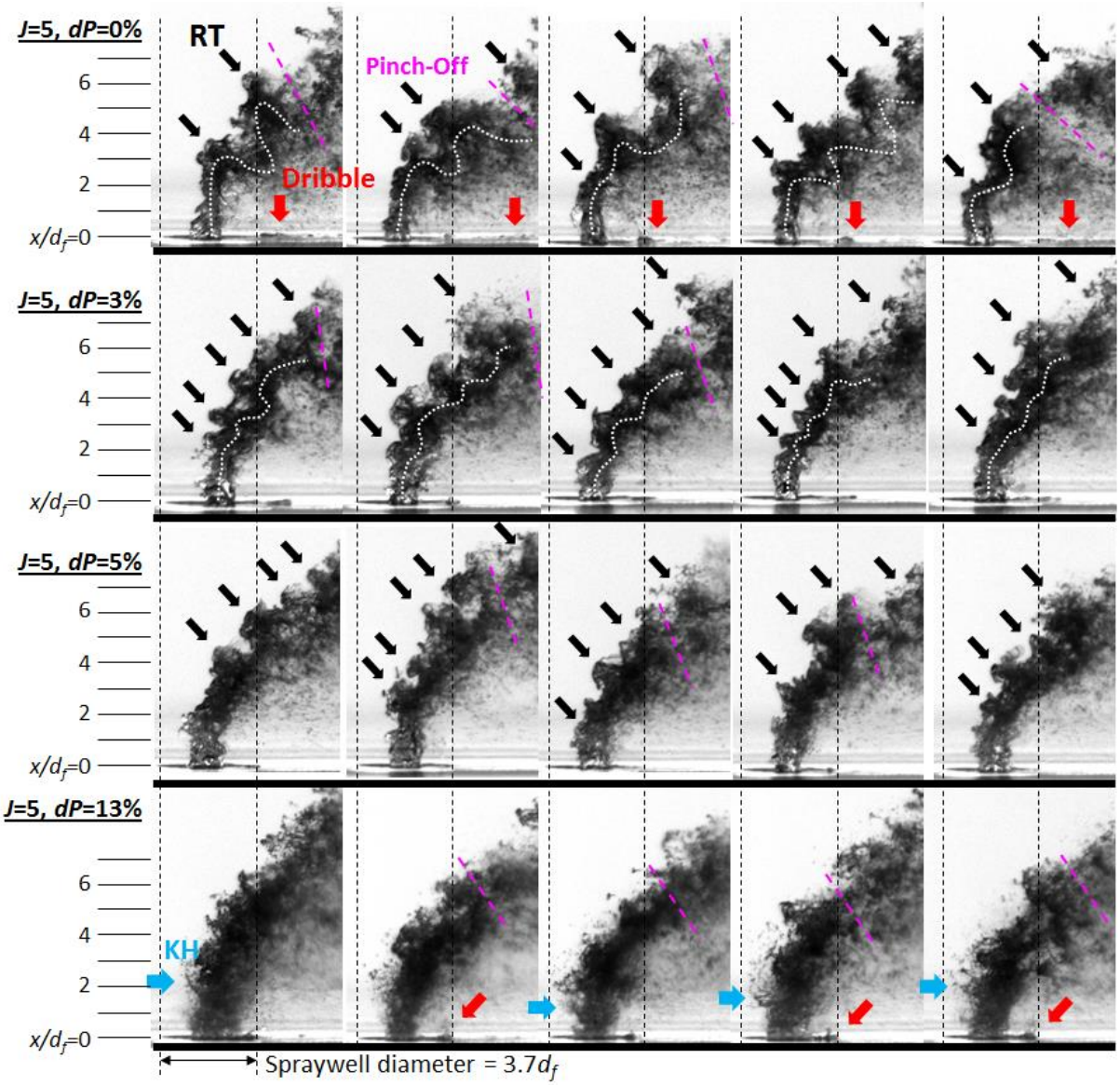

Figure 5.1 – Instantaneous photos showing the effects of *dP* on the initial jets' structures at *J*=5, We_{cf}=350. White dotted-lines: sinuous oscillation of the jet.

Figure 5.1 shows that when *dP* was increased to 3%, the RT-waves' wavelengths were generally reduced, as seen from the more closely-spaced black arrows. At the same time, the amplitudes of the jet's RT-waves were also reduced. Since the windward-edge disturbances of the jet was dominated by RT-waves at these conditions, the measured jet profile thickness (t_ω) is essentially a measure of the RT-waves amplitude. The reduced RT-wave amplitudes at *dP*=3%

is shown in Figure 5.2, where $t_\omega(dP = 3\%)$ is smaller than $t_\omega(dP = 0\%)$ throughout the plotted domain. Consequent of the reduced RT-waves amplitude, the magnitudes of the jet's motion and the droplets' dispersion were both reduced, as illustrated by the smaller fluctuations of the white dotted curves in Figure 5.1. This effect appears to detach/deflect the spray-core away from the wall. Figure 5.1 also shows that the region immediately next to the wall ($x/d_f \approx$ 0-2) becomes much less populated with droplets when *dP*=3% of air-assist was applied. Since the droplets found in this region at *dP*=0% were produced by fuel-crossflow surface-shearing (instead of gross jet breakup which happens further downstream), we reason that the significant reduction of droplets near the wall at *dP*=3% indicates a reduction in surface-shearing due to the sheathing provided by the air-assist.

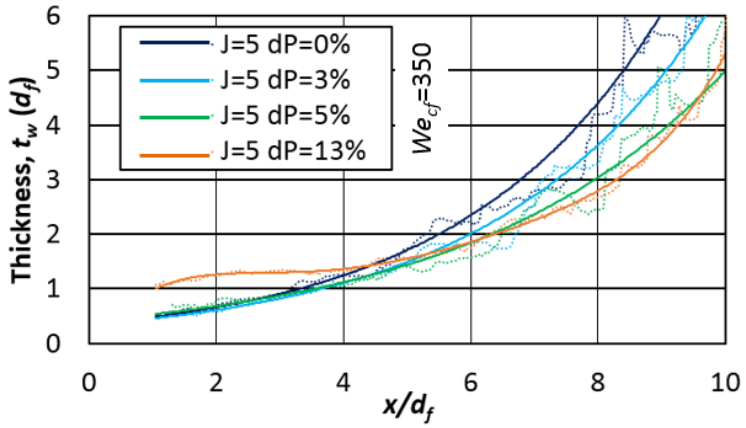

Figure 5.2 – Effects of *dP* on the profile thickness of *J*=5, We_{cf}=350 jets. *Dotted lines: raw data. Solid lines: curve-fits to more clearly bring out the trends of the otherwise noisy t_ω curves.

Since the AA-JICF regime is located next to the Classical-JICF regime on the spectrum of TF-JICF regimes, and since the AA-JICF essentially becomes a Classical-JICF in the low *dP* limit, we examined whether the RT-waves scaling models developed for Classical-JICF can also apply to AA-JICF, and, subsequently, whether the application of these models will provide any new understanding of the interactions between the air-assist and fuel jet. As reviewed in Section 2.1, the growth-rate and wavelength of RT-waves in Classical-JICF are described by the following expressions, respectively:

$$\eta = \left[k \left(\frac{2 C_D \rho_{cf} U_{cf}^2}{\pi \rho_f d_f} \right) - \frac{k^3 \sigma_f}{\rho_f} \right]^{0.5} \quad (1)$$

$$\frac{\lambda_{RT}}{d_f} = C_\lambda \sqrt{\frac{6\pi}{C_D}} We_{cf}^{-0.5} \quad (2)$$

where $k = 2\pi/\lambda_{RT}$, $C_\lambda \sim 1$ and $C_D = 1 + 10 Re_{cf}^{-\frac{2}{3}} = 1 + 10 \left(\frac{\rho_{cf} U_{cf} d_f}{\mu_{cf}} \right)^{-\frac{2}{3}}$ as reported by Ng et al. (2008). Substituting in our test-conditions into the equations above yields the following approximate proportionality:

$$\eta^2 \propto We_{cf}^{1.5} \quad (3)$$

Equations (2) and (3) express the RT-waves' average wavelength and growth-rate in terms of the crossflow's intensity (i.e., We_{cf}). In Classical-JICF, it is assumed that the jet experiences the same We_{cf} as the freestream crossflow; however, in AA-JICF where the air-assist can deflect the crossflow and modify the local flow-field around the fuel jet, we should treat We_{cf} around the jet as a local parameter that may differ from the freestream We_{cf}. Thus, Equations (2) and (3) suggest that if changes to *dP* affects the local We_{cf}, the resulting RT-waves' wavelength and amplitude should vary inversely and directly with We_{cf}, respectively. Contrary to the equations, the images in Figure 5.1 and the t_ω plot in Figure 5.2 show decreasing wavelength *and* decreasing amplitude with increasing *dP*. From this observation, it is difficult to infer whether the RT-waves' dependence on *dP* indicated locally higher or lower crossflow strength in the presence of air-assist. Additionally, the observed deviation in the RT-waves' characteristics from Equations (2) and (3) suggests the air-assist affected the RT-waves' development in a way not described by Classical-JICF RT-wave scaling laws. Future work should investigate this particular aspect of the RT-waves' sensitivities to air-assist.

Based on the described effects of air-assist on RT-waves and surface-shearing, we reason that when *dP* > 0%, the injected air formed an "air-sheath" around the fuel jet. The air-sheath isolated the fuel jet from the crossflow, resulting in inhibited surface-shearing and

reduced RT-wave amplitudes; at the same time, the interaction between the fuel and assisting air also served to modify the RT-waves' preferred wavelengths. Additionally, we note that the continued presence of RT-waves (which can only form in a crossflow) at *dP*=3% means the fuel jet was not *entirely* isolated from the crossflow by the air-sheath; i.e., the air-sheath likely protected the jet for a short initial distance before being entrained away by the crossflow, thus exposing the fuel jet to crossflow impingement, whereupon RT-waves began to develop. This interpretation is intuitively reasonable because the assisting air has a much lower momentum than the fuel in the AA-JICF regime and is, thus, more susceptible to crossflow stripping.

Next, the second and third row of Figure 5.1 show the effects of increasing *dP* from 3 to 5%. On average, the RT-waves' wavelengths appear unchanged but their amplitude appears to be smaller, which is reflected in Figure 5.2 where $t_\omega(dP = 5\%)$ is smaller than $t_\omega(dP = 3\%)$ Figure 5.1 shows the x/d_f=0-2 region remained devoid of droplets, indicating that the air-sheath continued to protect the initial jet from crossflow-induced surface-shearing. It is also worth noting that at *dP*=3 and 5%, the spraywell dribbles were absent, likely because the formation of an air-sheath around the liquid jet prevented fuel from splashing onto the spraywell's wall. The suppression of RT-waves, near-wall droplets and spraywell dribbles in the range of *dP*=3-5% demonstrates the air-assist's effectiveness in mitigating the risks of coking and flashback in the near-wall region, especially on an otherwise wall-attached Classical-JICF spray. The increase in air-assist flow-rates from 3 to 5% does not appear to produce a big difference, at least from a fuel atomization and dispersion standpoint. It is, however, unclear how the air-assist affected the velocities of the droplets and crossflow/air, all of which also affect coking and flashback risks. These remain a topic for future investigation.

Finally, the last row of Figure 5.1 shows a significant change in the initial jet's structures when *dP* was raised to 13%. The RT-waves appear to be replaced by fine-scale corrugations composed of ligaments and stripped droplets. When these images are zoomed-in,

as shown in Figure 5.3, we clearly see ligaments (e.g., see blue arrows) in the process of being stripped from the windward side of the jet, which does *not* occur in Classical-JICF. Furthermore, these ligaments were consistently stripped in the upwards (x) direction, suggesting the presence of Kelvin-Helmholtz (KH) instabilities due to strong shearing in a direction *parallel* to the jet; i.e., the flow of air immediately around the initial fuel jet was oriented in the x direction instead of the crossflow (z) direction. This upwards flow of air around the fuel jet is further evidence for the presence of an air-sheath, which acquired sufficient velocity at dP=13% to introduce its own shear-stripping along the jet surface.

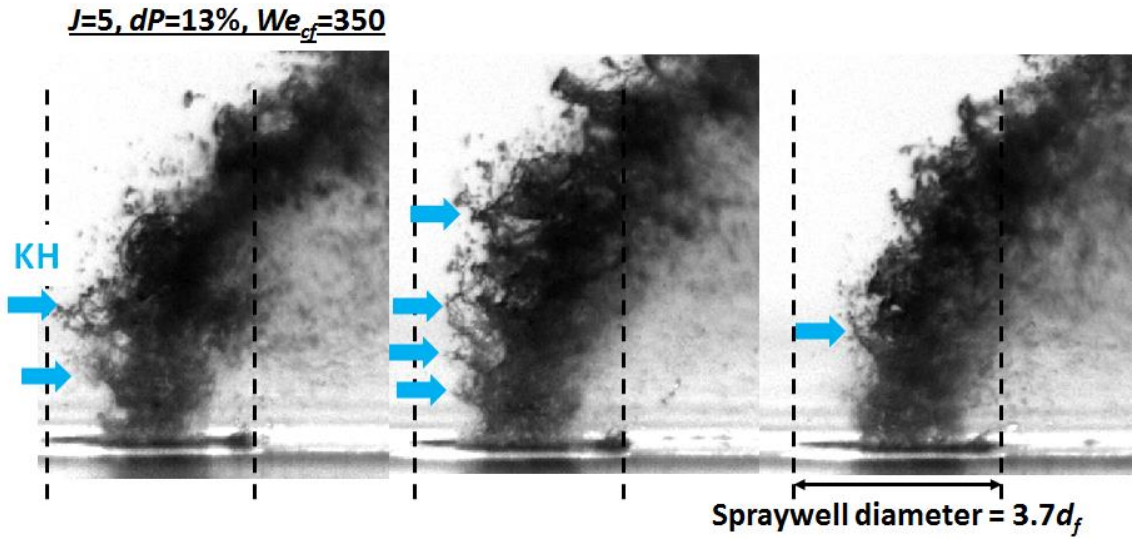

Figure 5.3 – Zoomed-in images showing the development of upwards-sheared liquid ligaments (i.e., KH instability).

Figure 5.2 showed that the t_ω values in the spatial domain of x/d_f > 6 were always inversely proportional to dP; i.e., the air-assist always inhibits (or at least delays) downstream RT-waves development in a J=5 jet. However, closer to the injection point (i.e., x/d_f=0-4), an air-assist level of 13% caused a significantly increase in t_ω, which we can associate with the observed onset of KH-corrugations (i.e., analysis of the raw images suggests the profile thickness in this region is dominated by the KH-corrugations). Interestingly, a plateau in $t_\omega(dP = 13\%)$ located between x/d_f=3-5 suggests that the KH-corrugations stopped growing

and perhaps even disappeared due to stripping of the fuel into the crossflow as they traveled further away from the injection point. This observation is consistent with the earlier proposition that the air-sheath only surrounds the initial portion of the fuel jet, because the KH-corrugations that are generated by fuel-air shearing can only be produced when the air-sheath is still present.

Next, to elucidate the effects of *dP* at different *J*, we refer to Figure 5.4 that contains series of *J*=40, We_{cf}=350 sprays images. Compared to *J*=5, the *J*=40 jets are less disturbed at all *dP*. In fact, it is difficult to identify the large-scale RT-waves in Figure 5.4. This difference is also reflected in the profile thickness plot in Figure 5.5, which shows that $t_\omega(J = 40)$ generally ranged from 0.5-1.3d_f in the same spatial domain where $t_\omega(J = 5)$ ranged from 0.5-6d_f. Note that at least for the case of *dP*=0%, the lower amplitude of RT-waves at higher *J* has been shown in Chapter 4 as being due to faster RT-wave convection at a constant temporal growth-rate (e.g., see Figure 4.6). The same reasoning may explain AA-JICF's lower t_ω at higher *J*, because RT-waves likely dominated the far-field disturbances even in the AA-JICF regime (i.e., after the protective air-sheath is stripped away).

Figures 5.4 and 5.5 show that unlike *J*=5, the application of air-assist in the range of *dP*=3-5% at *J*=40 increased the t_ω by a small amount. This was likely due to the fact that the air-sheath had very low penetrations in comparison to the *J*=40 jets and, therefore, only interacted with the jet in the near-wall region before the RT-waves had time to form and grow; i.e., the air-sheath did not significantly protect the fuel jet from the crossflow where it matters, and perhaps even introduced additional instabilities due to their 45^o impingement on the jet.

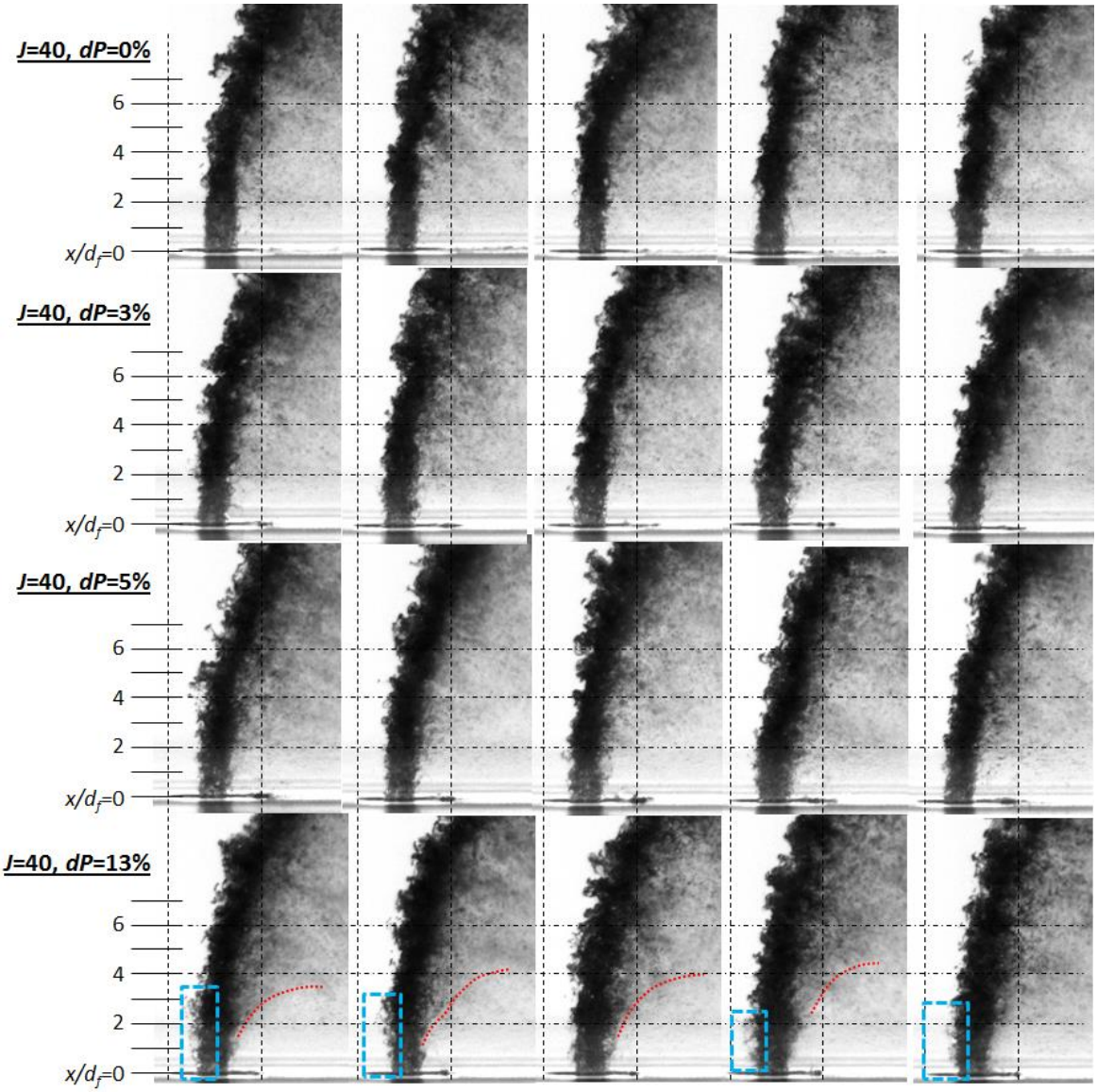

Figure 5.4 – Instantaneous photos showing the effects of *dP* on the initial jets' structures at *J*=40, We_{cf}=350. Red dotted lines: sudden increase in wake-side droplets population. Blue boxes: small droplets/corrugations on the windward-edge.

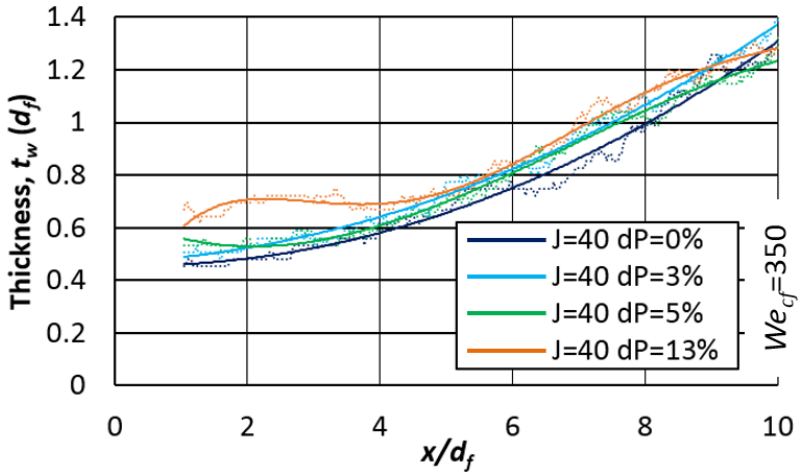

Figure 5.5 – Effects of *dP* on the profile thickness of the *J*=40, We_{cf}=350 jets.

Similar to the case of J=5 dP=13%, a local maximum in t_ω occurred at J=40 dP=13% in the region of x/d_f=0-4, which can be attributed to the development of KH-corrugations caused by fuel-air shearing. The plateauing of the KH-corrugations observed at J=5 was even more pronounced at J=40 as Figure 5.5 shows that t_ω decreased significantly after the maximum at $x/d_f \approx 2$, reaching a minimum at x/d_f=4 before growing again downstream, presumably due to the onset of RT-waves. Notably, when t_ω decreased between x/d_f=2-4 in Figure 5.5, we noticed the jet's wake-side droplets population increasing sharply in Figure 5.4 (outlined in red), which was often also accompanied by the disappearance of windward-side droplets and corrugations (highlighted in blue boxes). These observations suggest that the KH-corrugations produced by fuel-air shearing were allowed to build up around the jet while they were being shielded from the crossflow by the air-sheath. However, as soon as the air-sheath was stripped away by the crossflow and the corrugations became exposed, they were rapidly shed into the wake region due to their large drag areas and small inertia, thereby causing the wake-side droplets population to rise suddenly. Interestingly, the increase in wake-side droplets concentration due to rapid corrugation-shedding was only observed at higher J when the spray-core was far away from the wall and the near-wall region was relatively "clean". The same phenomenon was not observed in the J=5 AA-JICF's wakes, likely because the shedded droplets (if they were present) intermingled with the closely situated spray-core's droplets.

Finally, we examine Figure 5.6 to show the dependence of J=20 jets' t_ω values on We_{cf} in the range of 175-1050. It is evident that the J=20 jets' t_ω curves in the region of $x/d_f > 6$ did not change significantly when dP was varied between 0 to 13%; on the other hand, when We_{cf} was varied from 175 to 1050 the t_ω values generally increased by up to 25%. Like the J=40 cases, the J=20 t_ω's insensitivity to dP in the $x/d_f > 6$ region was likely also due to the fuel jet's high penetration relative to the air-sheath, which rendered the air-sheath incapable of protecting the fuel jet against the crossflow when the RT-waves began to develop. On the other

hand, at least for the case of *dP*=0%, the direct proportionality between t_ω and We_{cf} can be explained by the dependences of the RT-waves' growth-rates and convection velocity (i.e., fuel injection velocity) on We_{cf}. For example, Equation (3) showed that $\eta \propto We_{cf}^{0.75}$, while $U_f \propto We_{cf}^{0.5}$ for a fixed *J*. Thus, when the proportionalities are combined, we see that the amplitude of the RT-waves (h_{RT}) is weakly proportional to We_{cf}, as follows:

$$h_{RT} \propto \exp\left(\eta \frac{x_{RT}}{U_{RT,x}}\right) \propto \exp\left(We_{cf}^{0.25} x_{RT}\right) \tag{4}$$

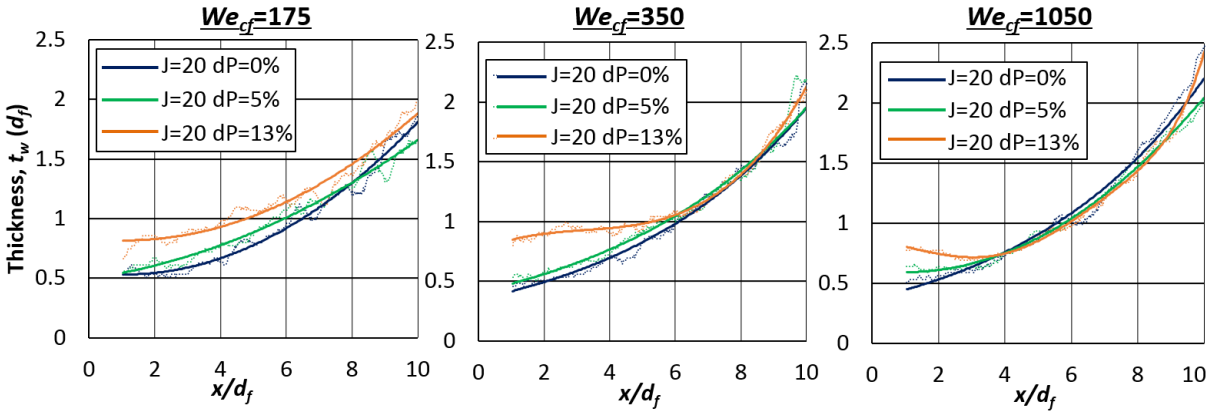

Figure 5.6 – Effects of *dP* on the profile thickness of *J*=20 jets at varying We_{cf}.

In contrast to the downstream portion of the t_ω curves, the *J*=20 jets' t_ω values at x/d_f < 4 (where the air-sheath is expected to act most strongly) were very sensitive to *dP* and We_{cf}. For example, Figure 5.6 shows that *dP*=13% of air-assist caused a local maximum to form in the t_ω curves of the We_{cf}=350 and 1050 cases, which (as described earlier) can be attributed to the growth and shedding of KH-corrugations. On the other hand, the We_{cf}=175 curve did not form a maximum; instead, its initially higher t_ω value converged gradually with the *dP*=0-5%'s curves in the downstream region. This gradual convergence suggests the absence of rapid KH-corrugations shedding at lower We_{cf}, which is likely because the corrugation structures and droplets are larger at lower We_{cf}. For example, Figure 5.7 shows the instantaneous images of two AA-JICF at identical *J* and *dP*, but with We_{cf} = 175 and 1050. The We_{cf} = 175 AA-JICF contained very rough corrugated textures on the windward-side, while the leeward side

contained relatively discrete-looking droplets/liquid parcels. On the other hand, the We_{cf} = 1050 AA-JICF appears "smoother" (i.e., lacking coarsely-textured structures), while also being more densely-populated with "fog-like" sub-pixel sized droplets in the wake region. The difference between the two AA-JICF in Figure 5.7 suggests the presence of larger (and perhaps less) droplets/structures at lower We_{cf}. These larger structures and droplets will have more inertia per drag area and will, consequently, resist the stripping by crossflow aerodynamic forces more strongly. Hence, they will resist being rapid stripped into the crossflow when the air-sheath is entrained away, causing the We_{cf} = 175's t_ω curve to lack a local maximum. This finding supports our hypothesis in Chapter 1 that results from investigations at near-atmospheric pressures may not be entirely representative of TF-JICF characteristics at jet-engine operating conditions.

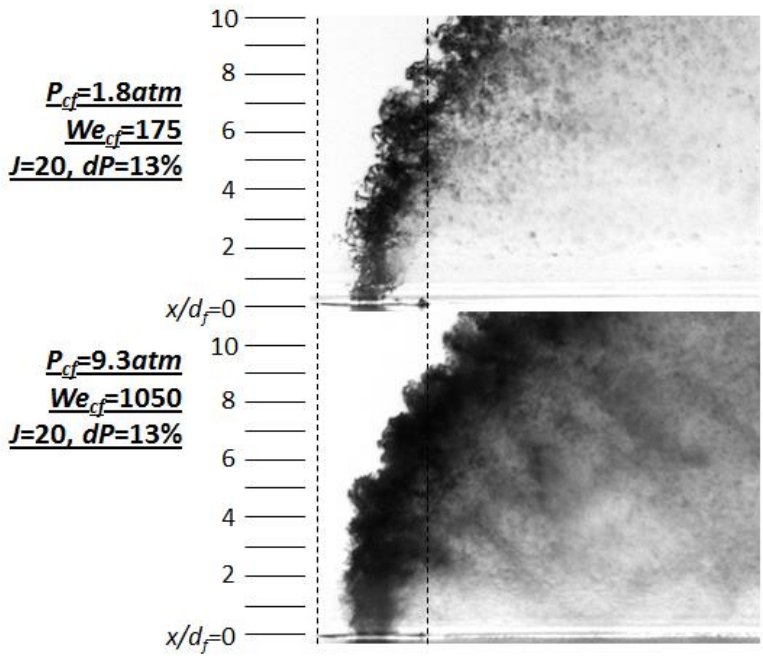

Figure 5.7 – Instantaneous photos comparing the droplets and corrugations' sizes at different We_{cf}, showing the effect of crossflow pressure.

5.2 Effects of Air-Assist on the *J*=5 Sprays' Global Characteristics

Having discussed the fuel, air-assist and crossflow interactions around the region of the initial jet, we will now examine how these interactions affect the global spray characteristics.

Figure 5.8 shows instantaneous and false-color average images of J=5 AA-JICF. Comparison between the first two rows of images shows that an air-assist of dP=3% significantly reduced the spray-core's dispersion, which resulted in the detachment of the spray-core from the wall at the location indicated by the white-arrow. Increasing dP to 13% did not produce any noticeable change in the average images. However, on the instantaneous images, the droplets in the wake region appear as discrete dots when dP=0-5%, but appear more blurred" when dP was increased to 13%. The "blurring" is an optical effect indicating the presence of droplets outside of the camera's plane of focus (i.e., the spray's central/injection plane). This suggests that at dP=13% the droplets in the wake region may be pushed laterally (±y direction) out of the central plane by air-assist.

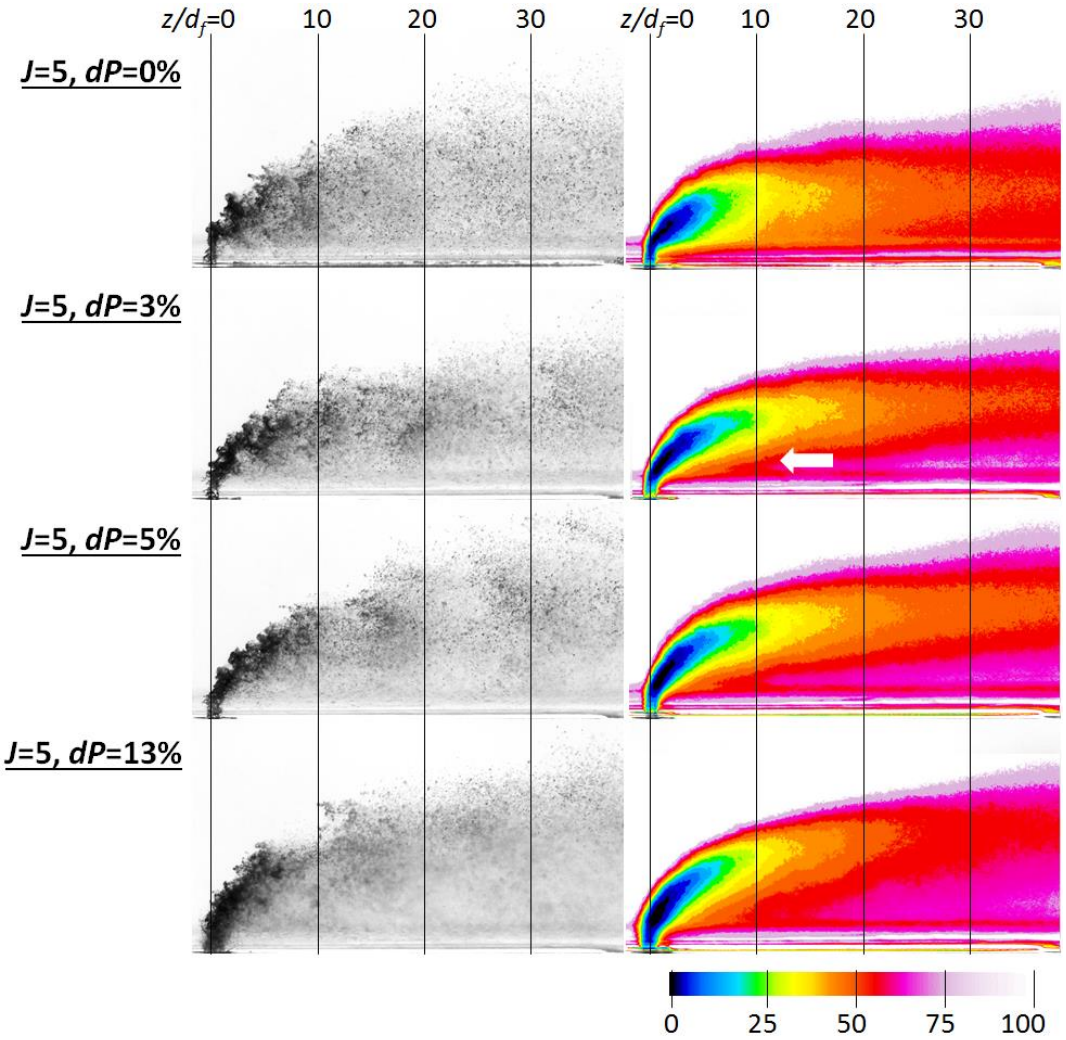

Figure 5.8 – Instantaneous and average images of Classical- and AA-JICF at J=5, We_{cf}=350. White-arrow: detachment of spray-core from the wall.

To quantitatively compare the dispersions of droplets at various *dP*, we refer to Figure 5.9, which plots the cross-sectional light-attenuation (*N*) profiles of the *J*=5 sprays at the three longitudinal locations of z/d_f=5, 15 and 25. The profiles in Figure 5.9 appear similar to a Gaussian distribution where the peak represents the location of the spray-core's centerline. *N* values decreased to near zero on the top of the profiles where the sprays' outer-edges were located, while *N* values near the wall remained high because the wake region was always occupied by droplets as shown in Figure 5.8. Without air-assist, the spray-core was "attached" to the wall and the degree of light-attenuation directly next to the wall were $N \approx 35$, 25 and 18% at the three cross-sections, respectively. Applying an air-assist of *dP*=5% deflected the dense spray-core upwards and away from the wall, thereby nearly halving the near-wall *N* values; i.e., air-assist "detached" the spray-core from the wall (as indicated qualitatively in Figure 5.8) and reduced near-wall fuel concentrations. Additionally, Figure 5.9 shows that although the centerlines' locations were deflected upwards by increasing *dP* from 0 to 5%, the outer-edges of the spray where *N* reached ~0% remained at approximately the same location. The combined effects imply that the spray-core's dispersion in the *x* direction was reduced by the air-assist.

Notably, the three cross-sections in Figure 5.9 show the spray *N* profiles spreading out and the peak *N* values decreasing as we move along the crossflow (*z*) direction, which suggests that the sprays were dispersing with distance. The profiles' dependence on *dP* was the same at the three cross-sections, which suggests the changes we observed (e.g., the spray-core's penetration-enhancement and dispersion-reduction by *dP*) were likely developed very early in the spray-formation process and simply propagated downstream as droplets were convected by the crossflow. In essence, the observed global effects of air-assist likely arose from fluid interactions near the initial jet. Considering the discussions in the previous section, we reasoned that these global effects were due to the fact that air-assist reduced the initial fuel jet's RT-wave amplitudes and surface-shearing, both of which will discourage jet breakup, thereby

reducing droplets dispersion and increasing penetration. It is *un*likely for the penetration-enhancement to be caused by the exchange of fuel and air momenta in the manner described in TF-JICF literature (see Section 2.2) because the fuel jets remained relatively intact in the *dP* range of 0-13%, which would have prevented them from being significantly accelerated by the assisting air.

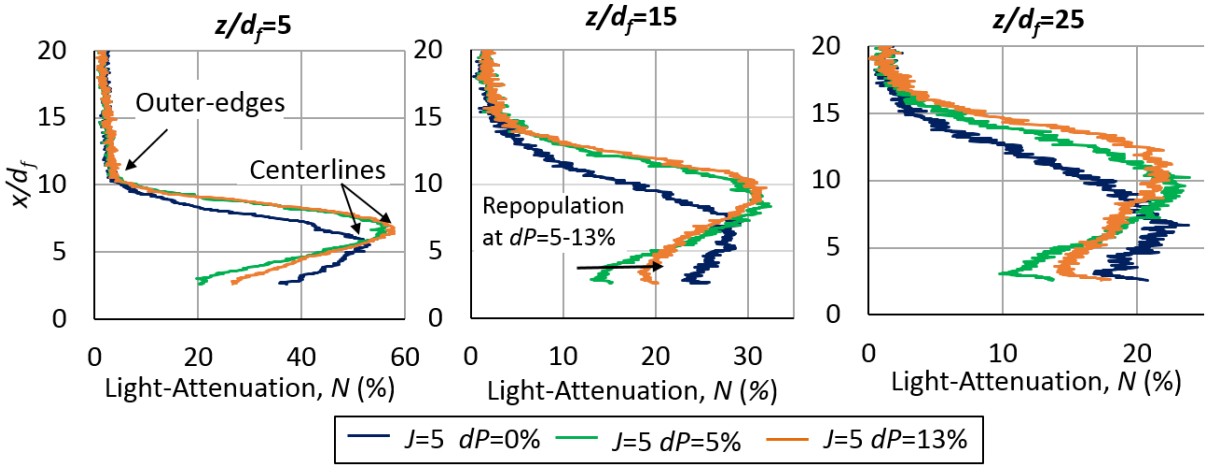

Figure 5.9 – Effects of *dP* on the light-attenuation profiles of *J*=5, We_{cf}=350 AA-JICF, demonstrating the detachment of the spray-core from the wall.

Figure 5.9 also shows that the spray-cores' penetrations and dispersions were insensitive to changes in *dP* between 5 and 13%. Based on the argument above that spray dispersion and penetration are directly related to RT-waves amplitude, we reasoned that the observed insensitivity to *dP* in Figure 5.9 was because the RT-waves amplitudes were also insensitivity to *dP* between 5 and 13%, as shown in Figure 5.2. While the spray-cores were not affected by *dP*, Figure 5.9 shows noticeable increase in near-wall spray-densities between *dP*=5 and 13%. Since the air-sheath enveloped the initial fuel jet and inhibited crossflow-induced atomization, and since the air-sheath had sufficient intensity to introduce its own shear-atomization at *dP*=13%, we can attribute the repopulation of the near-wall region to the shedding of air-induced KH-corrugations into the wake region.

Based on the observations above, an air-nozzle *dP* of 3-5% appears to be optimal for achieving the objective reducing fuel concentrations near the wall (at least at *J*=5). Higher *dP*

will not only fail to further enhance spray penetration, it also puts tougher demands on the air-supply system and *increases* near-wall fuel concentrations at close to *dP*=13%. This finding is in stark contrast to existing TF-JICF studies, which generally proposed applying stronger air whenever possible to achieve higher spray penetrations and larger spray-wall separation. Finally, the trends observed in Figure 5.9 are consistent across all tested We_{cf}, and will not be repeated for brevity.

5.3 Effects of Air-Assist on *J*=20-40 Sprays' Global Characteristics

In this section we discuss how air-assist affects the AA-JICF's global characteristics at *J*=20-40. As proposed in Chapter 4, the *J*=20-40 Classical-JICF differed from the *J*=5 Classical-JICF because of their higher penetrations, which detach their spray-cores from the wall and create distinct regions of spray-core versus spray-wake. This difference is shown here again in the false-color average images across the first row of Figure 5.10. Consequent of this difference, the *J*=20-40 AA-JICF's global characteristics seem to respond differently to air-assist compared to *J*=5. For example, the two rows of Figure 5.10 show that while the *J*=5 spray's dispersion was significantly affected by air-assist, any changes to the *J*=20-40 sprays when *dP* was raised to 5% were subtle and not readily identifiable from the average images.

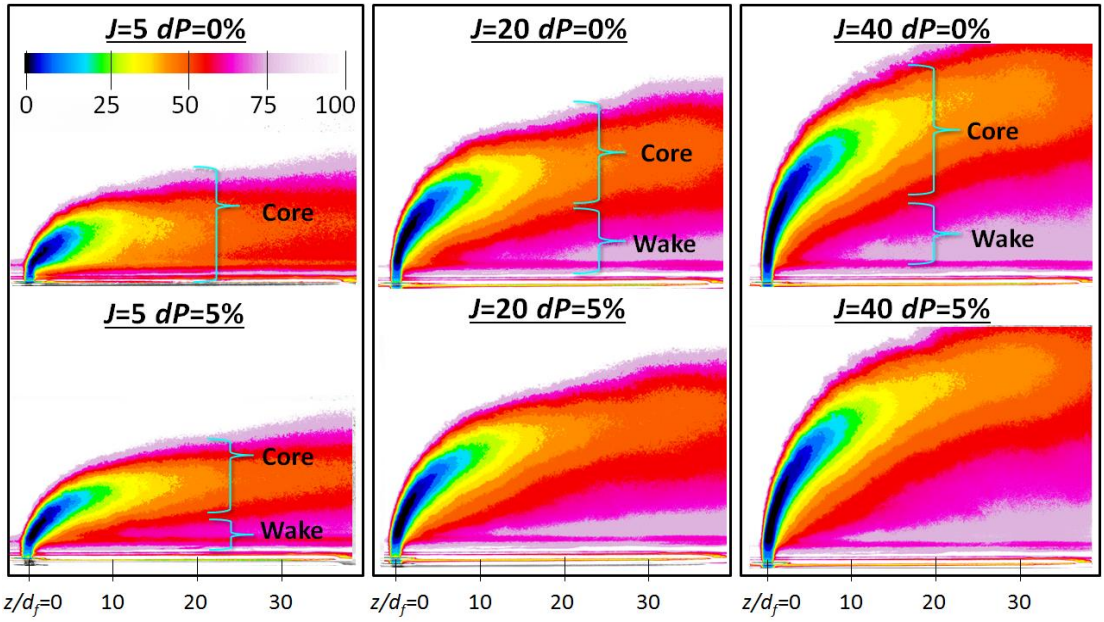

Figure 5.10 – Instantaneous images of JICF at *dP*=0 and 5%, for *J*=5 to 40 and We_{cf}=350.

To elucidate the effects of air-assist on the J=20-40 AA-JICF more quantitatively, we examine the light-attenuation profile plots in Figures 5.11 and 5.12. These figures reveal that when dP was increased from 0 to 13%, the locations of the J=20-40 spray-cores' centerlines were generally shifted upwards in the x direction while the outer-edge remained unchanged (i.e., enhanced penetration and reduced dispersion), but to a *much* lesser extent than observed for J=5 sprays in Figure 5.9. Interestingly, a comparison of Figures 5.11 and 5.12 suggests the J=40 sprays exhibited a larger response to dP than the J=20 sprays. Namely, the J=40 sprays developed a localized peak in N in the wake-region (see orange arrows), a feature which we call the "bifurcated-wake" and discuss in more details in Section 5.4 below. The trends described above are generally consistent across all tested We_{cf}.

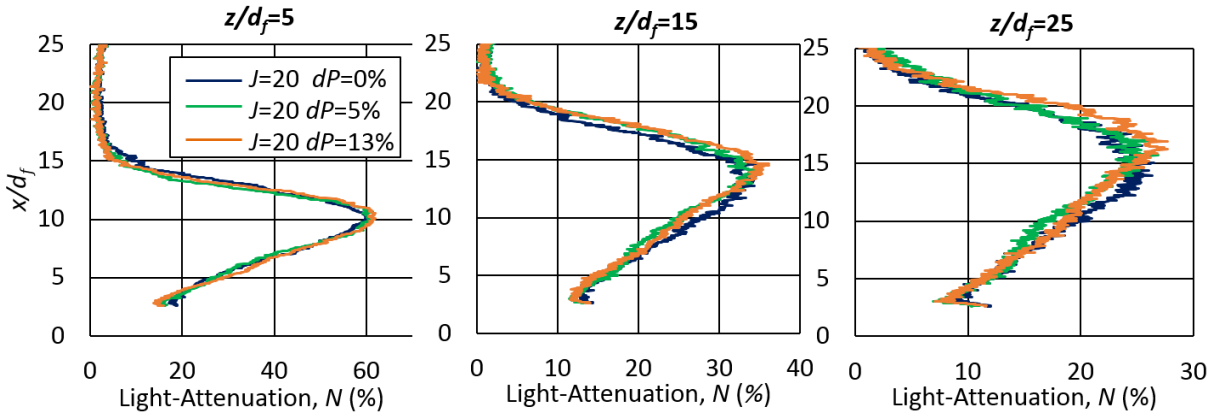

Figure 5.11 – The effects of dP on the light-attenuation profiles of J=20, We_{cf}=350 AA-JICF.

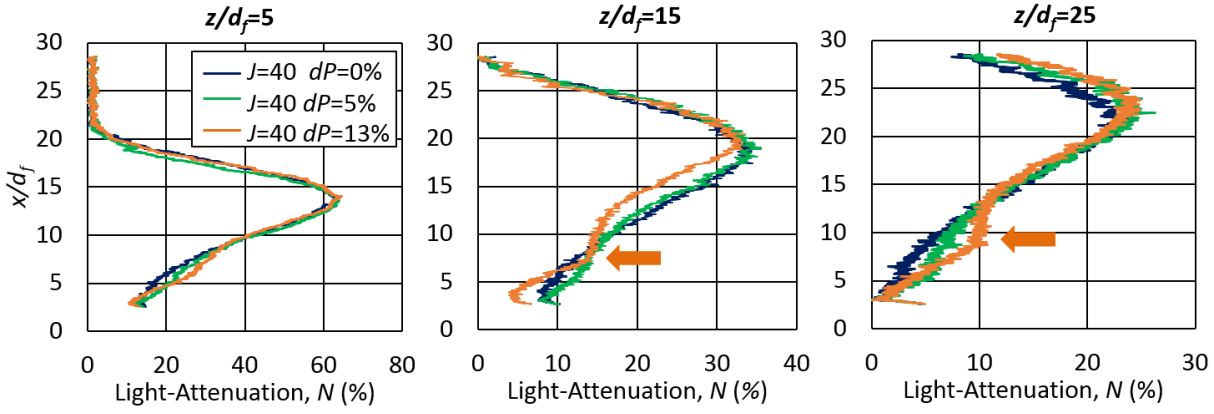

Figure 5.12 – The effects of dP on the light-attenuation profiles of J=40, We_{cf}=350 AA-JICF.

In general, the data shows that the penetration and dispersion of the spray-core are less sensitive to *dP* at higher *J*. In the previous section we proposed that the effects of air-assist on the *J*=5 spray-cores were connected to the inhibition of RT-waves on the initial jet. In line with this argument, the weak response of the *J*=20-40 spray-cores to air-assist was likely due to the *J*=20-40 initial jets' insensitivity to *dP*, as shown in Figures 5.5 and 5.6. In essence, a big driver of the spray-core's dispersion is the amplitude of RT-waves on the initial jet, since the RT-waves are responsible for jet pinch-off and spray-core formation (e.g., see Section 2.1). Thus, because the *J*=20-40 JICF have very low RT-wave amplitudes with or without air-assist (due to their RT-waves forming further downstream when the jets have penetrated above the protective air-sheath), their spray-cores' global characteristics are also less sensitive to air-assist.

5.4 The "Bifurcated-Wake" Structure

In this section we discuss the "bifurcated-wake" structure mentioned in Figure 5.12 in more details, and show that it is an important aspect of the AA-JICF spray-formation process. To examine this structure more carefully, the light-attenuation profiles of the *J*=20 and 40 AA-JICF in Figures 5.11 and 5.12 are replotted in Figure 5.13, but with *N* plotted as a percentage of the corresponding Classical-JICF's *N* (i.e., $N_{AA-JICF}/N_{Classical} \times 100\%$ for a given *J*). The plots are also zoomed-in on the wake region. Consequently, these plots clearly show the presence of a local light-attenuation peak near the wall when air-assist was applied (see arrows), which gives the spray-plume the appearance of being bifurcated into two branches. Hence, the reference to this structure as the "bifurcated-wake".

Furthermore, Figure 5.13 shows that the bifurcated-wakes were more prominent and "peaky" at higher *J* and *dP*, while their penetrations in the *x* direction appear to predominantly depend on *dP*. When we traced the bifurcated-wakes back to their origins near the initial jets (e.g., as shown with black arrows in Figure 5.14), we observed that they always connect to the

locations of rapid KH-corrugations shedding (e.g., the location of a local t_ω maximum in Figure 5.5). Additionally, the bifurcated-wakes were also generally present in the same *dP* range as the KH-corrugations. We therefore reasoned that the bifurcated-wakes' droplets originated from the KH-corrugations around the initial jet; i.e., as we will illustrate later in Figure 5.16, the KH-corrugations produced by the strong fuel-air shearing were rapidly shedded into the crossflow when the air-sheath was stripped away. The resulting droplets formed a locus of locally high droplets concentration stretching across the entire spray pattern, which we observed as the high-*N* bifurcated-wake. Since the behavior of rapid KH-corrugations shedding was observed to be more prominent at higher *J* and *dP*, this hypothesis also explains why the bifurcated-wakes were more prominent at higher *J* and *dP*.

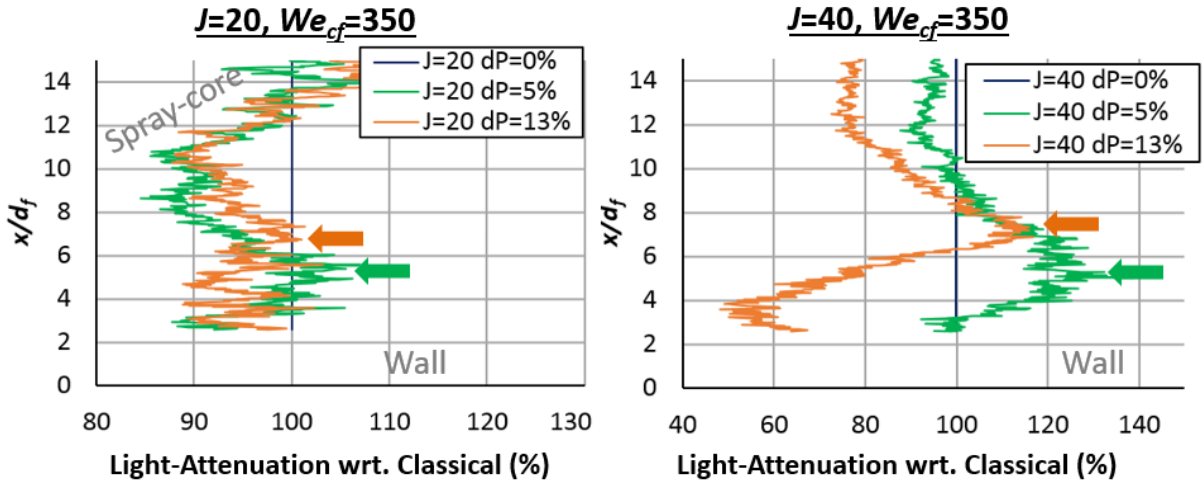

Figure 5.13 – Plots of normalized and zoomed-in light-attenuation profiles at z/d_f=15, demonstrating the development of the "bifurcated-wake" (see arrows) in *J*=20 and 40 AA-JICF.

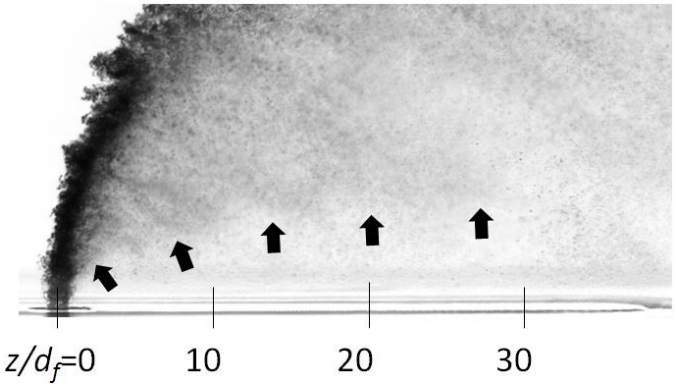

Figure 5.14 – Instantaneous image of *J*=40, *dP*=13% and We_{cf}=350 AA-JICF, showing the connection of the bifurcated-wake to the initial jet.

Figure 5.15 shows the bifurcated-wake's dependence on We_{cf}, where it is evident that they developed more prominently and sharply at higher We_{cf}. Following the previous argument, this dependence can be connected to the more rapid shedding of KH-corrugations at higher We_{cf} (as shown in Figure 5.6). We have previously hypothesized that this is because the smaller droplets found at higher We_{cf} are more susceptible to rapid shedding. In addition, Figure 5.15 shows that the bifurcated-wakes' penetrations were weakly inversely-proportional to We_{cf}. This dependence is likely also because the smaller bifurcated-wake droplets at higher We_{cf} penetrated lower due to their lower penetration inertia per drag area.

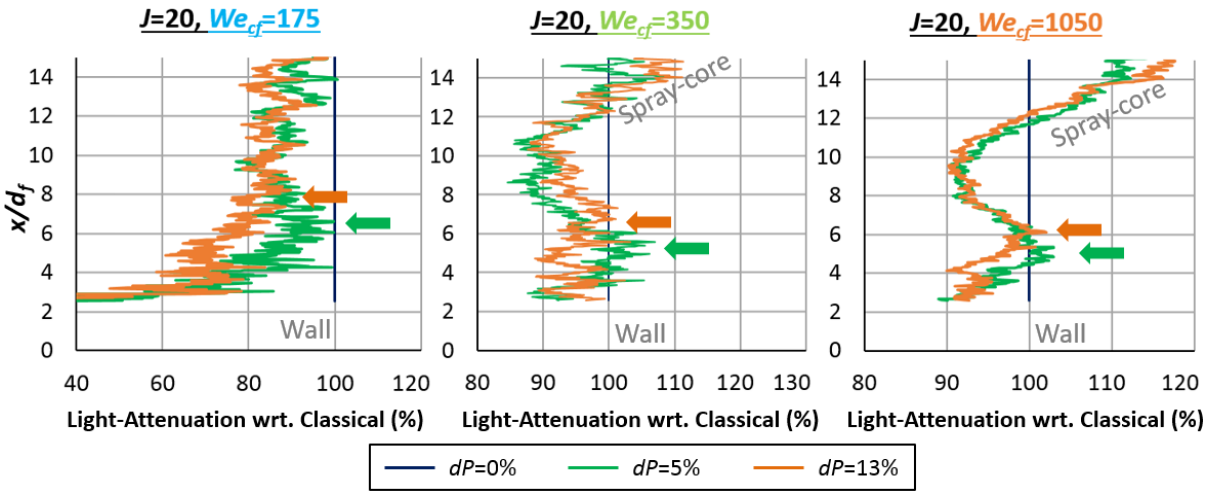

Figure 5.15 – Normalized and zoomed-in light-attenuation profiles at z/d_f=15, showing the dependence of the bifurcated-wakes on We_{cf}.

In summary, the bifurcated-wake is a structure formed by the rapid shedding of KH-corrugations from the initial jet when the protective air-sheath is stripped away by the crossflow. While the bifurcated-wake is more prominent at higher J, We_{cf} and dP (within the AA-JICF regime), its penetration into the crossflow is proportional to dP and weakly inversely-proportional to We_{cf}. We cannot ascertain at this point whether our bifurcated-wake is related to Sinha et al. (2015)'s reported spray-bifurcation phenomenon (see Figure 2.15). Although the bifurcated-wake is a relatively minor structure relative to the overall spray pattern, it is an

important manifestation of the interaction between fuel and assisting air, and thus merits attention in our understanding of AA-JICF.

5.5 Summary

Using the measured data, we have provided a qualitative description of the spray characteristics in the AA-JICF regime, as well as the most likely underlying mechanisms, which are summarized in Figures 5.16 and 5.17. The top-left schematic in Figure 5.16 shows that without air-assist, a wall-detached JICF at J=20-40 consists of an intact jet that penetrates far into the crossflow before disintegrating into a spray-core consisting of large droplet-clusters. In addition, due to the high We_{cf}, small droplets are continuously sheared from the surface of the jet immediately downstream of the injection orifice. These droplets are readily entrained into the wake region between the wall and the spray-core. The right schematic in Figure 5.16 shows the air-assist forming a protective "air-sheath" around the initial jet that inhibits the production of small droplets by crossflow-to-fuel surface-shearing. The air-sheath does not atomize or mix with the intact jet. Instead, it stays intact for a short distance before being entrained by the crossflow, whereupon the liquid jet becomes exposed to the crossflow and surface shear-atomization by crossflow commences. The introduction of air-assist does not significantly affect the spray-core's penetration and dispersion because there is no significant momentum-exchange between the intact fuel jet and air, and because the air-assist does not significantly affect the high-J jet's RT-wave amplitude.

At higher dP close to the upper limit of the AA-JICF regime, the increased velocity of the air induces its own KH shear-waves *around the entire* initial jet's surface (in contrast to crossflow-related KH-waves that grow on the jet's *lateral* sides), which produce fine-scale "corrugated" structures and sheared droplets. Some of these corrugations/droplets are energetically ejected by the assisting air into the crossflow and, thus, repopulates the wake region; however, the majority of them remains within a spatially growing fuel-air shear-layer

surrounding the jet, as shown in Figure 5.17. When the air-sheath is stripped away, the corrugations in the shear-layer become exposed to the crossflow that strips them off the fuel jet surface rapidly. This forms a branch of locally dense droplets in the wake region that we referred to as the "bifurcated-wake". Downstream of this point, the air-sheath is no longer present and Classical-JICF processes govern the fuel jet's evolution. Notably, since the strength of fuel-air shearing is proportional to We_{cf}, the development of the bifurcated-wake is likely a high-pressure phenomenon that is only encountered at near jet-engine operating conditions and not near-atmospheric experiments.

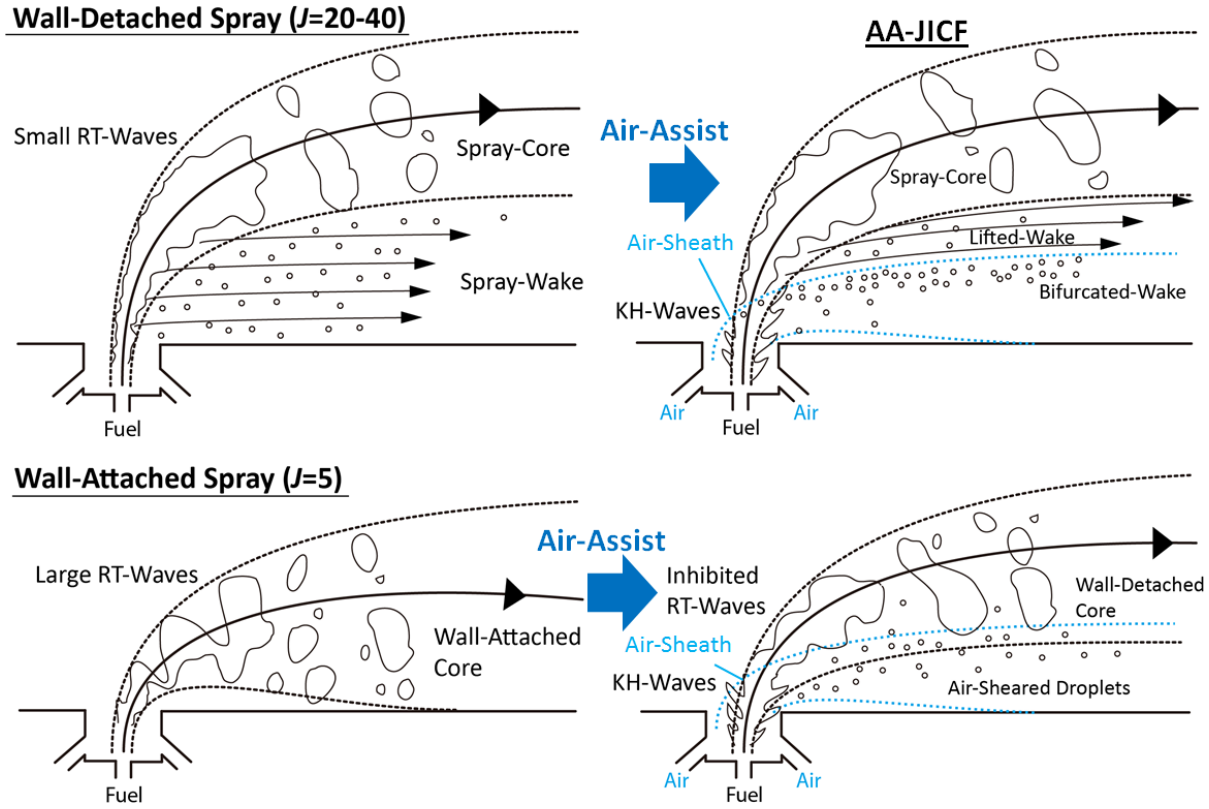

Figure 5.16 – Illustrations of the dominant spray-formation processes in the AA-JICF regime.

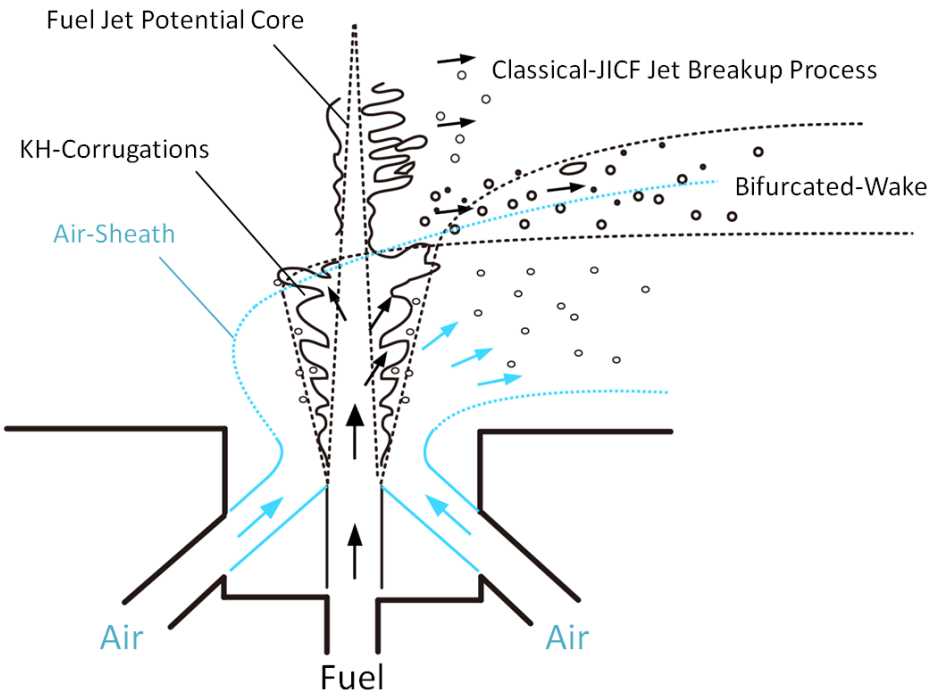

Figure 5.17 – Zoomed-in illustration of the fluid interactions around the initial-jet region.

Figure 5.16 also shows that a *J*=5 jet *without* air-assist develops very large RT-waves amplitudes, setting the jet into a sinuous motion that disperses fuel droplets very widely in the penetration direction. Additionally, since the *J*=5 jet also has very low penetration due to its low momentum-flux ratio, the wide dispersion and low penetration of the fuel cause the spray-core to become attached to the test-channel wall. When air-assist is applied, the air-sheath protects the jet from interacting with the crossflow, thus inhibiting the RT-wave development and surface shearing. Consequently, spray dispersion is significantly reduced and the spray-core's penetration is enhanced. These effects detach the spray from the wall and reduce near-wall fuel concentrations. As with the *J*=20-40 cases, the air-assist starts to shear-atomize the fuel jet as its velocity increases at higher *dP*. However, a distinct bifurcated-wake is not observed at *J*=5, likely because the corrugations and droplets that are shedded are not distinguishable from the closely located spray-core's droplets.

In summary, the *J*=5 Classical-JICF places large amounts of fuel near the wall, which can cause flashback and wall-coking in jet-engine fuel-air mixers. The application of air-assist in the general range of *dP*=3-5% will reduce the near-wall fuel concentrations, thus likely

reducing the risks of flashback and coking. The application of dP=3-5% of air-assist will have less pronounced effects on J=20-40 JICF. On the other hand, an air-assist level of dP=13% will increase near-wall fuel concentrations and is likely detrimental to fuel-air mixer operations.

CHAPTER 6. DISCUSSION:

THE AIRBLAST-JICF REGIME

This chapter discusses results and analyses from the Airblast-JICF regime, which generally ranges from dP ~ 25 to 75% as shown in Figures. 4.9-4.12 (the exact dP value being dependent on J and We_{cf}). Following the outline of Chapter 5, we begin by observing the airblast's effects on the initial fuel jets, followed by a discussion of the mechanisms responsible for those effects. We then analyze the airblast's effects on the global spray characteristics, and end the chapter by tying the observed characteristics and mechanisms together into a cohesive conceptual description of AB-JICF.

6.1 Two-Zone Atomization of the Initial Jet

The discussion begins with observations of the airblast's effects on the initial jets, as shown in Figure 6.1, which contains instantaneous images of J=5 jets at dP=13-75% and We_{cf}=350. The images show that when dP varied from 13% (AA-JICF) to 25% (AB-JICF), the jet's structures did not change significantly. All the injected fuel entered into the crossflow from the spraywell's center, barely touching its periphery (i.e., the dotted lines). The fuel subsequently broke up into large clusters of liquid, which remained narrowly dispersed throughout the domain of the images (i.e., up to x/d_f=8). In contrast, when dP was increased to 50%, dense populations of droplets that appear like fog (i.e., sub-pixel sized droplets) are present across the *entire* spraywell opening, albeit being more concentrated in the center. These droplets caused the initial jet/spray to appear more widely dispersed. Larger cluster of liquid that are opaque to the backlight can be found superposed within the "fog" of droplets (see regions denoted by orange arrows). These clusters likely consisted of fuel from the broken up jet and KH-corrugations, similar to the clusters in dP=13-25%. However, while the clusters survived for >8d_f in distance at dP=13%, they only survived for an average of ~5d_f before being

finely-atomized at *dP*=50%, whereupon the spray plume became translucent to the backlight. The differences in spray structures between *dP*=13 and 50% demonstrate the airblast's strong atomizing effect in the AB-JICF regime. Finally, at *dP*=75%, the fuel became even more uniformly dispersed across the entire spraywell area and the liquid clusters were no longer identifiable.

Notably, as discussed in Section 3.3, the contact point between the 45^o blasting air and the fuel jet was nearly flushed with the test-channel wall (i.e., x/d_f=0) and not within the spraywell. Thus, the presence of droplets across the entire spraywell area at x/d_f=0, as seen in Figure 6.1, suggests the occurrence of nearly instantaneous atomization of the jet and dispersion of droplets, which can only be accomplished by the prompt-atomization mechanism described in Section 2.3. This new mechanism is distinct from the slower KH-wave or RT-wave breakup mechanisms observed in the AA-JICF regime so far.

Next, we examine the plot of initial jets profile thickness (t_ω) in Figure 6.2 to determine the dependence of t_ω upon *dP*. The plot shows that increasing *dP* from 13 to 25% produced, on average, a slight increase in t_ω. Also, the local t_ω maximum found around x/d_f=2-3 at *dP*=13% disappeared at *dP*=25%. Since the maximum is formed by the rapid shedding of KH-corrugations, its disappearance suggests the rapid shedding process did not occur at *dP*=25%. When *dP* was increased from 25% to 50%, the t_ω values in the x/d_f=0-5 region continued to increase with *dP*, but t_ω in the x/d_f>5 region decreased significantly with *dP*. Raising *dP* up to 75% did not produce a marked change relative to *dP*=50%. Thus, the figure shows a significant shift in the t_ω curves between *dP*=13-25 and 50-75%, indicating that the two *dP* ranges may be governed by different sets of spray-formation mechanisms. Notably, based on Figure 6.1, t_ω at *dP*≥50% likely does not measure the amplitude of RT-waves or KH-corrugations, but rather the width of space where prompt-atomized droplets can be found on the windward side.

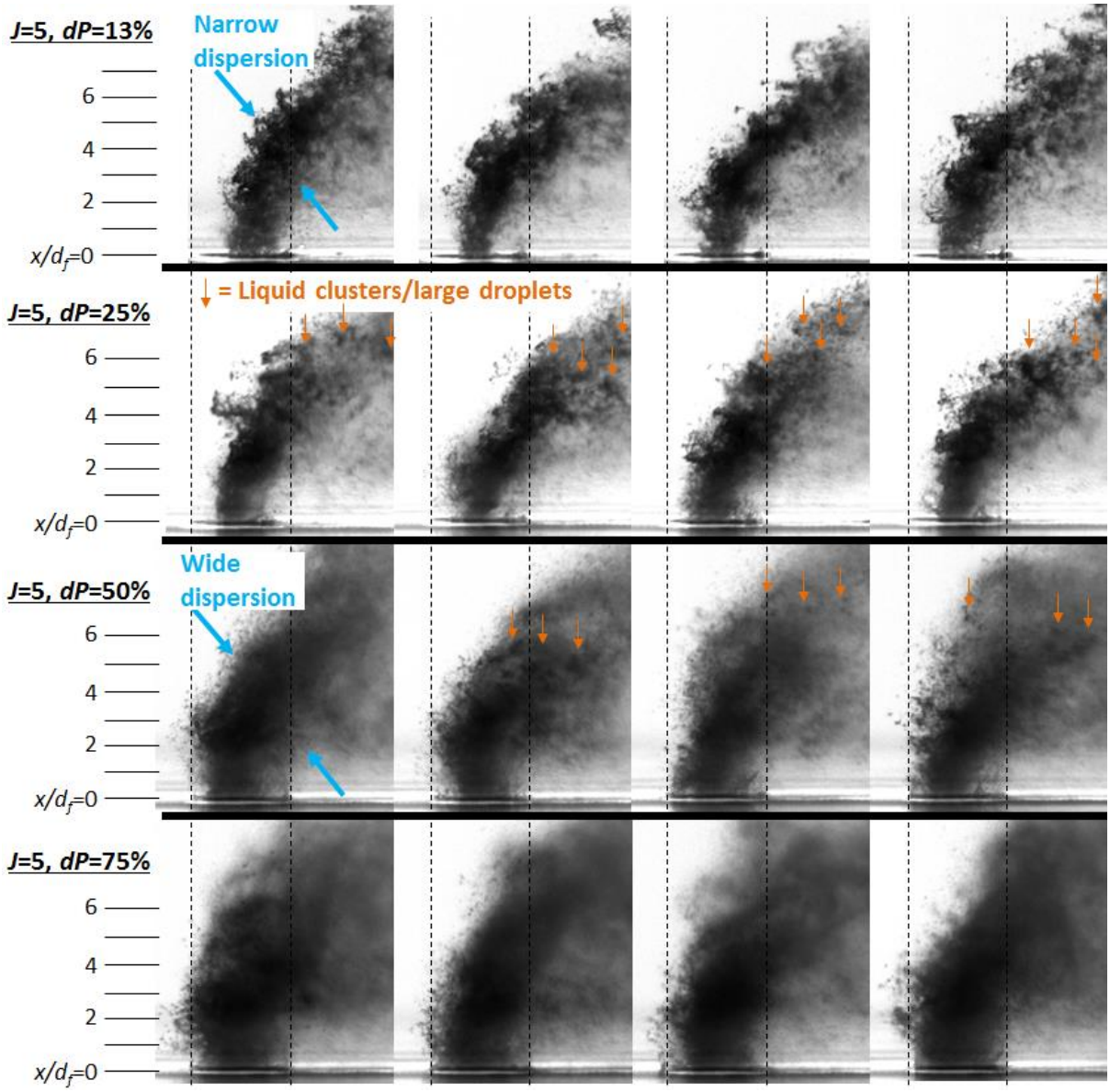

Figure 6.1 – Instantaneous images of the initial-jets at J=5, We_{cf}=350, for dP=13, 25, 50 and 75%.

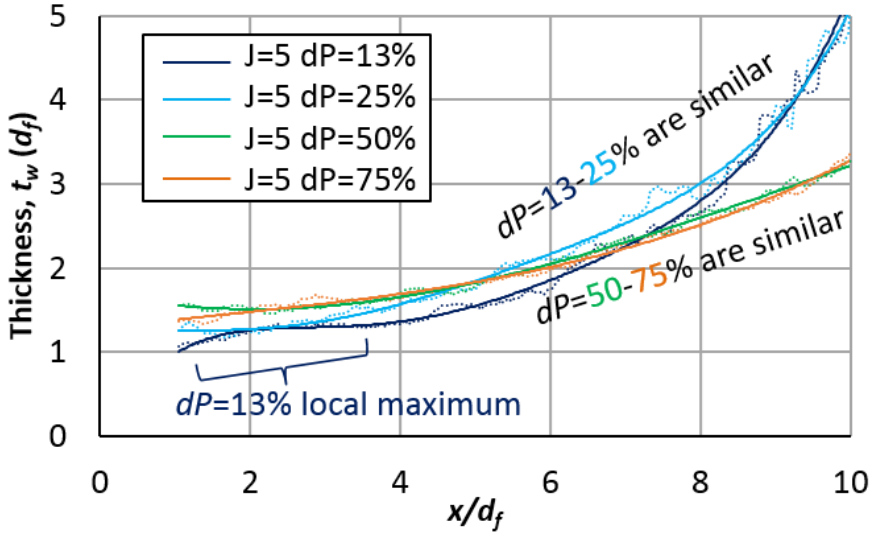

Figure 6.2 – Jet profile thicknesses as a function of dP for J=5, We_{cf}=350.

Next, to examine the airblast's effects at the high J value of 40, we refer to the instantaneous images in Figure 6.3. They show that the J=40 jets remained relatively intact and resisted the disruptive effects of the airblast more than the J=5 jets. For example, the injected fuel was not significantly prompt-atomized and dispersed across the spraywell area until dP=75% at J=40, whereas the same process occurred at dP=50% for J=5. Furthermore, Figure 6.3 shows that although some droplets had dispersed to the edges of the spraywell at dP=75%, their concentrations were significantly lower than in the case of J=5 dP=75%. Thus, Figure 6.3 suggests that the fuel jet is more resistant to prompt-atomization at higher J. This indicates that the degree of prompt-atomization decreases when the fuel-to-airblast momentum-flux ratio (which is proportional to J for a fixed dP) increases. This behavior is in qualitative agreement with the dependence of prompt-atomization upon fuel-air momentum-flux ratio for TF-jets in *quiescent* gas, which we reviewed in Section 2.3.

Figure 6.3 also shows that the fuel jet often developed a bifurcation on the wake-side at dP=25-50% (see regions circled in red). The development of the bifurcation was also consistently accompanied by the vanishing of the smaller-sized droplets and corrugations on the windward edge (boxed in blue) at approximately the same location. These phenomena are due to the rapid KH-corrugations shedding process described in Chapter 5, where "corrugation structures" created by fuel-air shearing around the jet are rapidly shed when the protective air-sheath is stripped away, thereby creating a locally dense branch of droplets in the wake. Notably, the rapid shedding and bifurcation were absent at J=40 dP=75%, suggesting that the process only occurs in a limited range of dP between the AA-JICF and AB-JICF regimes.

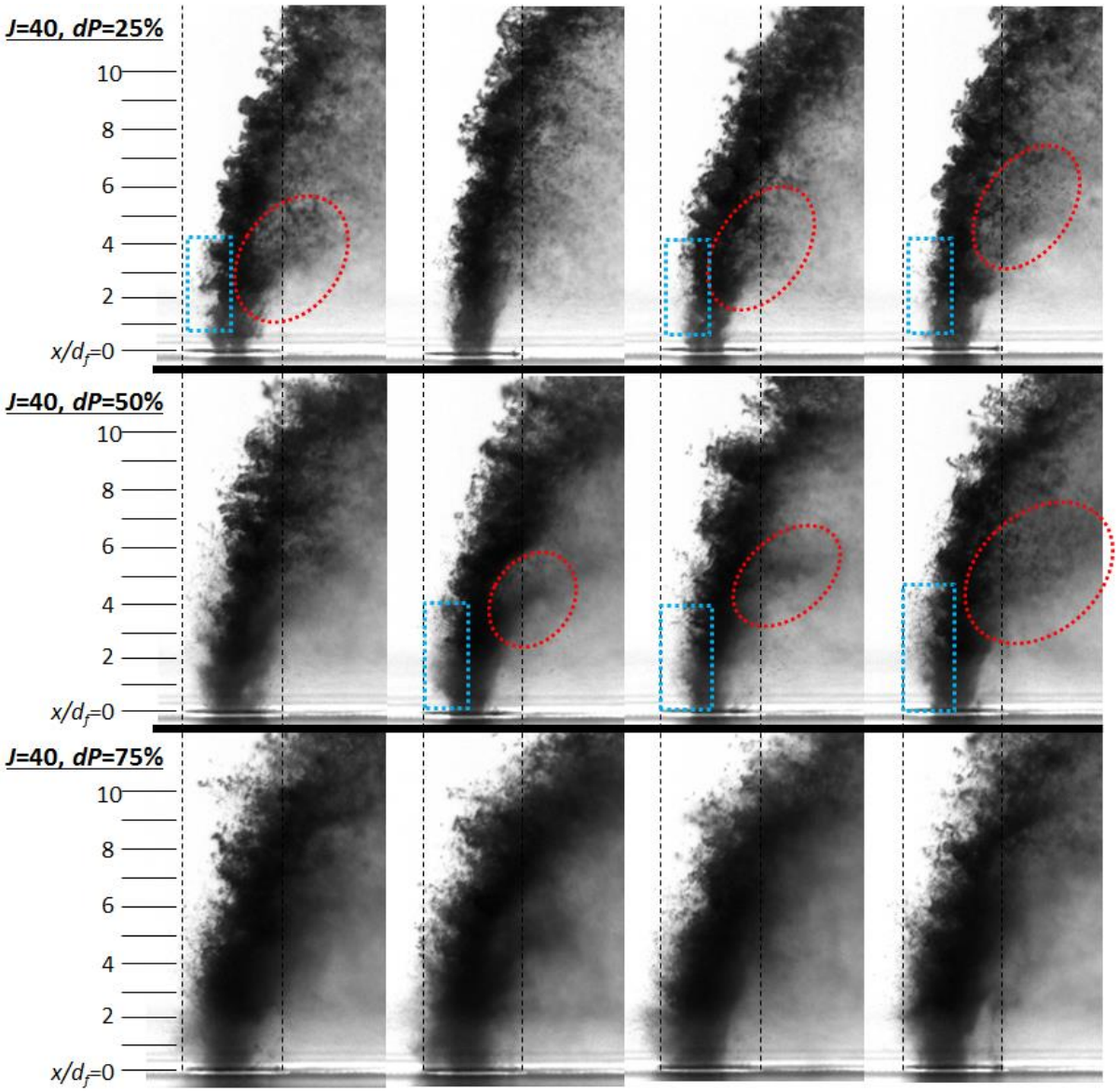

Figure 6.3 – Instantaneous images of the initial-jets for *dP*=25, 50 and 75% (*J*=40, We_{cf}=350). *Box*: Presence of small droplets on the windward edge; *circle*: dense clusters of droplets being shed into the crossflow.

Figure 6.4 shows the dependence of the *J*=40 jets' profile thickness (t_ω) on *dP* for the *dP*=13-75% range, at a We_{cf} of 350. At *dP*=13%, the t_ω curve exhibits a local maximum at x/d_f ≈ 2.5, which was previously proposed as being due to the rapid KH-corrugations shedding process. Downstream of the shedding, t_ω values increased with distance due to growing RT-waves because this portion of the jet was exposed to the crossflow (since the protective air-sheath had been stripped away). As *dP* was increased to 25%, the magnitude of the local t_ω maximum also increased, indicating increasing amplitudes of KH-corrugations due to

intensifying fuel-air shearing. At the same time, the location of the maximum shifted from x/d_f ≈ 2.5 to 3.5, suggesting that the location of rapid KH-corrugations shedding was pushed downstream. When *dP* increased to 50%, the t_ω maximum continued to shift downstream, but its magnitude had become less pronounced. At *dP*=75%, no local t_ω maximum was observed. Notably, Figure 6.4 shows that downstream of the t_ω maxima, the jets' t_ω values also generally increased with *dP*. This suggests that not all of the KH-corrugations and disturbances generated by the airblast were rapidly shed into the crossflow when the air-sheaths were stripped away; instead, a significant portion of the disturbances may continue to travel with the jet, thus increasing the jet's downstream t_ω values.

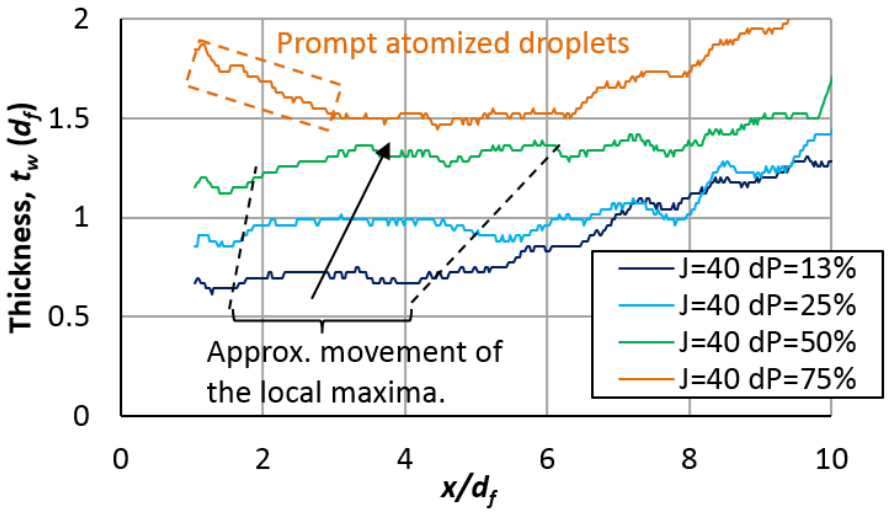

Figure 6.4 – Jet profile thicknesses as a function of *dP* for *J*=40, We_{cf}=350. *Solid lines: raw data. Curve-fits have not been added due to the clear trends in t_ω at this *J* and *dP* range.

Finally, Figure 6.4 shows that t_ω immediately next to the wall (i.e., see dotted box at x/d_f=1-3) is significantly increased when *dP* was raised to 75%. This increase coincides with the onset of prompt-atomization (see Figure 6.3) that dispersed droplets to the periphery of the spraywell. Thus, the increased t_ω next to the wall at *dP*=75% is likely attributable to the presence of prompt-atomized droplets around the initial jet (i.e., the t_ω measurement algorithm considers the widely-dispersed prompt-atomized droplets as part of the profile thickness, t_ω). Interestingly, the portion of the t_ω curve where prompt-atomization dominated (see dotted box)

decreases in magnitude further away from the wall, reaching a minimum at $x/d_f \approx 4.5$. Downstream of the minimum, t_ω grew with distance once again, presumably due to the growing RT-waves. We hypothesize that this inverse relation between the prompt-atomization's t_ω and x/d_f is because outside of the fuel-air impingement zone (whose dimension was likely of the order of the air-nozzles' width) the prompt-atomization process likely ceased and no new "prompt droplets" were produced. Subsequently, the existing "prompt droplets" will be progressively stripped away as they penetrate deeper into the crossflow, causing the amount of prompt droplets around the jet and, hence, t_ω to decrease. This mechanism is similar to the rapid KH-corrugations shedding mechanism that we proposed in order to explain the t_ω maxima at dP=13-50%.

To determine the effects of We_{cf} on the jet disturbances, Figure 6.5 plots the t_ω curves of J=20 jets in the We_{cf} range of 175 to 1050. It shows that the t_ω maxima associated with rapid KH-corrugations shedding (see dotted circles) can be found at We_{cf}=350 and 1050, although in the We_{cf}=1050 case, they were located very close to the wall, often partially below x/d_f=1, where t_ω cannot be measured due to the presence of window stains. On the other hand, such maxima were not present at We_{cf}=175, likely because the larger droplets and corrugation structures found at lower We_{cf} were more resistant to rapid stripping by the crossflow, thus preventing the formation of a clear t_ω maximum (as discussed in Chapter 5). Nonetheless, when they were present, the t_ω maxima penetrated further into the crossflow with increasing dP, until they eventually disappeared at dP~75%, which is similar to trends observed in the J=40 AB-JICF case in Figure 6.4.

On the other hand, the t_ω maxima created by prompt-atomization can be found at all We_{cf}, as indicated by arrows in Figure 6.4. However, they seem to begin developing at lower dP when We_{cf} was higher (i.e., We_{cf}=175 did not show prompt-atomization until dP=75%), thus suggesting a direct proportionality between the intensity of prompt-atomization and We_{cf}. This

proportionality can be further demonstrated in the instantaneous spray images in Figure 6.6, which show significantly more droplets exiting from the edges of the spraywell (i.e., a larger degree of prompt-atomization) at higher We_{cf} when J and dP were both fixed.

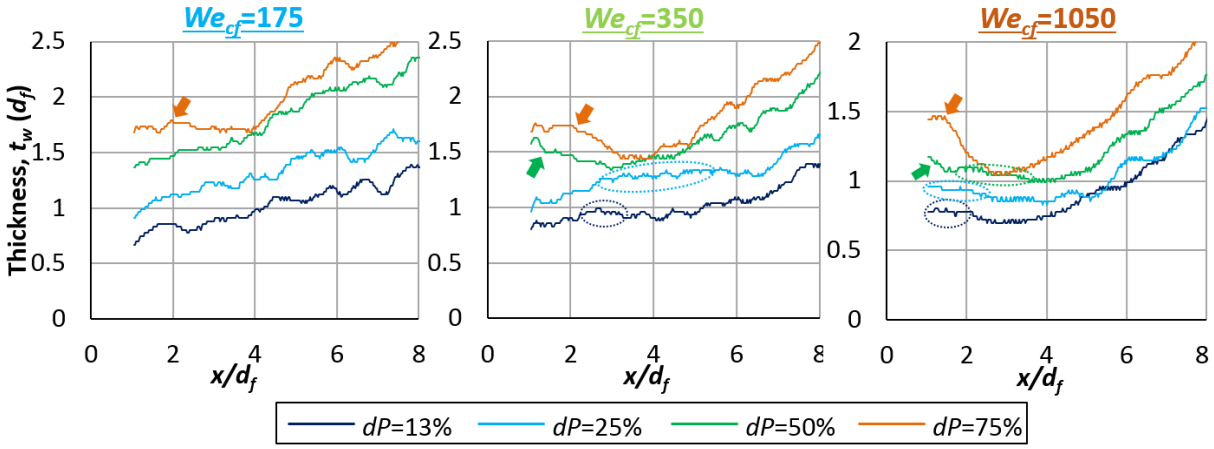

Figure 6.5 – Jet profile thicknesses as a function of *dP* for *J*=20 jets at We_{cf}=175, 350 and 1050. Arrows: local maxima in t_ω due to prompt-atomization. Circles: local maxima in t_ω due to KH-corrugations.

Furthermore, Figure 6.5 also shows that as We_{cf} increased, the t_ω created by prompt-atomization exhibited sharper "peaks", which were subsequently located closer to the test-channel wall. On the other hand, increasing dP caused these "peaks" to be larger and moved away from the test-channel wall. These trends suggest that more prompt-atomized droplets were produced at higher dP, and their penetration into the crossflow was directly proportional to dP and inversely proportional to We_{cf}. To explain the dependence on dP, we first reason that because the prompt-atomized droplets were very small (i.e., they were generally unresolvable on the images), they can exchange momentum with the high-velocity blasting air very rapidly. Hence, the airblast increased the droplets' penetration velocity by a magnitude proportional to U_{air} (which is $\propto dP^{0.5}$), resulting in higher penetrations at higher dP. On the other hand, the droplets penetration's inverse proportionality to We_{cf} can be due to two reasons: (i) since U_{air} is independent of We_{cf} for a given percentage dP, the prompt-atomized droplets may be accelerated by the airblast to the same velocity regardless of We_{cf}, which would mean their penetration momentum-flux ($\rho_f U_{droplet}^2 = \text{const.}$) decreases relative to the crossflow

momentum-flux ($\rho_{cf}U_{cf} \propto We_{cf}$ for a fixed U_{cf}) when We_{cf} increases, leading to lower penetrations, (ii) as previously discussed and evident from Figure 6.6, the spray's droplets and corrugation structures were generally smaller at higher We_{cf}, suggesting that the prompt-atomized droplets were also smaller at higher We_{cf}. This means they had lower inertia per drag area at higher We_{cf} and, consequently, were more readily entrained into the crossflow, resulting in lower penetrations.

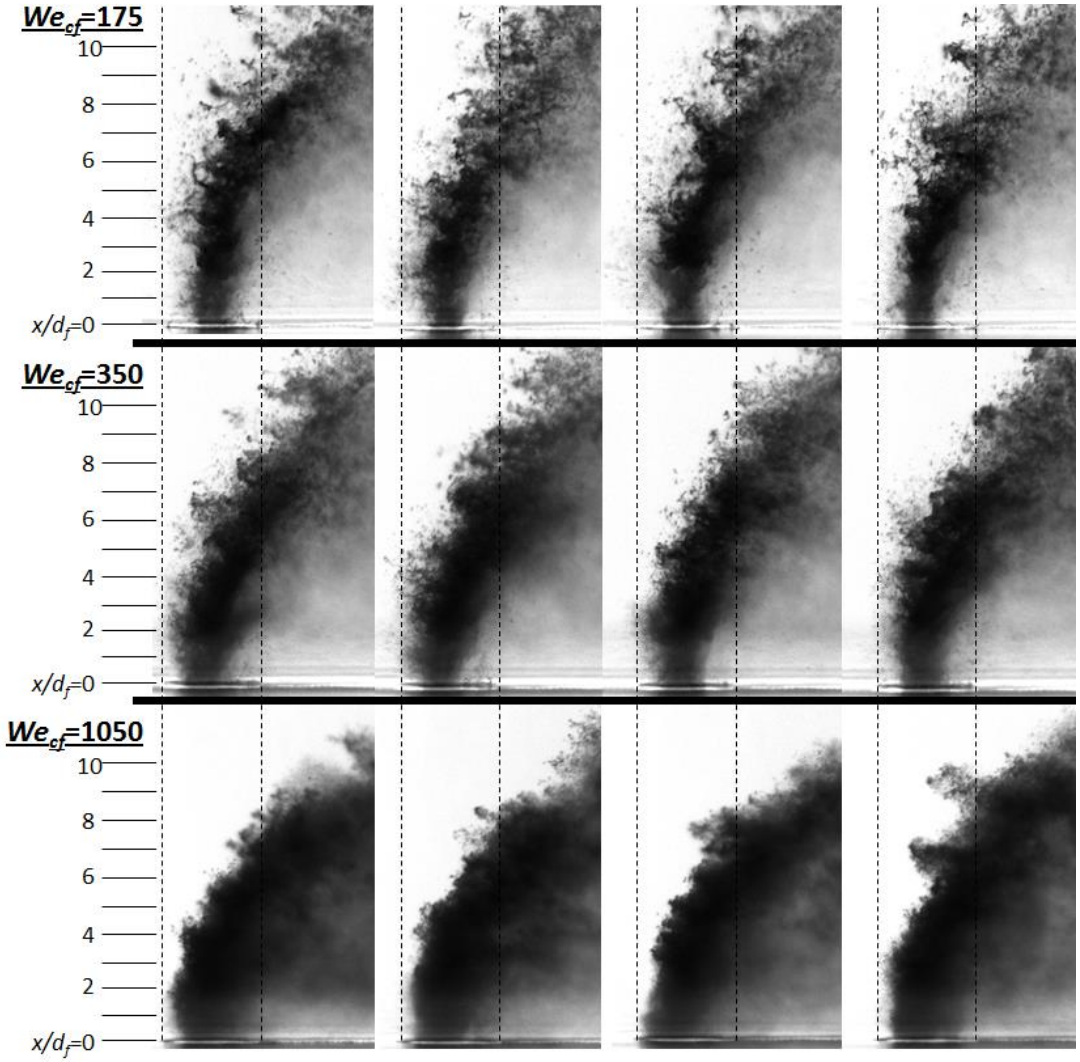

Figure 6.6 – Instantaneous images of initial jets at different We_{cf} for a fixed *J* of 20 and *dP* of 50%.

Next, we present a scaling analysis that was performed in an effort to better understand the dependence of prompt-atomization on *J*, *dP* and We_{cf}, as well as to elucidate underlying

physics that may not be immediately apparent from the plots and images. In this analysis, we first assumed that the AB-JICF's spray-formation process is similar to a TF-jet in *quiescent* air around the region of fuel-air impingement. This is because the crossflow's local velocity is low in the boundary-layer where the injection orifice was located (i.e., $U_{cf,boundary\text{-}layer}$<<70*m/s*), especially relative to the high *dP* airblast's velocity (U_{air}>100*m/s*). Thus, we followed the approach of Lasheras & Hopfinger (2000)'s study of TF-jets and postulate that the driving force behind prompt-atomization is provided by the momentum of the impinging airblast. In this case, the mass flow-rate of the prompt-atomized fuel ($\dot{m}_{prompt}$) can be related to the airblast's momentum-flux as follows:

$$\dot{m}_{prompt}U_f = C\dot{m}_{air}U_{air} = CA_{air}\rho_{air}U_{air}^2 \tag{1}$$

where C is a constant that takes the fuel-air impingement angle into account. Next, dividing both sides by the total fuel mass flow-rate ($\dot{m}_f = A_f\rho_f U_f$) and rearranging, we obtain:

$$\frac{\dot{m}_{prompt}}{\dot{m}_f} = C\frac{A_{air}}{A_f}\frac{\rho_{air}U_{air}^2}{\rho_f U_f^2} \equiv C_0\frac{\rho_{air}U_{air}^2}{\rho_f U_f^2} \propto \left(dP, J^{-1}\right) \tag{2}$$

Hence, the fraction of the jet being prompt-atomized ($\dot{m}_{prompt}/\dot{m}_f$) is related to the air-fuel momentum-flux ratio, which is proportional to *dP* and inversely proportional to *J* for a fixed We_{cf}. These proportionalities agree qualitatively with our experimental results. On the other hand, when We_{cf} changes while *dP* and *J* are fixed (as was the case with Figures. 6.5 and 6.6), the following proportionalities are applicable: $\rho_{air} \propto We_{air} \propto We_{cf}$ and $U_f \propto We_{cf}^{0.5}$, while U_{air} and ρ_f are constant. Substituting in these proportionalities to Equation (2) yields:

$$\frac{\dot{m}_{prompt}}{\dot{m}_f} = C_0\frac{We_{cf}U_{air}^2}{\rho_f We_{cf}} \propto \frac{We_{cf}}{We_{cf}} = 1 \tag{3}$$

In contrast to the trends exhibited by the measured data, Equation (3) suggests no first-order dependence of $\dot{m}_{prompt}/\dot{m}_f$ on We_{cf}. In an attempt to resolve this discrepancy, we introduce

surface-tension into Equation (2), to consider the possibility that surface-tension energy may be significant relative to fluid kinetic energies because the prompt-atomized droplets are very small (i.e., large surface areas per mass). The following new relation is obtained:

$$\frac{\dot{m}_{prompt}}{\dot{m}_f} = \frac{\rho_{air} U_{air}^2}{C_1 \rho_f U_f^2 + B\sigma_f/\delta} \tag{4}$$

Where C_1 and B are constants, σ_f is surface-tension and δ is a characteristic length-scale that can be equated to the prompt-atomized droplets' diameter (d_{drop}). The form of Equation (4) is based on the works of Lasheras & Hopfinger (2000). To solve this equation the dependence of d_{drop} on We_{cf} has to be known. Unfortunately, we can only *estimate* this dependence since it is generally unclear how d_{drop} varies with We_{cf} during the *partial* prompt-atomization of a jet (i.e., a literature knowledge-gap identified in Section 2.3). In one estimation, we assumed that the *SMD*-vs-We_{cf} relationship for Classical-JICF (see Figure 2.6) is approximately applicable to prompt-atomization, since this relationship essentially describes the general competition between disruptive aerodynamic forces and cohesive surface tension forces on a droplet. Using this relationship, $d_{drop} \propto We_{cf}^{-D}$, where $D < 1$. In another estimation, we can try to employ Lefebvre (1992 *JEGTP*)'s correlation of *SMD* for a *fully* prompt-atomized jet (i.e., $\dot{m}_{prompt}/\dot{m}_f = 1$). His correlation assumes the air's kinetic energy is converted into the surface-tension energy of the atomized droplets and, hence, higher *dP* produces smaller droplets (*instead* of higher $\dot{m}_{prompt}/\dot{m}_f$). The following is Lefebvre's correlation:

$$SMD = \frac{3}{\left[\frac{2}{d_f} + \frac{C^* \rho_f U_{air}^2}{4\sigma_f (1 + \frac{\dot{m}_f}{\dot{m}_{air}})}\right]} \tag{5}$$

where C^* is the energy conversion constant. In this expression, only the mass flow-rates are dependent upon crossflow Weber number for fixed *J* and *dP*, where $\dot{m}_f = \rho_f A_f U_f \propto We_{cf}^{0.5}$

and $\dot{m}_{air} = \rho_{air} A_{air} U_{air} \propto We_{cf}$. Substituting in these proportionalities we obtain the following:

$$SMD = \frac{3}{\left[\frac{2}{d_f} + \frac{C^* \rho_f U_{air}^2}{4\sigma_f (1 + C^{**} We_{cf}^{-0.5})}\right]} \tag{6}$$

where C^{**} is a new constant. From this new expression, we see that *SMD* decreases with We_{cf}, but with less than a first order proportionality. Furthermore, as We_{cf} becomes large, the bottommost denominator approaches the constant $4\sigma_f$ and *SMD* is no longer sensitive to We_{cf}. It is possible that Equation (6) also roughly applies to our partially prompt-atomized jet; i.e., droplets size decreases *while* $\dot{m}_{prompt}/\dot{m}_f$ increases as *dP* increases.

From the *SMD* scaling-laws described above, we can hypothesize that d_{drop} should be inversely but not strongly proportional to We_{cf}, in which case Equation (4) may take on the following form:

$$\frac{\dot{m}_{prompt}}{\dot{m}_f} \propto \frac{We_{cf}}{C_2 We_{cf} + B_1 We_{cf}^D} = \frac{1}{C_2 + B_1 We_{cf}^{D-1}} \tag{7}$$

where C_2 and B_1 are constants of proportionality, and $D - 1 < 0$. Hence, the fraction of jet being prompt-atomized should increase weakly with We_{cf}. Though only an approximation, the introduction of surface tension to arrive at Equation (7) allows the relationship between $\dot{m}_{prompt}/\dot{m}_f$ and We_{cf} to become consistent with experimental observations. Consequently, the analysis suggests that surface-tension is likely an important force to consider in the prompt-atomization process of AB-JICF; i.e., the AB-JICF will be more prone to prompt-atomization at higher engine operating pressure/temperature.

Next, we perform another scaling analysis in an effort to understand the evolution of the KH and air-induced RT-waves in the *dP* range of 13-25% (i.e., between the AA-JICF and AB-JICF regimes, and *prior* to significant prompt-atomization, where KH and RT-waves were likely still the dominant disturbances). In Chapter 4 we proved that RT-waves have a constant

temporal growth-rate and thus their amplitudes (t_ω) can be scaled by convection time (e.g., see Figure 4.6). Now we will examine how the t_ω curves at *dP*=13-25% scale. As discussed, these curves can generally be divided into an initial region where t_ω measures KH-corrugations and a downstream region where t_ω measures RT-waves, separated in between by the local t_ω maximum due to rapid KH-corrugations shedding. The left of Figure 6.7 shows that when the logarithm of t_ω is plotted versus the convection time (i.e., spatial coordinate scaled by the fuel injection velocity, in accordance with the RT-wave scaling law), the downstream regions of the plotted curves become relatively linear and closely-collapsed. This supports our proposition that the downstream disturbances were dominated by RT-waves in this *dP* range; i.e., after the air-sheath was stripped away, the remaining fuel jet did not interact with the airblast/air-assist anymore and developed Classical-JICF RT-waves instability, which may then cause the jet to undergo the Classical-JICF jet breakup by jet-pinching. Notably, the downstream portion of the t_ω curves in the left of Figure 6.7 are closely but not perfectly collapsed because (as previously noted) the air-sheath does have some influence on the RT-waves' preferred wavelengths and amplitudes, which is not captured by the convection time scaling.

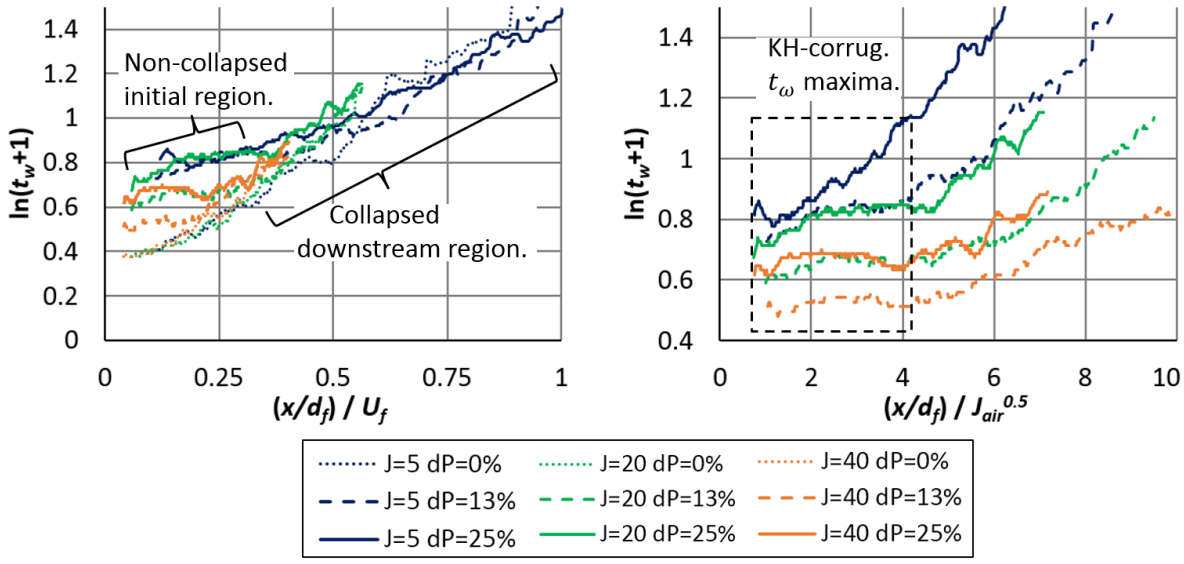

Figure 6.7 – Attempts at correlating the t_ω of We_{cf}=350 TF-JICF based on RT-wave scaling (*left*) and air-sheath scaling (*right*).

By contrast, the left of Figure 6.7 shows that the initial region of t_ω where KH-corrugations dominated cannot be scaled by convection time, evident from the curves' significant separation. To scale the KH-corrugations, we make use of the hypothesis from Chapter 5 that described the KH-corrugations as being rapidly stripped from the jet and shed into the crossflow when the protective air-sheath is stripped away. This hypothesis suggests that the region where KH-corrugations develop around the fuel jet should be proportional to the air-sheath in size. Specifically, the location of the maximum KH-corrugation amplitude (i.e., local t_ω maximum) should coincide with the air-sheath's outer-edge penetration. Thus, to scale the t_ω maxima, we need to obtain a scaling law for the air-sheath's penetration.

As a first-order approximation, we reason that because the fuel jet was likely thin relative to the air-sheath (i.e., large A_{air}/A_f nozzle area ratio), the injected air may behave like a classical *gaseous*-JICF, whose penetration are known to scale with the air-to-crossflow momentum-flux ratio: $J_{air}^{0.5}$. The applicability of $J_{air}^{0.5}$ as a scaling parameter for the air-sheath/t_ω maxima was tested by normalizing the spatial coordinates of the t_ω curves by their corresponding $J_{air}^{0.5}$ values, as shown on the right of Figure 6.7. With this new scaling, the local t_ω maxima are now well-aligned along the *x* direction (see dotted box), which suggests that the $J_{air}^{0.5}$ parameter is a good scaling parameter and that the location of rapid KH-corrugations shedding is indeed connected to the air-sheath's outer-edge penetration.

Figure 6.8 below shows that the $J_{air}^{0.5}$-scaling for the t_ω maxima's locations does not hold across different We_{cf}, because higher We_{cf} resulted in earlier shedding at a given *dP* (i.e., given J_{air}). The earlier shedding was explained in Chapter 5 as being due to the presence of smaller droplets at higher We_{cf}, which were more readily entrained by the crossflow. An additional We_{cf}-related parameter would be required to correlate the shedding locations across different We_{cf}, because the J_{air} parameter does not capture the We_{cf}-dependence of droplet sizes. The development of such a correlation for the KH-corrugations remains a topic for future work.

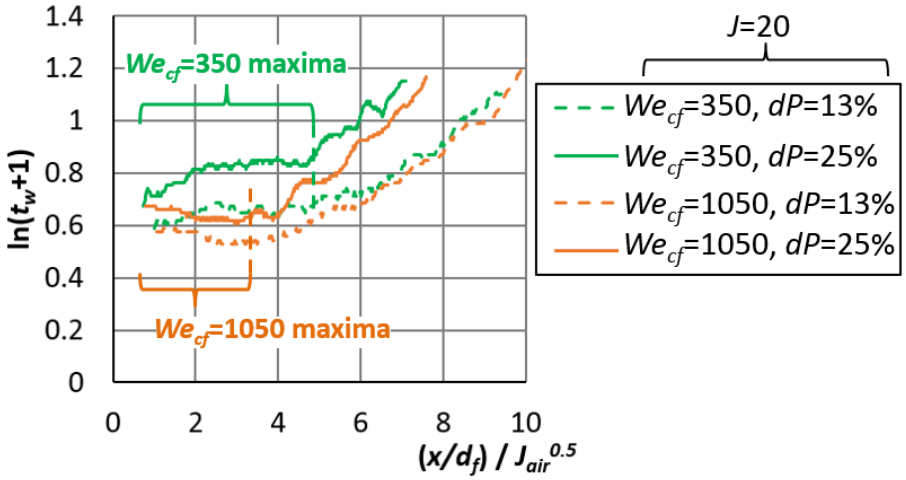

Figure 6.8 – Plot of J_{air}-scaled t_ω, showing the locations of KH-corrugations shedding as a function of We_{cf}.

6.2 The Evolution of the Bifurcated-Wake and the Wall-Plume

In this section, we discuss the evolution of the bifurcated-wake structure as *dP* varied across the AB-JICF regime. In addition, we identify the onset of a new global spray structure referred to as the "wall-plume", and then connect its development to the near-field fluid interactions described in the previous section. Figure 6.9 below shows the instantaneous and average images of J=40 We_{cf}=350 AB-JICF, while Figure 6.10 shows their corresponding light-attenuation profiles at the location of z/d_f=15. The bifurcated-wakes can be observed highlighted by black arrows in these images and plot. They suggest the bifurcated-wake was a temporary structure that began developing at *dP*≈13%, becoming most prominent at *dP*=25-50% and disappearing at *dP*≥75%. In the same *dP* range, the entire wake region above and below the bifurcated-wakes had higher *N* (i.e., repopulated with higher droplets concentration) as *dP* increased.

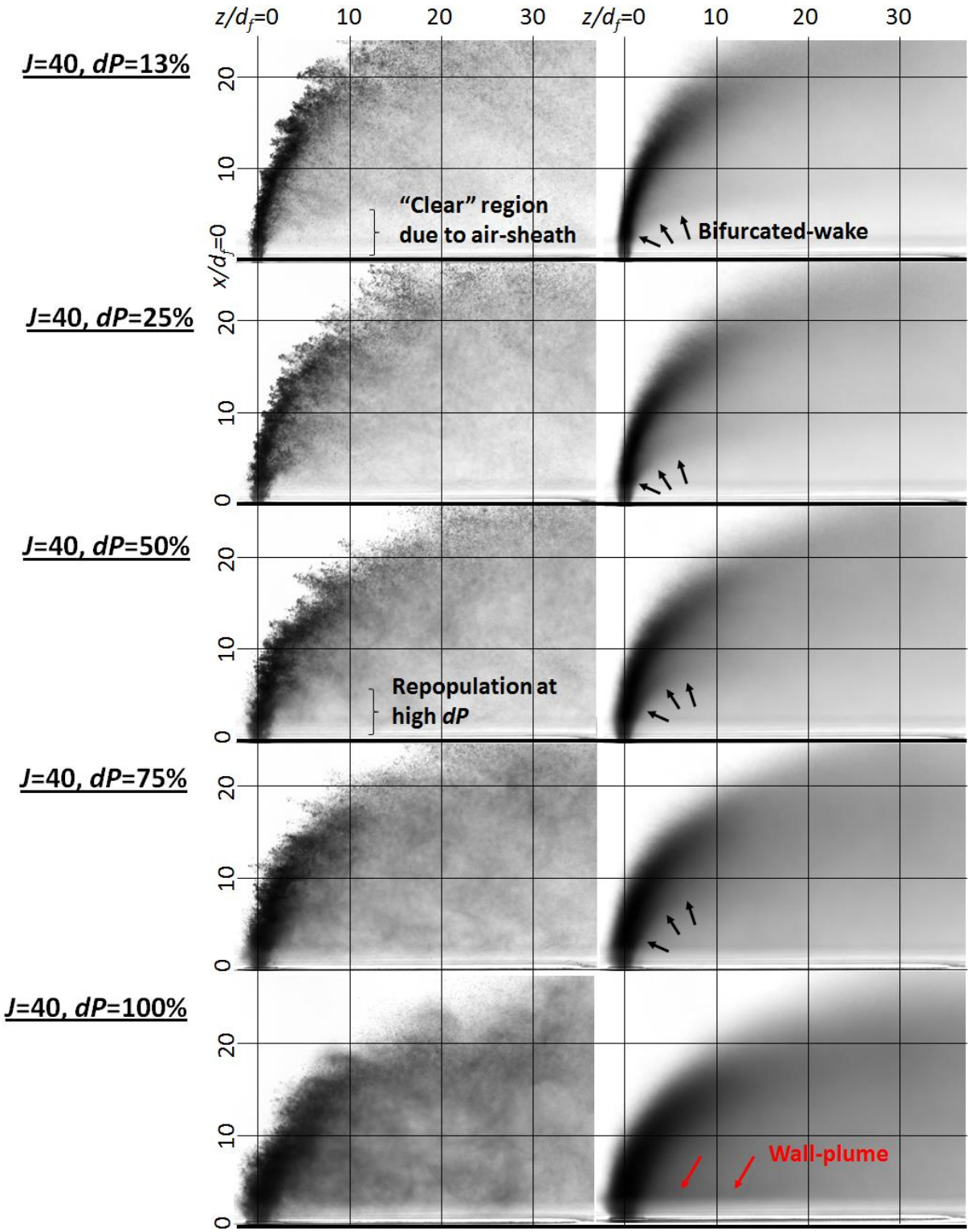

Figure 6.9 – Instantaneous and average images of J=40, We_{cf}=350 TF-JICF.

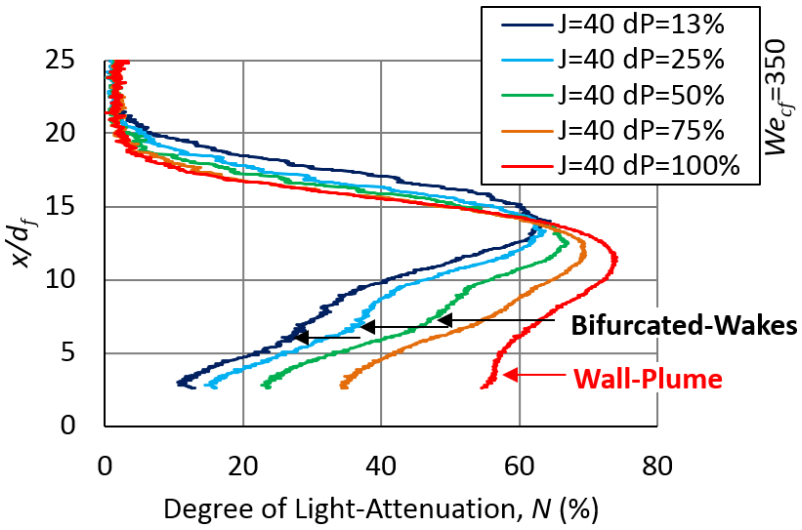

Figure 6.10 – Light-attenuation profiles at z/d_f=5, showing the evolution of the bifurcated-wake and the wall-plume as a function of *dP*.

We propose three hypotheses to explain the behaviors of the bifurcated-wakes and the trend of wake-repopulation, connecting them to the characteristics of the initial-jets described in the previous section. These hypotheses are listed as follows:

i. As *dP* increases, the interaction between the fuel and airblast becomes more energetic and turbulent, likely resulting in the formation of intense eddies that "tear/rupture" the air-sheath, which will cause the droplets/KH-corrugations contained therein to be released and mixed into the crossflow in an unsteady manner. In essence, these corrugations and droplets are no longer rapidly shedded into the crossflow from a constant location. Consequently, when the images were averaged, the bifurcated-wake (Figure 6.9) and local t_ω maximum (Figure 6.4) both became more spread out and less pronounced at higher *dP*, until they eventually vanish altogether.

ii. The bifurcation between the KH-corrugations/droplets and the jet's trajectories can be attributed to their different inertia and surface areas; i.e., the intact jet likely travelled at close to the fuel injection velocity, whereas the KH-corrugations were likely accelerated by the airblast to a much higher velocity. However, the KH-

corrugations had significantly larger drag area per mass compared to the jet; hence, they bifurcated from the jet and penetrated less into the crossflow. However, as *dP* increased, the KH-corrugations gained more inertia from acceleration by airblast, while the jet became increasingly destabilized (i.e., its penetration momentum affected) and disintegrated (i.e., larger drag area). Consequently, the KH-corrugations and the jet's drag and inertia began to approach each other at high *dP*, causing the bifurcation between their trajectories to gradually vanish.

iii. The average images in Figures 6.9 show that the bifurcated-wakes' penetrations increased with *dP* until they were eventually located almost directly behind the initial jet/spray-core. In the same *dP* range, the jet/spray-core became an increasingly wider obstacle to the crossflow due to the development of larger corrugation structures. It is possible that when the bifurcated-wake was located very close to the wide spray-core, its droplets were caught in the spray-core's recirculation zone, whereupon the two structures merged into one and the bifurcation vanished. This hypothesis does not, however, explain the gradual disappearance of the t_ω maximum on the *windward* side of the jet.

In addition to the bifurcated-wake, Figures 6.9 and 6.10 show a new peak in *N* developing very close to the wall at *dP*=75-100% (referred to as the "wall-plume"; see red arrows). Since Figure 6.10 shows the wall-plume developing far away from where the bifurcated-wakes were located, we can confidently conclude that the two were different spray structures. An additional feature of the wall-plume is shown in Figure 6.11, which contains two average top-view images. The left image shows the spray having a parabolic windward-edge (i.e., a single vertex) when the wall-plume did not form, while the right image shows the spray with a "double-crested" windward-edge when the wall-plume formed. Although the top-view image alone does not show where the double-crested edge was located in the *x* direction, we

reasoned that it was located next to the wall and belonged to the wall-plume, since anything further away from the wall was swept into the crossflow (z) direction and not visible from the top-view anymore. In essence, Figure 6.11 suggests that droplets in the wall-plume were dispersed very widely and unevenly in the radial directions.

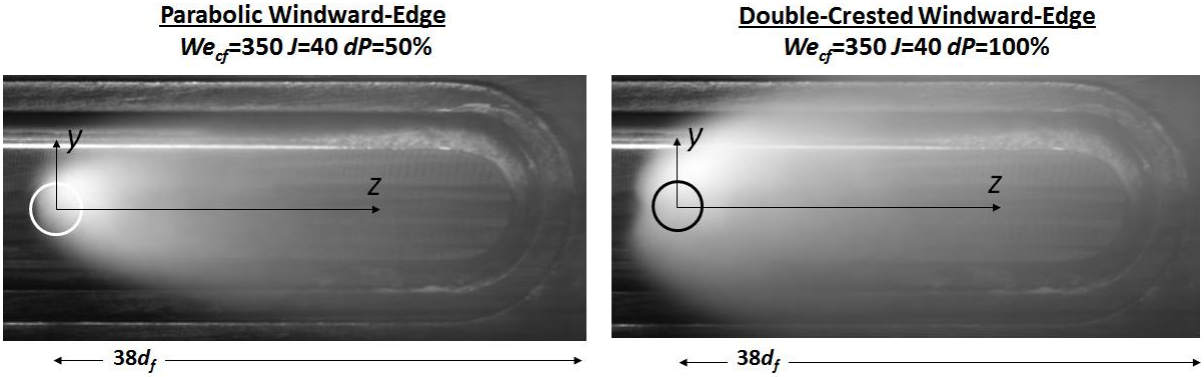

Figure 6.11 – Average top-view images of the spray, showing the development of a double-crested windward-edge at high *dP*. Circles outline the spraywell's edge.

Having established that the bifurcated-wake and the wall-plume are two distinct structures, the following argument hypothesizes how the wall-plumes were formed. We first observed that the wall-plume in Figure 6.10 began forming at the same *dP* value as the onset of intense prompt-atomization in Figures 6.3 and 6.4. Subsequently, it was observed from the t_ω curves in Figure 6.4 that the prompt-atomized droplets were shed into the crossflow at locations very close to the test-channel wall, where the wall-plumes were observed to form in Figure 6.10. These observations suggest that the wall-plume most likely consisted of prompt-atomized droplets that were rapidly shedded into the crossflow; i.e., in the same manner where the bifurcated-wake was formed by the rapid shedding of KH-corrugations. This conclusion is further supported by the observation that the wall-plume's two windward crests in Figure 6.11 aligned with the positions of the air-nozzles in the spraywell (see Figure 3.11); i.e., the areas where the wall-plumes were most widely dispersed coincided with the center of the air-nozzles, where the airblast's velocity is expected to be the highest.

In summary, the bifurcated-wake and the wall-plume are formed by the shedding of KH-corrugations and prompt droplets, respectively. These spray structures are likely unique to an injector configuration where the fuel and blasting air impinge, allowing for two zones of fuel-air interactions to form. They are also unique to TF-JICF (i.e., not found in TF-jets in quiescent gas), because a crossflow is required to strip and bifurcate the prompt droplets, KH-corrugations and spray-core into different trajectories.

6.3 Evolution of the AB-JICF's Global Spray Characteristics

This section discusses how *dP*, *J* and We_{cf} affect the global spray characteristics in the AB-JICF regime. Figure 6.12 plots the far-field (z/d_f=15) light-attenuation profiles of the AB-JICF at ranges of *J* and *dP* while We_{cf} is fixed to 350. As with the near-field, the far-field sprays' wake region droplets population increased with *dP*, opposite to the trend observed in the AA-JICF regime. This repopulation phenomenon occurred across the entire wake region, as well as in localized peaks (i.e., the bifurcated-wake and the wall-plume). Figure 6.12 also shows that the spray's centerline penetrations (i.e., locations of maximum *N* values, as connected by the red arrows) generally declined with increasing *dP*. Meanwhile, the spray's outer-edge penetrations (indicated by black arrows) decreased with *dP* at high *J* and increased with *dP* at the lower *J*. The presence of an inverse proportionality between spray penetration and *dP* (which we call "trajectory-reversal") is opposite to the trends observed in the AA-JICF regime and reported in the TF-JICF literature. It is counter to the general understanding that airblast provides the fuel with more penetration momentum.

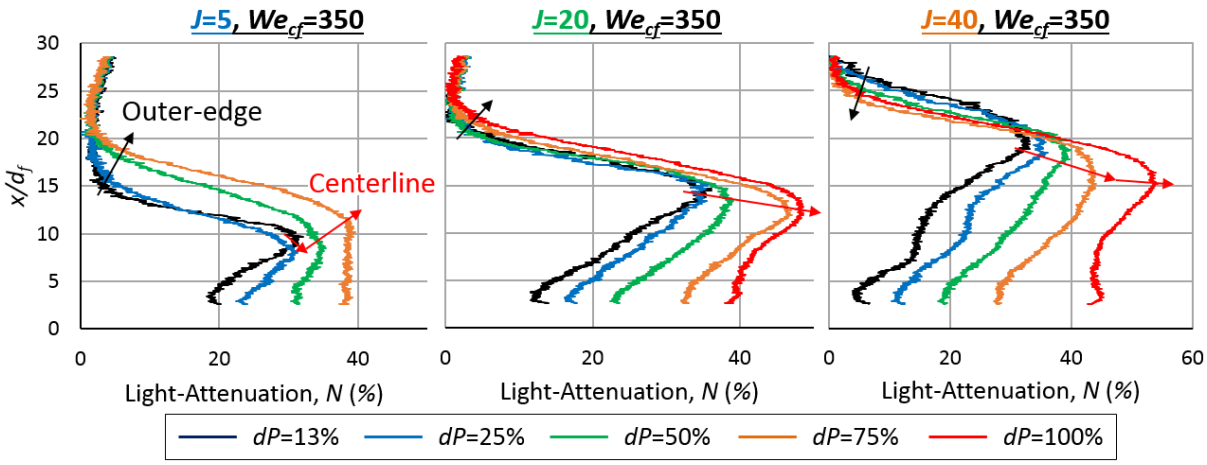

Figure 6.12 – Variations in the light-attenuation profiles at z/d_f=15, as a function of *dP* and *J*.

Figure 6.13 shows the dependence of the light-attenuation profiles on We_{cf} and *dP* at a fixed *J* of 20. The plot shows that the spray-densities around the core and wake regions (i.e., at and below the centerline) increased with *dP* much more significantly when We_{cf} was higher, which indicates that the degree of wake repopulation due to airblast was proportional to We_{cf}. This trend is most likely because, for a given *dP*, the airblast's Weber number scales proportionally with We_{cf}. This, in turn, means the atomization intensity of the fuel jet due to prompt-atomization and KH-corrugations (and, consequently, the amount of droplets that are released into the wake) also scales up with We_{cf}. On the other hand, although all the cases in Figure 6.13 exhibited trajectory-reversal, it is not clear whether the degree of "reversal" was dependent on We_{cf}.

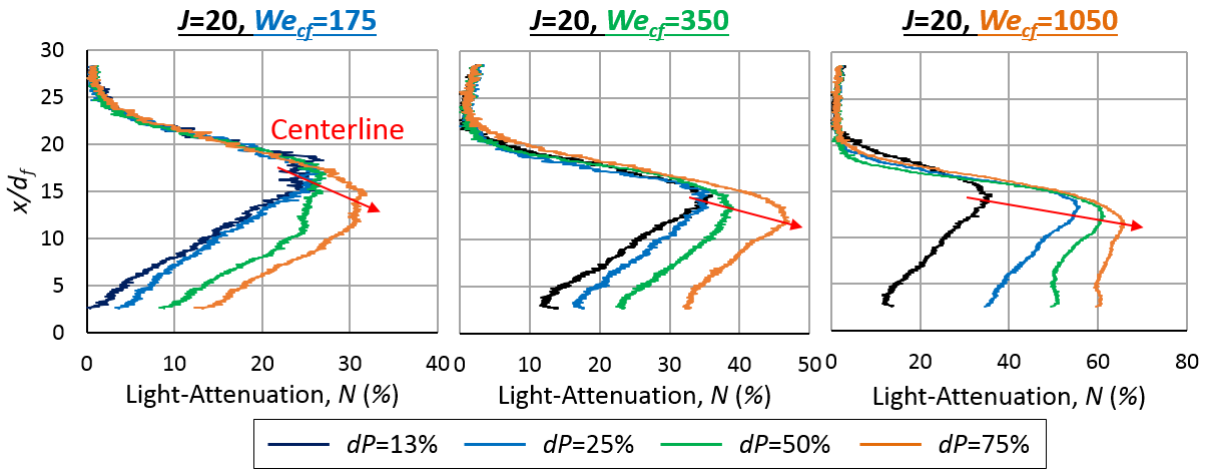

Figure 6.13 – Variations in the light-attenuation profiles at z/d_f=15, as a function of *dP* and We_{cf}.

The following analysis was performed in an effort to explain the trajectory-reversal behavior. In their investigation of high-*dP* and high-*ALR* TF-JICF (see Section 2.2), Leong et al. (2000, 2001 *JPP*, 2001 *JEGTP*) proposed that the fuel and airblast's momenta are rapidly exchanged, such that the high-velocity airblast significantly enhanced the spray's penetration. In contrast, although we observed in Chapter 5 that air-assist enhanced the spray penetrations by a small degree, the enhancement was caused by the entirely different mechanism of inhibiting large-scale RT-wave development and jet breakup. Notably, the fuel and air momenta were *not* significant exchanged in the AA-JICF regime because the fuel jets always remain intact. In the current AB-JICF regime, we observed that (i) higher *dP* caused more of the jet's outer-layer to be atomized prior to entering the crossflow, (ii) the fuel remained intact or narrowly dispersed close to the injector in most cases, hence the fuel jet and air's momenta were likely not significantly exchanged and (iii) the jet became increasingly corrugated at higher *dP*, potentially increasing its drag. To analyze how these observed effects influence the spray penetration, we begin with the following expression for a Classical-JICF's trajectory:

$$\left(\frac{x}{d_{jet}}\right) = C_0 \times J^{C_1} \times \left(\frac{z}{d_{jet}}\right)^{C_2} \tag{8}$$

Rearranging Equation (8) to express it in terms of absolute distances, we obtained:

$$x = C_0 \times J^{C_1} \times z^{C_2} \times d_{jet}^{1-C_2} \tag{9}$$

where $C_0 \approx \pi/C_D$, C_D is the jet's drag coefficient and $C_2 \approx 0.5$ according to Equation (10) in Section 2.1. Equation (9) expresses the spray penetration (x) as a function of underlying physical parameters such as the jet/spray's drag (C_0), the fuel's momentum-flux relative to the crossflow (J), the convection distance (z) and the fuel jet's size and inertia (d_{jet}). Next, we determine how the addition of airblast likely influenced each of these parameters in order to produce the trajectory-reversal phenomenon (i.e., to identify which physical processes most likely caused the trajectory-reversal).

First, even though the fuel and airblast momenta did not mix effectively in the AB-JICF regime, the shearing of high-speed airblast against the fuel jet's surface likely imparted a small amount of penetration momentum to the jet, which can be modeled in Equation (9) as an increase in the effective value of *J*. However, this change would cause spray penetration to increase, instead exhibiting trajectory-reversal. In contrast, the application of airblast caused the jet to become highly corrugated, which likely increased the jet's drag coefficient and reduced the C_0, thereby contributing to the reduction in penetration at higher *dP*. Also, since a significant portion of the jet was prompt-atomized and/or shear-atomized by airblast at high *dP*, the remaining intact jet's total mass and inertia were reduced. We may interpret this as a reduction in the jet's effective diameter (d_{jet}). In combination, if the reductions in C_0 and d_{jet} dominated the increase in J, the jet/spray-core penetration (x) will decrease with *dP* to provide the observed trajectory-reversal trend. Thus, this analysis suggests that trajectory-reversal occurred because the disruptions to the jet's penetration inertia and drag area by airblast were more significant than the momentum the airblast imparted on the jet in the AB-JICF regime.

Figures 6.12 and 6.13 also showed that trajectory-reversal was primarily only exhibited by the spray centerline. This is likely because, based on the existing understanding of JICF, the outer-edge of the spray generally consists of the largest and/or fastest droplets. These droplets' high inertia will cause them to be less susceptible to the airblast's disruptive effects compared to the smaller-sized droplets found around the centerline.

Finally, the scaling analysis above has another ramification: when the fuel jet approaches the state of complete atomization by airblast due to increasing *dP*, the terms C_0 and d_{jet} will reach their minimum values. At the same time, the enhancement to J becomes large, because the atomized droplets can exchange their momentum very rapidly with the high velocity airblast. The combined effects will cause the spray penetrations to increase once again with increasing *dP*. This ramification may explain the unusual trend of the *J*=5 sprays in Figure

6.12, where the centerlines only exhibited a momentary trajectory-reversal between *dP*=13-25% before increasing in penetration once again. Specifically, since the *J*=5 jets are more easily prompt/shear-atomized than the *J*=20-40 jets, they may achieve the state of complete atomization and, thus, cease to exhibit trajectory-reversal at lower *dP* values.

6.4 Summary

Using the measured data, we have provided a qualitative description of the spray characteristics and underlying processes in the AB-JICF regime. These findings are summarized in Figures 6.14 and 6.15. Figure 6.14 shows the interactions of fuel and airblast around the initial jet are comprised of two zones. The first zone occurs when the injected blasting air impinges on the fuel jet at just below the plane of the test-channel wall. The energetic impingement rapidly atomizes the liquid jet's outer-layer into very small droplets through the prompt-atomization mechanism reviewed in Section 2.2. The prompt droplets are dispersed throughout the blasting air (e.g., like tracer particles) and exit into the crossflow from the entire opening of the spraywell. The second fuel-air interaction zone is located downstream of the prompt-atomization zone, where the remaining intact fuel jet continues to be sheared by the air-sheath. KH-corrugations develop in this zone in the same manner as observed in the AA-JICF regime in Chapter 5. Eventually, the air-sheath is stripped away by the crossflow. Fuel that is not disintegrated into KH-corrugations penetrates beyond the air-sheath, where it then undergoes surface shear-breakup and RT-waves breakup similar to a Classical-JICF.

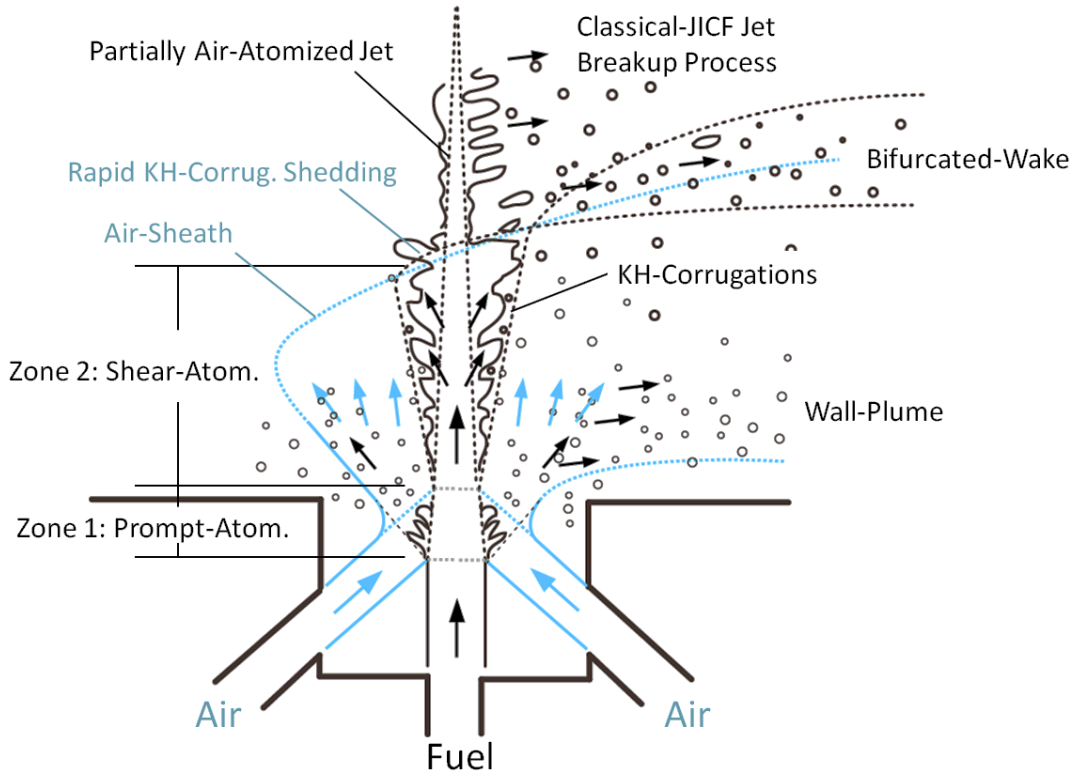

Figure 6.14 – A two-zone model of fluid interactions around the initial jet.

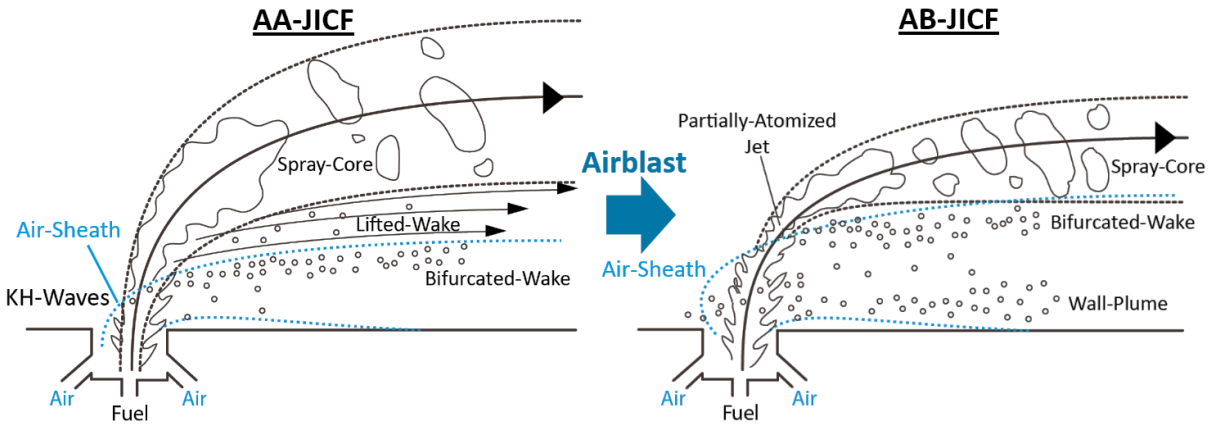

Figure 6.15 – The transitions in global spray characteristics from the AA-JICF to AB-JICF regime.

Figure 6.15 shows that the prompt-atomized droplets are rapidly entrained into the crossflow due to their small sizes. They form a locally dense branch of droplets that travels almost immediately next to the test-channel wall (i.e., "Wall-Plume" in Figures. 6.14 and 6.15). On the other hand, the KH-corrugations are shedded and form the bifurcated-wake when the air-sheath is stripped away. The bifurcated-wake is located further into the crossflow at higher *dP*, because the air-sheath's penetration is proportional to *dP*. At the lower *dP* range, the

bifurcated-wake becomes more pronounced with increasing *dP* because more KH-corrugations are produced by faster air. However, when *dP* is very high, the intense turbulence of the air-sheath prevents the KH-corrugations from rapidly shedding at a fixed location, thus making the bifurcated-wake weaker and more spread out.

Downstream of the bifurcated-wake, the remaining fuel jet that is not atomized by the prompt-mechanism or KH-waves continues to penetrate into the crossflow and undergo Classical-JICF disintegration, thus forming the spray-core. Nonetheless, because a significant portion of the jet has been atomized by airblast (i.e., lower inertia) and because the jet is now highly corrugated (i.e., higher drag), the spray-core's penetration is lower relative to its penetration in the AA-JICF regime.

In terms of application to jet-engine fuel-air mixers, the AB-JICF generally produces lower spray penetrations and higher near-wall fuel concentrations than the AA-JICF. These characteristics are detrimental towards wall flashback and coking risks. Additionally, the AB-JICF also requires a higher level of air-nozzle *dP*, which may not be readily available in jet-engines. Therefore, operating in this regime may generally be disadvantageous to fuel-air mixers.

CHAPTER 7. DISCUSSION:

THE AIRBLAST-SICF REGIME

This chapter discusses results from the Airblast-*Spray*-in-Crossflow (AB-SICF) regime, the highest *dP* regime investigated in this thesis. As described in Figures 4.9-4.12, the AB-SICF regime generally occurred at *dP* higher than 75% (the exact *dP* values being dependent on *J* and We_{cf}). Similar to the earlier chapters, we describe the air's effects on the AB-SICF's initial-jet and global characteristics, propose the underlying mechanisms, and end the chapter by tying the findings into a cohesive description of AB-SICF.

7.1 Evolution of Prompt-Atomization and the Wall-Plume in AB-SICF Regime

Prompt-atomization and the wall-plume are important TF-JICF characteristics that first appeared in the upper *dP* range of the AB-JICF regime. This section describes the dependence of prompt-atomization on *dP* in the AB-SICF regime and, subsequently, how the wall-plume (which consisted of prompt droplets) varied with prompt-atomization. This section will also demonstrate that the fuel-air interactions remained two-zoned in the AB-SICF regime (i.e., separate zones of prompt-atomization and KH-waves shear-atomization).

Figure 7.1 shows instantaneous and average images of the initial fuel jets/sprays in the *dP* range of 50-150% (i.e., from AB-JICF to AB-SICF) for J=20 and We_{cf}=350. As Chapter 6 described, a *dP* of >50% caused the jet's outer-layer to be prompt-atomized and the resulting droplets to enter the crossflow from across the entire spraywell opening. Figure 7.1 suggests that more droplets were found close to the edge of the spraywell as *dP* increased towards 150% (as evident from increasing darkness of the shadowgraph near the dotted lines). This suggests that the prompt-atomization and dispersion processes intensified with increasing *dP*. However, as is evident in the averaged images, the edge of the spraywell continued to have lower spray-densities than the center even at *dP*=150%; i.e., the droplets were not uniformly dispersed. This

suggests that the intensity of the fuel-air impingement at *dP*=150% was still insufficient to prompt-atomize the *entire* jet and disperse the generated droplets uniformly across the entire spraywell area. In essence, although the air-nozzles were choked and the *dP* value was in the typical range of an *airblast* atomizer, prompt-atomization of the *complete* fuel jet as described in TF-JICF literature (see Section 2.2) was likely not achieved. Therefore, the fuel-air interactions likely occurred in two zones in the AB-SICF regime; i.e., similar to what was observed in the previously discussed AB-JICF regime.

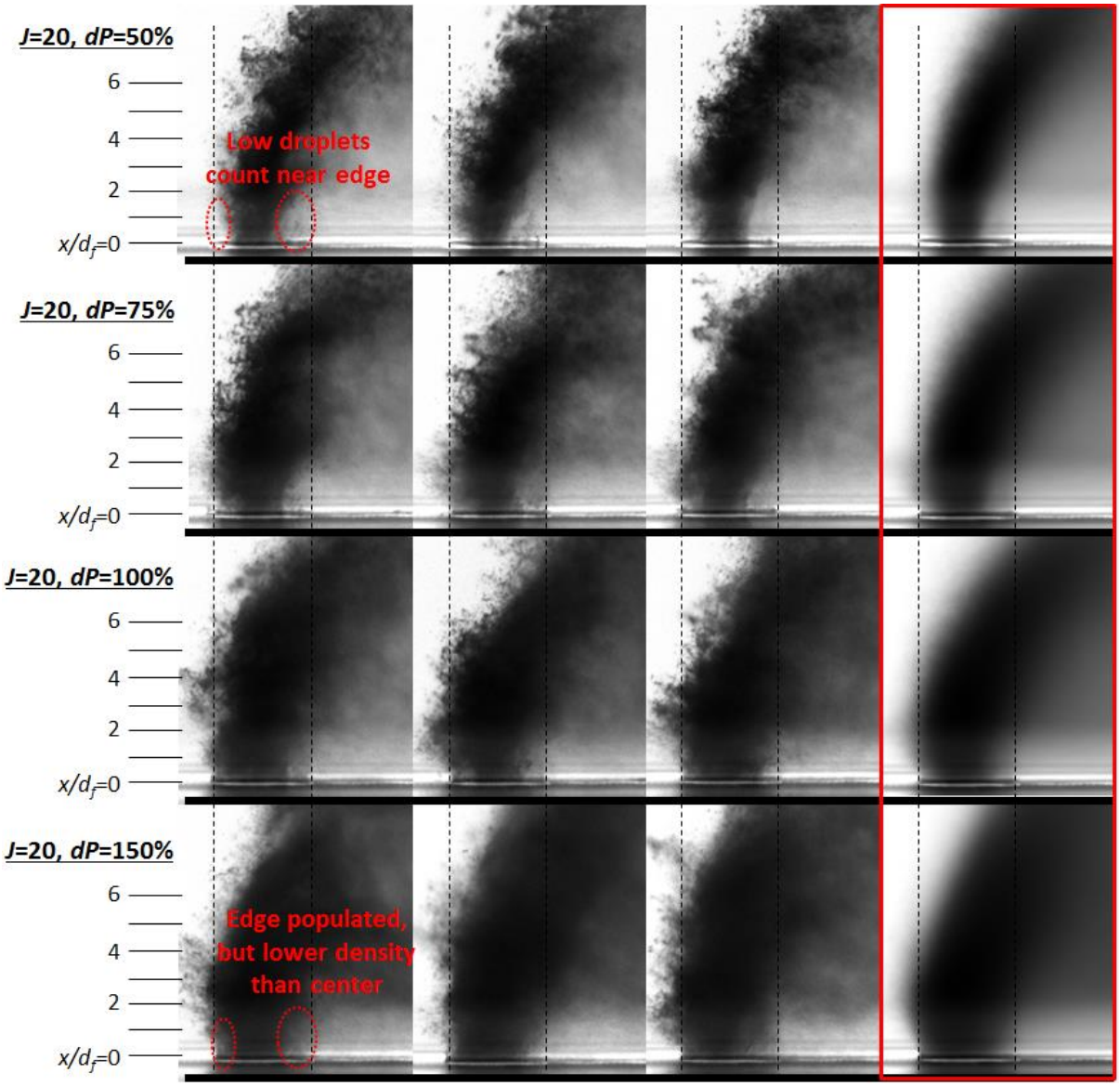

Figure 7.1 – Photos of the initial jets/sprays in the AB-JICF regime (*J*=20, We_{cf}=350). *Columns 1-3*: instantaneous images. *Col 4:* average images.

Unfortunately, the dense initial sprays generated in the AB-SICF regime were opaque to the shadowgraph backlight, as shown in Figure 7.1, and it is not possible to examine the evolution of the fuel jet within the spray plume in order to verify our hypothesis of a two-zone interaction. Instead, the existence of the two zones could be inferred from the spray's global characteristics. Specifically, if the fuel is *fully* prompt-atomized and well-mixed with the air, the mixture that would be discharged into the crossflow would be spatially homogenous. In such a case, the mixture would develop into a single spray plume in the crossflow. On the other hand, if the spray-formation process consists of separate phases of prompt-atomization, shear-atomization and, perhaps, even crossflow-atomization, we can expect each phase of the process to create different droplet sizes, velocities and to occur at different locations. In such a scenario, the resulting spray will bifurcate into separate plumes when subjected to crossflow stripping (e.g., as manifested in the form of the bifurcated-wakes and wall-plumes in the AA-JICF and AB-JICF regimes).

Figure 7.2 shows that at dP=50-75%, the light-attenuation profiles each have a pronounced peak in N near x/d_f=12.5, which represents the dense spray-core. N values in the wake-region (x/d_f<12.5) are significantly lower than the spray-core's maximum N. In essence, most of the fuel droplets were concentrated in the spray-cores. As dP increased, the wake region's N values also increased, at a rate faster than the increase in the spray-core's N. At dP=100%, a wall-plume began to form near the wall, indicating the diversion of fuel from the spray-core into the wall-plume, which was formed by the prompt-atomization mechanism. At $dP \geq 120\%$, the wall-plume's N began to exceed the spray-core's N (a phenomenon that we will refer to as the "dominant wall-plume"), suggesting that most of the injected fuel may be prompt-atomized and, consequently, distributed into the wall-plume. However, even though the spray-core's N was low relative to the dominant wall-plume at $dP \geq 120\%$, the two were unmistakably still separate structures based on the bimodal shape of the N profile (see inset

plot in Figure 7.2); i.e., the spray bifurcated into two plumes and was not "homogenous". This phenomenon is further demonstrated in the average images of Figure 7.3, which shows a very prominent wall-plume developing and bifurcating the spray into two "branches" when *dP* was increased to 150%. Thus, based on the plots and images shown in Figures 7.2 and 7.3, we conclude that because the spray bifurcated at *dP*=150%, the fuel-air interactions around the initial jet/spray likely consisted of two zones in which prompt-atomization and KH instabilities controlled the spray formation. This means the fuel jet was likely not fully prompt-atomized and dispersed by air in the AB-SICF regime.

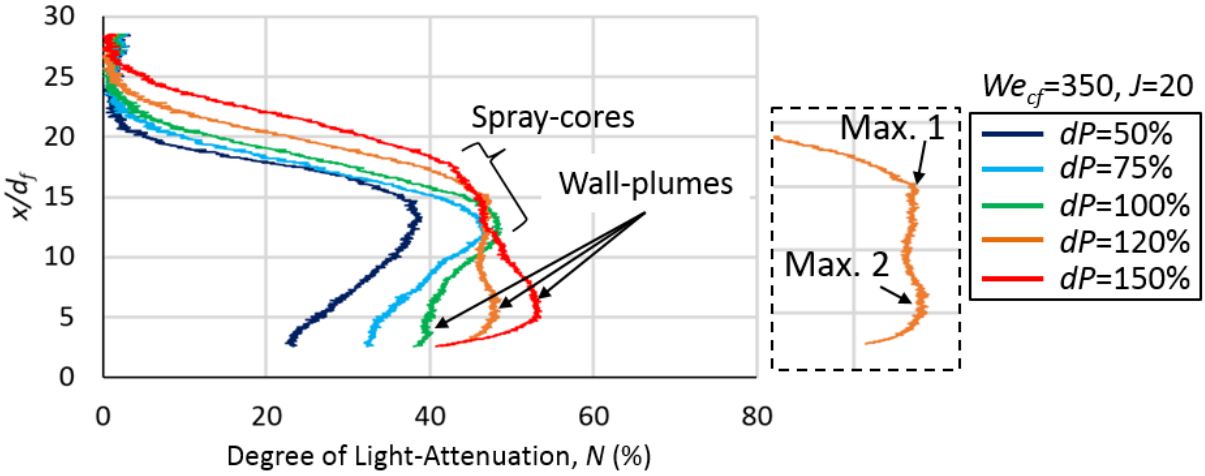

Figure 7.2 – z/d_f=15 light-attenuation profiles as a function of *dP*, showing the evolution of the spray-core's *N* relative to the wall-plume. *Inset*: Zoomed-in of *dP*=120%'s profile, showing bimodal *N* distribution.

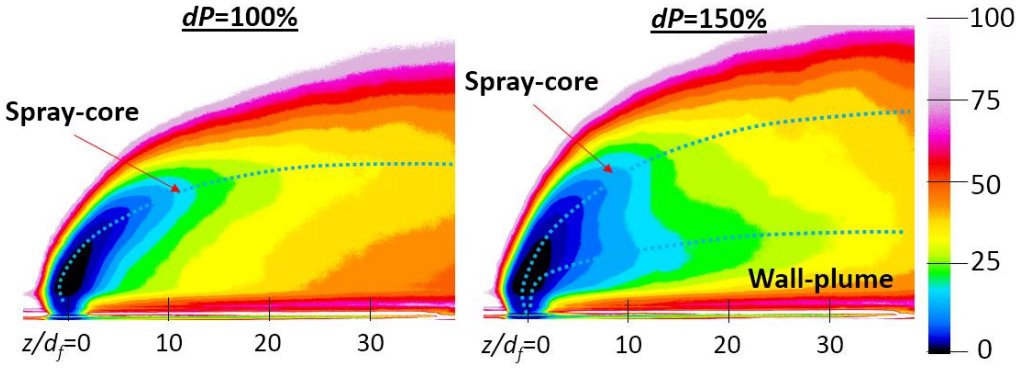

Figure 7.3 – False-color average images showing the development of a dense wall-plume on *J*=20 We_{cf}=350 AB-SICF as *dP* increased.

In Chapter 6, we presented a scaling analysis that explained why the wall-plume began to form at lower *dP* levels when *J* was lower and We_{cf} was higher. The analysis proposed that the extent of prompt-atomization becomes larger when the air's kinetic energy is increased relative to the fuel's kinetic energy and surface tension energy, which are proportional to *J* and inversely proportional to We_{cf}, respectively. Based on this argument, we hypothesized that the dominant wall-plume (which forms when the majority of the injected fuel is prompt-atomized) will occur at lower *dP* when *J* decreases and when We_{cf} increases. Figure 7.4 shows that the experimental result agrees with our hypothesis: the dominant wall-plume is observed at *dP*=150% for *J*=20-40 AB-SICF and at *dP* as low as 75% for *J*=5. Furthermore, the *N* profiles for *dP*=150% remained more bi-modal at higher *J*, which suggests prompt-atomization affected a smaller fraction of the fuel jet when *J* was higher. On the other hand, the dependence of the dominant wall-plume on We_{cf} is described in Figure 7.5. It shows that the We_{cf}=175 AB-SICF did not form a dominant wall-plume in the tested *dP* range, while the We_{cf}=350 AB-SICF formed a dominant wall-plume at *dP*=150% and the We_{cf}=1050 AB-SICF at *dP*=100%.

Finally, it is worth noting that when the wall-plumes first form, they were always located immediately next to the test-channel wall. However, when *dP* was increased the wall-plume's penetration into the crossflow was also observed to increase; e.g., Figures 7.4 and 7.5 show the dominant wall-plumes having substantial separations from the wall at *dP*=150%. Based on these observations, we expect the wall-plume to penetrate even further into the crossflow for *dP* larger than 150%, whereupon the fuel concentrations near the wall will likely become significantly smaller. This new trend is a reverse of the wake-repopulation effect of *dP* observed in the AB-JICF regime. This trend also agrees with Leong et al. (2001, *JPP*)'s observations of high-*ALR* TF-JICF where "airblasting" the fuel jet was found to detach the resulting spray from the wall and to reduce the near-wall fuel concentrations. Thus, based on these observations, our AB-SICF regime appears to exhibit many of the characteristics of the

high-*dP* and high-*ALR* TF-JICF reported in literature. The reduction in near-wall fuel concentrations and the rapid atomization provided by AB-SICF may be beneficial to fuel-air mixer applications, although the required levels of *dP* may be prohibitive from an engine design standpoint.

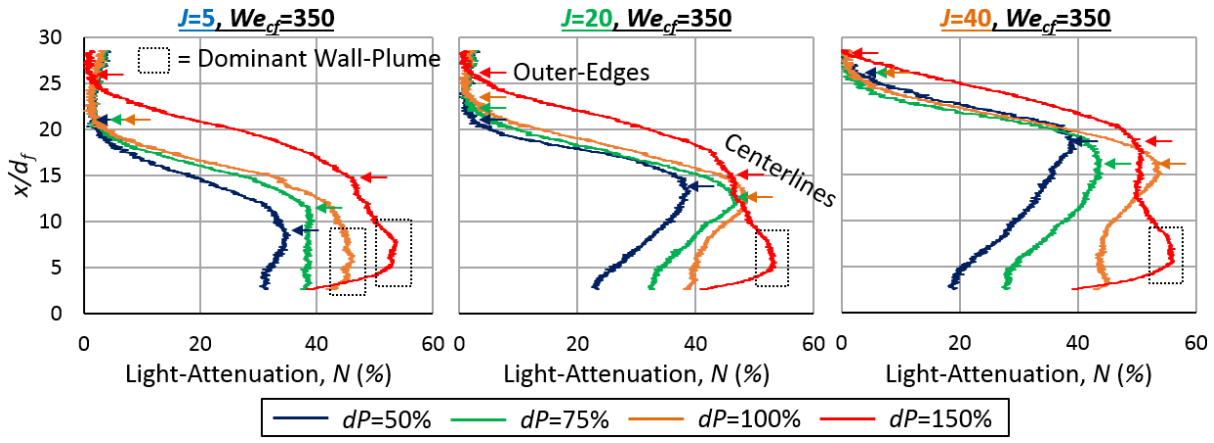

Figure 7.4 – z/d_f=15 light-attenuation profiles, showing the effect of J on the development of dominant wall-plumes. Approximate locations of the spray centerlines and outer-edges are marked by arrows.

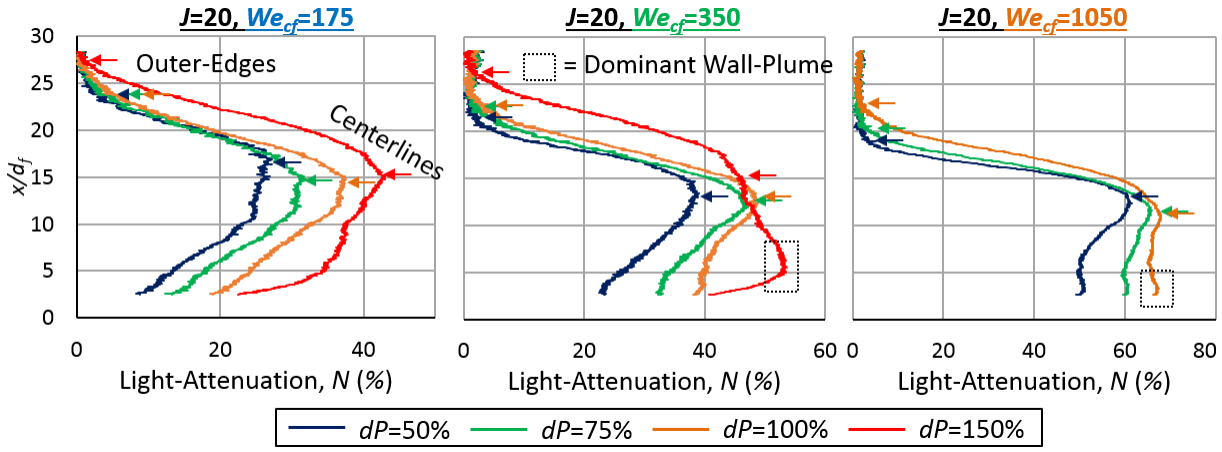

Figure 7.5 – z/d_f=15 light-attenuation profiles, showing the effect of We_{cf} on the development of dominant wall-plumes. Approximate locations of the spray centerlines and outer-edges are marked by arrows.

7.2 AB-SICF's Spray Penetration Trend and the Existence of an Intact Jet

Our discussion to this point has suggested that the fuel-air interactions in the AB-SICF regime comprised of two zones (i.e., prompt-atomization followed by airblast-induced shear-

atomization). However, we have not determined whether the second zone completely atomized the fuel jet; i.e., whether intact jets and/or large clusters of non-atomized fuel penetrated beyond the second zone to disintegrate within the crossflow in the AB-SICF regime, as they did in the AA-JICF and AB-JICF regimes. Since the initial sprays were very dense and the flow structures highly turbulent in the AB-SICF regime, it is not possible to examine the outer-edge of the air-sheath and the intact jet (if one existed) directly from the spray images. Thus, similar to the previous section's analysis, we infer the existence of an intact jet outside of the fuel-air interaction zone based on the spray's downstream behavior. Specifically, according to the trajectory-reversal mechanism proposed in Section 6.3, increasing *dP* will cause a *reduction* in the spray's centerline penetration if the airblast (i) reduces the fuel jet's penetration inertia by stripping away fluid mass from the jet via prompt/shear-atomization and (ii) increases the fuel jet's drag area by introducing KH-corrugations and disturbances, while (iii) imparting negligible added penetration momentum to the jet because the airblast and intact jet cannot exchange momentum effectively. Thus, for as long as trajectory-reversal occurs, we may argue that processes (i) through (iii) are still applicable, which indicates the presence of an intact fuel jet (or at least large non-atomized liquid clusters) that eventually penetrates into the crossflow beyond the fuel-air interaction zones. On the other hand, if the fuel jet is completely atomized into a fine spray within the fuel-air interaction zones, processes (i)-(ii) will have reached an asymptote (i.e., the fuel jet is fully atomized and cannot be "disturbed" much further by increasing the airblast *dP*). At the same time, process (iii) will no longer be applicable, because the finely-atomized fuel droplets can be effectively accelerated by the airblast. Hence, trajectory-reversal will stop, and the spray's penetration should once again *increase* with *dP*.

Figures 7.4 and 7.5 above show that when *dP* was increased in the AB-SICF regime the trajectory-reversal effect ceased and the spray's centerline and outer-edge penetrations (marked by arrows) generally increased with *dP*. Furthermore, Figure 7.4 shows that while the

sprays' centerline penetrations were strongly proportional to J in the lower dP range (e.g., dP=50%), their penetrations became nearly the same across J=5-40 when dP=150%. This suggests that at the highest dP range, the spray penetration was primarily governed by the air's momentum, further indicating the presence of effective fuel-air momentum exchange. In fact, as previously shown in Figure 4.14, the trajectories in the AB-SICF regime can be effectively correlated by the J_{eff} parameter, which was derived by Leong et al. under the assumption that the fuel is fully prompt-atomized and exchanges momentum rapidly with the air. Therefore, the experimental data suggests that the fuel jets were likely fully atomized by the air (via a two-zoned process) before encountering the crossflow in the AB-SICF regime, which is the reason for naming this regime "airblast *spray*-in-crossflow".

Figure 7.4 also shows that trajectory-reversal stopped (i.e., the jet became fully atomized by the air) at lower values of dP when J was lower. For example, the J=5 spray's centerline penetration was enhanced by air at dP>50%, whereas the J=40 spray exhibited the same behavior only at dP>100%. On the other hand, Figure 7.5 shows that for a fixed J, the dP values at which trajectory-reversal ceased were insensitive to We_{cf}. These trends agree with our previous analyses, which found the degrees of prompt-atomization and KH-waves shear-atomization (i.e., the degree by which the fuel jet was atomized by air) to be inversely proportional to J and only weakly proportional to We_{cf} for a given dP.

7.3 Gas-Like Shear-Layer Eddies

In addition to the dominant wall-plume and the effect of resumed penetration-enhancement by airblast, another important characteristic of the AB-SICF regime is the development of large vortical structures on the spray-plume's windward-edge. These structures are shown in the instantaneous images of the spray in Figure 7.6 where they are pointed out by arrows. The figure shows that these structures only develop at the highest dP range of the AB-SICF regime. Furthermore, it shows that when We_{cf} increased while J was fixed, the vortical

structures began to develop at lower *dP* levels. On the other hand, the instantaneous images in Figure 7.7 show that when *J* increased while We_{cf} was fixed, the structures began to develop at higher *dP* levels. Since the described proportionalities that governed the vortical structures' development are the same proportionalities which governed the degrees of the fuel jets' atomization by airblast, we hypothesize that the vortical structures' development was likely connected to the degree of the jet's atomization.

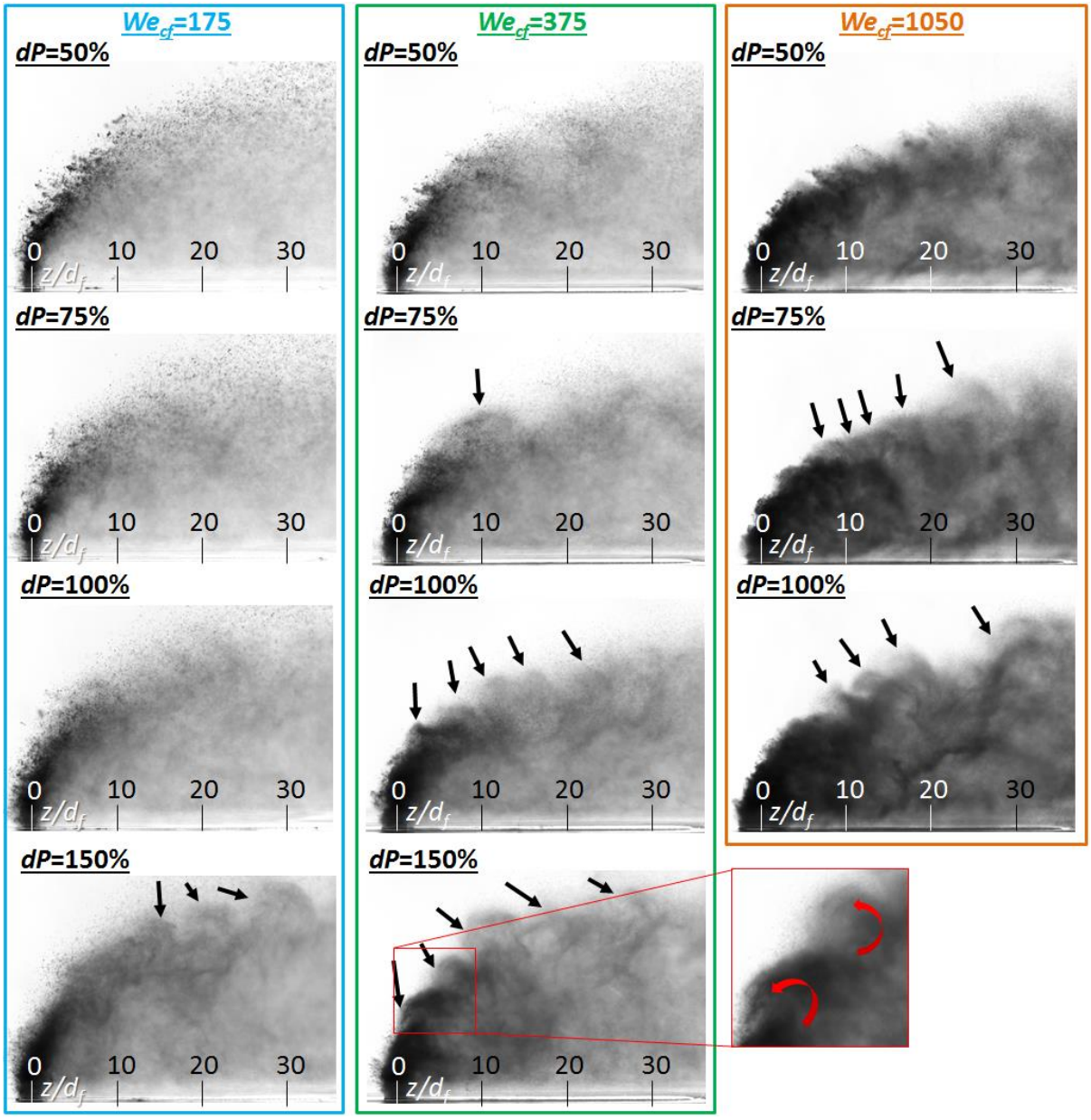

Figure 7.6 – Instantaneous spray images showing the effects of *dP* and We_{cf} on the formation of the windward-edge vortical structures at *J*=20. *Inset:* zoomed-in view of the hook-like vortical structures showing counter-clockwise rolling.

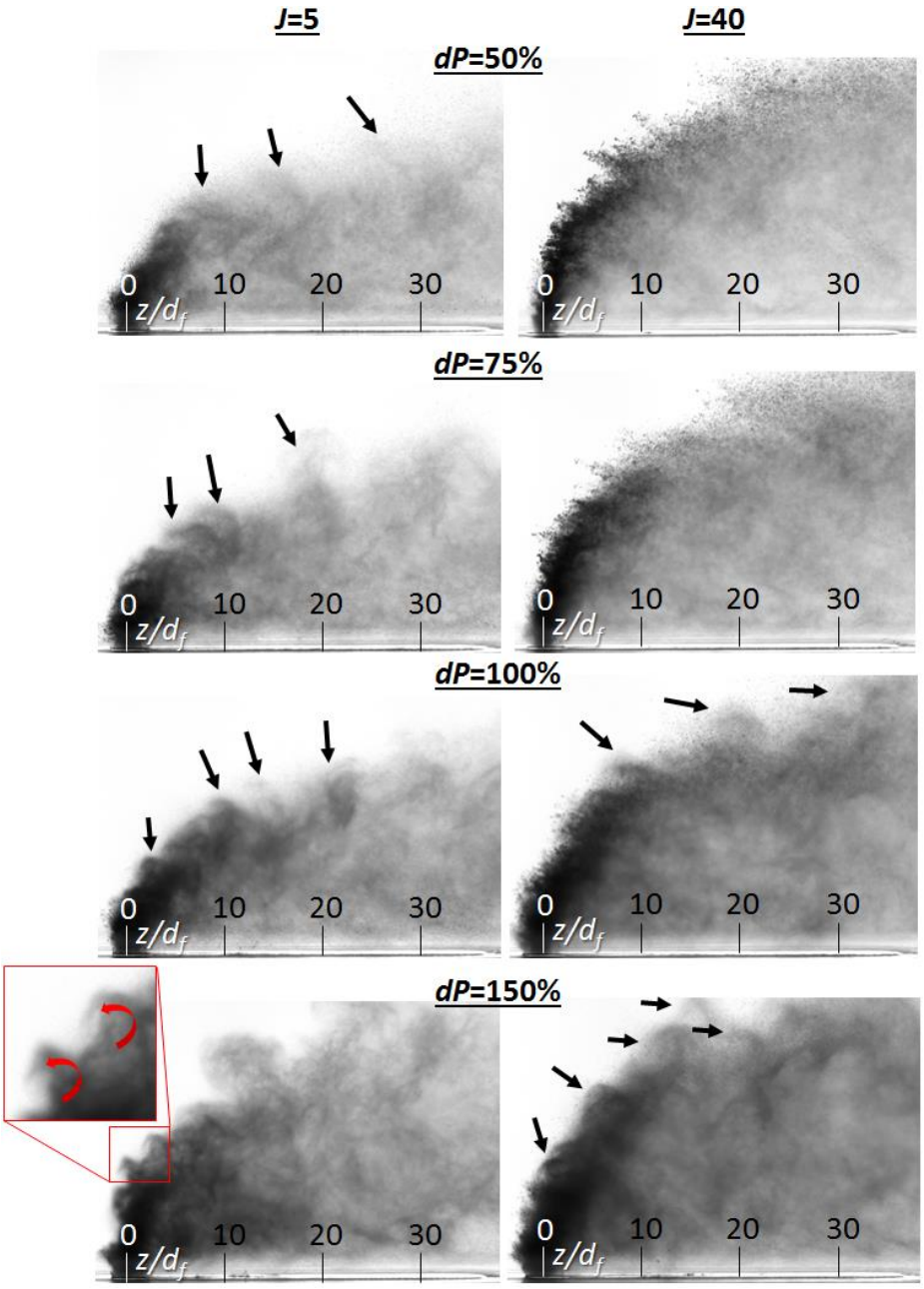

Figure 7.7 – Instantaneous spray images showing the effects of *J* on the formation of the windward-edge vortical structures at We_{cf}=350. *Inset:* zoomed-in view of the hook-like vortical structures showing counter-clockwise rolling.

Figures 7.6 and 7.7 also show that the vortical structures are generally "hook-shaped", where the tip of the hook describes the direction of vortex rolling (e.g., see the inset images in Figures 7.6 and 7.7). The images show that the structures consistently roll in the counter-clockwise direction (i.e., counter-clockwise vortices). This rolling direction can be used to infer the directions and magnitudes of the shear forces involved in the vortices' formation. For example, as Figure 7.8 illustrates, to attain a counter-clockwise vortical motion in a droplet-

laden flow, the sum of the moment of shear forces around the center of the vortex must also be counter-clockwise. Since the only velocity components contributing to shearing on the spray's windward-edge were (i) the crossflow velocity that tend to impart a clockwise moment and (ii) the spray's upwards velocity that provides counter-clockwise moment, we reason that the vertical velocity component "overpowers" the horizontal velocity component to produce the observed counter-clockwise rolling. This conclusion raises the following question: since the crossflow's velocities were in the 65-72*m/s* range and the fuel injection velocities were only in the 12-50*m/s* range, where did the higher upwards velocity originated from? One probable source for the high upwards velocity was the high-velocity airblast air, which ranged between 100-140*m/s* in the *dP* range of 50-150%. This implies that the droplets exhibiting counter-clockwise rolling were likely significantly accelerated by the air; i.e., significant exchange of fuel-air momenta occurred in order to produce the counter-clockwise vortex structures. Furthermore, we reason that since the highest upwards airblast velocity was likely to be found near the point of injection (i.e., before the air expands and disperses), the observed vortical structures were likely generated near the injection point. Their presence in the downstream locations, as shown in Figures 7.6 and 7.7, was likely a result of convection by the crossflow.

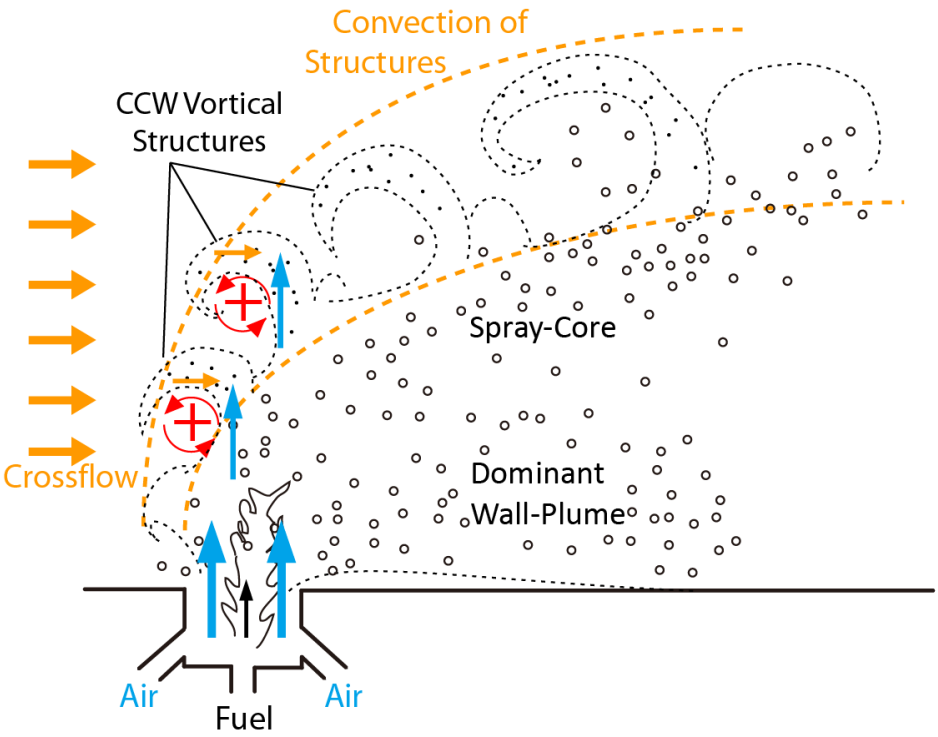

Figure 7.8 – Illustration showing the development of counter-clockwise vortices about centroids "+" due to a net counter-clockwise moment (red arrows) produced by stronger upwards velocity (blue arrows) compared to horizontal crossflow velocity (orange arrows).

Notably, the windward-edge vortical structures described above are not usually found in Classical-JICF. Instead, they are more commonly observed on the windward edge of *gaseous* JICF (e.g., see the works of Wilde, 2014). This is because the large heavy droplets found in Classical-JICF (especially at low We_{cf}) cannot be supported in a vortical motion by the surrounding air; i.e., they will be readily ejected out of the vortex due to centrifugal forces. Hence, the droplets that formed the vortical structures must be very small. This hypothesis is supported by Figures 7.6 and 7.7, showing that the vortical structures consistently exhibit a fog-like appearance, indicating that they were composed of sub-pixel sized droplets. A brief analysis was performed to estimate the sizes of these droplets, based on the ideas that (i) the vortical structures developed at a certain frequency and, hence, (ii) the droplets following these vortices' motions had to be smaller than a certain size in order to respond to that frequency. The frequency (f_ω) at which the vortical structures were produced can be estimated from the structures' average size (L_ω) and their convection velocity (U_ω), as follows:

$$f_\omega = \frac{U_\omega}{L_\omega} \tag{1}$$

Based on Figures 7.6 and 7.6, L_ω was approximately $7.5d_f$ ($3.8mm$). On the other hand, since we proposed that the structures were formed by droplets that were significantly accelerated by the blasting air, their convection velocity should be between the fuel injection velocity and airblast velocity. Using the fuel injection velocities as U_ω, Equation (1) provided a frequency range of f_ω =3-13kHz. On the other hand, if the air's velocities were used, the resulting frequencies became f_ω =26-37kHz.

Melling (1997) and TSI (2005) provided the following expression to describe the response frequency (C) of particles (i.e., droplets) in a fluid flow, where the flow's density is significantly lower than the particle's:

$$C = \frac{18\mu_{air}}{\rho_f d_{drop}^2} \tag{2}$$

For the droplets to follow the vortices' motions, their C value has to be greater than or equal to f_ω. Thus, substituting f_ω into Equation (2) and rearranging yields the maximum diameter of the vortical structures' droplets (d_{drop}):

$$d_{drop} \leq \sqrt{\frac{18\mu_{air}}{\rho_f f_\omega}} \tag{3}$$

The dynamic viscosity of air at the test temperature of ~150^oC was approximately μ_{air} = 2.4×10^{-5} $kg/m{\cdot}s$ (Edwards, 2013 and *The Engineering Toolbox*). Substituting this value into Equation (3), we estimated the maximum droplet sizes in the vortical structures to be 6.5-13.5μm for f_ω=3-13kHz, and 3.8-4.6 μm for f_ω=26-37kHz. These estimated droplets sizes are applicable for We_{cf} = 175 to 1050. Thus, the maximum droplets sizes are estimated to be below the resolving capabilities of the image pixels ($13.52\mu m/px$), in agreement with the appearance of the sprays in the images in Figures 7.6 and 7.7.

Notably, in the AA-JICF and AB-JICF regimes, we observed that the wall-plume, KH-corrugations and spray-core generally bifurcated into different trajectories as they traveled downstream. We also proposed that the bifurcations were caused by the varying inertia of the droplets (i.e., smaller and slower droplets are more susceptible to crossflow entrainment). Additionally, we proposed that the low density (hence, low inertia) air was generally entrained into the crossflow before droplets entrainments occurred. On the other hand, in their study of high-*ALR* TF-JICF, Leong et al. (2000) found that the injected air and prompt-atomized droplets generally remained well-mixed throughout the spray-plume. They proposed that the droplets and air had a synergistic relation, in which the high-speed air helped to accelerate the droplets further into the crossflow while the dense droplets helped to shield the low-density air from crossflow entrainment (this process is true, of course, *only* when rapid fuel-air momentum-exchange occurs). In the AB-SICF images in Figures 7.6 and 7.7, we consistently find sub-pixel sized droplets along the windward-edge of the spray-plume (especially when the vortical structures are present), a region typically occupied only by the largest/fastest droplets. Furthermore, we have reasoned that the formation of vortical structures indicate rapid momentum-exchange between the fuel and high-speed air. Therefore, based on these findings, it is likely that the vortical structures (and, hence, the entire AB-SICF spray-plume in general) contain a significant amount of air which originated from the air-nozzles. In essence, in the AB-SICF regime, the fuel and air were likely well-mixed throughout the spray-plume, similar to the high-*ALR* TF-JICF described by Leong et al. (2000) and different from the behavior of the flows in the AA-JICF and AB-JICF regimes of this study. This "uniform mixing" hypothesis satisfies the assumptions of the physics-based J_{eff} correlation function and further explains why the spray trajectories in the AB-SICF regime roughly followed this correlation (e.g., see Figure 4.14).

7.4 Summary

Using acquired spray images, we have provided a qualitative description of the AB-SICF's characteristics and underlying mechanisms, which are summarized in Figures 7.9 and 7.10. Figure 7.9 shows the difference between the dominant spray structures in the AB-JICF and AB-SICF regimes while Figure 7.10 illustrates the fluids interactions close to the point of injection. They show that increasing *dP* intensifies the prompt-atomization and shear-atomization of the initial jet to the extent where the entire jet becomes atomized by the air prior to encountering the crossflow (hence "AB *spray*-in-crossflow"). Droplets produced by prompt-atomization form the wall-plume, while droplets produced by fuel-air shear-atomization form the spray-core (note: the bifurcated-wake has merged into the spray-core at this *dP* range).

As *dP* increases, the fraction of fuel atomized by the prompt mechanism also increases, causing the fuel droplets to be redistributed from the spray-core into the wall-plume. Eventually, at very high *dP* levels, the wall-plume's *N* becomes higher than the spray-core's *N*, suggesting higher droplets concentration in the wall-plume (e.g., referred to as the "dominant wall-plume" in Figure 7.9). The wall-plume's penetration into the crossflow also increases with *dP* due to the added penetration momentum from the air, causing it to detach from the wall, thereby lowering the near-wall fuel concentrations. We expect the fuel jet to eventually become *entirely* prompt-atomized if *dP* increases beyond our tested range, whereupon the spray-core would disappear and be replaced by a single dominant wall-plume.

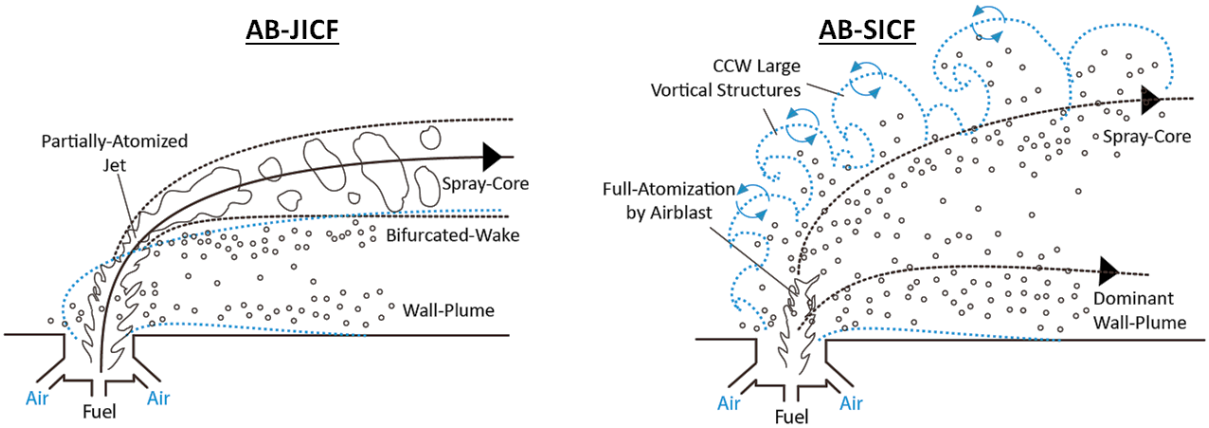

Figure 7.9 – Transitions in dominant spray structures going from the AB-JICF to AB-SICF regime.

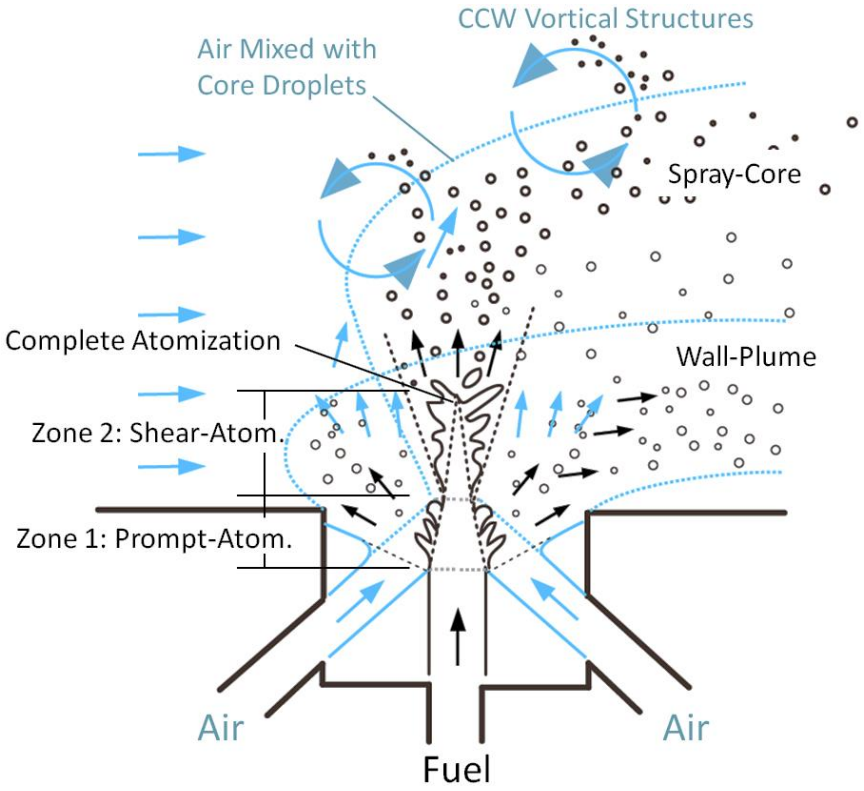

Figure 7.10 – An expanded view of fluid interactions around the initial jet/spray region in the AB-SICF regime.

Figure 7.9 also shows that contrary to the "trajectory-reversal" phenomenon observed in the AB-JICF regime, the spray penetration in the AB-SICF regime is directly proportional to *dP* for two reasons: (i) since the fuel jet is now completely atomized, increasing the air velocity no longer significantly reduces the jet's penetration inertia and (ii) the atomized droplets, having high surface-to-volume ratios, can rapidly exchange momentum with the high-speed air, which helps to propel them further into the crossflow. As a consequence of fuel-air

momentum exchange, the droplets and air remain well-mixed throughout the spray-plume and do not exhibit the bifurcations of fuel and air observed in the AA-JICF and AB-JICF regimes. Therefore, small droplets and air can now be found along the windward-edge of the spray, where they often develop into large counter-clockwise vortical structures.

In summary, the spray characteristics in the AB-SICF regime resemble those reported by Leong et al. (2000, 2001 *JPP*, 2001 *JEGTP*), Li et al. (2006, 2010 *Part 1*, 2010 *Part 2*) and Sinha et al. (2013, 2015) for high-*dP* and high-*ALR* TF-JICF. Many of these characteristics (e.g., rapid atomization and mixing, as well as spray-wall detachment) are potentially beneficial for fuel-air mixer applications. However, due to the high fuel flow-rates encountered in typical jet-engine operations, a prohibitively high level of air-nozzle *dP* will be required to achieve the characteristics of AB-SICF.

CHAPTER 8. CONCLUSION AND RECOMMENDATIONS FOR FUTURE WORK

8.1 TF-JICF Image and Trajectory Data

TF-JICF is being considered for application in the fuel-air mixers of next-generation jet-engines to reduce the concentration of near-wall fuel. In particular, designers plan to employ TF-JICF with low levels of air-nozzle *dP* and *ALR*, such that no additional compressor is required to supply the air and such that the changes to the resulting flow-field is minimal when compared against existing Classical-JICF fuel-air mixers. However, TF-JICF is a relatively new flow configuration that is not well understood in terms of its spray characteristics and underlying spray-formation mechanisms. Existing investigations by Leong et al. (2000, 2001 *JPP*, 2001 *JEGTP*), Li et al. (2006, 2010 *Part 1*, 2010 *Part 2*) and Sinha et al. (2013, 2015) focused on high-*ALR* and/or high-*dP* TF-JICF at near-atmospheric operating conditions. They concluded that co-injecting air with the liquid jet enhances the rate of atomization and the liquid's penetration. The resulting spray trajectories were proposed to follow the J_{eff} correlation model:

$$\frac{x}{d_f} = c_0 \times J_{eff}^{c_1} \times \left(\frac{z}{d_f}\right)^{c_2} \tag{1}$$

$$J_{eff} = \frac{\rho_{mix} U_{mix}^2}{\rho_{cf} U_{cf}^2} = \frac{A_{air}\rho_{air} U_{air}^2 + A_f \rho_f U_f^2}{A_{total}\rho_{cf} U_{cf}^2} \tag{2}$$

Although the J_{eff} correlation model was developed based on high-*ALR* and/or high-*dP* data, Equations (1)-(2) are currently employed throughout the TF-JICF community without explicit limitations on its applicability; e.g., they are often employed to correlate trajectories of TF-JICF together with *dP*=0 Classical-JICF.

This dissertation contributes to the existing knowledgebase by characterizing a TF-JICF across a wide range of operating conditions: dP = 0-150%, We_{cf} = 175-1050 and J = 5-40, with resulting ALR = 0-1.2. These conditions cover the ranges tested by Leong et al. (2000, 2001 *JPP*, 2001 *JEGTP*), Li et al. (2006, 2010 *Part 1*, 2010 *Part 2*) and Sinha et al. (2013, 2015), as well as the low-dP, low-ALR and high-We_{cf} range that is not previously studied but immediately relevant to next-generation jet-engines. Notably, crossflow pressure at the We_{cf}=1050 test-points was close to 10*atm* in order to reproduce the high-pressure liquid break-up processes in jet-engines. This pressure level was accommodated by the specialized high-pressure and high-temperature facility described in Section 3.1, and is an experimental condition rarely achieved in the JICF literature. The number of test-points employed in this investigation also significantly exceeds those found in the cited TF-JICF literatures (see Figure 3.24), which maximized the chance that both persisting and transient TF-JICF characteristics were captured.

Dye-based shadowgraph imaging was used to characterize the TF-JICF, as described in Section 3.4. The resulting images are of sufficient quality and resolution to elucidate both macroscopic and subtle small-scale characteristics of TF-JICF, many of which formed the basis for our discussion of TF-JICF spray-formation processes. These images are provided throughout this dissertation (e.g., see Figure 4.7) and form an important contribution to the TF-JICF knowledgebase, because images of similar quality (i.e., showing similar level of detailed spray structures) are not available from Leong et al. (2000, 2001 *JPP*, 2001 *JEGTP*) and Li et al. (2010 *Part 1*, 2010 *Part 2*).

Following the most common approach in JICF studies (as discussed in Chapter 2), the acquired shadowgraph images were post-processed to obtain the sprays' outer-edge and centerline trajectories. These trajectories were then curve-fitted to the following log-based shape-function:

$$\left(\frac{x}{d_f}\right) = P_1 \times f\left(\frac{z}{d_f}\right) = P_1 \times \ln\left[\frac{z}{d_f} - \frac{z}{d_{f,origin}} + 1\right] \quad (3)$$

where the empirical parameters P_1, $z/d_{f,origin}$ and relevant test conditions are discussed in Chapter 4's Figures 4.9 to 4.12 and listed in Appendix 2. The provided trajectory data can be compared against CFD simulation results and applied to TF-JICF injector design.

8.2 TF-JICF Regimes and the Deviation from J_{eff} Behavior

As described above, the J_{eff} correlation model is currently widely adopted in the TF-JICF community. The second major contribution of this dissertation work is the discovery that this model does not apply at the low-*dP* and low-*ALR* conditions where next-generation jet-engines are expected to operate. For example, Figures 4.13 and 4.14 demonstrates that the J_{eff} model generally over-predicts the penetration of the spray plume at these conditions.

Following the discovery of the non-J_{eff} behavior at low-*dP* and low-*ALR*, the third major contribution of this dissertation is the proposition that TF-JICF can be classified into four different regimes, only one of which exhibits J_{eff} behavior. For example, Figures 4.9 to 4.12 show that the spray penetrations increased with *dP* by a smaller amount than J_{eff} predicts in the lowest *dP* range of 0 to ~13%. In the middle range of *dP*~25-75% the spray exhibited the "trajectory reversal" behavior where penetration decreased with increasing *dP*. This is a new behavior not reported in the literature and opposite to J_{eff}'s prediction. In the highest tested *dP* range, the spray penetrations followed the J_{eff} model. Notably, the successful reproduction of J_{eff} behavior at high *dP* using our injector gives confidence that the non-J_{eff} behaviors at lower *dP* levels are not injector-dependent, but rather a different regime of TF-JICF that has not been reported before. Using the trends of penetration versus *dP*, we proposed the classification of TF-JICF into four regimes: (i) the Classical-JICF regime (*dP*=0%), (ii) the Air-Assist JICF regime (*dP*~3-13%) where the introduction of air mildly assists the spray's penetration, (iii) the Airblast JICF regime (*dP*~25-75%) where trajectory-reversal occurs and (iv) the Airblast Spray-ICF regime (*dP*>75%) where penetration follows the J_{eff} model. The listed *dP* range for

each regime is approximate, as the transitions from a lower to higher regime were observed to occur at lower *dP* when *J* is lower and We_{cf} is higher, as shown in Figures 4.9 to 4.12.

8.3 Spray-Formation Processes

The classification of TF-JICF regimes as described above was based on the hypothesis that changes in the trend of penetration versus *dP* indicate transitions in the underlying dominant spray-formation processes. The final major contribution of this dissertation is the identification of these processes through analyses of the instantaneous spray images, the sprays' cross-sectional light-attenuation profiles (*N*) and the jets' windward-edge profile thicknesses (t_ω).

Figure 8.1 summarizes the spectrum of TF-JICF characteristics and atomization mechanisms that were observed and discussed in Chapters 5 to 7. The horizontal axis of the figure shows the regimes and *dP* levels where they occurred. Notably, the listed *dP* levels are approximate, where exact values depend upon *J* and We_{cf}. In the AA-JICF regime, the introduction of air around the fuel jet inhibited the development of crossflow-induced RT- and KH-waves. At the same time, droplets number-density in the spray's wake was reduced and the spray penetration was mildly enhanced. In the AB-JICF regime, significant KH-corrugations and shear-atomization occurred on the jet surface, the spray's wake region became increasing repopulated by droplets and, in certain *dP* ranges, the KH-corrugations bifurcated from the jet and were shed into the wake region ("bifurcated-wake"). In the upper range of the AB-JICF regime, prompt-atomization of the initial jet due to fuel-air impingement became significant while KH-corrugations/shear-atomization continued to be present (i.e., two zones of fuel-atomization due to the injected air). The prompt-atomized droplets were also bifurcated from the jet and traveled very close to the wall, forming the "wall-plume" that significantly repopulated the wake region. In the AB-SICF regime, the jet was fully atomized by air prior to entering the crossflow. The wall-plume's concentration became very high relative to the spray-

core, and counter-clockwise vortical structures developed along the spray plume's windward-edge. The transfer of momentum from the air to the fuel strongly enhanced the spray penetration in accordance with the J_{eff} model, resulting in the reduction of wake droplets number density when *dP* was very high. The AB-SICF regime's characteristics and trends were found to most closely resemble the high-*ALR* and high-*dP* results reported by Leong et al. (2000, 2001 *JPP*, 2001 *JEGTP*), Li et al. (2006, 2010 *Part 1*, 2010 *Part 2*) and Sinha et al. (2013, 2015). The AB-JICF regime contained some of the characteristics recently observed but not thoroughly studied by Sinha et al. (2015) at medium levels of *dP*.

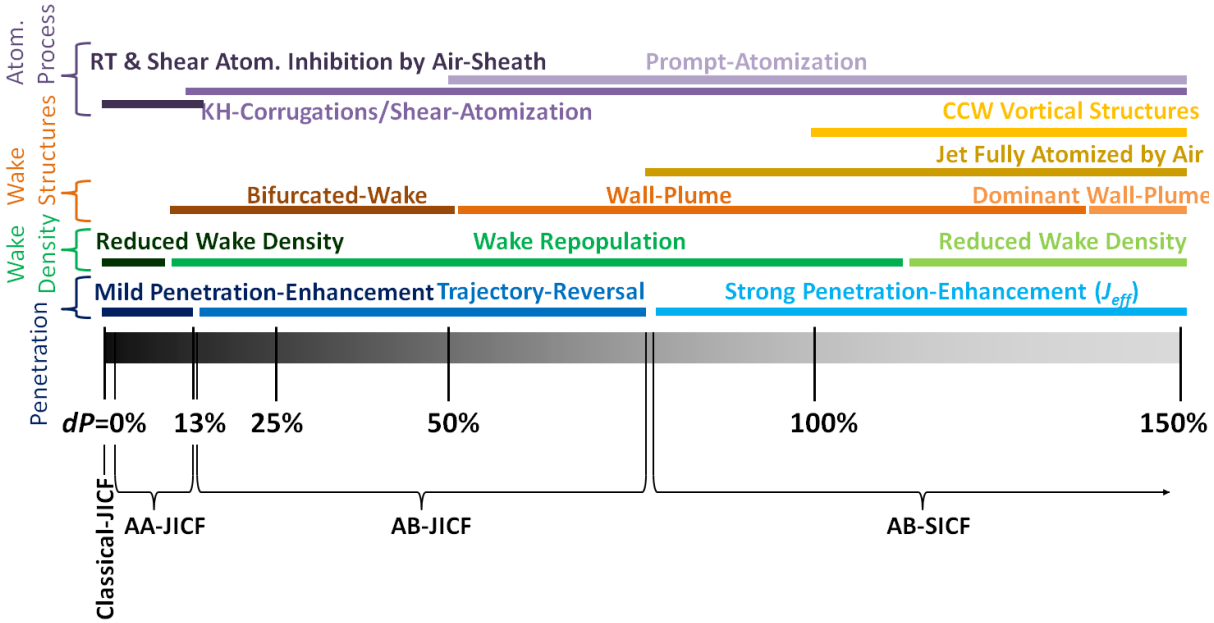

Figure 8.1 –TF-JICF regimes and characteristics.

In order to develop analytical models (e.g., a multi-regime trajectory correlation equation) for TF-JICF, it is necessary to not only identify the relevant underlying spray-formation processes but also to understand how each local process interact with another to form the resulting spray. To address this, Chapters 5 to 7 provide in-depth discussions of the spray-formation processes, their interactions, as well as their dependence on *J*, *dP* and We_{cf}. The resulting conceptual model of fuel-air-crossflow interactions close to the point of injection and

in the far-field are summarized at the end of each chapter, as well as illustrated in diagrams that are reproduced here in Figure 8.2.

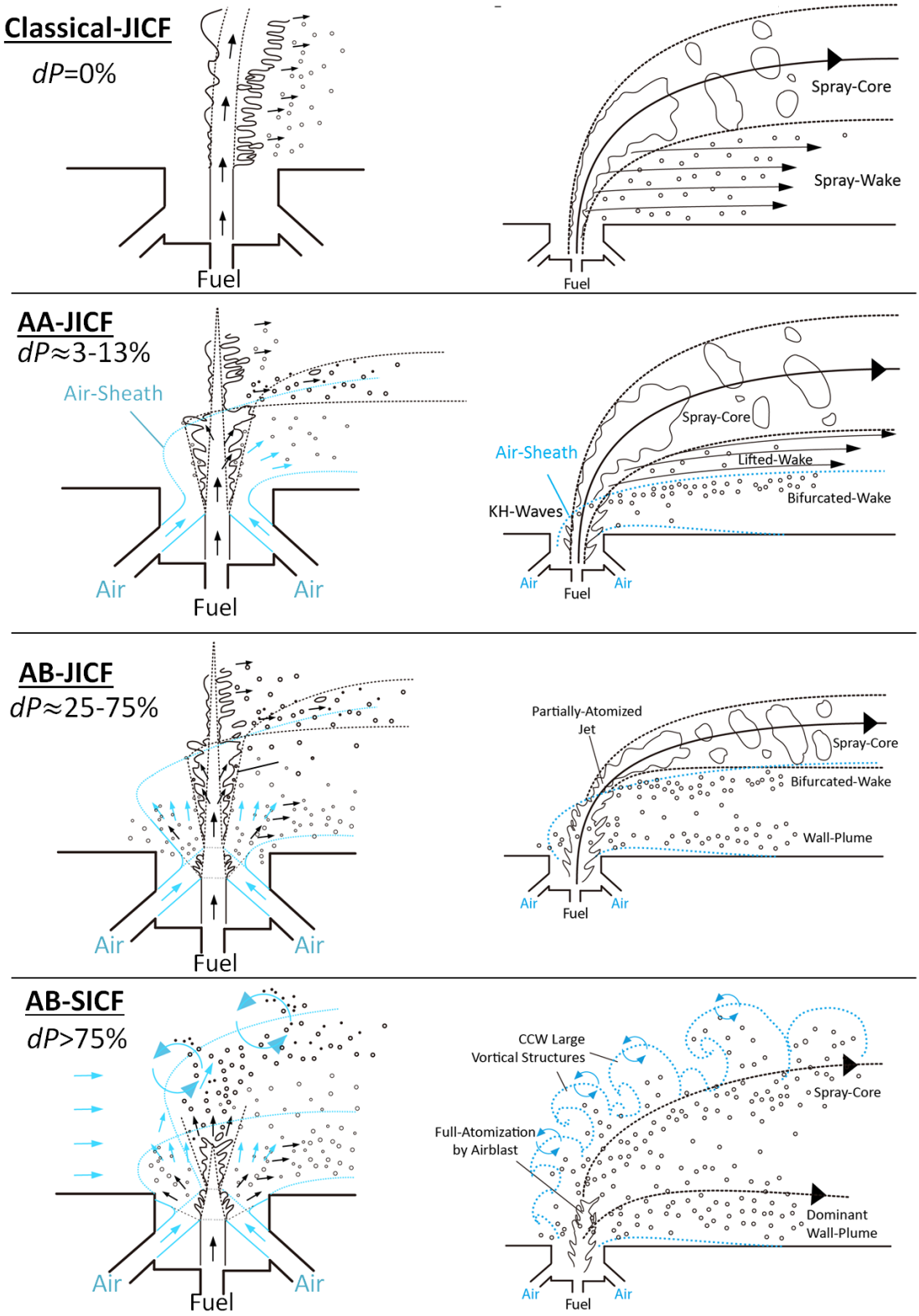

Figure 8.2 – Summary of the near-field (*left*) and global (*right*) spray characteristics in the four TF-JICF regimes.

8.4 Recommendations for Future Experimental Work

The shadowgraph images in this investigation revealed a spectrum of new TF-JICF characteristics that led to the proposition of multiple regimes and their associated spray-formation processes. However, the shadowgraph imaging technique's capability stops short of quantifying many of these characteristics. The following is a list of recommended future experiments to address the remaining gaps:

i. In this investigation, the distribution of fuel droplets concentration was inferred from the spray's light transmissivity. The results can be further refined by applying planar laser-induced fluorescence (PLIF) to quantitatively map the fuel concentration distributions. The PLIF method will involve exciting the Jet-A fuel to fluoresce using a 266*nm* laser-sheet at the desired plane of measurement. At the crossflow temperature of less than $150^{o}C$, the resulting fluorescence intensity is expected to be insensitive to temperature (Baranger, 2005) and oxygen collisional quenching, since fuel vaporization is negligible (see Appendix A) and oxygen does not significantly penetrate droplets in the residence time of the test-channel. Consequently, the PLIF signal intensity is expected to be directly proportional to fuel concentration, especially in the downstream dilute spray region. In the near-injector region, the initial-jet and dense-spray is expected to attenuate the laser-sheet as it propagates, rendering the fuel concentration measurements inaccurate. Nonetheless, measured fuel concentration distribution from the spray's dilute region will be useful for direct comparison against CFD results or for application in TF-JICF injectors design. As an alternative to Jet-A PLIF, the fuel concentration *and* temperature distributions along a plane can be simultaneously mapped by planar laser-induced phosphorescence, which operates similar to PLIF but requires seeding of the fuel with specialized phosphor tracer particles and a two-camera imaging system, as described in Tan et al. (2014).

ii. This dissertation proposed that the processes of prompt-atomization, KH shear-atomization and crossflow-driven atomization generate droplets of different size ranges, which lead to bifurcations of the spray-plume. These conclusion can be further supported by employing Phase Doppler Particle Analyzer to characterize droplet sizes along cross-sections of the spray plume (similar to Figure 2.6), especially in regions containing the bifurcated-wake (formed by KH-corrugations), the wall-plume (formed by prompt-atomization) and the spray-core. Data of droplet sizes will also support the prediction of fuel vaporization rates in TF-JICF, which significantly affect mixing and combustion performance.

iii. As suggested in Chapter 5, the low-velocity wake-region/recirculation zone behind the dense initial spray and the wall boundary-layer are regions of long residence time in a Classical-JICF, which pose the highest risks of unwanted fuel ignition and coking. We hypothesize that the injection of air (i.e., local addition of fluid flux) may enhance the flow velocities or even nullify the development of recirculation in these regions. To validate this hypothesis, particle image velocimetry or particle tracking velocimetry can be performed to study the effects of air on the fuel droplet's velocity-field.

iv. This dissertation suggested the existence of an air-sheath surrounding the fuel jet in the AA-JICF and AB-JICF regimes, as well as uniform fuel-air mixing in the AB-SICF regime. A diagnostic technique capable of visualizing the air's distribution (e.g., fluorescence-imaging with acetone-seeded air) will help to validate the hypothesized air-sheath and fuel-air mixing. It will also help to elucidate the structures that the air may develop at different injection and crossflow conditions (e.g., large-scale turbulent eddies), which will improve our understanding of the many TF-JICF processes directly affected by the air's flow-field (e.g., the rapid KH-corrugations shedding and wall-plume formation).

8.5 Recommendations for Future Theoretical Work

Future investigations of TF-JICF should also build upon the current work from a theoretical standpoint. Chiefly, this dissertation provided a qualitative description of TF-JICF characteristics and their underlying mechanisms; however, a theoretical model of TF-JICF (e.g., a correlation model for the penetration parameter P_1 across all four regimes) was not achieved because many of the underlying mechanisms that make up the TF-JICF are themselves not well understood. The following future investigations are recommended to address this gap:

i. As described in Chapters 5-7, the rate of liquid-removal from the fuel jet is an important aspect of TF-JICF. The jet breakup can be separated into three zones (i.e., prompt-atomization, KH shear-atomization and crossflow-driven atomization), each with different liquid-removal/atomization rates. These zones are coupled because processes in the upstream zones directly affect the initial condition of the downstream zone. As such, having accurate models of each zone is essential towards a complete analytical description of atomization in TF-JICF. Atomization in the crossflow-driven zone is well understood from Classical-JICF research, while atomization in the KH shear-atomization zone can likely be described by adapting models developed for TF-jets in quiescent gas (i.e., this assumes the liquid is unaware of the crossflow's presence while shrouded within the air-sheath). In contrast, existing studies of prompt-atomization focused on the scenario where the entire jet is prompt-atomized, while the TF-JICF scenario where only the jet's outer-layer is prompt-atomized is not well understood. To complete the model of TF-JICF, a quantitative description of liquid-removal rate by prompt-atomization as a function of dP, J and We_{cf} (or other fundamental physical parameters such as relative velocity) has to be developed.

ii. Once the rates of atomization as a function of operating conditions have been modelled for the three zones, these models can be naturally extended to describe the relative

mass-distributions of fuel in the spray-core, the bifurcated-wake and the wall-plume, since each of these structures is supplied with fuel droplets from one of the three atomization zones, as described in Chapter 6. An accurate determination of the fuel distributions in the spray pattern is important, because they will directly affect the downstream flame structures and, consequently, engine performance and durability.

iii. An important area left to be addressed in future work is the development of a multi-regime TF-JICF trajectory correlation model. Notably, in addition to describing the spray's outer-edge and centerline trajectories, a model should also be developed to describe the wall-plume's and bifurcated-wake's trajectories. The model(s) must account for the unique trajectory-reversal phenomenon that was uncovered in this investigation and be able to predict non-monotonic P_1 versus dP (e.g., see Figures 4.9 to 4.12). This will likely involve developing governing equations for the transfers of momenta between the fuel, air and crossflow in the initial-jet/spray region, particularly if the eventual model is to share similar form with the existing J and J_{eff} models where penetration is scaled by ratios of momentum-fluxes.

iv. Finally, although TF-JICF data are commonly reported as a function of J, J_{eff}, dP and ALR, our investigation found that these are likely not the physically-correct scaling parameters for TF-JICF, as they do not correlate characteristics such as penetration or regime-transition. For example, Figures 4.9 to 4.12 shows that regime transition depends simultaneously on dP, J and We_{cf}. The correct scaling parameters for TF-JICF remains to be determined, likely only *after* the appropriate models and governing equations for atomization rate, momentum-exchange and spray trajectory (i.e., recommendations i to iii) have been developed.

APPENDIX A. DROPLETS VAPORIZATION ESTIMATION

The experiment's crossflow temperatures were maintained at close to 150^oC (i.e., below typical jet-engine operating temperatures) to minimize the vaporization of droplets in the test-channel, in order to exclude the physics of vaporization from the investigation and to minimize the amount of fuel that may become gaseous and invisible in the shadowgraph images. This appendix shows the procedures used to estimate droplets lifetime in our TF-JICF to assess the impact of vaporization on the shadowgraph results' accuracy.

The *D*-square law approach outlined in Turns (2012) was employed. Based on the *D*-square law, a droplet having the initial diameter of D_0 has a lifetime of t_d before complete vaporization:

$$t_d = D_0^2/K \tag{1}$$

where the evaporation constant *K* is given by:

$$K = \frac{8\rho\mathcal{D}_{AB}}{\rho_f}\ln(1+B_Y) \equiv \frac{8\rho\mathcal{D}_{AB}}{\rho_{f,liq}}\ln\left(1+\frac{Y_{f,s}-Y_{f,\infty}}{1-Y_{f,s}}\right) \tag{2}$$

where $\mathcal{D}_{AB}$ is the binary diffusivity of air and fuel vapor, Y_f is the mass fraction of fuel at the droplet surface ($Y_{f,s}$) and at infinity ($Y_{f,\infty}$), which we will treat as zero (i.e., the worst case scenario of maximum vaporization rate). ρ is the gaseous mixture density, which can be approximated as the crossflow air's density, since fuel mass fraction drops off rapidly with distance from the surface. ρ_f is the liquid fuel density. The most challenging (and physically important) part of this analysis is to determine the values of $\mathcal{D}_{AB}$ and $Y_{f,s}$ at our operating conditions.

A.1 Estimation of Binary Diffusivity

Riazi (2005) provides the following expression for estimating gas-gas diffusivities in low-pressure conditions where the ideal gas law remains a good approximate (i.e., in this investigation's test-conditions):

$$\mathcal{D}_{AB} = \frac{3\times\pi}{8} \times 10^{-1} \times \left(\frac{k_B^3}{\pi^3}\right)^{\frac{1}{2}} \left(\frac{1}{2m_A} + \frac{1}{2m_B}\right)^{\frac{1}{2}} \frac{T^{\frac{3}{2}}}{P\frac{1}{4}(d_A+d_B)^2} \tag{3}$$

where $k_B = 1.381 \times 10^{-23} J/K$ is the Boltzmann constant, *T* is temperature in *K*, *P* is pressure in *bar*, *m* is the per-molecule mass in *kg*, and *d* is the hard sphere molecular diameter in *m*. $\mathcal{D}_{AB}$ has the unit of cm^2/s in this expression.

According to Riazi (2005), *d* could be determined from viscosity by the following:

$$\mu = \frac{2}{3\pi^{\frac{2}{3}}} \frac{\sqrt{mk_BT}}{d^2} \tag{4}$$

where μ is the dynamic viscosity in $Pa \cdot s$. For pressure less than 60% of the critical pressure (i.e., our experiment), viscosity is primarily a function of temperature only, and the following correlation can be used:

$$\mu = \frac{AT^B}{\left(1+\frac{C}{T}+\frac{D}{T^2}\right)} \tag{5}$$

where the error is typically about 5%. Jet-A (or kerosene) is a complex fuel containing many types of hydrocarbon molecules. To make the analysis tractable, we consider *n*-decane as a good single-species surrogate for Jet-A, in accordance with Honnet et al. (2009)'s findings. The correlation constants are given below:

Table A.1 – Empirical constants for Equation (5) from Riazi (2005).

	A	B	C	D	*MW* (*g/mol*)
Air	1.4241×10^{-6}	5.0390×10^{-1}	1.0828×10^{2}	0.0000	28.97
n-Decane	2.6408×10^{-8}	9.4870×10^{-1}	7.1000×10	0.0000	142.29

A.2 Estimation of Surface Mass Fraction

The conversion of liquid fuel to vapor on the surface, which drives the surface mass fraction, is a key parameter to determining evaporation rate. In droplets vaporization analysis, the process is typically assumed to be at a steady-state condition where the surface of the droplet is saturated with fuel vapor; i.e., $P_{f,s} = P_{f,saturate}(T_{cf})$. Thus, the surface mole fraction $X_{f,s}$ is given by:

$$X_{f,s} = \frac{P_{f,sat}}{P_{cf}} \tag{6}$$

The surface mass fraction is then given by:

$$Y_{f,s} = \frac{X_{f,s}MW_f}{MW_{mix}} \equiv \frac{X_{f,s}MW_f}{\sum X_i MW_i} \tag{7}$$

where MW is molecular weight. $\frac{P_{f,sat}}{P_{cf}}$ in Equation (6) was determined through integrating the Clausius-Clapeyron equation:

$$\frac{dP_{sat}}{P_{sat}} = \frac{h_{fg}}{R_u/MW_f}\frac{dT_{sat}}{T_{sat}^2} \tag{8}$$

Equation (8) is integrated from the reference boiling temperature at crossflow pressure, $T_{boil}\left(P = P_{cf}\right)$, to T_{cf}, which yields the following expression:

$$\frac{P_{f,sat}}{P_{cf}} = \exp\left[-\frac{h_{fg}}{R_u/MW_f}\left(\frac{1}{T_{cf}} - \frac{1}{T_{boil}}\right)\right] \tag{9}$$

The determination of T_{boil} and the latent heat of vaporization (h_{fg}) is needed to close this problem. T_{boil} of *n*-decane under atmospheric condition ("normal boiling point, $T_{b,normal}$" in *K*) can be estimated from the Riazi-Daubert Correlation (Riazi, 2005):

$$T_{b,normal} = 3.76587e^{3.7741\times10^{-3}MW + 2.98404SG - 4.25288\times10^{-3}MW\cdot SG}MW^{0.40167}SG^{-1.58262}$$

where MW is the molecular weight in *g/mol*, and *SG* is the specific gravity. The dimensionless *SG* can be estimated from the "API gravity", defined as:

$$SG = \frac{141.5}{API_{gravity} + 131.5} \tag{10}$$

The conversion of normal boiling point to elevated pressure boiling point ($T_{b,elev} = T_{cf}$) is also given by Riazi (2005):

$$T'_{b,normal} = \frac{748.1QT_{b,elev}}{1+T_{b,elev}(0.3861Q-0.00051606)} \tag{11}$$

$$T_{b,normal} = T'_{b,normal} + 1.3889F(K_W - 12)\log_{10}\frac{P}{760} \tag{12}$$

$$F = -3.2985 + 0.009T_{b,normal} \tag{13}$$

$$Q = \frac{6.412631-0.989679\log_{10}P}{2770.085-36\log_{10}P} \tag{14}$$

where the pressure *P* is given in *mmHg*, and temperatures *T* are in *K*. Solving for $T_{b,elev}$:

$$T_{b,elev} = \left(\frac{748.1Q}{T'_{b,normal}} - 0.3861Q + 0.00051606\right)^{-1} \tag{15}$$

The following properties for *n*-decane are given in Riazi (2005) as: $API_{gravity} = 61.2$ and $K_W = 12.67$.

To close the problem, the heat of vaporization h_{fg} in unit of *J/K* has to be known. We use Riazi (2005)'s simple correlation for enthalpy of vaporization at atmospheric condition:

$$h_{fg,normal} = \frac{R_u}{MW_f/1000}T_{b,normal}\left(4.5 + \ln T_{b,normal}\right) \tag{16}$$

Subsequently, the heat of vaporization at the correct temperature (T_{cf}) can be calculated using the Watson relation:

$$h_{f,g} = h_{fg,normal}\left(\frac{1-T_{cf}/T_c}{1-T_{b,normal}/T_c}\right) \tag{17}$$

where T_c is the critical temperature of *n*-decane: 617.7*K*.

A.3 Results

Results from the calculations are shown in Figure A.1 below. The plot describes the % of droplet projected area that is lost due to vaporization by the time they reach the downstream location of $40d_f$ (i.e., end of the imaged volume). The calculation assumed droplets convection

velocity equal to U_{cf} and a far-field fuel mass fraction of zero. In the limit of geometric optics, the loss in projected area is directly proportional to the loss in the spray's light-attenuation tendency.

We expect droplets sizes to be on the order of 10-150μm in our TF-JICF. The plot shows that on the small end near 5μm, up to 25% of the projected droplet area can be lost by the time it reaches the end of the imaged volume. However, the loss percentages decrease rapidly with increasing droplet sizes. At 10μm, only 6% of area is lost in the worst case. When droplets exceed 25μm, the loss becomes less than 1% and is essentially negligible. In summary, at $T_{cf} \approx 150^{o}C$, droplet vaporization has negligible impact on the physics of the problem, as well as the shadowgraph images.

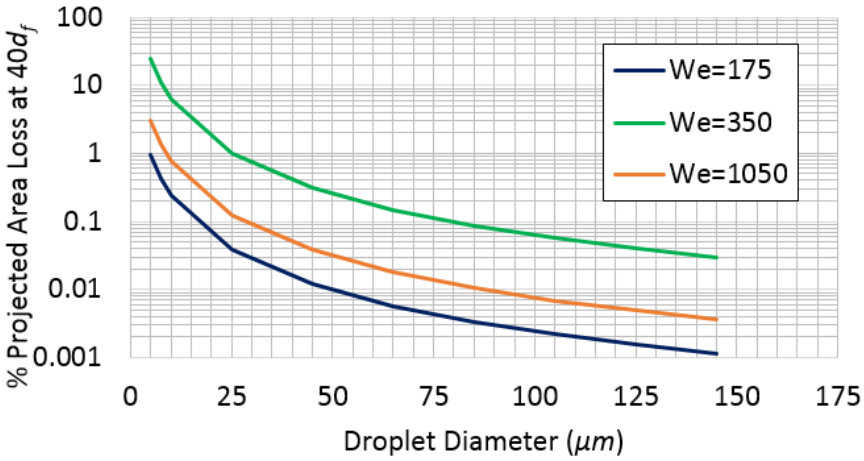

Figure A.1 – Estimated loss of droplets projected area due to vaporization.

APPENDIX B. TEST-CONDITIONS AND SPRAY-PENETRATION DATA

This appendix provides the exact test conditions achieved during the TF-JICF experiments, as well as the P_1 and $z/d_{f,origin}$ values that describe the spray's centerline and outer-edge trajectories at each test-point using the log-based trajectory curve-fit function:

$$\left(\frac{x}{d_f}\right) = P_1 \times \ln\left[\frac{z}{d_f} - \frac{z}{d_{f,origin}} + 1\right] \quad (1)$$

where x is the spray penetration from the test-channel wall at a given position z, and $z/d_{f,origin}$ is an empirical adjustment for the spray's virtual origin. $z/d_{f,origin}$ is typically non-zero at high-dP conditions when the spray-plume is "blasted" forward from its actual injection point by air. The adjustment is applied to the outer-edge trajectories only and set to zero for centerlines.

For the cases of AB-SICF where the dominant wall-plume formed, the centerline trajectory continues to refer to the spray-core's centerline, instead of the wall-plume. The largest error of the P_1 parameter comes from the deviation of the raw trajectory from the curve-fit shape-function. This error is expressed in terms of the standard deviation of the raw trajectory from the fit.

Table B.1 – Test conditions and trajectory constants for We_{cf}≈175, J≈10 test-points.

We_{cf}≈175, J≈10								
J	10.07	9.74	9.92	9.27	9.58	9.29	9.48	8.83
%dP	-2.69	5.83	13.36	23.36	51.59	74.56	97.07	147.51
We_{cf}	178.62	181.24	179.48	187.83	181.60	183.98	179.07	179.07
T_{cf} (^oC)	132.06	127.24	126.29	125.42	124.19	122.77	122.16	121.46
P_{cf} (atm)	1.85	1.88	1.86	1.89	1.88	1.88	1.83	1.83
U_{cf} (m/s)	64.36	63.88	63.85	64.71	63.74	64.08	63.99	63.93
T_f (^oC)	64.89	60.94	59.82	58.48	55.71	53.37	51.80	49.68
T_{air} (^oC)	20.36	18.32	17.67	17.13	17.01	16.98	16.98	16.98
ALR	0	0.11	0.17	0.21	0.30	0.37	0.43	0.57
VR	0	4.88	7.26	8.61	11.64	13.78	15.21	16.19
P_1,outer (stdev)	5.94 (0.29)	6.13 (0.20)	6.12 (0.11)	5.99 (0.16)	6.83 (0.23)	6.84 (0.14)	6.65 (0.13)	7.02 (0.28)
$\frac{z}{d_{f,origin}}$	-0.35	-0.77	-1.50	-1.84	-2.65	-3.29	-3.69	-3.69
P_1,center (stdev)	4.19 (0.34)	4.57 (0.23)	4.67 (0.32)	5.01 (0.22)	4.11 (0.28)	3.92 (0.34)	4.25 (0.27)	4.80 (0.47)

Table B.2 – Test conditions and trajectory constants for We_{cf}≈175, J≈20 test-points.

We_{cf}≈175, J≈20								
J	19.22	19.55	18.61	18.98	18.98	18.92	19.32	19.15
%dP	-2.54	5.49	12.66	23.52	48.52	68.72	95.58	145.14
We_{cf}	178.32	179.24	177.67	177.27	180.21	180.79	181.46	179.30
T_{cf} (^oC)	105.83	107.30	107.81	108.79	110.49	111.18	112.11	113.32
P_{cf} (atm)	1.84	1.87	1.83	1.83	1.89	1.88	1.88	1.87
U_{cf} (m/s)	6230	62.10	62.56	62.57	62.19	62.50	62.65	62.68
T_f (^oC)	54.33	48.34	50.41	48.55	46.92	45.39	44.28	42.67
T_{air} (^oC)	16.97	16.47	16.00	15.75	15.95	16.01	15.99	15.99
ALR	0	0.07	0.11	0.15	0.21	0.25	0.30	0.39
VR	0	3.14	4.86	6.11	8.08	9.48	10.58	11.02
P_1,outer (stdev)	7.43 (0.40)	7.85 (0.26)	7.71 (0.10)	7.49 (0.16)	7.47 (0.25)	7.56 (0.27)	7.48 (0.19)	7.56 (0.17)
$\frac{z}{d_{f,origin}}$	-0.72	-0.88	-1.23	-1.79	-2.38	-2.91	-3.61	-3.87
P_1,center (stdev)	5.61 (0.31)	5.95 (0.32)	5.93 (0.25)	5.92 (0.20)	6.01 (0.25)	5.23 (0.38)	5.00 (0.27)	5.35 (0.29)

Table B.3 – Test conditions and trajectory constants for We_{cf}≈350, J≈5 test-points.

We_{cf}≈350, J≈5								
J	4.75	5.24	5.30	4.65	5.14	4.64	4.00	5.17
%dP	-3.80	5.19	12.52	23.24	48.20	70.92	92.44	169.34
We_{cf}	342.96	343.75	342.91	341.60	337.11	341.31	342.98	339.07
T_{cf} **(ºC)**	186.35	190.50	190.85	191.15	190.98	190.85	190.86	190.15
P_{cf} **(atm)**	3.79	3.83	3.82	3.85	3.81	3.80	3.84	3.84
U_{cf} **(m/s)**	66.34	66.39	66.40	66.03	65.93	66.44	66.21	65.81
T_f **(ºC)**	81.97	75.45	76.31	70.12	70.58	66.12	64.85	58.09
T_{air} **(ºC)**	52.65	35.11	33.20	31.22	29.07	27.66	26.09	24.18
ALR	0	0.18	0.27	0.41	0.58	0.74	0.93	1.18
VR	0	4.10	5.97	8.53	11.53	14.22	16.69	15.08
P_1***,outer (stdev)***	4.21 (0.28)	4.54 (0.21)	4.58 (0.08)	4.81 (0.10)	5.47 (0.15)	5.70 (0.14)	5.83 (0.19)	7.28 (0.28)
$\frac{z}{d_{f,origin}}$	-0.61	-0.80	-1.68	-1.98	-2.89	-2.99	-3.10	-2.81
P_1***,center (stdev)***	3.10 (0.34)	3.40 (0.34)	3.60 (0.24)	3.20 (0.31)	3.13 (0.27)	3.97 (0.33)	4.33 (0.28)	4.56 (0.43)

Table B.4 – Test conditions and trajectory constants for We_{cf}≈350, J≈20 test-points.

We_{cf}≈350, J≈20								
J	19.44	19.38	19.57	19.60	21.34	20.01	19.62	19.47
%dP	-2.62	4.57	12.79	24.10	45.16	72.92	93.19	142.71
We_{cf}	345.33	345.48	343.33	342.92	342.92	342.76	342.85	335.33
T_{cf} **(ºC)**	179.92	182.48	183.26	183.92	184.74	185.81	186.44	187.69
P_{cf} **(atm)**	3.79	3.79	3.79	3.79	3.79	3.79	3.79	3.79
U_{cf} **(m/s)**	66.11	66.32	66.17	66.17	66.22	66.27	66.35	65.70
T_f **(ºC)**	75.82	69.22	63.11	62.04	58.30	57.23	56.40	55.10
T_{air} **(ºC)**	29.13	24.83	24.73	24.40	23.97	24.00	23.68	22.78
ALR	0	0.09	0.15	0.20	0.27	036	0.42	0.55
VR	0	2.00	3.16	4.18	5.36	6.88	7.59	7.81
P_1***,outer (stdev)***	6.78 (0.48)	6.74 (0.28)	6.67 (0.08)	6.55 (0.09)	6.65 (0.19)	6.43 (0.20)	6.36 (0.16)	7.12 (0.28)
$\frac{z}{d_{f,origin}}$	-0.96	-1.02	-1.58	-1.84	-2.43	-3.10	-3.45	-3.55
P_1***,center (stdev)***	4.91 (0.49)	5.09 (0.32)	5.26 (0.21)	5.20 (0.18)	4.77 (0.26)	4.83 (0.48)	4.77 (0.39)	5.14 (0.39)

Table B.5 – Test conditions and trajectory constants for We_{cf}≈350, J≈40 test-points.

We_{cf}≈350, J≈40

J	39.17	40.13	40.36	39.42	38.96	38.35	38.14	37.48
%dP	-2.86	5.24	12.25	23.70	44.97	71.65	118.01	171.64
We_{cf}	343.44	330.58	328.98	334.21	335.72	338.39	337.46	332.02
T_{cf} **(°C)**	176.65	173.83	172.84	172.13	171.16	170.37	169.31	168.33
P_{cf} **(atm)**	3.81	3.79	3.79	3.79	3.79	3.79	3.79	3.79
U_{cf} **(m/s)**	65.50	64.23	64.01	64.47	64.55	64.71	64.55	63.96
T_f **(°C)**	77.20	70.22	70.61	67.79	67.40	62.58	55.80	54.99
T_{air} **(°C)**	39.79	34.42	31.97	30.55	29.06	27.95	25.68	24.81
ALR	0	0.06	0.10	0.14	0.20	0.26	0.35	0.44
VR	0	1.26	2.13	2.95	4.04	5.01	5.57	5.71
P_1***,outer (stdev)***	9.60 (0.63)	9.26 (0.39)	9.34 (0.32)	8.88 (0.24)	8.50 (0.31)	7.97 (0.32)	7.44 (0.16)	8.15 (0.19)
$\frac{z}{d_{f,origin}}$	-1.15	-1.15	-1.34	-1.58	-2.00	-2.67	-3.61	-3.66
P_1***,center (stdev)***	6.97 (0.46)	7.00 (0.28)	7.14 (0.22)	6.92 (0.19)	6.55 (0.29)	5.95 (0.38)	5.45 (0.23)	5.91 (0.33)

Table B.6 – Test conditions and trajectory constants for We_{cf}≈1050, J≈5 test-points.

We_{cf}**≈1050,** J**≈5**					
J	5.14	5.16	5.14	5.06	4.95
%dP	-3.02	5.25	13.61	25.86	51.43
We_{cf}	1048.37	1045.37	1046.45	1046.11	1045.66
T_{cf} **(°C)**	149.03	146.50	144.78	142.93	141.23
P_{cf} **(atm)**	9.29	9.31	9.31	9.33	9.34
U_{cf} **(m/s)**	70.97	70.61	70.50	70.25	70.06
T_f **(°C)**	57.99	53.70	51.81	49.00	43.96
T_{air} **(°C)**	62.10	49.31	41.27	34.84	29.26
ALR	0	0.25	0.41	0.57	0.84
VR	0	2.36	3.76	4.98	6.76
P_1***,outer (stdev)***	3.83 (0.31)	3.87 (0.24)	3.92 (0.20)	4.10 (0.25)	4.87 (0.17)
$\frac{z}{d_{f,origin}}$	-1.07	-1.31	-1.55	-1.90	-2.59
P_1***,center (stdev)***	2.08 (0.28)	2.53 (0.23)	2.68 (0.17)	2.68 (0.19)	2.79 (0.26)

Table B.7 – Test conditions and trajectory constants for We_{cf}≈1050, J≈20 test-points.

We_{cf}**≈1050,** J**≈20**							
J	20.34	20.17	20.39	20.31	19.84	19.96	19.72

%dP	-4.78	5.05	13.57	25.22	50.97	77.66	104.46
We_{cf}	1042.63	1040.56	1034.55	1036.02	1039.30	1031.96	1031.55
T_{cf} ***(ºC)***	118.69	120.11	121.53	123.66	138.08	135.78	130.85
P_{cf} ***(atm)***	9.31	9.33	9.32	9.32	9.33	9.30	9.31
U_{cf} ***(m/s)***	68.13	68.12	68.07	68.30	69.60	69.28	68.80
T_f ***(ºC)***	47.05	42.19	41.34	40.36	41.87	40.96	39.23
T_{air} ***(ºC)***	29.32	24.03	23.99	23.99	25.66	23.77	23.10
ALR	0	0.13	0.22	0.29	0.42	0.53	0.63
VR	0	1.16	1.86	2.44	3.36	4.03	4.38
P_1***,outer (stdev)***	6.38 (0.49)	6.48 (0.36)	6.48 (0.33)	6.22 (0.32)	5.91 (0.34)	5.90 (0.23)	6.17 (0.17)
$\frac{z}{d_{f,origin}}$	-1.42	-1.44	-1.63	-1.79	-2.35	-2.78	-3.02
P_1***,center (stdev)***	4.16 (0.29)	4.59 (0.36)	4.76 (0.35)	4.70 (0.31)	4.20 (0.32)	3.78 (0.34)	4.41 (0.35)

Table B.8 – Test conditions and trajectory constants for We_{cf}≈1050, J≈25 test-points.

We_{cf}**≈1050,** J**≈25**								
J	27.07	26.03	25.76	25.42	25.17	24.41	23.76	23.79
%dP	-4.75	5.72	13.79	26.08	52.20	77.17	102.38	128.59
We_{cf}	1033.66	1031.50	1027.99	1028.89	1025.96	1023.14	1020.85	1019.89
T_{cf} ***(ºC)***	169.74	172.83	174.93	177.06	179.49	181.23	182.95	184.44
P_{cf} ***(atm)***	9.27	9.29	9.30	9.30	9.31	9.30	9.31	9.31
U_{cf} ***(m/s)***	72.26	72.39	72.39	72.58	72.65	72.70	72.72	72.83
T_f ***(ºC)***	57.29	52.68	51.40	50.24	48.34	46.50	45.45	45.46
T_{air} ***(ºC)***	49.71	42.20	36.80	32.93	29.25	26.23	24.85	24.13
ALR	0	0.12	0.20	0.27	0.39	0.49	0.58	0.66
VR	0	1.17	1.77	2.37	3.13	3.74	4.07	4.11
P_1***,outer (stdev)***	7.28 (0.54)	7.14 (0.40)	7.16 (0.37)	6.95 (0.32)	6.44 (0.43)	6.15 (0.33)	6.18 (0.16)	6.56 (0.15)
$\frac{z}{d_{f,origin}}$	-0.91	-0.96	-1.07	-1.28	-1.74	-2.19	-2.57	-2.73
P_1***,center (stdev)***	5.02 (0.48)	5.14 (0.43)	5.20 (0.29)	5.22 (0.30)	4.84 (0.23)	4.30 (0.28)	4.29 (0.24)	4.80 (0.58)

REFERENCES

"Dry Air Properties." *The Engineering ToolBox*. <http://www.engineeringtoolbox.com/dry-air-properties-d_973.html> 8 Sept 2016.

Adelberg M. "Mean Drop Size Resulting from the Injection of a Liquid Jet into a High-Speed Gas Stream." *AIAA Journal*, Vol. 6, No. 6, pp. 1143-1147 (1968).

Aegis Electronic Group, Inc. "Foculus FO531SB/SC IEEE1394 Digital CCD Camera." *Aegis Electronic Group, Inc.* <http://www.aegis-elec.com/foculus-fo531sb-sc-ieee1394-digital-ccd-camera.html> 2015, 11 April 2016.

Ahn K., Kim J. and Yoon Y. "Effects of Orifice Internal Flow on Transverse Injection into Subsonic Crossflows: Cavitation and Hydraulic Flip." *Atomization and Sprays*, Vol. 16, pp. 15-34 (2006).

Bachalo W., Chigier N. and Reitz R. *Spray Technology Short Course Notes: Volume 1*. Chapter 6, pp. 1-26.

Baranger P., Orain M. and Grisch F. "Fluorescence Spectroscopy of Kerosene Vapour: Application to Gas Turbines." *43rd AIAA Aerospace Sciences Meeting and Exhibit*. (2005).

Becker J. and Hassa C. "Breakup and Atomization of a Kerosene Jet in Crossflow at Elevated Pressure." *Atomization and Sprays*, Vol. 11, pp. 49-67 (2002).

Behzad M., Ashgriz N. and Karney B. W. "Surface Breakup of a Non-Turbulent Liquid Jet Injected into a High Pressure Gaseous Crossflow." *International Journal of Multiphase Flow*, Vol. 80, pp. 100-117 (2016).

Behzad M., Ashgriz N. and Mashayek A. "Azimuthal Shear Instability of a Liquid Jet Injected into a Gaseous Cross-Flow." *J. Fluid Mech.*, Vol. 767, pp. 146-172 (2015).

Bernal L. P. and Roshko A. "Streamwise Vortex Structure in a Plane Mixing Layer." *J. Fluid Mech.*, Vol. 170, pp. 499-525 (1986).

Catton I., Hill D. E. and McRae R. P. "Study of Liquid Jet Penetration in a Hypersonic Stream." *AIAA Journal*, Vol. 6, No. 11, pp. 2084-2089 (1968).

Chen, T. H. et al. "Multi-zone Behavior of Transverse Liquid Jet in High-Speed Flow." *31st Aerospace Sciences Meeting & Exhibit* (1993).

Chigier N. "Spray Science and Technology: Keynote Lecture." *ASME Winter Annual Meeting* (1993).

Chigier N. and Reitz R. D. "Regimes of Jet Breakup and Breakup Mechanisms (Physical Aspects)." *Recent Advances in Spray Combustion: Spray Atomization and Drop Burning Phenomena Volume I*, Kenneth K. K., Vol. 166, Chapter 4, pp. 109-135 (1995).

Dimotakis P. E. “Two-Dimensional Shear Layer Entrainment.” *AIAA Journal*, Vol. 24, No. 11, pp. 1791-1796 (1986).

Dodds W. “Twin Annular Premixing Swirler (TAPS) Combustor.” *The Roaring 20th Aviation Noise & Air Quality Symposium* (2005).

Edelman R. B., Economos C. and Boccio J. “Mixing and Combustion in Two-Phase Flows with Application to the B-O-H-N System.” *AIAA Journal*, Vol. 9, No. 10, pp. 1935-1940 (1971).

Eslamian M., Amighi A. and Ashgriz N. “Atomization of Liquid Jet in High-Pressure and High-Temperature Subsonic Crossflow.” *AIAA Journal*, Vol. 52, No. 7, pp. 1374-1385 (2014).

Exciton. “Pyrromethene 567.” <http://www.exciton.com/pdfs/p567.pdf> 25 June 2016.

Farago Z. and Chigier N. “Morphological Classification of Disintegration of Round Liquid Jets in a Coaxial Air Stream.” *Atomization and Sprays*, Vol. 2, No. 2, pp. 137-153 (1992).

Foust M. J., Thomsen D., Stickles R., Cooper C. and Dodds W. “Development of the GE Aviation Low Emissions TAPS Combustor for Next Generation Aircraft Engines.” *50th AIAA Aerospace Sciences Meeting including the New Horizon Forum and Aerospace Exposition* (2012).

Fric T. F. and Roshko A. “Vortical Structure in the Wake of a Transverse Jet.” *J. Fluid Mech.*, Vol. 279, pp. 1-47 (1994).

Fu Z., Lin Y., Li L. and Zhang C. “Experimental and Numerical Studies of a Lean-Burn Internally-Staged Combustor.” *Chinese Journal of Aeronautics*, Vol. 27, No. 3, pp. 488-496 (2014).

Fuller R. P., Wu P.-K., Kirkendall K. A. and Nejad A. S. “Effects of Injection Angle on Atomization of Liquid Jets in Transverse Airflow.” *AIAA Journal*, Vol. 38, No. 1, pp. 64-72 (2000).

Furuichi N., Cheong K.-H., Terao Y., Nakao S., Fujita K. and Shibuya K. “New Discharge Coefficient of Throat Tap Nozzle Based on ASME Performance Test Code 6 for Reynolds Number from 2.4×10^5 to 1.4×10^7.” *Journal of Fluids Engineering*, Vol. 136 (2014).

Geery, E. L. and Margetts, M. J. “Penetration of a High Velocity Gas Stream by a Water Jet.” *Journal of Spacecraft*, Vol. 6, No. 1 (1969).

Goldstein R. J. and Keuhn T. H. “Optical Systems for Flow Measurement: Shadowgraph, Schlieren, and Interferometric Techniques.” *Fluid Mechanics Measurements*, 2nd Edition, Chapter 7, pp. 451-455 (1996).

Gopala, Y., Zhang, P., Bibik, O., Lubarsky, E. and Zinn, B. T. “Liquid Fuel Jet in Crossflow-Trajectory Correlations Based on the Column Breakup Point,” *48th AIAA Aerospace Sciences Meeting Including the New Horizons Forum and Aerospace Exposition* (2010).

Greensted A. “Otsu Thresholding.” *The Lab Book Pages: An Online Collection of Electronics Information.* <http://www.labbookpages.co.uk/software/imgProc/otsuThreshold.html> 2015, 28 May 2015.

Haenlein A. “Disintegration of a Liquid Jet.” *NASA Technical Memorandum No. 659, Forschung auf dem Gebeite des Ingenieurwesens,* Vol. 2, No. 4 (1931).

Han K. S. and Chung M. K. “Numerical Simulation of Two-Phase Gas-Particle Jet in a Crossflow.” *Aerosol Science and Technology,* Vol. 16, No. 2, pp. 126-139 (1992).

Hanson, A. R. et al. “Shock Tube Investigation of the Breakup of Drops by Air Blasts.” *The Physics of Fluids,* Vol. 6, No. 8 (1963).

Hojnacki, J. T. “Ramjet Engine Fuel Injection Studies.” AD-754 862 (1972).

Honnet S., Seshadri K., Niemann U. and Peters N. “A Surrogate Fuel for Kerosene.” *Proceedings of the Combustion Institute,* Vol. 32, No. 1, pp. 485-492 (2009).

Hopfinger E. J. and Lasheras J. C. “Explosive Breakup of a Liquid Jet by a Swirling Coaxial Gas Jets.” *Physics of Fluids,* Vol. 8, pp. 1696-1698 (1996).

Hsieh, Hsiao, Li and Mongia. “Air-Assisted Fuel Injector for Mixer Assembly of a Gas Turbine Engine Combustor.” US 7,464,553 B2. (2008).

Inamura T. and Nagai N. “Spray Characteristics of Liquid Jet Traversing Subsonic Airstreams.” *Journal of Propulsion and Power,* Vol. 13, No. 2, pp. 250-256 (1997).

Inamura T., Nagai N., Watanabe T. and Yatsuyanagi N. “Disintegration of Liquid and Slurry Jets Traversing Subsonic Airstreams.” *Experimental Heat Transfer, Fluid Mechanics, and Thermodynamics,* pp. 1522-1529 (1993).

Ingebo R. B. “Capillary and Acceleration Wave Breakup of Liquid Jets in Axial-Flow Airstream.” NASA-TP-1791 (1981).

Ingebo R. D. “Aerodynamic Effect of Combustor Inlet Air Pressure on Fuel Jet Atomization.” *J. Propulsion,* Vol. 1, No. 2, pp. 137-142 (1985).

Ko N. W. M. and Au H. “Coaxial Jets of Different Mean Velocity Ratios.” *Journal of Sound and Vibration,* Vol. 100, No. 2, pp. 211-232 (1985).

Kush, E. A. Jr. and Schetz, J. A. “Liquid Jet Injection into a Supersonic Flow.” *AIAA Journal,* Vol. 11, No. 9 (1973).

Lasheras J. C. and Hopfinger E. J. “Liquid Jet Instability and Atomization in a Coaxial Gas Stream.” *Annu. Rev. Fluid Mech.,* Vol. 32, pp. 275-308 (2000).

Laven P. “MiePlot: A Computer Program for Scattering of Light from a Sphere using Mie Theory and the Debye Series.” *MiePlot.* <http://www.philiplaven.com/mieplot.htm> 20 October 2016, 21 November 2016.

Lefebvre A. H. “Airblast Atomization.” *Prog. Energy Combust. Sci.,* Vol. 6, pp. 233-261 (1980).

Lefebvre A. H. “Energy Considerations in Twin-Fluid Atomization.” *Journal of Engineering for Gas Turbines and Power,* Vol. 114, pp. 89-96 (1992).

Lefebvre A. H. “Twin-Fluid Atomization: Factors Influencing Mean Drop Size.” *Atomization and Sprays*, Vol. 2, pp. 101-119 (1992).

Leong M. Y., McDonell V. G. and Samuelsen G. S. “Effect of Ambient Pressure on an Airblast Spray Injected into a Crossflow.” *Journal of Propulsion and Power*, Vol. 17, No. 5, pp. 1076-1084 (2001).

Leong M. Y., McDonell V. G. and Samuelsen S. “Mixing of an Airblast-Atomized Fuel Spray Injected into a Crossflow of Air.” *NASA/CR-2000-210467* (2000).

Leong M. Y., Smugeresky C. S., McDonell V. G. and Samuelsen G. S. “Rapid Liquid Fuel Mixing for Lean-Burning Combustors: Low-Power Performance.” *Journal of Engineering for Gas Turbines and Power*, Vol. 123, pp. 574-579 (2001).

Less D. M. and Schetz J. A. “Transient Behavior of Liquid Jets Injected Normal to a High-Velocity Gas Stream.” *AIAA Journal*, Vol. 24, No. 12, pp. 1979-1986 (1986).

Li L. K. B. “An Experimental Study on Air-Blast Atomization of Viscoelastic Liquids.” *Thesis*. The University of British Columbia (2006).

Li L. K. B., Dressler D. M., Green S. I., Davy M. H. and Eadia D. T. “Experiments on Air-Blast Atomization of Viscoelastic Liquids, Part 1: Quiescent Conditions.” *Atomization and Sprays*, Vol. 19, No. 2, pp. 157-190 (2009).

Li L. K. B., Green S. I., Davy M. H. and Eadie D. T. “Viscoelastic Air-Blast Sprays in a Cross-Flow. Part 1: Penetration and Dispersion.” *Atomization and Sprays*, Vol. 20, No. 8, pp. 697-720 (2010).

Li L. K. B., Green S. I., Davy M. H. and Eadie D. T. “Viscoelastic Air-Blast Sprays in a Cross-Flow. Part 2: Droplet Velocities.” *Atomization and Sprays*, Vol. 20, No. 8, pp. 721-735 (2010).

Liang J. Y. and Kang S. “Experimental Visualization of the Flow Structure for Jet in Crossflow with a Curved Hole Passage.” *Advances in Mechanical Engineering*, Vol. 2012 (2012).

Lichtarowicz A., Duggins, R. K. and Markland E. “Discharge Coefficients for Incompressible Non-Cavitating Flow Through Long Orifices.” *Journal Mechanical Engineering Science*, Vol. 7, No. 2, pp. 210-219 (1965).

Lin S. P. and Reitz R. D. “Drop and Spray Formation from a Liquid Jet.” *Annu. Rev. Fluid Mech.*, 30, pp. 85-105 (1998).

Lubarsky E., Reichel J. R., Zinn B. T. and McAmis R. “Spray in Crossflow: Dependence on Weber Number.” *Journal of Engineering for Gas Turbines and Power*, Vol. 132 (2010).

Lubarsky E., Shcherbik D., Bibik O., Gopala Y. and Zinn B. T. “Fuel Jet in Cross Flow-Experimental Study of Spray Characteristics.” *Advanced Fluid Dynamics*.

Madabhushi, R. K. “A Model for Numerical Simulation of Breakup of a Liquid Jet in Crossflow.” *Atomization and Sprays*, Vol. 13, No. 4, pp. 413-424 (2003).

Marmottant P. and Villermaux, E. “On spray Formation.” *J. Fluid Mech.*, Vol. 498, pp. 73-111 (2004).

Mashayek A., Jafari A. and Ashgriz N. “Improved Model for the Penetration of Liquid Jets in Subsonic Crossflows.” *AIAA Journal*, Vol. 46, No. 11, pp. 2674-2686 (2008).

Mazallon J., Dai Z. and Faeth G. M. “Primary Breakup of Nonturbulent Round Liquid Jets in Gas Crossflows.” *Atomization and Sprays,* Vol. 9, pp. 291-311 (1999).

Mazallon, J. et al. “Aerodynamic Primary Breakup at the Surface of Nonturbulent Round Liquid Jets in Crossflow.” *36th Aerospace Science Meeting & Exhibit* (1998).

Melling, A. “Tracer Particles and Seeding for Particle Image Velocimetry.” *Meas. Sci. Technol.*, Vol. 8, no. 12, pp. 1406-1416 (1997).

Myers W. J. Jr., Mancini A. A., Hsiao G. C.-C., Li S.-C., Hsieh S.-Y. and Mongia H. C. “Method and Apparatus for Actively Controlling Fuel Flow to a Mixer Assembly of a Gas Turbine Engine Combustor.” *United States Patent*, Patent No.: US 8,607,575 B2 (2013).

Nejad, A. S. and Schetz, J. A. “Effects of Properties and Location in the Plume on Droplet Diameter for Injection in a Supersonic Stream.” *AIAA Journal*, Vol. 21, No. 7, pp. 956-961 (1983).

Nejad, A. S. and Schetz, J. A. “Effects of Viscosity and Surface Tension on a Jet Plume in Supersonic Crossflow.” *AIAA Journal*, Vol. 9, No. 8, pp. 458-459 (1984).

Net: New Electronic Technology. “FO531TB/TC.” *IEEE1394 Digital CCD Camera*. < https://net-gmbh.com/files/downloads/camera/tech_data/FO531TB_TC.pdf> 2010, 11 April 2016.

Ng C.-L., Sankarakrishnan R. and Sallam K. A. “Bag Breakup of Nonturbulent Liquid Jets in Crossflow.” *International Journal of Multiphase Flow*, Vol. 34, pp. 241-259 (2008).

Nguyen T. T. and Karagozian A. R. “Liquid Fuel Jet in Subsonic Crossflow.” J. Propulsion, Vol. 8, No. 1, pp. 21-29 (1992).

Photonics Industries International, Inc. “DS Series Diode Pumped UV Lasers.” < http://www.photonic.solutions.zen.co.uk/downloads/acrobat/photonicsindustries/PSdsseriesuv.pdf> 11 April 2016.

Rachner, M., Becker J., Hassa C. and Doerr T. “Modeling of the Atomization of a Plain Liquid Fuel Jet in Crossflow at Turbine Conditions.” *Aerospace Science and Technology*, Vol. 6, pp. 495-506 (2002).

Raynal L. *Instabilite et entrainement a l’interface d’une couche de melange liquide-gaz*. These de Doctorat, Universite Joseph Fourier, Grenoble (1997).

Rehab H., Villermaux E. and Hopfinger E. J. “Flow Regimes of Large-Velocity-Ratio Coaxial Jets.” *J. Fluid Mech.*, Vol. 345, pp. 357-381 (1997).

Reichel J. R., Gopala Y., Lubarsky E., Bibik O., Zinn B. T. “Liquid Fuel Jet in Crossflow-Comparison Between Sharp Edged and Smooth Injection Orifice.” *43rd AIAA/ASME/SAE/ASEE Joint Propulsion Conference & Exhibit* (2007).

Reitz R. D. “Atomization and Other Breakup Regimes of a Liquid Jet.” *Ph.D. Thesis Princeton Univ.*, NJ (1978).

Riazi M. R. *Characterization and Properties of Petroleum Fractions*. American Society for Testing and Materials (2005).

Rizk N. K. and Lefebvre A. H. “Influence of Atomizer Design Features on Mean Drop Size.” *AIAA Journal*. Vol. 21, No. 8, pp. 1139-1142 (1983).

Rockwell, Ken. “Nikon 55*mm* f/2.8 Al-s: Micro-NIKKOR (1979-today).” *KenRockwell.com*. < http://www.kenrockwell.com/nikon/55f28ais.htm> May 2012, 11 April 2016.

Sallam K. A., Aalburg C. and Faeth G. M. “Breakup of Round Nonturbulent Liquid Jets in Gaseous Crossflow.” *AIAA Journal,* Vol. 42, No. 12 (2004).

Salzman R. N. and Schwartz S. H. “Experimental Study of a Solid-Gas Jet Issuing into a Transverse Stream.” Journal of Fluids Engineering, Vol. 100, pp. 333-338 (1978).

Samuelsen G. S., Sowa W. A. and Shaffar S. W. “Lean Burn Injector for Gas Turbine Combustor.” *US Patent No. 5,477,685* (1995).

Schetz J. A., Kush E. A. Jr. and Joshi P. B. “Wave Phenomena in Liquid Jet Breakup in a Supersonic Crossflow.” *AIAA Journal*, Vol. 18, No. 7, pp. 774-778 (1979).

Sedarsky D., Paciaroni M., Berrocal E., Petterson P., Zelina J., Gord J. and Linne M. “Model Validation Image Data for Breakup of a Liquid Jet in Crossflow: Part I.” Exp. Fluids., Vol. 49, pp. 391-408 (2010).

Shahangian N., Honnery D., and Ghojel J. “Homogenisation of High Pressure Diesel Fuel Spray Combustion using Porous Ceramic Media.” *ASME 2012 Internal Combustion Engine Division Fall Technical Conference.* (2012)

Sharp D. H. “An Overview of Rayleigh-Taylor Instability.” *Physica D,* Vol. 12, pp. 3-18 (1984).

Sherman A. and Schetz J. “Breakup of Liquid Sheets and Jets in a Supersonic Gas Stream.” *AIAA Journal*, Vol. 9, No. 4, pp. 666-673 (1971).

Sinha A. and Ravikrishna R. V. “Studies on Spray in Crossflow for a Cavity Combustor.” *Joint Propulsion Conferences* (2013).

Sinha A., Prakash R. S., Mohan A. M. and Ravikrishna R. V. “Airblast Spray in Crossflow – Structure, Trajectory and Droplet Sizing.” *International Journal of Multiphase Flow*, Vol 72, pp. 97-111 (2015).

Smith S. H. and Mungal M. G. “Mixing, Structure and Scaling of the Jet in Crossflow.” *J. Fluid Mech.*, Vol. 357, pp. 83-122 (1998).

Spraying Systems Co. “Section F- Air Atomizing Spray Nozzles.” *Spraying Systems Co.: Experts in Spray Technology*. < http://www.spray.com/cat70m/cat70mpdf/ssco_cat70m_f.pdf> 11 April 2016.

Stenzler, J. N. “Penetration of Liquid Jets in a Cross-Flow.” *Atomization and Sprays*, Vol. 16, No. 8, pp. 887-906 (2006).

Tambe S. B., Jeng S.-M., Mongia H. and Hsiao G. “Liquid Jets in Subsonic Crossflow.” *43rd AIAA Aerospace Sciences Meeting and Exhibit* (2005).

Tan, Z. P., Lubarsky E., Bibik O., Shcherbik D. and Zinn B. T. “Application of Planar Laser-Induced Phosphorescence to Investigate Jet-A Injection into a Cross-Flow of Hot Air.” *ASME Turbo Expo 2014: Turbine Technical Conference and Exposition* (2014).

Tan Z. P., Zinn B. T., Lubarsky E., Bibik O., Shcherbik D. and Shen L. “A Moments-Based Algorithm for Optimizing the Information Mined in Post-Processing Spray Images.” *Experiments in Fluids*, Vol. 57, No. 19 (2016).

Thomas R. H. and Schetz J. A. “Distributions Across the Plume of Transverse Liquid and Slurry Jets in Supersonic Airflow.” *AIAA Journal*, Vol. 23, No. 12, pp. 1892-1901 (1985).

Thomson L., Natsui G., Velez C., Kapat J. S. and Vasu S. S. “Experiment Study of Transverse Jet Mapping Using PLIF.” *AIAA SciTech, 53rd AIAA Aerospace Sciences Meeting* (2015).

TSI. “Phase Doppler Particle Analyzer (PDPA)/Laser Doppler Velocimeter (LDV).” *Operations Manual*. P/N 1990048, Rev. B, pp. A-19-21 (2005).

Turns S. R. An Introduction to Combustion: Concepts and Applications, 3rd edition. *The McGraw-Hill Companies* (2012).

Villermaux E. “Mixing and Spray Formation in Coaxial Jets.” *Journal of Propulsion and Power*, Vol. 14, No. 5, pp. 807-817 (1998).

Villermaux E., Rehab H. and Hopfinger E. J. “Breakup Regimes and Self-Sustained Pulsations in Coaxial Jets.” *Meccanica*, Vol. 29, pp. 393-401 (1994).

Wilde B. R. “Dynamics of a Variable Density Ratio Reacting Jets in Unsteady, Vitiated Crossflows.” *Ph.D. Thesis, Georgia Institute of Technology* (2014).

Wotel, G. J. et al. “High Speed Turboramjet combustor Technology Program.” TR-91-2043 (1991).

Wu P. K., Kirkendall K. A. and Fuller R. P. “Spray Structures of Liquid Jets Atomized in Subsonic Crossflows.” *Journal of Propulsion and Power*, Vol. 14, No. 2, pp. 173-182 (1998).

Wu, P. K., Kirkendall, K. A. and Fuller, R. P. “Breakup Processes of Liquid Jets in Subsonic Crossflows.” *Journal of Propulsion and Power*, vol. 13, no. 1, pp. 64-73 (1997).

Wu, P. K., Miranda, R. F., and Faeth, G. M. “Effects of Initial Flow Conditions on Primary Breakup of Nonturbulent and Turbulent Liquid Jets.” *32nd Aerospace Sciences Meeting & Exhibit* (1994).

Yates, C. L. “Liquid Injection into a Supersonic Stream.” AFAPL-TR-71-97 (1972).